RICE UNIVERSITY

Graphene Chemistry: Synthesis and Modulation

by

Zhengzong Sun

A THESIS SUBMITTED
IN PARTIAL FULFILLMENT OF THE
REQUIREMENTS FOR THE DEGREE

Doctor of Philosophy

APPROVED, THESIS COMMITTEE

James M. Tour, Chair
T. T. and W. F. Chao Professor,
Chemistry

Pulickel M. Ajayan
Benjamin M. and Mary Greenwood
Anderson Professor,
Materials Science

W. E. Billups
Professor,
Chemistry

HOUSTON, TEXAS
Sep 2011

Abstract

Graphene Chemistry: synthesis and modulation

by

Zhengzong Sun

This thesis investigates the chemistry of graphene from its basic synthesis to further modulation of its structure, geometry and surface chemical functional groups. A series of wet chemistry and dry chemistry experiments were performed. The wet chemistry includes the diazonium salt functionalization, graphene oxidation and reduction, nanotube unzipping chemistry, graphite intercalation and exfoliation. The dry chemistry includes chemical vapor deposition and solid carbon source synthesis of graphene, the control of domain size and stacking order, graphene hydrogenation and lithographically patterned graphene superlattices. With all these chemical approaches, graphene's electrical and optical properties, solubility in organic solvents, crystallography, and chemical reactivity were carefully investigated and discussed. In addition to the fundamental chemistry of graphene, the bio- and environmental impact of this new material was also taken into consideration and investigated.

Acknowledgments

First of all, I want to say thank you to my "coach" and "life model", Dr. Tour. He is my prime teacher in this country and I feel so thankful that I choose to start my graduate study in this group 4 years ago. As one of the top 10 best chemists in the world, though famous and busy, he still spends a lot of time with his students. In most of the time, he can be found in his office from 6 am to 6 pm from Monday to Saturday whole year except the Thanksgiving. That's an amazing number of working hours and days. Although, sometimes, he has to leave his office and travel like an "iron man" to get funding which feed his 20 hungry young people in the group. All of them are so ambitious to explore science, do experiments and of course spend money without any borders. His working spirit affects all the students and colleagues around him, including me.

Dr. Tour teaches me in many ways, most of them are in the science. We have more than 400 group meetings, 200 lab safety announcements and 16 times lab cleaning together in the last 4 years. He went through all my 200 reports (that is about 4000 for 20 people), 19 co-author papers, 3 patents and 1 thesis in the 4 years. And most of them are not only for one time but multi times. I still remember my first draft of paper, which he gave me a hard time. We went back and forth with about 20 different versions and several Gigabytes data stored in my computer, even it was not the most important work happening in his lab, he still guided me with his

enormous patience and cautiousness. To work with him is one of the most valuable experiences I've had in my life.

I also want to thank Dr. Dustin K. James. He is always the first reader of my papers and this thesis when they are still "ugly". His suggestions on my writings and research are so valuable to me. I could not imagine my graduate life without him. His marathon story is a legendary, which inspires me of my own training. Maybe someday I can have a chance to run a marathon like him.

My special thanks to my family, especially my Mum and Dad, Shangjuan Ji and Fangjing Sun. They don't know much of chemistry and the nanotechnology I am working on. However, they are the most understanding and supportive parents in the world. On each stage of my science life, they trust my intuitions and support me with no hesitation to today. I am so proud that I am the first PhD in my family. On the other hand, I feel not that proud for spending so little time with them in the last 4 years. In order to pursue my dreams, I had to sacrifice most of the family holidays. This Mid-Autumn Festival, the "Chinese Thanksgiving" is 9 days after my defense, hope I could make it this time. (I actually made it, sharing a wonderful time with my parents and my fiancée, Gaoya li, at home.) Just want to say "Thank you and love you all!"

Finally, I want to thank all my friends, colleagues and mentors, whoever participated in my life and researches. Thank you all for giving me your love and laughter, sharing ideas and teaching me the different sides of life and science. I feel so lucky to be with you and can not wait to explore the future with you!

Contents

Chapter 1

INTRODUCTION

1.1. Introduction

Graphene can be viewed as less than 10 layers of graphite[1]. Hence, monolayer graphene is single-atom-thick sheet of sp^2-carbon atoms, while bilayer graphene is two sheets. Since graphene has a structure analogous to benzene and polycyclic aromatic hydrocarbons (PAHs), the chemistries of the compounds can be thought to be similar. Breaking and formation of conjugated sp^2 C-C bonds (basal plane) or sp^2 C-H bonds (edge) are important in this chemistry. To synthesize graphene, various forms of carbon are transformed into the monolayer hexagonal symmetrical conjugated sp^2 structure. To chemically modify graphene, these sp^2 bonds are broken and new bonds are made to exogenic functional groups. However, modification of the flat, rigid structure of graphene is challenging, because of the necessity for overcoming the high energy barriers associated with intralayer conjugation and interlayer Van de Walls forces, thereby usually requiring high

temperature or energetic species to complete the reactions. Under moderate reaction conditions, the yields of the reactions are usually low. For such reasons, new synthetic procedures are needed to optimize graphene's structures and manipulate its properties.

In this thesis we will focus on graphene chemistry that is targeted to produce specific sizes, geometries, bandgaps, doping levels and/or functionalized addends, all modifications that could be applied to the production of graphene-based electronic and optical devices. Other direct applications, such as chemistry to produce graphene-based composite materials and graphene-based nanomedicine products will not be covered in detail in this thesis.

1.2. Synthesis of Graphene

Generally, a material's electrical and optical properties are closely related to its size and dimensions. This is particularly reflected in the dimension control of graphene, both vertically and laterally (Fig. 1.1). Zero bandgap semimetal graphene was first discovered by mechanically reducing the thickness from 3D bulk graphite to a 2D single layer sheet[2]. Soon after this, researchers found that graphene's bandgap could be opened through gating bilayer graphene or shrinking its lateral size to sub-10 nm narrow ribbons[3,4]. However, for most of these early studies, the availability of mechanically exfoliated graphene sheets was limited due to the extremely low yield; in addition, there was no control over graphene's spatial structure. Since it is a mechanical process, there is no chemical method for optimizing the synthesis of mechanically exfoliated graphene. Therefore, for a short

time, graphene represented a precious material that was only available in picogram quantities. Chemically oxidization and exfoliation of graphene oxide and its reduction process produced a large quantity of graphene sheets called chemically converted graphene (CCG), which increased the yield dramatically compared to the mechanically exfoliated method[5-7]. But this technique has its own drawbacks. The harsh oxidization process interrupts the conjugation of graphene, thus requiring additional chemical steps to convert the graphene oxide back to its pristine form, which is never completely attainable[8]. More than that, it is difficult to increase the sheet size and control the geometry of the CCG to produce materials with varied thicknesses and well-defined lateral structures as described in Fig. 1.

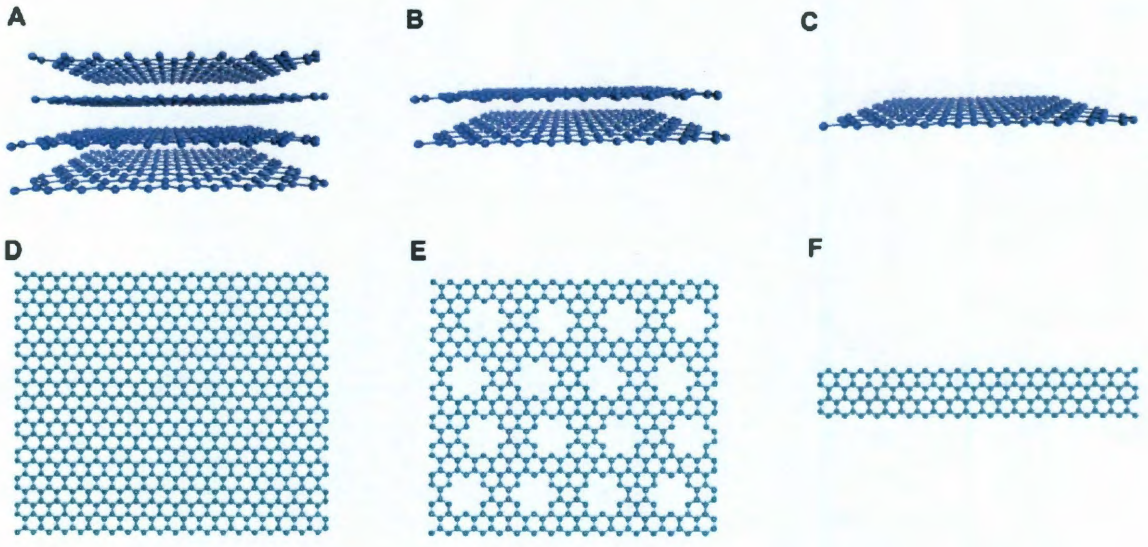

Fig. 1.1 The manipulation of the geometry of graphene. Vertical control of graphene from (A) few-layer graphene, (B) bilayer graphene to (C) monolayer graphene. Lateral control of graphene from (D) plane sheet, (E) graphene mesh to (F) graphene ribbons.

1.2.1. Monolayer Large-Size Graphene

Monolayer large-size graphene could be used to make electronic devices such as field effect transistors (FETs) through top-down lithographic approaches[9]. Also, large size graphene could replace indium-tin-oxide (ITO) for transparent conductive electrodes used in touch screen electronics; however, the graphene will likely have to be used in concert with a metallic grid to rival the low resistance and transparency of ITO[10,11]. Mechanically exfoliated graphene was generally produced only in micron-size sheets, which makes it impossible to use for wafer-size device manufacture[2]. Fortunately, the ability to make larger sheets of graphene has been improved using different methods, shown in Fig. 1.2. Sublimation of Si from SiC was developed to make wafer size graphene, growing epitaxial graphene layers directly atop the SiC substrates[12]. In Fig. 1.2A, the outer hexagonal patterns in the low-energy electron diffraction (LEED) suggest the crystalline structure of the epitaxial graphene. The atomic force microscopy (AFM) image characterizes the continuous surface morphology of graphene film after growth (Fig. 1.2B). Although, this method grows large sheets of graphene film directly atop the insulating substrate without the need to transfer to another substrate, the SiC wafer is relatively expensive. Moreover, the growth is performed at a high processing temperature (~1400 °C) under ultra high vacuum, thereby increasing the cost of energy used in the process. The high temperature can also cause dopant migration or depletion in the silicon wafer; therefore, if there is the desire for embedded electronics in the silicon layer, a subsequent dopant injection would be required. Because there is relatively low

single layer coverage, this technique needs optimization before mass production can begin[13].

The chemical vapor deposition (CVD) method uses gaseous carbon sources such as CH_4 or C_2H_2 to deposit mono- or a few-layer graphene films atop transition metal catalysts, such as Ni, Cu and Ru[10,14-16]. For varied metal substrates, monolayer graphene has been synthesized and optimized with different coverage. By using a single crystal metal surface, single crystal graphene is obtained[17]. According to these reports, Cu has produced the largest continuous high quality graphene films due to its unique surface catalytic mechanism, which yields graphene with monolayer coverage over 95% of the surface and crystal sizes as large as hundreds of microns[18]. In the first work that reported using Cu as the catalyst to grow graphene[15], shown in Fig. 1.2C and 2D, wafer-size graphene could be obtained and transferred to both SiO_2 wafers and other transparent substrates, paving the way for graphene-based electronics and optics applications. Other than gaseous carbon sources, solid carbon sources such as poly(methyl methacrylate) (PMMA) also produce monolayer graphene films atop metal surfaces (Fig. 1.2E). An additional benefit of this method is that it operates at lower growth temperatures from 800 to 1000 °C and produces high quality graphene films[19]. However, both the CVD and the solid carbon source methods need an additional transfer step from the metal substrates to the substrate of choice before fabrication of the electronic device can be completed. The wet etching and physical transferring steps produce inevitable problems due to damage of the graphene; the electronic properties of the

transferred graphene are degraded, scattering impurities can be introduced and surface folding or breaking of the graphene can occur.

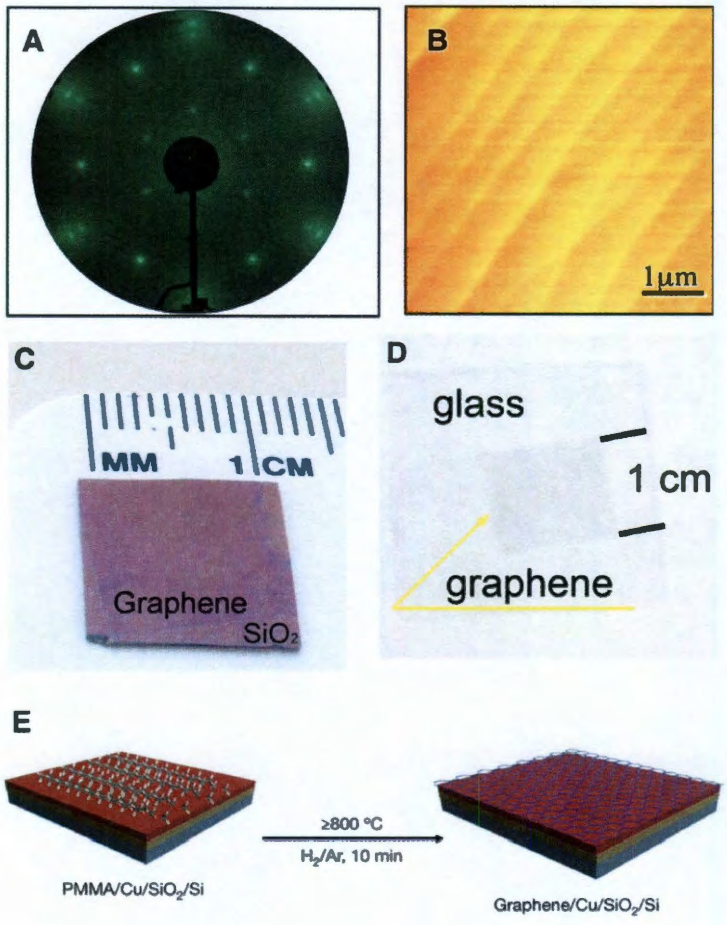

Fig. 1.2 Wafer-size graphene synthesis for epitaxial graphene, CVD graphene and solid carbon sources graphene. (A) LEED pattern (71 eV) of epitaxial graphene and (B) AFM image of epitaxial graphene, showing extended terraces. (C and D) Centimeters of CVD graphene films transferred onto a SiO_2/Si substrate and a glass plate, respectively. (E) Scheme for monolayer graphene derived from solid PMMA films on Cu substrates by heating in an H_2/Ar atmosphere at 800 °C or higher (up to 1,000 °C). (Reprinted from refs 12, 15 and 19.)

Even with these different synthetic methods, the challenge to produce large-size monolayer graphene remains. One step that can be optimized is to find a cleaner transfer of the graphene to another substrate and this has been done using other polymers; alternately, a transfer-free method could be developed[20,21]. The production of graphene with large domain size is also important. Graphene that is grown on polycrystalline Cu has hundreds of micro-domain sizes, still far away from wafer-size single crystals[18]. If a process could be developed that produced a larger domain size, performance differences between graphene-based devices would be minimized, a requirement for industrial mass production of graphene-based electronics.

1.2.2. Graphene Ribbons and Meshes

Graphene is known as a zero-bandgap material. However, to be usable in the existing semiconductor industry, a tunable bandgap is desirable. Theoretical and experimental data has suggested that a bandgap could be opened in graphene ribbons with a sub-10 nm width[4]. Similar to the discovery of graphene, the first synthesis of graphene nanoribbons (GNRs) was accomplished through mechanical exfoliation in solution, with an extremely low yield.[4] The synthesis of GNRs became higher yielding after carbon nanotubes (CNT) were used as precursors[22,23]. By treatment in concentrated sulfuric acid, followed by with 500 wt% $KMnO_4$ for 1 h at room temperature (22 °C) and 1 h at 55–70 °C, the CNTs (both single-wall CNT and multi-wall CNT) are longitudinally unzipped[22]. The oxidation process produces graphene oxide nanoribbons (Fig. 1.3A) in large amounts. By using a

complementary process of metal intercalation (Fig. 1.3B), GNRs without surface oxidation can be synthesized and dispersed in solution in large lab batches[22]; the potassium intercalation and splitting involves no harsh oxidation conditions, thereby only forming GNRs with their conjugation largely intact[24]. Both of the methods for synthesizing graphene oxide nanoribbons and GNRs produce the products in much higher yield than the original mechanical exfoliation method. In addition, the bulk production and the high solubility of the graphene oxide nanoribbons and GNRs in solution promise a lower cost of mass production of transparent electrodes, composite additives and even drug delivery vehicles[25]. Another route using CNTs as the precursors to make GNRs was developed by Dai, H. *et al.* using a polymer (PMMA) mask and controlled O plasma etching to fabricate GNRs directly atop SiO_2/Si wafers[23]. With the GNR-FET electrical measurement, the sub 10 nm nanoribbons show quantum-confined semiconducting characteristics with an I_{on}/I_{off} ratio of > 10 as predicted[23]. Other than using CNT precursors, wafer-sized graphene can be thinned to sub-10-nm widths to open the bandgap. Conventional lithographic methods are limited by the wavelength of the light and the resolution of the photoresist, making it difficult to make sub-10 nm graphene structures. Therefore, unconventional lithographic methods are used to make these confined structures. With nanowires as a physical mask in oxygen plasma etching, GNRs were successfully fabricated and tested on dielectric substrates[26]. However, each individual GNR must be located using an SEM and then fabricated into a device, which makes mass production of devices very difficult. To solve this problem, a

process using anisotropic hydrogen plasma etching to synthesize oriented arrays of GNRs, preferentially producing zigzag-edged ribbons, was recently disclosed[27].

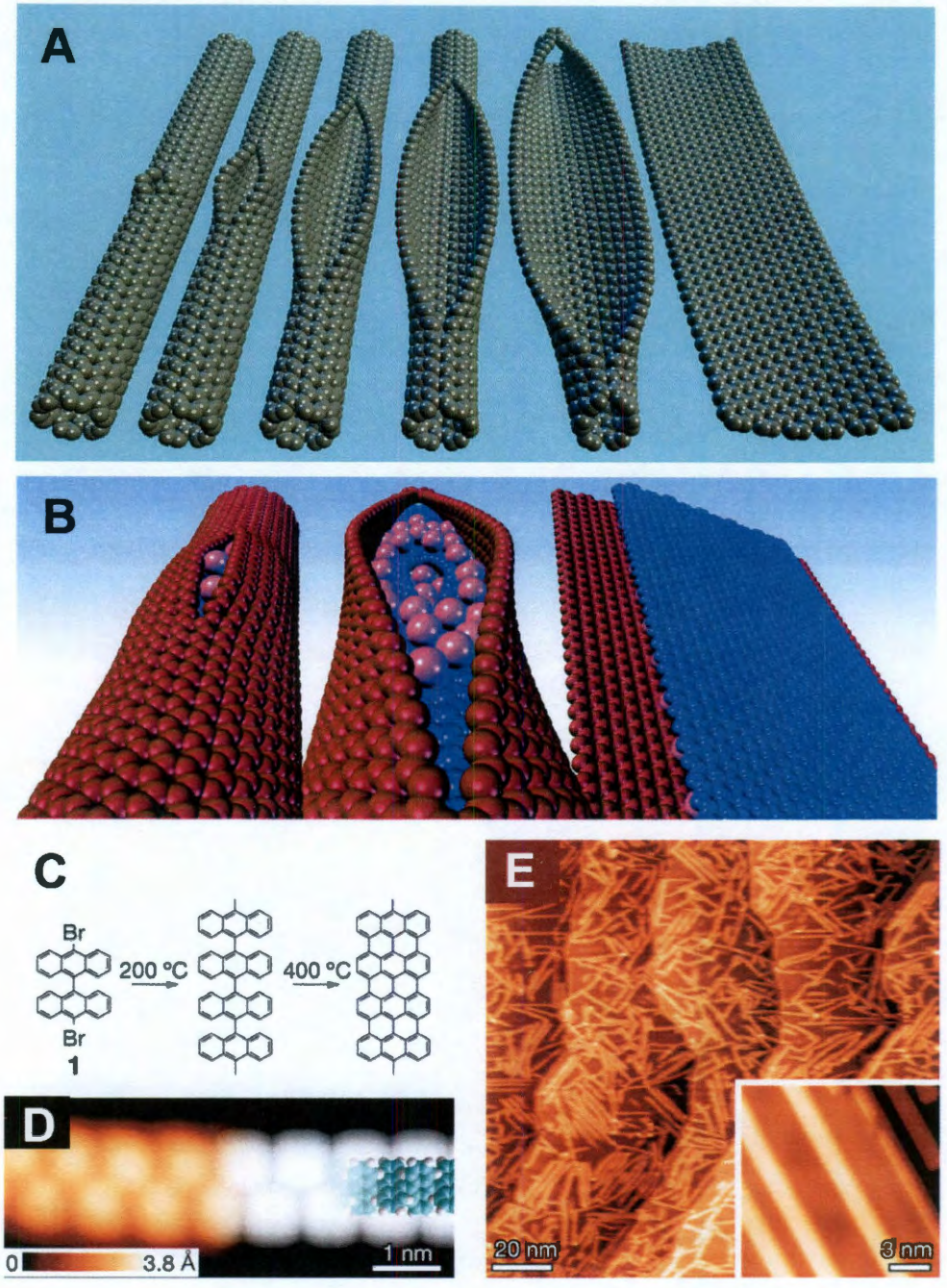

Fig. 1.3 Graphene nanoribbons. (A) Oxidation and (B) reduction approaches to unzip CNTs into GNRs. (C) Bottom-up synthesis of GNRs from precursor **1** to

straight GNR. STM images taken (D) after surface-assisted C–C coupling at 200 °C, showing a polyanthrylene chain and (E) after the final cyclodehydrogenation step at 400 °C, showing a straight GNRs structure. (Reprinted from refs 22, 24 and 30.)

The production of graphene nanomeshes is another promising approach to confine the graphene geometry and open the bandgap without the need for tedious microscopy. Large-size graphene nanomeshes have been synthesized using self-assembled colloid spheres and a deposited metal mask to fill the space between the spheres. After removing both the colloid spheres and the graphene underneath the spheres, only the graphene mesh under the metal mask was retained[28]. The width of the graphene mesh structure was manipulated by changing the diameter of the colloid spheres or with reactive ion etching (RIE)[29]. In addition, using the organic synthetic strategy of surface-assisted C–C coupling (at 200 °C) and cyclodehydrogenation (at 400 °C) (Fig. 1.3C), a variety of GNRs have been synthesized using a bottom-up approach[30]. STM characterization confirmed the width (<3 nm) and length (<100 nm) of the ribbons derived from bianthryl monomers (Fig. 1.3D and E). Using these techniques, the lateral geometry of graphene is well defined and optimized.

1.2.3. Graphene Thickness Control

Graphene with one or two layers (mono- and bilayer) are of the most interest to the community. Since the electrical properties of graphene are closely related to its thickness, controlling the thickness is as important as controlling the width. Bilayer graphene has a tunable band gap, while monolayer graphene does not[31]. In

addition, the stacking order and coupling between the graphene layers also affects the electrical properties of the material[3]. It would be possible to use CVD-synthesized monolayer graphene as building block to produce the required thickness through layer-by-layer transfer and stacking[32]. However, without better orientation techniques, this process would not produce AB (Bernal) stacked graphene due to the random orientation between the two transferred layers. With better control of the CVD system and solid carbon graphene growth, bilayer graphene can be grown directly atop metal substrates[19,33,34]. Typically, bilayer graphene is grown by feeding the growth system a higher rate of carbon or a lower rate of reduction gases (H_2). The exact growth conditions vary from one system to the next due to process differences. In Fig. 1.4A, CVD bilayer graphene could be grown atop Cu substrates through deposition[33]. The presence of bilayer graphene can be confirmed using both Raman spectroscopy and UV-visible spectroscopy transmittance (Fig. 1.4B and C). For bilayer Raman spectra, the 2D peak (~2700 cm^{-1}) can be deconvoluted into 4 separated Lorentz peaks and the G peak (~1580 cm^{-1}) is about 0.8 of the 2D peak. In the UV-visible absorption spectrum, bilayer graphene displays a transmittance of ~ 94% at 550 nm wavelength, compared to the 97% for monolayer graphene[19]. In selected area electron diffraction (SAED) patterns of Bernal bilayer graphene, the intensity ratio of the outer peaks from the {1-210} planes is approximately twice that of the inner peaks from {1-100}[33, 34].

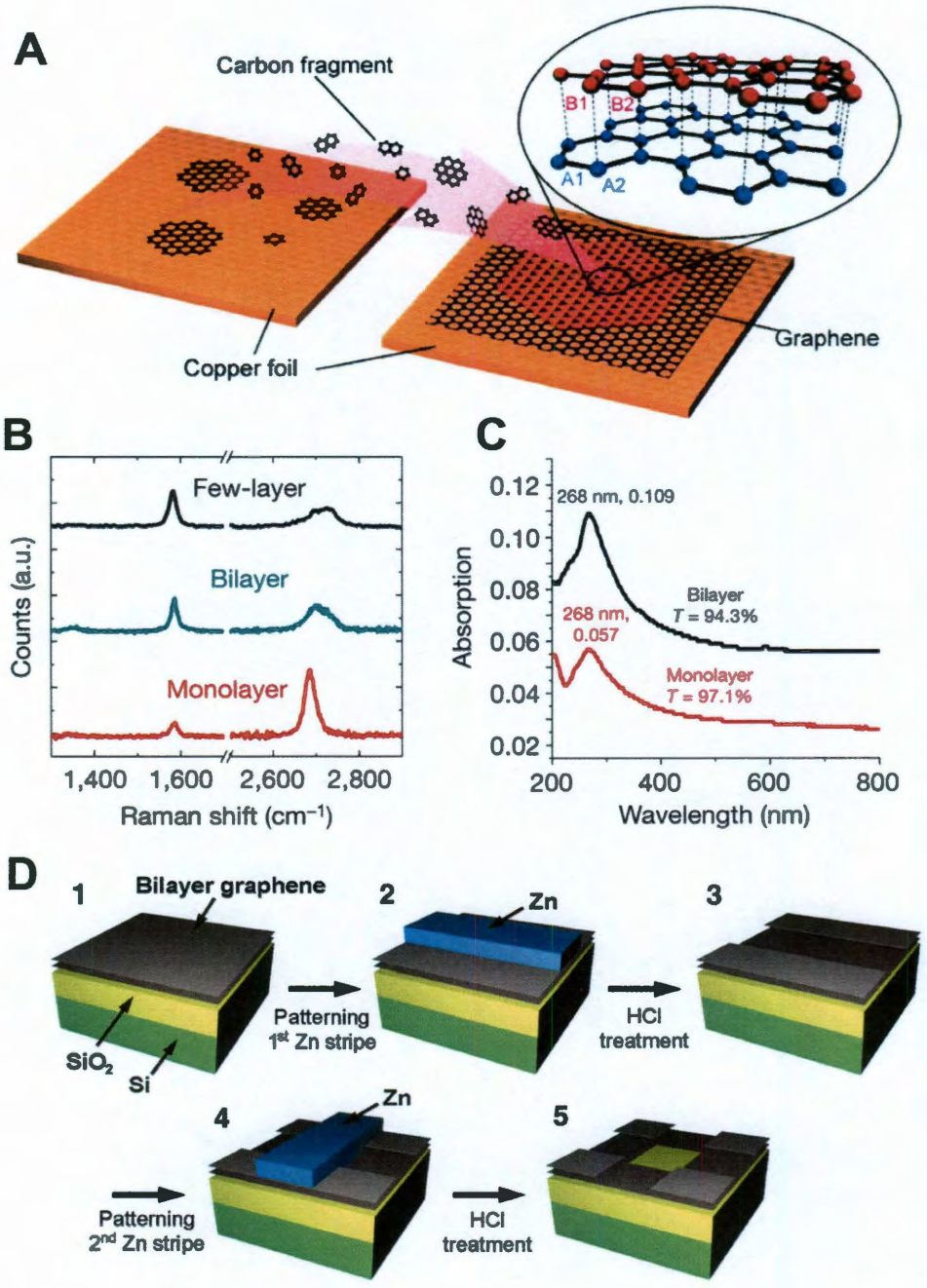

Fig. 1.4 Graphene thickness: bottom-up and top-down strategies. (A) CVD method to grow bilayer Bernal graphene. (B) Raman spectra of few-layer, bilayer, and monolayer graphene derived from PMMA and (C) the UV-visible absorption spectra of monolayer graphene and bilayer graphene derived from PMMA. (D)

Schematic illustration of the layer-by-layer graphene removal method. (Reprinted from refs 19, 33 and 35.)

Most recently, starting with a multilayer graphene film, the desired graphene thickness can be obtained through a top-down layer-by-layer removal technique, a vertical lithographic method shown in Fig. 1.4D[35]. In this method, only one layer at a time is removed from multilayer graphene or graphene oxide flakes by covering them with a sputtered Zn layer, followed by HCl etching. The technique provides a vertical resolution of one carbon atom thick, about 0.34 nm based on the interlayer graphene spacing. Contrary to the method using monolayer graphene as the building unit to produce stacks of non-Bernal graphene, the layer-by-layer removal technique does not change the crystalline orientation, therefore producing the same stacking order as the originate graphite. With the lateral lithography and layer-by-layer removal techniques, there are now methods to manipulate the width and thickness of graphene, with high resolution in both the lateral and vertical dimensions.

1.3. Doping

In the semiconductor industry, not only is the bandgap important, but the type of charge carriers present in the substrate are essential to the electrical characteristics of the device. Pristine graphene displays ambipolar behavior in its FET devices with a neutrality point at zero[2]. For silicon, the dopants (usually phosphorus or boron atoms) provide an excess of electrons or holes as the charge

carriers, producing both n-type and p-type semiconductors. Similarly, substitution of carbon atoms in the structure of graphene with heteroatoms could produce a material with either electrons or holes, exhibiting both n-type and p-type behaviors. Since graphene with p-type behavior is easily made by the adsorption of small molecules such as water from the air, n-type graphene is of the most interest because it is more difficult to make[36]. Several methods have been used to synthesize nitrogen doped graphene. For example, during the CVD process, ammonia gas or N-containing molecules such as melamine can be introduced into the growth system[37,19]. Indeed, N-doped monolayer graphene has been fabricated using this method and the graphene FET devices exhibited typical n-type behavior. Due to the intrinsic properties of C-N bonding, the N atomic concentration in monolayer doped graphene is ~ 2% and it appears to be self-limiting[19]. Making graphene with higher N content remains a challenge. Other than direct growth, chemical treatment of pristine graphene films has also produced N-doped graphene. For example, annealing reduced graphene oxide in ammonia gas atmosphere will produce N-doped graphene flakes[38]. Wafer-size N-doped graphene can also be prepared by exposure of the pristine graphene to ammonium plasma[39]. Electrical annealing of GNRs in ammonia gas will edge dope the GNRs and change their electronic properties to n-type behavior[40]. The chemical environment of the N in the graphene lattices can be determined using XPS. For graphitic-type N, the N1s peak is located at 401.1 eV. The pyridinic-type N are also found in this N-doped graphene, which has an N1s peak around 398.2 eV (Fig. 1.5A and 1.5B) [38]. Other than N doping, heteroatoms such as B, P and Si are also promising candidates for graphene lattice

substitution, but have never been successfully delivered as monolayer doped graphene.

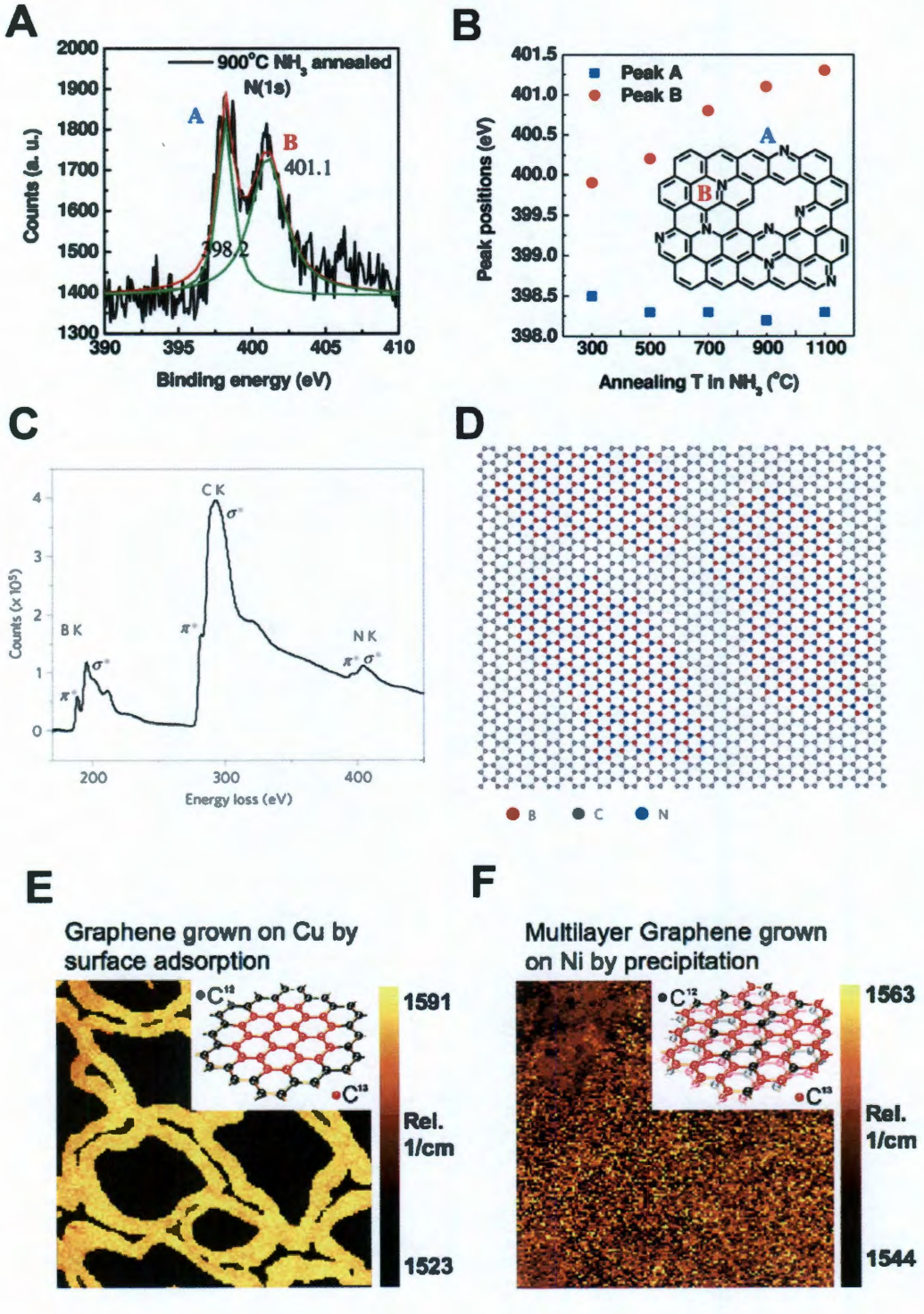

Fig. 1.5 Graphene doping and hybrids structures. Characteristics of nitrogen-doped graphene: (A) N1s Peak in the high resolution XPS spectrum fitted into a lower energy peak (398.2 eV) and a higher energy peak (401.1 eV). (B) Schematic representation of chemical environment of the nitrogen atoms in the N-doped graphene. The 401.1 eV peak represents "graphitic" N and the 398.2 eV peak corresponds to "pyridinic" N. Characteristics of *h*-BNC film (C) K-shell excitations of B, C and N are revealed from the core EELS spectra and (D) atomic model of the hybridized *h*-BN and graphene domains. Raman mapping of ^{12}C and ^{13}C hybrid CVD graphene produced on (E) Cu with surface catalyst mechanism and (F) Ni with precipitation mechanism. Insets are the atomic models for the ^{12}C and ^{13}C hybrid structures. (Reprinted from refs 38, 41 and 42.)

There are other two unusual doping methods that substitute carbon atoms without breaking the structure of pristine graphene. The first is the *h*-BCN hybrid films, discovered by Ajayan[41]. By simultaneously supplying a CVD system with C and BN sources (methane and ammonia borane, respectively), the 2D monolayer *h*-BCN hybrid film was grown atop a Cu foil. In this new material, the presence of boron and nitrogen atoms are confirmed by the electron energy loss spectroscopy (EELS); the carbon atoms of graphene are replaced with continuous *h*-BN patches (Fig. 1.5C and 5D). Since the composition of the BN and C phases could be tuned, the hybrid film's electrical behavior can be distinguished from pure graphene films[41]. Unique electronic properties are expected if the BN-graphene patterns can be controlled rather than containing randomly distributed domains. The other method for special doping is the ^{13}C replacement of ^{12}C during CVD graphene growth[42]. Because the

same vibration modes of ^{13}C and ^{12}C atoms appear as different peaks in their Raman spectrum, this "doped" material is used to interpolate the CVD growth mechanism with alternate carbon isotope growth. With the Raman mapping of different carbon isotopes in Fig. 1.5E and F, graphene growth on Ni and Cu displays different growth mechanisms: Cu shows a surface catalytic mechanism while Ni exhibits a precipitation mechanism for the growth of graphene[42].

1.4. Surface Covalent Functionalization

Graphene is a chemically inert material, stable in air up to 200 °C[43], therefore it needs relatively high energetic species to break its sp^2 bonds and initiate functionalization reactions. Atomic H generated with a hot tungsten filament has enough reactivity to reduce the graphene to graphane (Fig. 1.6A) [44]. The first successful hydrogenation was performed on mechanically exfoliated graphene and the success of the hydrogenation was confirmed by comparing both electrical measurements and SAED patterns of the graphane to those for graphene[45]. Typical hydrogenated graphene shows a p-type behavior according to its electrical tests with an insulator transition. Specifically, for patterned hydrogenation of graphene on Ir(111) substrate, a bandgap opening around the Fermi level of at least 450 meV was observed[46]. However, with more reactive H plasma, graphene was etched with zigzag preferred edges[27].

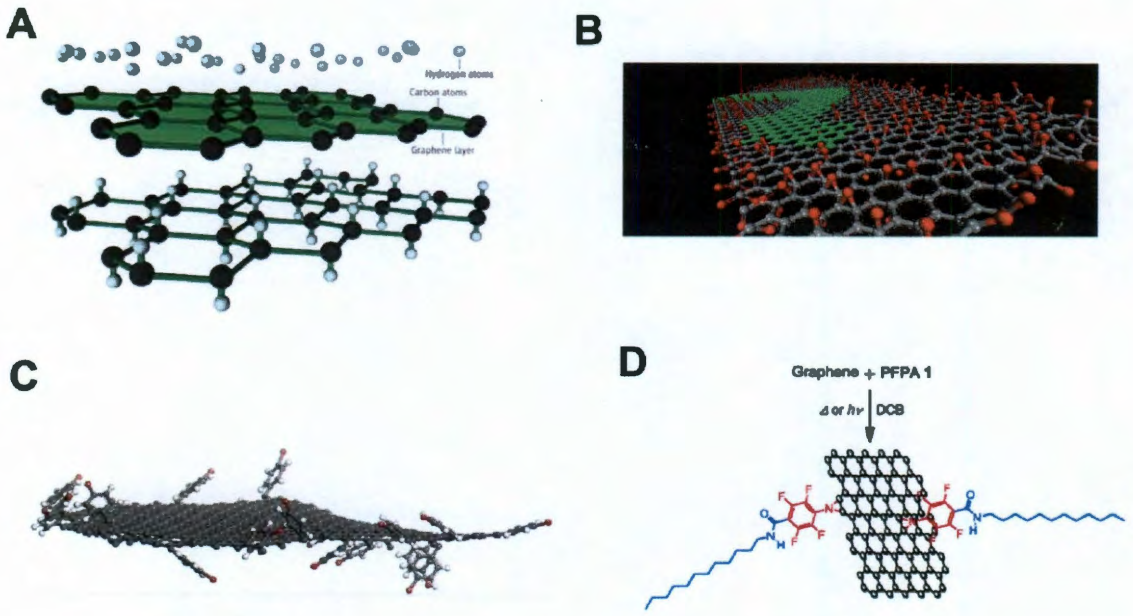

Fig. 1.6 Covalent chemistry to functionalize graphene basal plane and edges. (A) Scheme of graphene hydrogenation. (B) Atomic model of graphene oxide with a "green" conductive graphene pathway. Red spheres represent oxygen atoms. (C) Soluble graphene flakes with an edge aryl functionality derived from diazonium functionalization of graphite followed by solution exfoliation. (D) Azide reaction on graphene. (Reprinted from refs 44, 49 and 52.)

Aryl diazonium salts are one of the moderately reactive species used to covalently functionalize graphene. The functionalization reaction is thought to proceed through a free radical mechanism. Graphene substrates originating from different chemical processes have varied reactivity toward aryl diazonium salts. For example, CCG, which is made from reducing graphene oxide, shows very high reactivity to the diazonium salts, with both the basal plane and the edges becoming functionalized[47]. Epitaxial graphene grown from SiC is also efficiently surface grafted by functionality using diazonium salts[48]. However, the diazonium reaction

with graphite or mechanically exfoliated graphene shows preferentially edge reactivity[49,50]. Soluble graphene could be obtained through the exfoliation from such edge functionalized graphite (Fig. 1.6C). The kinetics of the functionalization on CCG with diazonium salts was investigated by tracking the changes in electrical properties of graphene-based FET devices and the results showed that the reaction was 60% complete in the first 5 min[51]. Azide chemistry is another functionalization approach similar to diazonium chemistry (Fig. 1.6D). The reactive intermediates are nitrenes formed from themolysis or photolysis of azides[52].

Strain and topological defects affect the covalent reactivity of graphene[53,54]. The ideal graphene structure is a flat single crystal with no defects, which would be uniformly reactive everywhere on the sheet except at its edges. However, in synthesized graphene sheets, ripples and topological defects exist, which affect its chemical reactivity. It was found that the strained and defective graphene spots are more reactive than the domains located in a perfect, flat basal plane[53,54]. This is consistent with the results found in the diazonium reaction with different graphene substrates.

The oxidation of graphene using Hummer's method ($KMnO_4$, $NaNO_3$, H_2SO_4) represents a non-controllable way to covalently functionalized the basal plane of graphene since GO is cut into small pieces with potential topological holes on its surface. Most recently, methods have been developed to optimize the synthesis of GO and graphene oxide nanoribbons with much lower defects[55,56]. This optimized method excludes the $NaNO_3$ and increases the amount of $KMnO_4$, and is performed in a 9:1 mixture of H_2SO_4/H_3PO_4. The electrical and TEM measurement suggest that

the basal plane of the GO is less disrupted than when using Hummer's method, and the yield in the optimized reaction is much higher.

1.5. Future Challenges

Even though the field of graphene research is still in its early stages, a blooming and active branch of chemistry and techniques have been developed with the number of publications growing rapidly in the past few years[57]. The remaining scientific goals for this material are no longer, How it can be synthesized? Or, can its electronic properties be predicted? Instead, chemists are being called to make "purer or hybrid" large crystalline graphene sheets; to optimize the transfer technique to the active substrate after synthesis (or avoid transfers altogether); to manipulate this large single molecule's physical shapes and properties; and finally to make commercial products that work faster, more efficiently, save energy or transfer energy. As one of the few nanomaterials that bridge the low dimensional and the 3D worlds, graphene offers chemists unique challenges and opportunities to broaden the application of chemical techniques to a new material domain.

References

1. Geim, A. K; Novoselov, K. S. The Rise of Graphene. *Nat. Mater.* **2007**, *6*, 183-191.
2. Novoselov, K. S.; Geim, A. K.; Morozov, S. V.; Jiang, D.; Zhang, Y.; Dubonos, S. V.; Grigorieva, I. V.; Firsob, A. A. Electric Field Effect in Atomically Thin Carbon Films. *Science* **2004**, *306*, 666-669.
3. Ohta, T.; Bostwick, A.; Seyller, T.; Horn, K.; Rotenberg, E. Controlling the Electronic Structure of Bilayer Graphene. *Science* **2006**, *313*, 951-954.
4. Li, X.; Wang, X.; Zhang, L.; Lee, S.; Dai, H. Chemically Derived, Ultrasmooth Graphene Nanoribbon Semiconductors. *Science* **2008**, *319*, 1229-1232.
5. Hummers, W. S.; Offeman, R. E. Preparation of Graphitic Oxide J. Am. Chem. Soc. **1958**, *80*, 1339– 1339.
6. Li, D.; Müller, M. B.; Gilje, S.; Kaner, R. B.; Wallace, G. G. Processable Aqueous Dispersions of Graphene Nanosheets. *Nat. Nanotechol.* **2008**, *3*, 101-105.
7. Stankovich, S.; Dikin, D. A.; Piner, R. D.; Kohlhaas, K. A.; Kleinhammes, A.; Jia, Y.; Wu, Y.; Nguyen, S. T.; Ruoff, R. S. Synthesis of Graphene-based Nanosheets *via* Chemical Reduction of Exfoliated Graphite Oxide. *Carbon* **2007**, *45*, 1558-1565.
8. Gao, W.; Alemany, L. B.; Ci, L.; Ajayan, P. M. New Insights into the Structure and Reduction of Graphite Oxide. *Nat. Chem.* **2009**, 1, 403-408.
9. Schwierz, F. Graphene Transistors. *Nat. Nanotechnol.* **2010**, *5*, 487-496.

10. Kim, K. S.; Zhao, Y.; Lee, S. Y.; Kim, J. M.; Kim, K. S.; Ahn, J. H.; Kim, P.; Choi, J. Y.; Hong, B. H. Large-Scale Pattern Growth of Graphene Films for Stretchable Transparent Electrodes. *Nature* **2009**, *457*, 706-710.
11. Bae, S.; Kim, H.; Lee, Y.; Xu, X.; Park, J. S.; Zheng, Y.; Balakrishnan, J.; Lei, T.; Kime, H. R.; Song, Y. I.; *et al.* Roll-to-Roll Production of 30-inch Graphene Films for Transparent Electrodes. *Nat. Nanotechnol.* **2010**, *5*, 574-578.
12. Berger, C.; Song, Z.; Li, X.; Wu, X.; Brown, N.; Naud, C.; Mayou, D.; Li, T.; Hass, J.; Marchenkow, A. N.; *et al.* Electronic Confinement and Coherence in Patterned Epitaxial Graphene. *Science* **2006**, *312*, 1191-1196.
13. Faugeras, C.; Nerrière, A.; Potemski, M.; Dujardin, E.; Berger, C.; Heer, W. A. de Few-Layer Graphene on SiC, Pyrolitic Graphite, and Graphene: a Raman Scattering Study. *Appl. Phys. Lett.* **2008**, *92*, 011914.
14. Reina, A.; Jia, X.; Ho, J.; Nezich, D.; Son, H.; Bulovic, V.; Dresselhaus, M. S.; Kong, J. Large Area, Few-layer Graphene Films on Arbitrary Substrates by Chemical Vapor Deposition. *Nano Lett.* **2009**, *9*, 30-35.
15. Li, X.; Cai, W.; An, J.; Kim, S.; Nah, J.; Yang, D.; Piner, R.; Velamakanni, A.; Jung, I.; Tutuc, E.; *et al.* Large-Area Synthesis of High Quality and Uniform Graphene Films on Copper Foils. *Science* **2009**, *324*, 1312-1314.
16. Sutter, P.; Hybertsen, M. S.; Sadowski, J. T.; Sutter, E. Electronic Structure of Few-Layer Epitaxial Graphene on Ru (0001). *Nano Lett.* **2009**, *9*, 2654-2660.
17. Pan, Y.; Zhang, H.; Shi, D.; Sun, J.; Du, S.; Liu, F.; Gao, H. Highly Ordered, Millimeter-Scale, Continuous, Single-Crystalline Graphene Monolayer Formed on Ru (0001). *Adv. Mater.* **2009**, *21*, 2777-2780.

18. Li, X.; Magnuson, C. W.; Venugopal, A.; An, J.; Suk, J. W.; Han, B.; Borysiak, M.; Cai, W.; Velamakanni, A.; Zhu, Y.; *et al.* Graphene Films with Large Domain Size by a Two-Step Chemical Vapor Deposition Process. *Nano Lett.* **2010**, *10*, 4328-4334.

19. Sun, Z.; Yan, Z.; Jun, Y.; Beitler, E.; Zhu, Yu,; Tour, J. M. Growth of Graphene from Solid Carbon Sources. *Nature* **2010**, *468*, 549-552.

20. Lin, Y. C.; Jin, C.; Lee, J. C.; Jen, S. F.; Suenaga, K.; Chiu, P. W. Clean Transfer of Graphene for Isolation and Suspension. *ACS Nano* **2011**, *5*, 2362-2368.

21. Regan, W.; Alem, N.; Alemán, B.; Geng, B.; Girit, Ç.; Maserati, L.; Wang, F.; Crommie, M.; Zettl, A. A Direct Transfer of Large-area Graphene. *Appl. Phys. Lett.* **2010**, 96, 113102.

22. Kosynkin, D. V.; Higginbotham, A. L.; Sinitskii, A.; Lomeda, J. R.; Dimiev, A.; Price, B. K.; Tour, J. M. Longitudinal Unzipping of Carbon Nanotubes to Form Graphene Nanoribbons. *Nature* **2009**, *458*, 872-876.

23. Jiao, L.; Zhang, L.; Wang, X.; Diankov, G.; Dai, H. Narrow Graphene Nanoribbons from Carbon Nanotubes. *Nature* **2009**, *458*, 877-880.

24. Kosynkin, D. V.; Lu, W.; Sinitskii, A.; Pera, G.; Sun, Z.; Tour, J. M. Highly Conductive Graphene Nanoribbons by Longitudinal Splitting of Carbon Nanotubes using Potassium Vapor. *ACS Nano* **2011**, *5*, 968-974.

25. Zhu, Y.; Lu, W.; Sun Z.; Kosynkin, D. V.; Yao, J. Tour, J. M. High Throughput Preparation of Large Area Transparent Electrodes using Non-Functionalized Graphene Nanoribbons. *Chem. Mater.* **2011**, *23*, 935-939.

26. Bai, J.; Duan, X.; Huang, Y. Rational Fabrication of Graphene Nanoribbons Using a Nanowire Etch Mask. *Nano Lett.* **2009**, *9*, 2083-2087.

27. Yang, R.; Zhang, L.; Wang, Y.; Shi, Z.; Shi, D.; Gao, H.; Wang, E.; Zhang, G. An Anisotropic Etching Effect in the Graphene Basal Plane. *Adv. Mater.* **2010**, *22*, 4014-4019.

28. Bai, J.; Zhong, X.; Jiang, S.; Huang, Y.; Duan, X. Graphene Nanomesh. *Nat. Nanotechnol* **2010**, *5*, 190-194.

29. Sinitskii, A.; Tour, J. M. Patterning Graphene Through the Self-Assembled Templates: Toward Periodic Two-Dimensional Graphene Nanostructures with Semiconductor Properties. *J. Am. Chem. Soc.* **2010**, *132*, 14730-14732.

30. Cai, J.; Ruffieux, P.; Jaafar, R.; Bieri, M.; Braun, T.; Blankenburg, S.; Muoth, M.; Seitsonen, A. P.; Saleh, M.; Feng, X.; *et al.* Atomically Precise Bottom-Up Fabrication of Graphene Nanoribbons. *Nature* **2010**, *466*, 470-473.

31. Zhang, Y.; Tang, T. T.; Girit, C.; Hao, Z.; Martin, M. C.; Zettl, A.; Crommie, M. F.; Shen, Y. R.; Wang, F. Direct Observation of a Widely Tunable Bandgap in Bilayer Graphene. *Nature* **2009**, *459*, 820-823.

32. Li, X.; Zhu, Y.; Cai, W.; Borysiak, M.; Han, B.; Chen, D.; Piner, R. D.; Colombo, L.; Ruoff, R. S. Transfer of Large-Area Graphene Films for High-Performance Transparent Conductive Electrodes. *Nano Lett.* **2009**, *9*, 4359-4363.

33. Yan, K.; Peng, H.; Zhou, Y.; Li, H.; Liu, Z. Formation of Bilayer Bernal Graphene: Layer-by-Layer Epitaxy by Chemical Vapor Deposition. *Nano Lett.* **2011**, *11*, 1106-1110.

34. Lee, S.; Lee, K.; Zhong, Z. Wafer scale homogeneous bilayer graphene films by chemical vapor deposition *Nano Lett.* **2010**, 10, 4702-4707.

35. Dimiev, A.; Kosynkin, D. V.; Sinitskii, A.; Slesarev, A.; Sun, Z.; Tour, J. M. Layer-by-Layer Removal of Graphene for Device Patterning. *Science* **2011**, *331*, 1168-1172.

36. Schedin, F.; Geim, A. K.; Morozov, S. V.; Hill, E. W.; Blake, P.; Katsnelson, M. I.; Novoselov, K. S. Detection of Individual Gas Molecules Adsorbed on Graphene. *Nature Mater.* **2007**, *6*, 652-655.

37. Wei, D.; Liu, Y.; Wang, Y.; Zhang, H.; Huang, L.; Yu, G. Synthesis of N-Doped Graphene by Chemical Vapor Deposition and its Electrical Properties. *Nano Lett.* **2009**, *9*, 1752-1758.

38. Li, X.; Wang, H.; Robinson, J. T.; Sanchez, H.; Diankov, G.; Dai, H. Simultaneous Nitrogen Doping and Reduction of Graphene Oxide. *J. Am. Chem. Soc.* **2009**, *131*, 15939-15644.

39. Lin, Y. C.; Lin, C. Y.; Chiu, P. W. Controllable Graphene N-Doping with Ammonia Plasma. *Appl. Phys. Lett.* **2010**, *96*, 133110.

40. Wang, X.; Li, X.; Zhang, L.; Yoon, Y.; Weber, P. K.; Wang, H.; Guo, J.; Dai, H. N-Doping of Graphene Through Electrothermal Reactions with Ammonia. *Science* **2009**, *324*, 768-771.

41. Ci, L.; Song, L.; Jin, C.; Jariwala, D.; Wu, D.; Li, Y.; Srivastava, A.; Wang, Z. F.; Storr, K.; Balicas, L.; *et al.* Atomic Layers of Hybridized Boron Nitride and Graphene Domains. *Nat. Mater.* **2010**, *9*, 430-435.

42. Li, X.; Cai, W.; Colombo, L.; Ruoff, R. S. Evolution of Graphene Growth on Ni and Cu by Carbon Isotope Labeling. *Nano Lett.* **2009**, *9*, 4268-4272.

43. Chen, S.; Brown, L.; Levendorf, M.; Cai, W.; Ju, S. Y.; Edgeworth, J.; Li, X.; Magnuson, C. W.; Velamakanni, A.; Piner, R. D.; *et al.* Oxidation Resistance of Graphene-Coated Cu and Cu/Ni Alloy. *ACS Nano* **2011**, *5*, 1321-1327.

44. Savchenko, A. Transforming Graphene. *Science* **2009**, *323*, 589-590.

45. Elias, D. C.; Nair, R. R.; Mohiuddin, T. M. G.; Morozov, S. V.; Blake, P.; Halsall, M. P.; Ferrari, A. C.; Boukhvalov, D. W.; Katsnelson, M. I.; Geim, A. K.; *et al.* Control of Graphene's Properties by Reversible Hydrogenation: Evidence for Graphane. *Science* **2009**, *323*, 610-613.

46. Balog, R.; Jorgensen, B.; Nilsson, L.; Andersen, M.; Rienks, E.; Bianchi, M.; Fanetti, M.; Lægsgaard, E.; Baraldi, A.; Lizzit, S.; *et al.* Bandgap Opening in Graphene Induced by Patterned Hydrogen Adsorption. *Nat. Mater.* **2010**, *9*, 315-319.

47. Lomeda, J. R.; Doyle, C. D.; Kosynkin, D. V.; Hwang, W. F.; Tour, J. M. Diazonium Functionalization of Surfactant-Wrapped Chemically Converted Graphene Sheets. *J. Am. Chem. Soc.* **2008**, *130*, 16201-16206.

48. Bekyarova, E.; Itkis, M. E.; Ramesh, P.; Berger, C.; Sprinkle, M.; Heer, W. A. de.; Haddon, R. C. Chemical Modification of Epitaxial Graphene: Spontaneous Grafting of Aryl Groups. *J. Am. Chem. Soc.* **2009**, *131*, 1336-1337.

49. Sun, Z.; Kohama, S.; Zhang, Z.; Lomeda, J. R.; Tour, J. M. Soluble Graphene Through Edge-Selective Functionalization. *Nano Research* **2010**, *3*, 117-125.

50. Lim, H.; Lee, J. S.; Shin, H. J.; Shin, H. S.; Choi, H. C. Spatially Resolved Spontaneous Reactivity of Diazonium Salt on Edge and Basal Plane of Graphene Without Surfactant and its Doping Effect. *Langmuir* **2010**, *26*, 12278-12284.

51. Sinitskii, A.; Dimiev, A.; Corley, D. A.; Fursina, A. A.; Kosynkin, D. V.; Tour, J. M. Kinetics of Diazonium Functionalization of Chemically Converted Graphene Nanoribbons. *ACS Nano* **2010**, *4*, 1949-1954.

52. Liu, L. H.; Yan, M. Functionalization of Pristine Graphene with Perfluorophenyl Azides. *J. Mater. Chem.* **2011**, *21*, 3273-3276.

53. Boukhvalov, D. W.; Katsnelson, M. I. Enhancement of Chemical Activity in Corrugated Graphene. *J. Phys. Chem. C.* **2009**, *113*, 14176-14178.

54. Boukhvalov, D. W.; Katsnelson, M. I. Chemical Functionalization of Graphene with Defects. *Nano Lett.* **2008**, *8*, 4373-4379.

55. Marcano, D. C.; Kosynkin, D. V.; Berlin, J. M.; Sinitskii, A.; Sun, Z.; Slesarev, A.; Alemany, L. B.; Lu, W.; Tour, J. M. Improved Synthesis of Graphene Oxide. *ACS Nano* **2010**, 4, 4806-4814.

56. Higginbotham, A. L.; Kosynkin, D. V.; Sinitskii, A.; Sun, Z.; Tour, J. M. Lower-Defect Graphene Oxide Nanoribbons from Multiwalled Carbon Nanotubes. *ACS Nano* **2010**, *4*, 2059-2069.

57. Geim, A. K. Graphene: Status and Prospects. *Science* **2009**, *324*, 1530-1534.

Chapter 2

SOLUBLE GRAPHENE THROUGH EDGE-SELECTIVE FUNCTIONALIZATION

2.1. Introduction

Graphene is defined as sheets of sp^2-hybridized carbon, where the number of stacked sheets is <10[1]. The production of chemically converted graphene from the reduction of graphene oxide is a convenient method to produce large amounts of graphene[2-4], however, even with efficient reducing agents such as hydrazine or H_2, and annealing at high temperature, the original crystalline structure of graphene is not restored. Graphene oxide is heavily functionalized with many permanent chemical defects, such as holes introduced into the basal plane. These holes are not readily healed even upon annealing. Micromechanically cleaved graphene affords crystalline single sheets of graphene using highly ordered pyrolytic graphite and

adhesive tape[5]. While this method opened an avenue for many fundamental studies, it is likely impossible to scale for the production of larger quantities.

The exfoliation of graphene in the liquid phase, by continuously sonicating graphite in a high surface-tension organic solvent[6, 7], is another route to obtain mono- or few-layered sheets of graphene that are suspended in a dark mixture. However, the suspended graphene sheets tend to aggregate due to the lack of stabilizing groups such as surfactants or polymers to reduce interlayer attractions[8]. Because of significant π–π interactions, unlike graphene oxide and chemically converted graphene, liquid phase exfoliated graphene cannot be stabilized as a concentrated mixture.

Chemical vapor deposition (CVD) techniques have been used to grow thin and highly crystalline graphitic layers atop catalysts[9,10]. At elevated temperatures, methane or other volatile carbon precursors are decomposed on metal catalysts, such as Ni or Cu, in a reductive atmosphere to produce graphene[11]. Epitaxial growth by annealing SiC at temperatures as high as 2000 °C produces graphene that is deposited directly on the SiC wafer[12–14]. This method is referred to as chemical solid deposition (CSD) since the precursor is a solid rather than a gas. While these growth methods, coupled with patterning, will likely be among the dominant growth methods for future wafer-size high performance graphene electronics, generating bulk scales of few-layered graphene for other materials applications will be problematic using the CVD and CSD approaches.

Recently, chemically converted graphene was successfully functionalized using diazonium salts and the product showed improved solubility in polar aprotic organic solvents compared to unfunctionalized chemically converted graphene[15]. In this chapter, thermally expanded graphite is predominantly edge-functionalized with 4-bromophenyl groups using in situ formation of the corresponding diazonium salt from 4-bromoaniline. Mild sonication in *N,N'*-dimethylformamide (DMF) then exfoliates thin chemically-assisted exfoliated graphene (CEG) sheets from the bulk functionalized graphite. CEG is more soluble than pristine graphene in DMF. In addition, more than 70% of the CEG flakes have less than 5 layers. The edge functional groups are detected by elemental mapping using energy filtered transmission electron microscopy (EFTEM). By taking advantage of the edge-selective functionalization, and low basal plane disruption, a bulk preparation of soluble yet more conductive graphene has been demonstrated.

2.2. Protocol for Chemical-Assisted Exfoliation

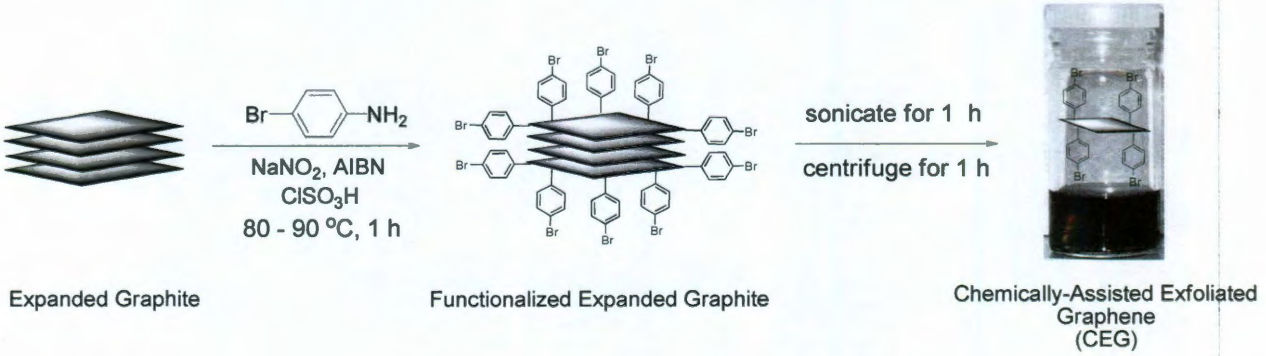

Scheme 2.1 Production of chemically-assisted exfoliated graphene (CEG)

Scheme 2.1 shows the experimental procedure for making CEG. Expanded graphite was first dispersed in chlorosulfonic acid, showing a relatively high solubility of 0.97 mg/mL. The diazonium salt was formed in situ from 4-bromoaniline in the presence of sodium nitrite and a catalytic amount of azobisisobutyronitrile (AIBN) and 4-bromophenyl groups were grafted mainly on the exposed edges of the expanded graphite flakes to produce functionalized expanded graphite. Because the diazonium salt of 4-bromoaniline is a relatively bulky molecule, it does not penetrate and react to the same degree with all of the graphene surfaces. In addition, the edges of the expanded graphite are more accessible than the interior basal plane surfaces that are stacked with strong π–π interactions. After 1 h of bath sonication of the functionalized expanded graphite flakes in DMF and 1 h of centrifugation at 3200 rpm, the CEG was collected from the supernatant. The functionalized CEG was much more soluble in DMF than the expanded graphite, as shown in Fig. 2.1.

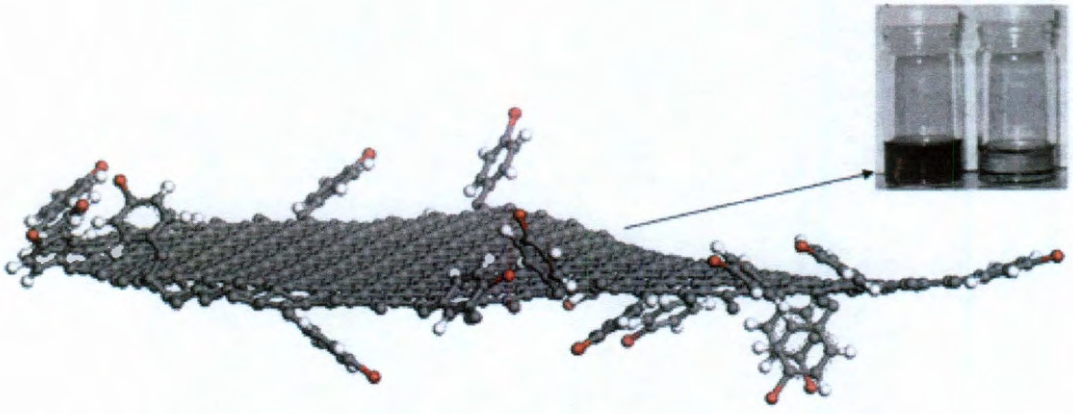

Fig. 2.1 CEG structure (gray: C atoms; red: Br atoms; white: H atoms). The inset shows the expanded graphite control supernatant (right vial) and the CEG supernatant (left vial) after both had been treated by sonication and centrifugation in DMF.

As shown in the inset to Fig. 2.1, expanded graphite and CEG were sonicated separately (ultrasonic cleaner Cole-Parmer model 08849-00) for 1 h in DMF, followed by centrifugation for 1 h at 3200 rpm (Adams Analytical centrifuge CT-3201) and the supernatant was decanted from the solid. The supernatant on the right in the inset to Fig. 2.1 is the expanded graphite control while the vial on the left holds the CEG supernatant; it has a much darker color and has remained stable for more than 3 months, indicating that the CEG is soluble in DMF while expanded graphite is poorly, if at all, soluble. The presumed CEG structure is shown in Fig. 2.1 with functional groups around the edges.

2.3. Functionality and Quality of Graphene Films

The CEG was analyzed by X-ray photoelectron spectroscopy (XPS), as shown in Fig. 2.2. The XPS spectrum had a Br 3d peak at 71 eV; unlike 4-bromophenyl diazonium functionalized chemically converted graphite (3.2% Br)[15], much less bromine was detected in the CEG (0.4%). Also, the sharp and symmetric C 1s peak at 285 eV confirmed the presence of a graphitic structure with minimal oxidation, indicating that a large number of crystalline domains remained after the reaction. Energy dispersive X-ray spectroscopy (EDX) was used as a supplemental technique

to investigate the Br concentration on single-sheet CEG flakes. The Br concentration varied from 0.56% to 0.67%, values that are comparable to the values obtained by XPS.

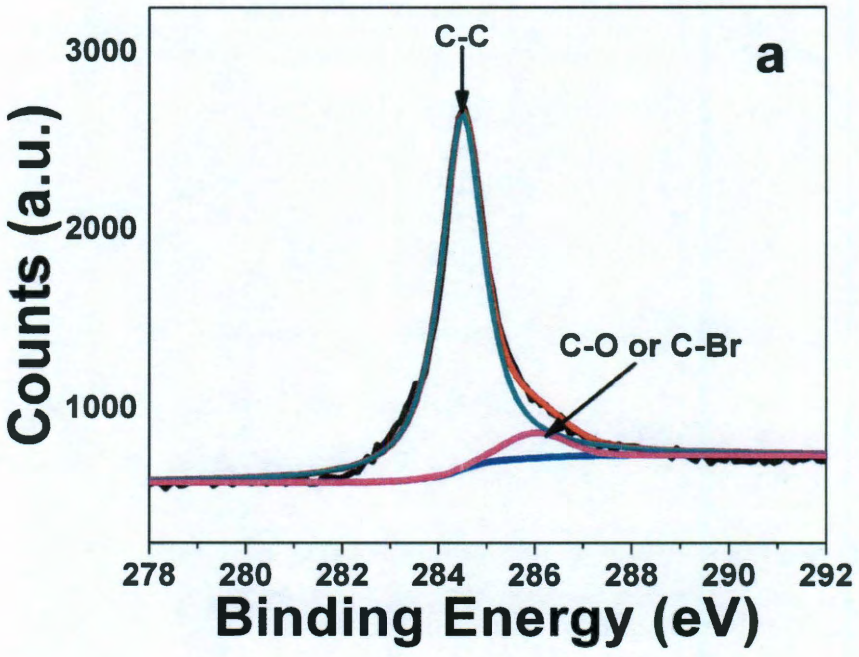

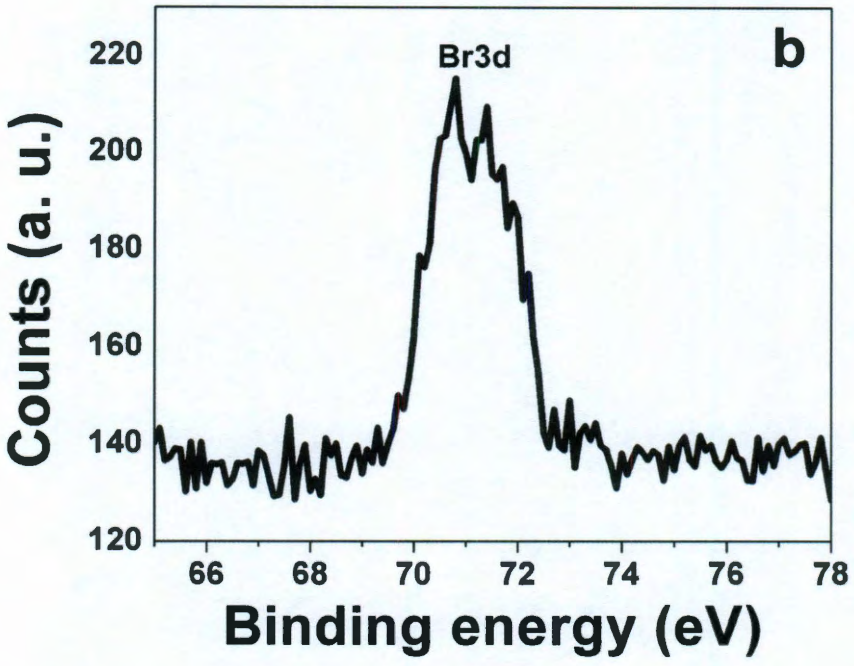

Fig. 2.2 XPS analysis of CEG. (a) High resolution C 1s peak (black) is fitted with C–C peak at 284.5 eV(green) and C–O or C–Br peak at 256 eV (purple). (b) Br 3d peak. XPS was carried out on a PHI Quantera SXM Scanning X-ray Microprobe with a base pressure of 5 × 10–9 Torr, with an Al cathode as the X-ray source set at 100 W and a pass energy of 140.00 eV (survey scan) and 26.00 eV (high-resolution scan), 45° takeoff angle, and a 100 μm beam size.

The crystalline structure of the CEG was confirmed by normal-incidence selected area electron diffraction (SAED) labeled with the Miller–Bravais (*hkil*) indices, as shown in Fig. 2.3. Fig. 2.3a shows a clear hexagonal electron diffraction pattern taken from a single-layer CEG. For single-layer graphene, the {2110} spots appear to be less intense relative to the {1100} spots [8]. The SAED of two stacked CEG

layers with a twist angle between the layers is shown in Fig. 2.3b. All CEG samples show a typical AB stacking structure.

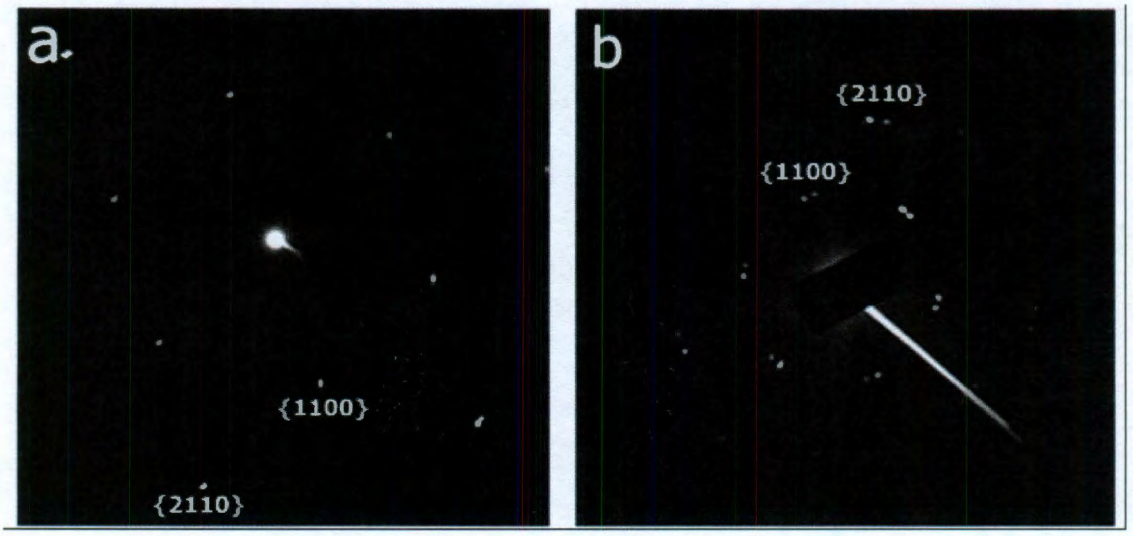

Fig. 2.3 Selected area electron diffraction (TEM) of (a) a single layer of CEG, and (b) two single-layer CEG flakes stacked with a slight twist angle. The ratios of the intensities of the {2110} and {1100} diffraction peaks are <1, which is a signature of graphene.

Analysis by high resolution transmission electron microscopy (HRTEM, JEOL 2100F field emission gun transmission electron microscope) was used to estimate the thickness of the CEG by focusing the HRTEM on the edge of the sheets. In Fig. 2.4, all four samples have fewer than 10 layers, which is consistent with the definition of graphene, where <10 layers is termed "graphene" [1]. Single-layer graphene must be imaged carefully since electron irradiation can easily generate defects (sp^3 C) in the graphene sheet [16]. The treated fast Fourier transform (FFT) HRTEM image (Fig. 2.4e) displays the lattice structure of a four-layer CEG overlaid with a polycyclic aromatic

hydrocarbon model. CEG has fewer defects than graphene oxide and chemically converted graphene[17], and thus the polycyclic aromatic hydrocarbon model is a viable simulation of the structure. Crystalline graphene edges can be assigned as having either zigzag or armchair configurations[18, 19]. Energetically, zigzag edges are more stable than armchair edges[18]. Therefore, the reactivity sequence of edge C atoms should be: dangling C > armchair C > zigzag C. The edge structure was also simulated and overlaid on the image. As shown in Fig. 2.4e, the white and black lines represent zigzag and armchair directions, respectively. The real edges are marked with red and green lines. However, based on the HRTEM results, the CEG edges analyzed are neither strictly zigzag nor armchair, except for a few small zigzag fragments.

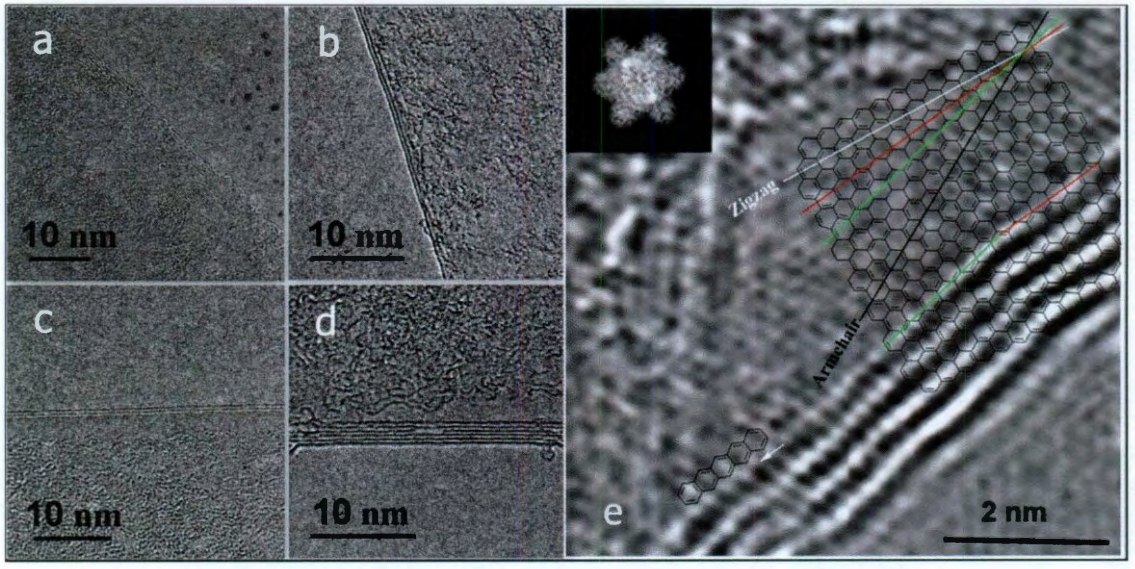

Fig. 2.4 HRTEM of the edges of various CEG samples. (a) Single-layer CEG; (b) two-layer CEG; (c) three-layer CEG; (d) six-layer CEG; (e) simulated four-layer CEG edge (inset is the FFT) overlaid on an HRTEM; the white line is the zigzag direction

while the black line shows the armchair direction. The red and green lines indicate the direction of real edges.

There are several reasons for problems with the graphene edge simulation. First, the simulated edge may not be the real edge of the CEG, since functional groups and heteroatoms attached directly to the edges would blur the graphene boundary. It is difficult to differentiate functional groups from the graphene backbone by ordinary HRTEM. Secondly, defects and functional groups on graphene determine its surface profile. Vacancies and sp^3 bonds interrupt the conjugation and make the graphene surface buckle over short ranges. This is different from long-range roughness due to the intrinsic flexibility of single graphene sheets[20], which can be overcome by tilting and focusing on a small area. Lastly, short-range surface fluctuation, especially curvature around the edge, will change the direction of the edge line and make its edge structure unpredictable. Single- and few-layer graphene sheets are sensitive to their chemical and physical environment, and form ripples on the nm-scale. However, the simulated model is ideally flat and does not take into account the effects of rippling on the edge configuration. As shown in Fig. 2.4e, the edge of the graphene sheet is pointing out of the plane and appears to be rippled.

The Raman spectrum of the expanded graphite, as shown in Fig. 2.5a, has a weak D band around 1375 cm^{-1} and relatively strong G and 2D bands at 1585 and 2700 cm^{-1}, respectively. The D band could be ascribed to defects induced by thermal expansion and edge functionalization[21]. After the diazonium reaction, the G and 2D peaks in the spectrum of bulk CEG films (Fig. 2.5b) kept their intensity and

shape, which indicates that the quality of graphene was largely preserved. The D band increased slightly in size, presumably because the CEG contained more functional groups than the expanded graphite. Compared to graphene oxide or chemically converted graphene, which have larger D/G ratios [15], the CEG has a relatively small D/G ratio of ~0.1. This is consistent with the XPS results in suggesting that the CEG was lightly functionalized.

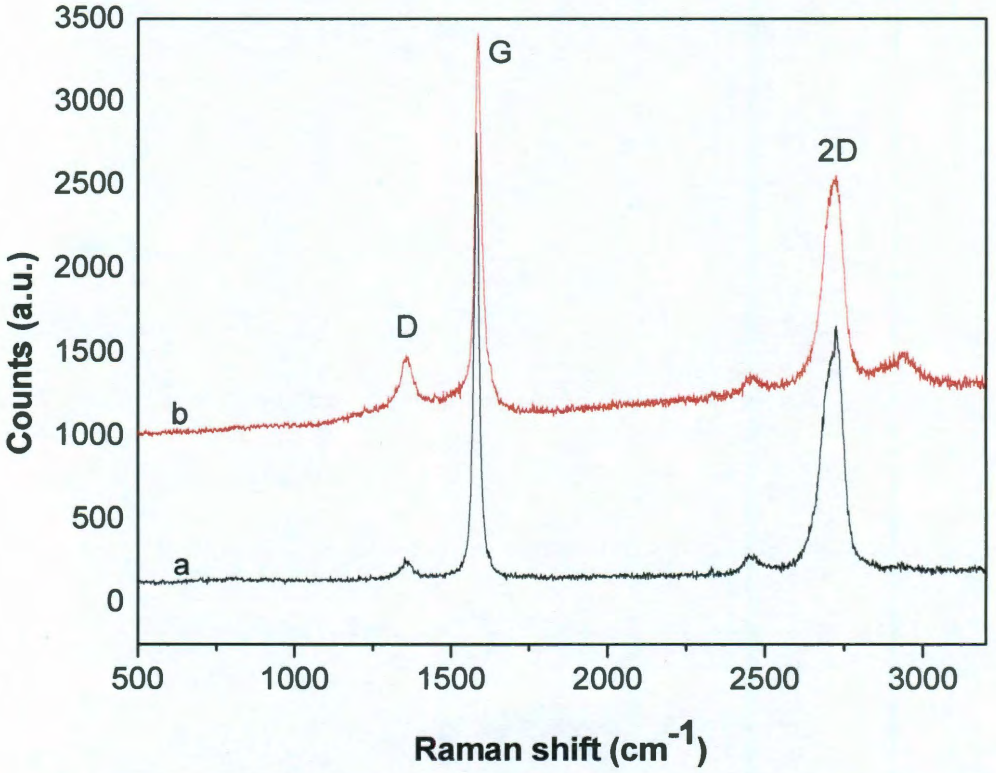

Fig. 2.5 (a) Raman spectrum of the expanded graphite before functionalization; (b) Raman spectrum of bulk CEG films. Spectra were obtained on a Renishaw Raman Scope at 514 nm Ar ion laser excitation at a laser power of 5% on a dry solid sample.

The electrical properties were measured on a CEG device built by e-beam lithography (GEOL 6500) using a Pt two-probe method. The sheet resistance was

about 560 Ω/sq (see Fig.2.6). The high conductivity shown by the CEG device was indicative of a material with few defects in the basal plane [8–10].

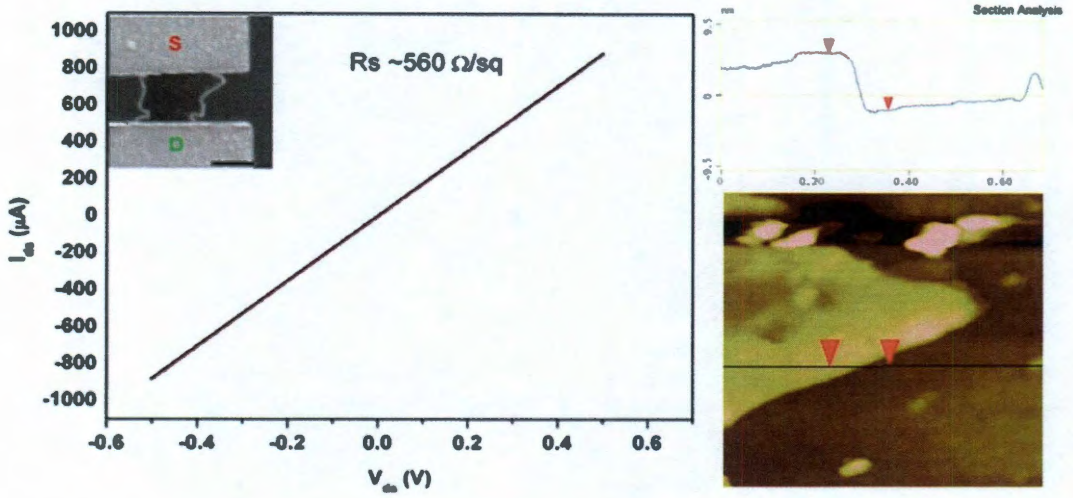

Fig. 2.6 *I/V* curve (left) of a CEG flake between two Pt electrodes (S= source; D= drain) that was made by e-beam lithography and the height profile (right) along the edge of the flake. Inset is the SEM image of the structure. Scale bar is 1 μm. The sheet resistance (Rs) is about 560 Ω/sq. The *I/V* data was obtained using an Agilent 4155C semiconductor parameter analyzer at room temperature under vacuum (10^{-6} Torr). The thickness of the flake is about 7.7 nm.

2.4. Edge Selectivity of Functionalization

One multi-layered expanded graphite flake has only two exposed faces. Except for their edges, functionalization of the faces of the inner sheets is retarded since the reagents cannot readily gain access to the spaces between the sheets. That the CEG sheets have more functional groups around their edges can be confirmed by

electron energy loss spectroscopy (EELS). Using elemental mapping under the energy filtered TEM (EFTEM) mode, the distribution of Br substituents can be directly obtained from the TEM image. Fig. 2.7a shows the zero loss TEM image of CEG. Fig.s 2.7b and 6c are the mapping of the C (K edge at 284 eV) and Br (M_{45} edge at 69 eV) elements present in the CEG flake. Therefore, based on the EFTEM images, the 4-bromophenyl functional groups are, in large part, bonded within ~70 nm of the edges of the CEG. It is this region that produces most of the Raman D signal [22]. Because the thermal expansion process opens the expanded graphite edges to a certain extent, the functionalization reagents penetrate into that limited depth and graft on those near-edge planes. The edge selectivity is directly related to the degree of exposure of the interior basal planes to the functionalization reagent.

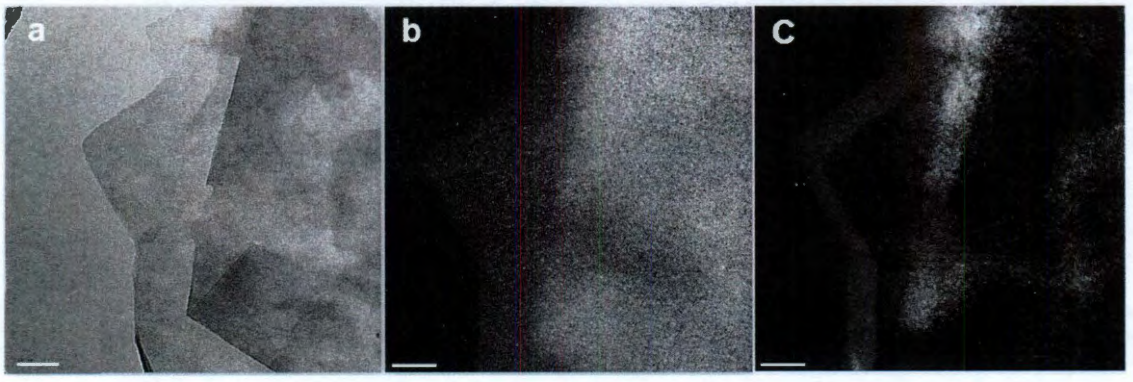

Fig. 2.7 EFTEM of CEG flakes: (a) zero loss image, (b) C mapping (C K edge at 284 eV), and (c) Br mapping (Br M45 edge at 69 eV). Scale bars are 100 nm. Note the elemental highlights near the edges. Br is only observed within ~70 nm of the edge.

2.5. Efficiency of Chemically-Assisted Exfoliation

The solubility of graphene could be increased by adding an external stabilizer. For example, 0.015 mg/mL expanded graphite can be dispersed in DMF with excess tetrabutylammonium hydroxide (TBAH)[23]. For CEG, with only a few functional groups on the edge, its solubility varies from 0.01 to 0.02 mg/mL in DMF, without the need for exogenous stabilizers. Due to graphene's large surface area and flexible planes, when large flakes were prepared for TEM by pipetting the CEG solution onto a 300 mesh lacey carbon grid, the flakes stacked or folded. Therefore, the TEM analysis was performed only on small flakes to estimate the number of layers per flake [8]. The TEM-generated histogram (Fig. 2.8) shows that > 70% of flakes have < 5 layers and about 10% are single-sheet. This is comparable with the liquid phase exfoliation method [24], which reported > 63% of flakes with 1–5 layers.

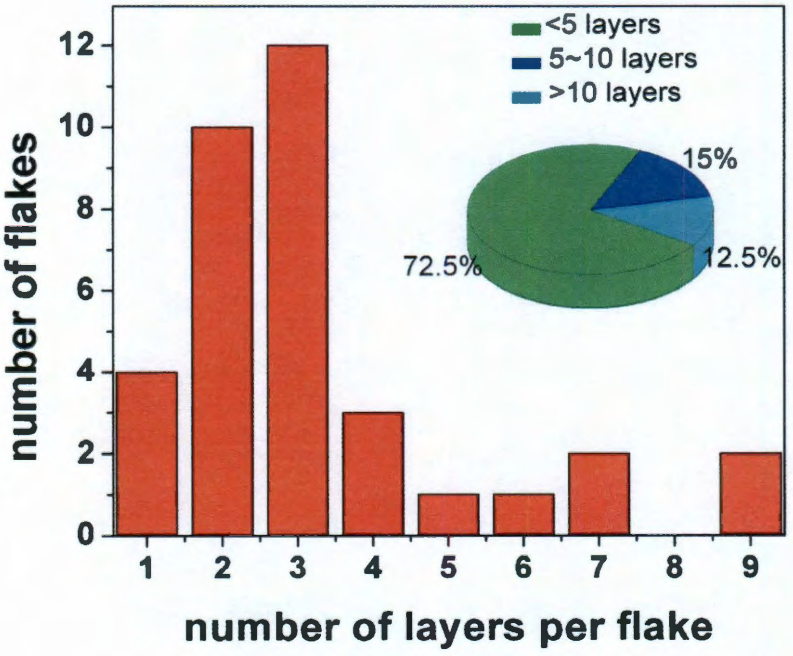

Fig. 2.8 Histogram of number of layers per CEG flakes counted by TEM over a commonly characteristic domain of study.

2.6. Morphology of CEG

The CEG sample was deposited directly on a lacey carbon TEM grid for SEM analysis. According to the SEM data (Fig. 2.9), the CEG flakes usually have a size around 1 μm. Some larger flakes could be visualized under an optical microscope on a 300 nm-thick layer of SiO_2 atop a Si wafer (Fig. 2.10). These flakes were noted in the final solution even after centrifugation. They are likely to have more functional groups that stabilize them in the DMF. The thickness of the CEG flakes was measured by atomic force microscopy (AFM, Digital Instruments Nanoscope III A, in tapping mode). Fig. 2.11 shows a height mode scan of a CEG solution spin-coated on mica. With a height of 1.7 nm in Fig. 2.11a and 1.4 nm in Fig. 2.11b, the CEG shows a thickness of 1 to 2 layers, which corresponds well to the TEM measurements.

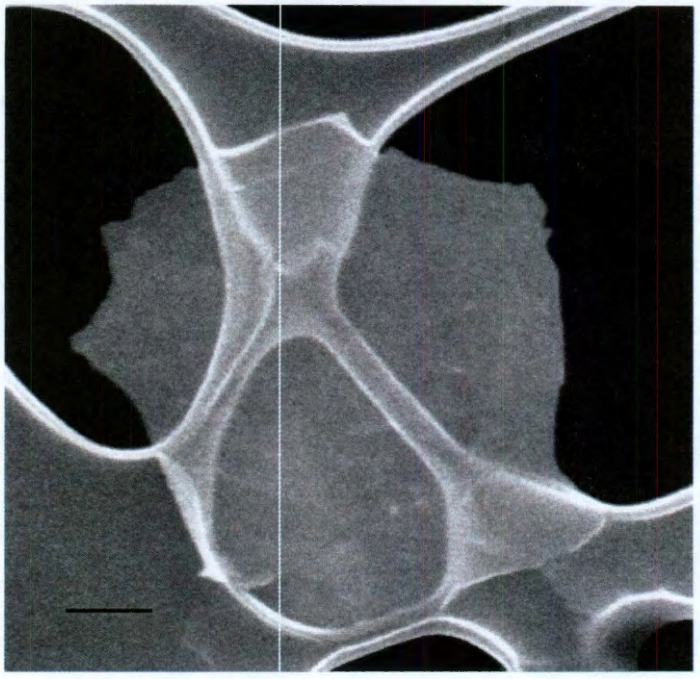

Fig. 2.9 SEM image of CEG flake atop a lacey carbon grid. Scale bar is 250 nm.

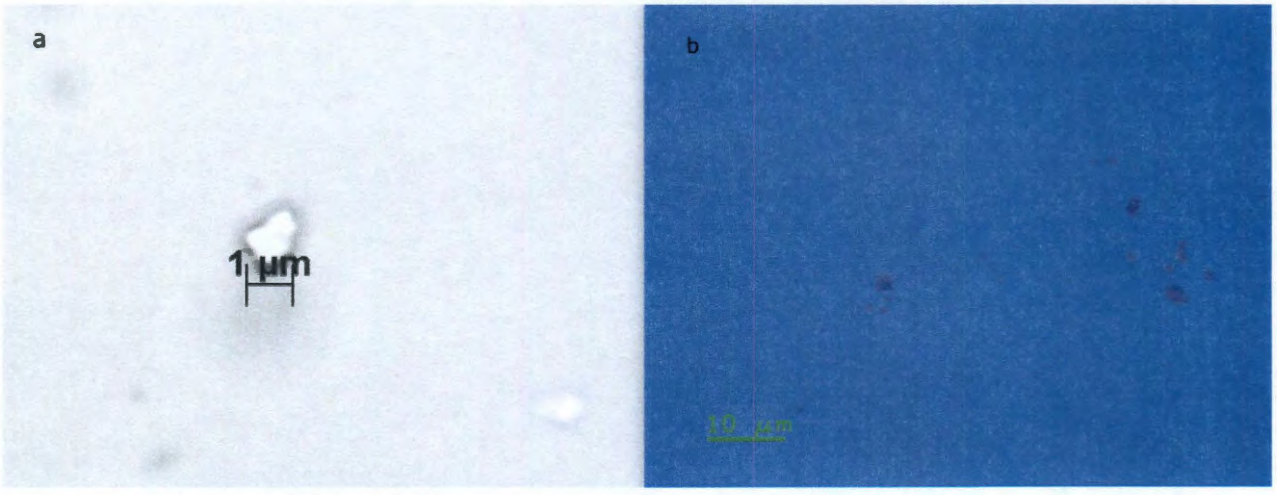

Fig. 2.10 Optical microscope image of CEG flakes (a) on glass slide (b) on 300-nm-SiO_2 film atop Si wafer.

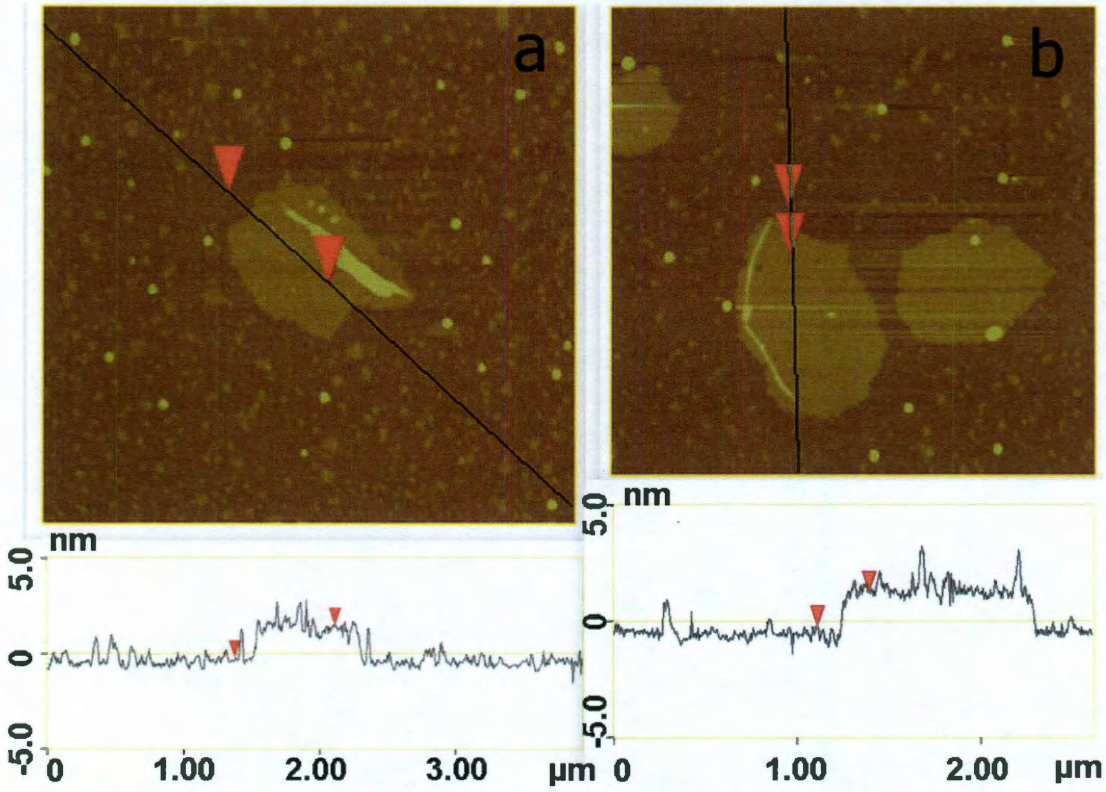

Fig.2.11 AFM of CEG on mica. (a) The edge of the image is 4 μm and the vertical distance marked is 1.7 nm; (b) the edge of the image is 2.5 μm and the vertical distance is 1.4 nm. The bottom plots show the height profiles along the black imaged lines above.

2.7. Conclusions

Expanded graphite can be converted via functionalization to CEG that is stable in DMF solvent without any added stabilizer. As established by EFTEM elemental mapping, these CEG sheets have functional groups predominantly bonded within 70 nm of the edges and retain the pristine graphene structure in the interior basal planes. Because of CEG's unique structure, its solubility is higher than that of

pure graphene, but CEG has no need for the addition of surfactants to increase its solubility. The microscopy data indicates that more than 70% of the CEG flakes are < 5 layers thick. In addition, the CEG preparation method is simpler than the multi-step method needed for preparing graphene oxide followed by reduction to chemically converted graphene. The process for preparing CEG is a promising method to achieve a high yield of soluble graphene.

Author Contributions:

Z. S. did all the wet chemistry and the characterizations. Zengxing Zhang performed the device fabrication and electrical measurement.

References

1. Geim, A. K.; Novoselov, K. S. The rise of graphene. *Nat. Mater.* **2007**, *6*, 183-191
2. Ruoff, R. Graphene: Calling all chemists. *Nat. Nanotech.* **2008**, *3*, 10-11.
3. Stankovich, S.; Dikin, D. A.; Piner, R. D.; Kohlhaas, K. A.; Kleinhammes, A.; Jia, Y.; Wu, Y.; Nguyen, S. T.; Ruoff, R. S. Synthesis of graphene-based nanosheets via chemical reduction of exfoliated graphene oxide. *Carbon.* **2007**, *45,* 1558-1565.
4. Wang, H.; Robinson, J. T.; Li, X.; Dai, H. Solvothermal reduction of chemically exfoliated graphene sheets. *J. Am. Chem. Soc.* **2009,** *131*, 9910-9911.
5. Novoselov, K. S.; Geim, A. K.; Morozov, S. V.; Jiang, D.; Zhang, Y.; Dubonos, S. V.; Grigorieva, I. V.; Firsov, A. A. Electric field effect in atomically thin carbon films. *Science.* **2004**, *306*, 666-669.
6. Hamilton, C. E.; Lomeda, J. R.; Sun, Z. Z.; Tour, J. M.; Barron, A. R. High-yield organic dispersions of unfunctionalized graphene *Nano Lett.* **2009**, *9*, 3460-3462.
7. Hernandez, Y.; Nicolosi, V.; Lotya, M.; Blighe, F. M.; Sun, Z. Y.; De, S.; McGovern, I. T.; Holland, B.; Byrne, M.; Gun'ko, Y. K.; Boland, J. J.; Niraj, P.; Duesberg, G.; Krishnamurthy, S.; Goodhue, R.; Hutchison, J.; Scardaci, V.; Ferrari, A. C.; Coleman, J. N. High-yield production of graphene by liquid-phase exfoliation of graphite. *Nat. Nanotech.* **2008**, *3*, 563-568.
8. Lotya, M.; Hernandez, Y.; King, P. J.; Smith, R. J.; Nicolosi, V.; Karlsson, L. S.; Blighe, F. M.; De, S.; Wang, Z.; McGovern, I. T.; Duesberg, G. S.; Coleman, J. N., Liquid phase production of graphene by exfoliation of graphite in surfactant/water solutions. *J. Am. Chem. Soc.* **2009,** 131, 3611-3620

9. Reina, A.; Jia, X. T.; Ho, J.; Nezich, D.; Son, H. B.; Bulovic, V.; Dresselhaus, M. S.; Kong, J. Large area, few-layer graphene films on arbitrary substrates by chemical vapor deposition. *Nano Lett.* **2009**, *9*, 30-35.

10. Jia, X. T.; Hofmann, M.; Meunier, V.; Sumpter, B. G.; Campos-Delgado, J.; Romo-Herrera, J. M.; Son, H. B.; Hsieh, Y. P.; Reina, A.; Kong, J.; Terrones, M.; Dresselhaus, M. S. Controlled formation of sharp zigzag and armchair edges in graphitic nanoribbons. *Science.* **2009**, *323*, 1701-1705.

11. Li, X. S.; Cai, W. W.; An, J. H. ; Kim, S.; Nah, J.; Yang, D. X.; Piner, R.; Velamakanni, A.; Jung, I.; Tutuc, E.; Banerjee, S. K.; Colombo, L.; Ruoff, R. S. Large-area synthesis of high-quality and uniform graphene films on Copper foils. *Science.* **2009**, 324, 1312-1314.

12. Robinson, J. A.; Puls, C. P.; Staley, N. E.; Stitt, J. P.; Fanton, M. A.; Emtsev, K. V.; Seyller, T.; Liu, Y. Raman topography and strain uniformity of large-area epitaxial graphene. *Nano Lett.* **2009**, *9*, 964-968.

13. Ni, Z. H.; Chen, W.; Fan, X. F.; Kuo, J. L.; Yu, T.; Wee, A. T. S.; Shen, Z. X. Raman spectroscopy of epitaxial graphene on a SiC substrate. *Phys. Rev. B.* **2008**, *77.* 115416.

14. Rohrl, J.; Hundhausen, M.; Emtsev, K. V.; Seyller, T.; Graupner, R.; Ley, L. Raman spectra of epitaxial graphene on SiC(0001). *App. Phys. Lett.* **2008**, *92*. 201918.

15. Lomeda, J. R.; Doyle, C. D.; Kosynkin, D. V.; Hwang, W. F.; Tour, J. M. Diazonium Functionalization of Surfactant-Wrapped Chemically Converted Graphene Sheets. *J. Am. Chem. Soc.* **2008**, *130*, 16201-16206.

16. Teweldebrhan, D.; Balandin, A. A. Modification of graphene properties due to electron-beam irradiation. *App. Phys. Lett.* **2009**, *94*, 013101.

17. Mkhoyan, K. A.; Contryman, A. W.; Silcox, J.; Stewart, D. A.; Eda, G.; Mattevi, C.; Miller, S.; Chhowalla, M. Atomic and electronic structure of graphene-oxide. *Nano Lett.* **2009**, *9*, 1058-1063.

18. Girit, C. O.; Meyer, J. C.; Erni, R.; Rossell, M. D.; Kisielowski, C.; Yang, L.; Park, C. H.; Crommie, M. F.; Cohen, M. L.; Louie, S. G.; Zettl, A. Graphene at the edge: stability and dynamics. *Science* **2009**, *323*, 1705-1708.

19. Liu, Z.; Suenaga, K.; Harris, P. J. F.; Iijima, S. Open and closed edges of graphene layers. *Phys. Rev. Lett.* **2009**, *102*. 015501.

20. Barnard, A. S.; Snook, I. K. Thermal stability of graphene edge structure and graphene nanoflakes. *J. Chem. Phys.* **2008**, *128*, 094707.

21. Pimenta, M. A.; Dresselhaus, G.; Dresselhaus, M. S.; Cancado, L. G.; Jorio, A.; Saito, R. Studying disorder in graphite-based systems by Raman spectroscopy. *Phys. Chem. Chem. Phys.* **2007**, *9*, 1276-1291.

22. Gupta, A. K.; Russin, T. J.; Gutierrez, H. R.; Eklund, P. C. Probing graphene edges via Raman scattering. *ACS Nano* **2009**, *3*, 45-52.

23. Hernandez, Y.; Lotya, M.; Rickard, D.; Bergin, S. D.; Coleman, J. N. Measurement of multicompoent solubility parameters for graphene facilities solvent discovery. *Langmuir,* **2009**, ASAP.

24. Li, X. L.; Zhang, G. Y.; Bai, X. D.; Sun, X. M.; Wang, X. R.; Wang, E.; Dai, H. J. Highly conducting graphene sheets and Langmuir–Blodgett films. *Nat. Nanotech.* **2008**, *3*, 538-542.

Chapter 3

OXIDATION, UNZIPPING, INTERCALATION AND EXFOLIATION CHEMISTRY

3.1. Introduction

Diazonium chemistry can functionalize graphene edges and enhance its solubility[1], while other wet chemistry such as oxidation, unzipping, intercalation and exfoliation are also promising protocols to functionalize and process this unique material, which is especially useful for the bulk production of graphene. With this purpose, the functionalization and processing of different forms of carbon materials such as MWCNTs, SWCNTs, carbon black and graphite flakes were investigated using these chemical procedures. The final products' properties were carefully studied with different microscopic techniques.

3.2. Carbon Black Oxidation

One of the most common carbon nanomaterials is carbon black, which is widely used as a pigment and reinforcement in rubber and plastic products[2]. Carbon black can have a wide size distribution, which has been optimized and selected by industry based on the application. Two different carbon black samples from CABOT were investigated, Vulcan 9A32 (24~33 nm) and Sterling NS1 N762 (70~96 nm). Inspired by the graphene oxide chemistry[3, 4], we sought to make nanoparticles of oxidized carbon from these nano-sized carbon particles, which hold great promises for nanomedicine applications[5]. The oxidized carbon blacks (OCB) were made using the same procedures as that we used to make graphene oxides[3, 4]. Compared to graphite oxide, which is oxidized and exfoliated from graphite flakes, only the outside surface of carbon black could oxidized, while its core remains pristine (Fig. 3.1). No exfoliation is observed for OCB. These harsh oxidations modify carbon black's surface properties by adding carboxylic groups. These carboxylic groups could serve as an "anchor" which could bridge with other functional groups. The functionalized radius is obvious under TEM and labeled with red lines (Fig. 3.1). Around 3~4 nm of the carbon black surface becomes more amorphous than its inner sphere, suggesting that abundant functional groups such as carboxylic, epoxide and hydroxyl groups accumulate on it. The surface elemental analysis using XPS allows us to determine the oxygen atomic concentration of ~35.5%. The Staudenmaier method has a higher carbon black oxidation level of ~40% oxygen.

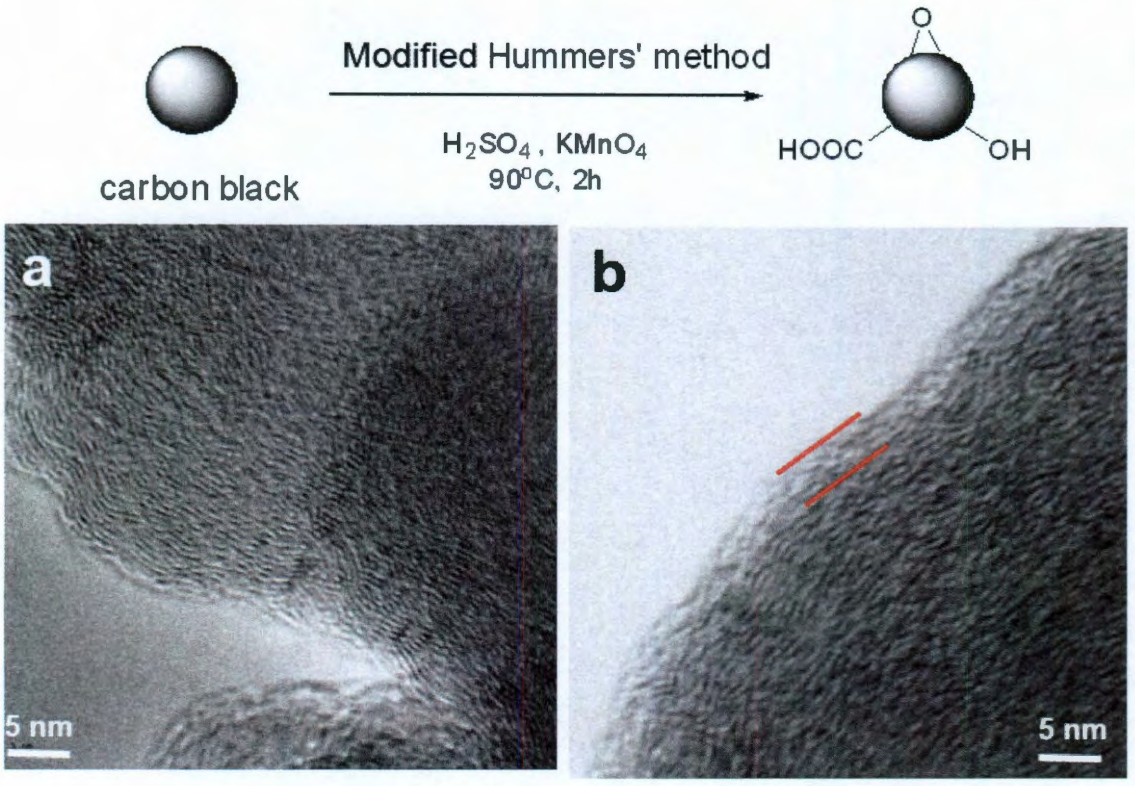

Fig. 3.1 Carbon black oxidation using a modified Hummers' method[6]. (a) Original carbon black with 1 or 2 layers of surface disruption. (b) Oxidized carbon black with ~ 4 nm of surface disruption.

3.3. Graphene Nanoribbon Unzipping

Besides carbon black, we also found that bulk CNTs dispersed in concentrated sulfuric acid (H_2SO_4) can be longitudinally unzipped into graphene oxide nanoribbons (GONRs) using the modified Hummers' method[6]. The bulk production of the GONRs is confirmed by SEM in Fig. 3.2.

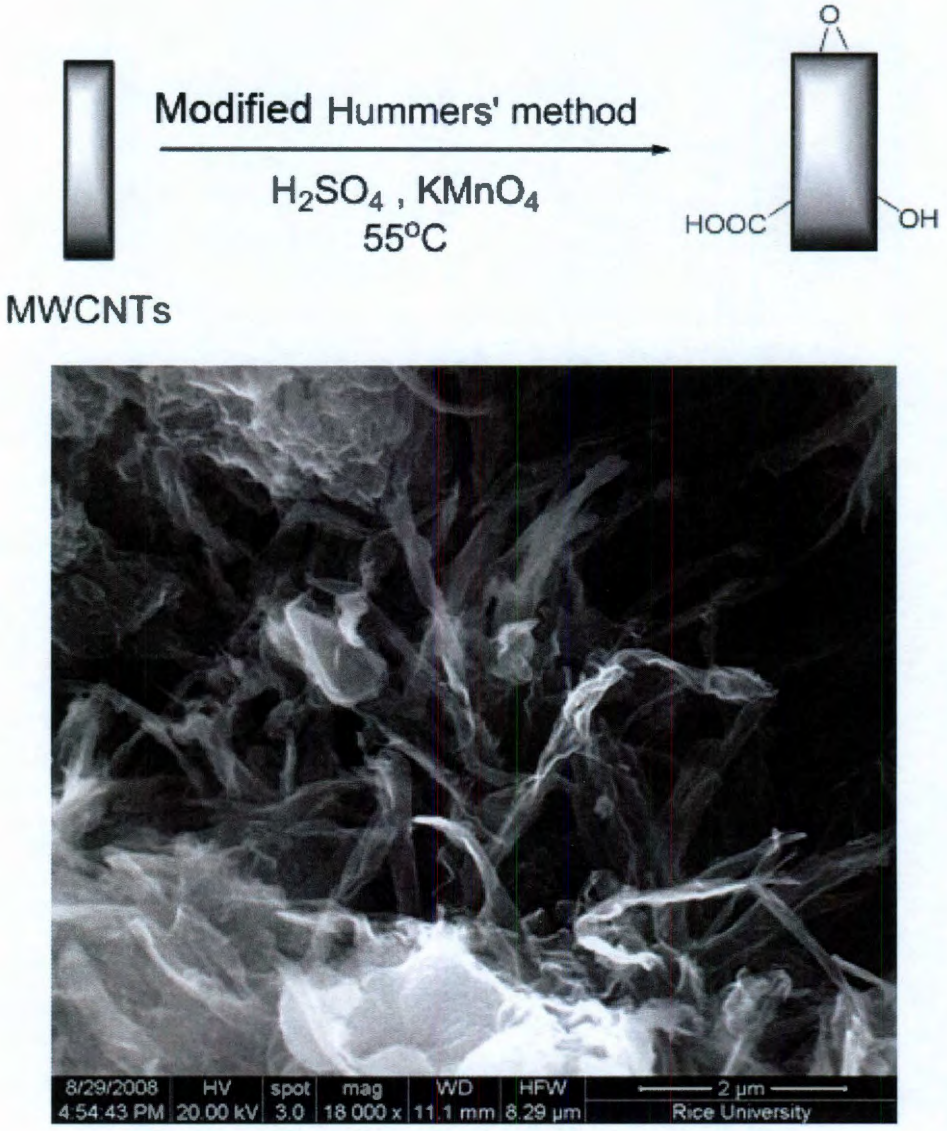

Fig. 3.2 SEM of GONRs produced by modified Hummers' method.

Using this unzipping protocol on CNT device structures, a direct on-chip conversion of the tube into a ribbon-based device was achieved. To produce the CNT

devices here, we used commercial multiwalled CNTs (MWCNTs) from Mitsui & Co., Ltd. as the source material (Endo's method, Lot No. 05072001K28). The MWCNTs were first ultrasonically dispersed into chloroform (CH_3Cl), and then the dispersion was spin-coated onto 200-nm oxide/silicon substrates. Through this method, the MWCNTs can be assembled on the substrates as individuals. We then fabricated devices by e-beam lithography atop the isolated MWCNTs using platinum (Pt) films. The electrode-bound MWCNTs were then prepared for oxidative unzipping. In a typical protocol, concentrated H_2SO_4 (10 mL) in a bottle was placed in an oil bath at 55 °C, and then $KMnO_4$ (100 mg, 0.63 mmol) was added. After the mixture was stirred to produce a solution, the fabricated MWCNT devices were immersed in the solution. Following the 90 min reaction, the devices were removed and rinsed with deionized (DI) water and dried in a gentle nitrogen gas flow.

It has been shown that graphene oxide (GO) starts losing oxygen when heated to about 200 °C; heat can therefore be used to reduce GONRs to nanoribbons (NRs). To reduce the unzipped devices, we heated the samples at 350 °C for 6 h under H_2 and Ar. The morphologies of the devices were characterized with SEM (GEOL 6500) and AFM (Digital Instruments Nanoscope III A, in tapping mode).

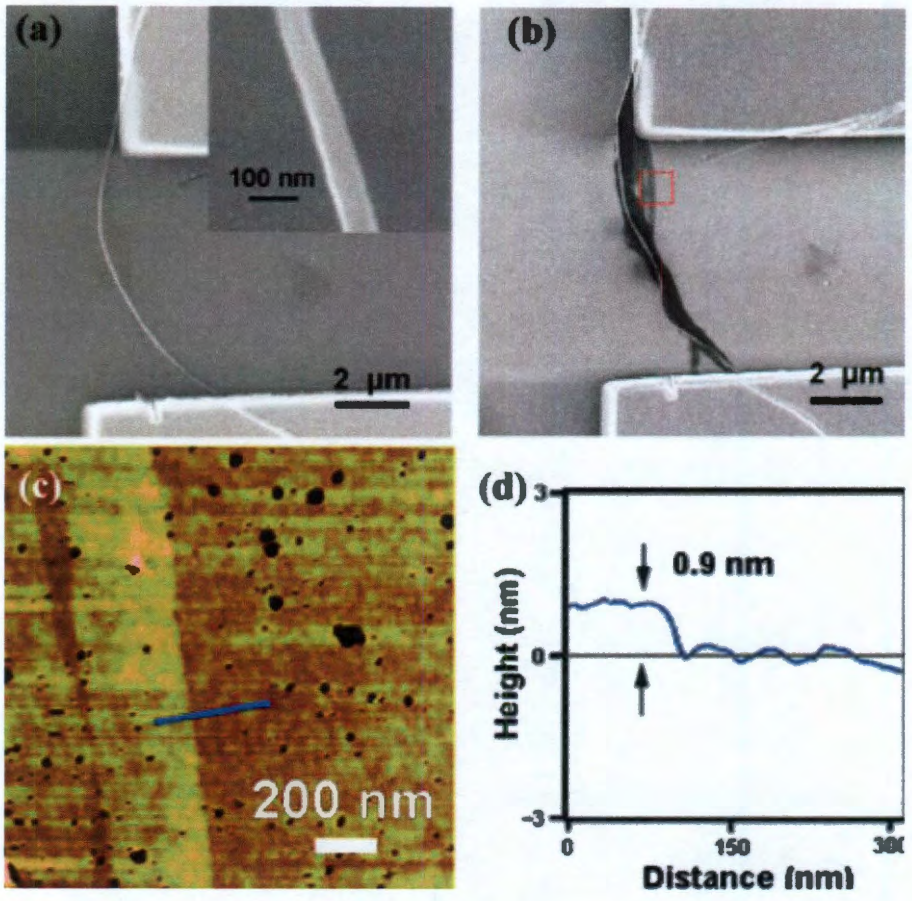

Fig. 3.3 Morphology analysis of a typical device. (a) SEM image of a MWCNT-based device before oxidative unzipping. The inset is a magnified SEM image of the MWCNT, indicating the diameter of the MWCNT is about 70 nm. (b) SEM image of the same device after oxidative unzipping to form the nanoribbon structures. (c) AFM image of the portion of the nanoribbons in the red box in b. (d) Height profile along the line shown in c, indicating that the thickness of the nanoribbon is 0.9 nm and therefore most likely single-layered.

Fig. 3.3a shows a SEM image of a typical MWCNT device. And Fig. 3.3b is the SEM image of the same device as in Fig. 3.3a after reaction with $KMnO_4$. It is obvious that treatment has changed the device. Whereas before treatment the MWCNT

between the two electrodes was tens of nm in width, after the treatment it was hundreds of nm in width. At either end nearest the electrodes the MWCNTs partially or wholly retained their structure, similar to a ribbon that has had both ends closed into cylinders. The portions of the MWCNTs under the Pt electrodes were protected from unzipping, preserving the electrical contact between the electrodes and the MWCNTs. It is difficult to microscopically assess whether the smallest diameter part of the MWCNT had unzipped along the entire channel length or whether the imaged line in Fig. 3.3b is part of a stacked-ribbon edge; however, the large excess of $KMnO_4$ and the extended time of the reaction would suggest that the smaller diameter, and hence more oxidatively reactive portion of the MWCNT, would also be converted into a nanoribbon. As seen in Fig. 3.3b, the unzipped MWCNT is comprised of undulating flattened structures. In the portion indicated by the red square, there are two narrow nanoribbons attached to the main nanostructure. Atomic force microscopy (AFM) in tapping mode was used to characterize the area in the box, and, as shown in Fig. 3.3c and d, the thickness of the nanoribbon is 0.9 nm. This thickness is close to the reported theoretical and experimental values for the thickness of single-layer GO[7, 8], and in further accordance with previous evidence from this oxidative protocol showing the formation of GONRs from MWCNTs[6].

Fig. 3.4 shows the I_{DS}-V_{DS} curves of a typical device at different stages. As shown in Fig. 3.3, the sections of the MWCNTs under the electrodes in the device are protected from unzipping, so that the contact between the electrodes and the nanostructure should not be changed. Thus, the changes in the electrical properties of the devices are due mainly to modifications of the MWCNTs between the two

electrodes. The MWCNT-based device shows excellent metal conductivity before unzipping and good Ohmic contact between the MWCNT and Pt electrodes. At 1 V, the current through the device increases to 200 μA (Fig. 3.4a). The GONR device exhibits relatively poor conductivity, decreasing almost 4 orders of magnitude compared to that before unzipping (Fig. 3.4b). The thermal treatment improves the conductivity of the device (Fig. 3.4c) to about 1 order of magnitude less than that of the MWCNT device in Fig. 3.4a.

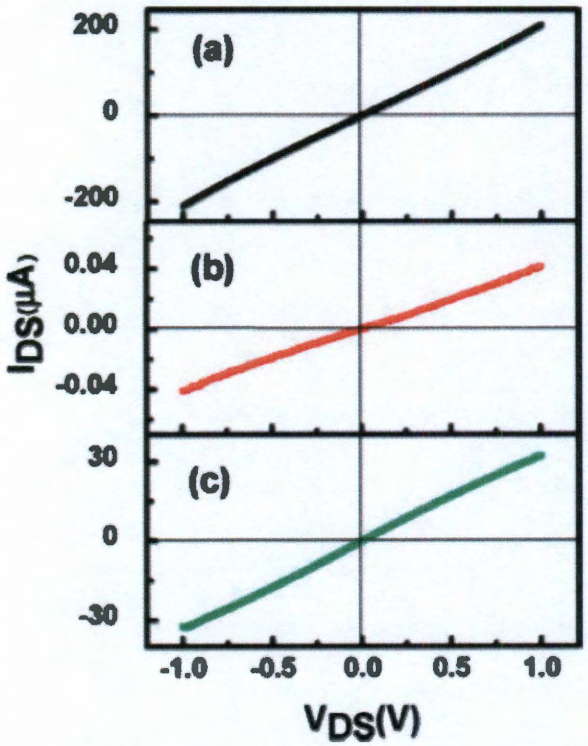

Fig. 3.4 Electrical characteristics of the device from Fig. 3.3 at different stages. (a) As-prepared MWCNT device. (b) After treatment with $KMnO_4$ to produce the NRs device. (c) GONR in the device after thermal treatment.

3.4. SWCNTs Unzipping

Following the same unzipping protocol, SWCNTs instead of MWCNTs were used to make graphene nanoribbons. The obtained ribbons are narrow, entangled with each other and heavily oxidized, which makes it a challenge to image them. SWCNTs before oxidation in TEM (Fig. 3.5) display the straight-wall structures of the tubes. After the unzipping processing, the wall structures of the SWCNTs are completely destroyed as seen in Fig. 3.6, while leaving a "ribbon-like" pathway on the TEM grid when changing the focus. Considering that the width of the nanoribbons after unzipping becomes wider than its precursor tubes, the "ribbon" structures shown in Fig. 3.6 are consistent with the unzipping theory. However, the exact edge structures (zigzag or armchair) of the graphene ribbons could not be distinguished due to the heavy oxidation.

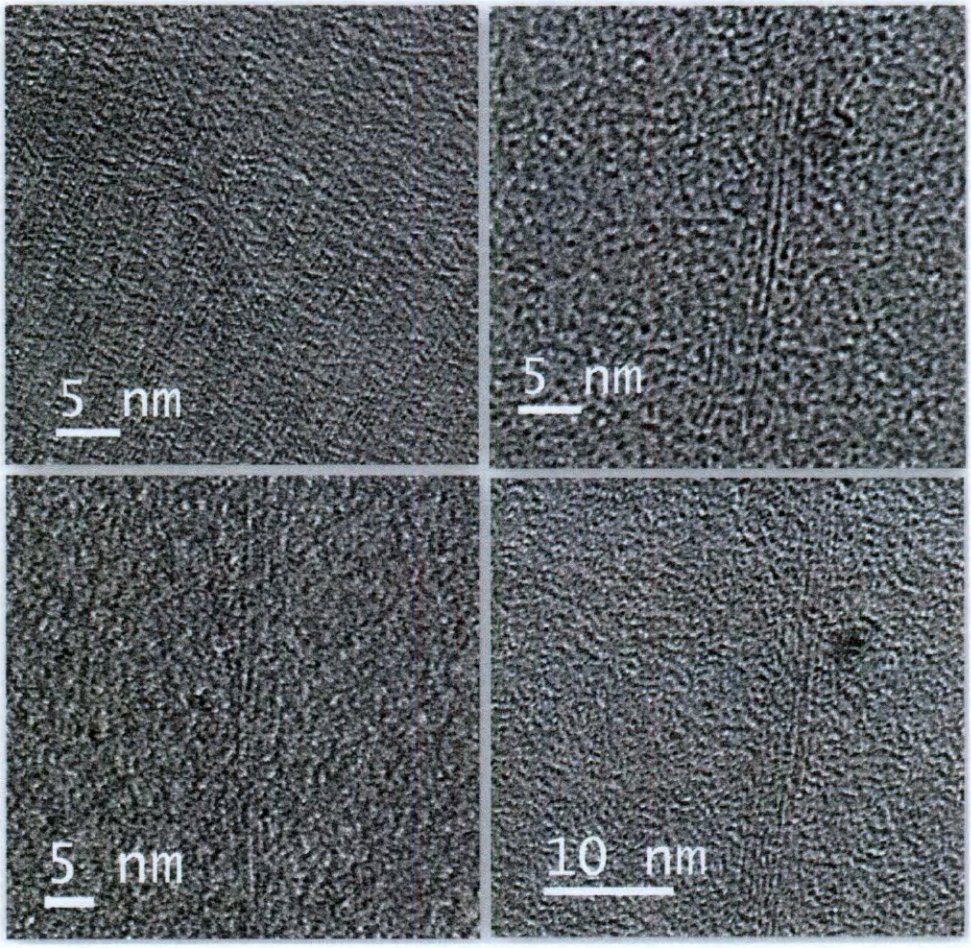

Fig. 3.5 TEM images of SWCNTs precursors before unzipping.

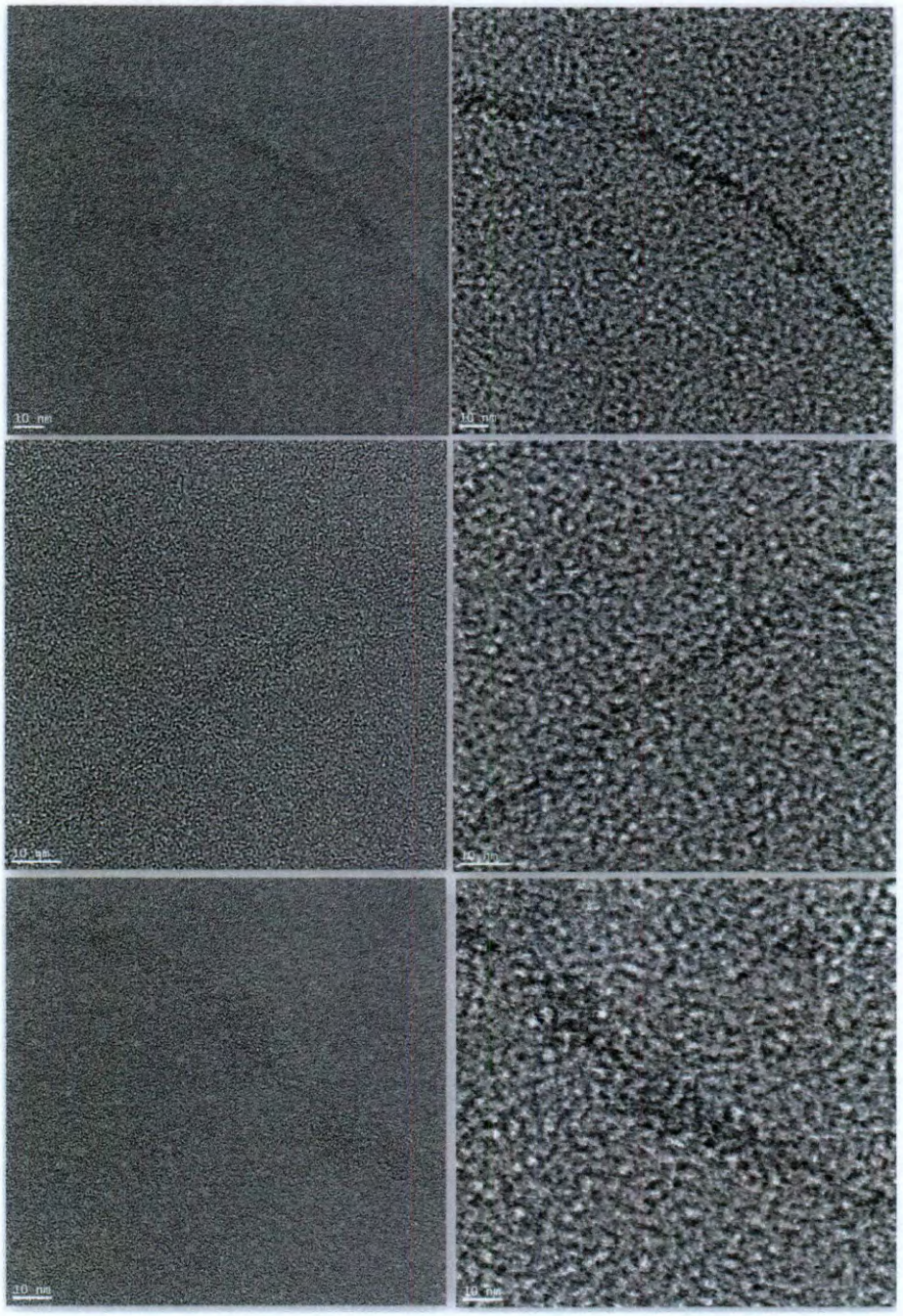

Fig. 3.6 TEM images of SWCNTs-derived "ribbon" structures after unzipping. Scale bar is 10 nm.

3.5. $FeCl_3$ Intercalation and Exfoliation

Graphite can be intercalated and exfoliated into graphene flakes, which is a promising and relatively inexpensive method to produce graphene on a large scale[9]. An n-staged graphite intercalated compound (GIC) is defined in Fig. 3.7. In a typical experiment, $FeCl_3$-intercalated graphite flakes can be obtained by baking the graphite flakes and anhydrous $FeCl_3$ in a sealed vacuum tube (10^{-2} Torr) at 200 °C for 5 h and at 300 °C for 1 d. A mild O_2 content is useful to oxidize $FeCl_3$ into Fe_2O_3 and release some Cl_2 gas into the system, which is essential to initiate the intercalation[10]. Without the Cl_2 gas, the only weight uptake is achieved and staging is inhibited[10]. The structure of the final GIC material could be determined by the Bragg equation with X-ray diffraction (XRD) because the repeated distance along the c direction changes from c_0 (graphite) to I_c (GIC) (Fig. 3.7).

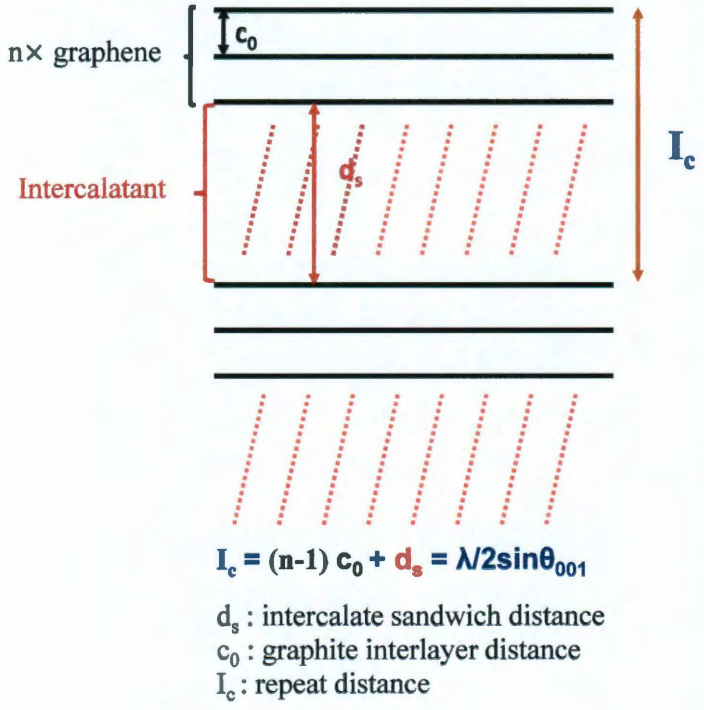

Fig. 3.7 Scheme of n-staged GIC. The repeated distance (I_c) is determined by the Bragg equation in XRD and it is the total thickness of both n-layer graphene ((n-1)c_0) and the intercalatant spacing (d_s).

In the XRD of $FeCl_3$ GIC, except for the graphite (002) peak at 26.8°, there are three new peaks shown at 9.5°, 19° and 28.5° (Fig. 3.8). This proves the successful intercalation of the $FeCl_3$. In order to further exfoliate the GIC material into graphene, an additional exfoliation step is needed: the $ClSOH_3$ dispersed GIC material was exfoliated by adding H_2O_2 (see section 3.6 materials and methods). O_2 gas forms during this process and is trapped between graphene layers, separating them from collapsing. The product's XRD has two peaks, the graphite peak at 26.8° and an un-indexed peak at 9.8°, suggesting successful exfoliation.

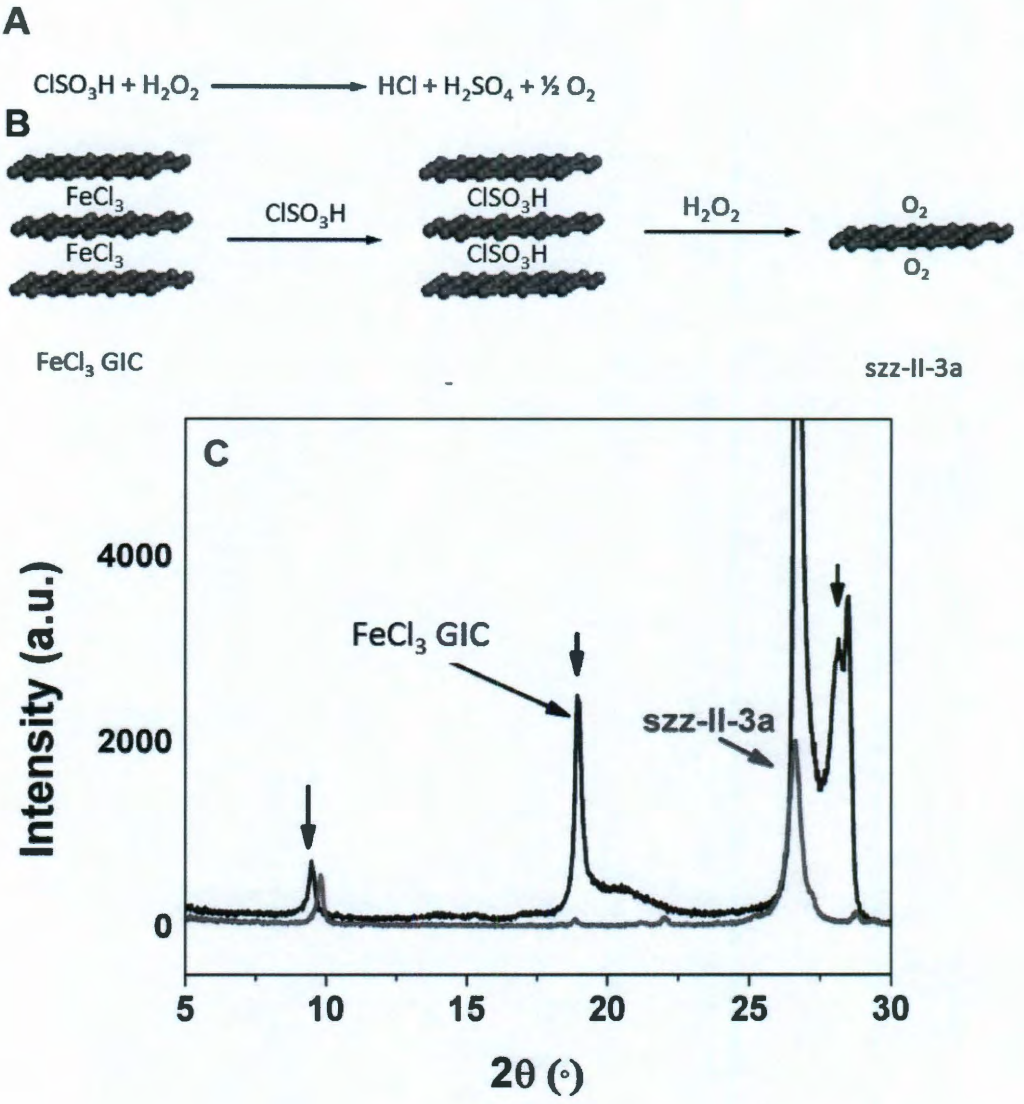

Fig. 3.8 $FeCl_3$ GIC exfoliation. (A) The reaction of $ClSO_3H$ and H_2O_2. (B) $FeCl_3$ GIC was dispersed in $ClSO_3H$ and further exfoliated with O_2 gas generated by adding H_2O_2 to $ClSO_3H$. (C) The XRD spectra before ($FeCl_3$ GIC) and after the exfoliation (szz-II-3a).

In the SEM in Fig. 3.9, the final product appears to be expanded after the exfoliation process and individual corrugated flakes were observed that are different from the original graphite flakes. The thickness of these flakes was

measured with TEM and most of their edges are less than 10 layers (Fig. 3.10), suggesting a good quality graphene.

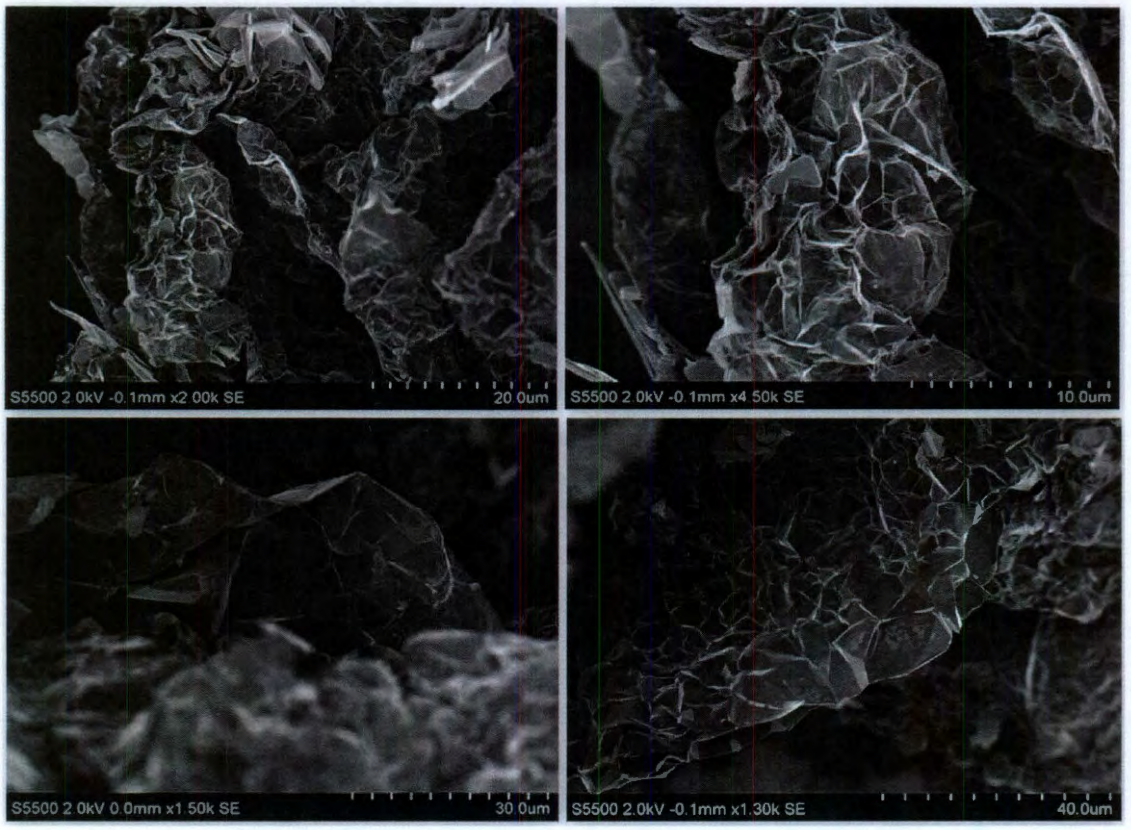

Fig. 3.9 SEM of graphene flakes exfoliated from $FeCl_3$ GIC.

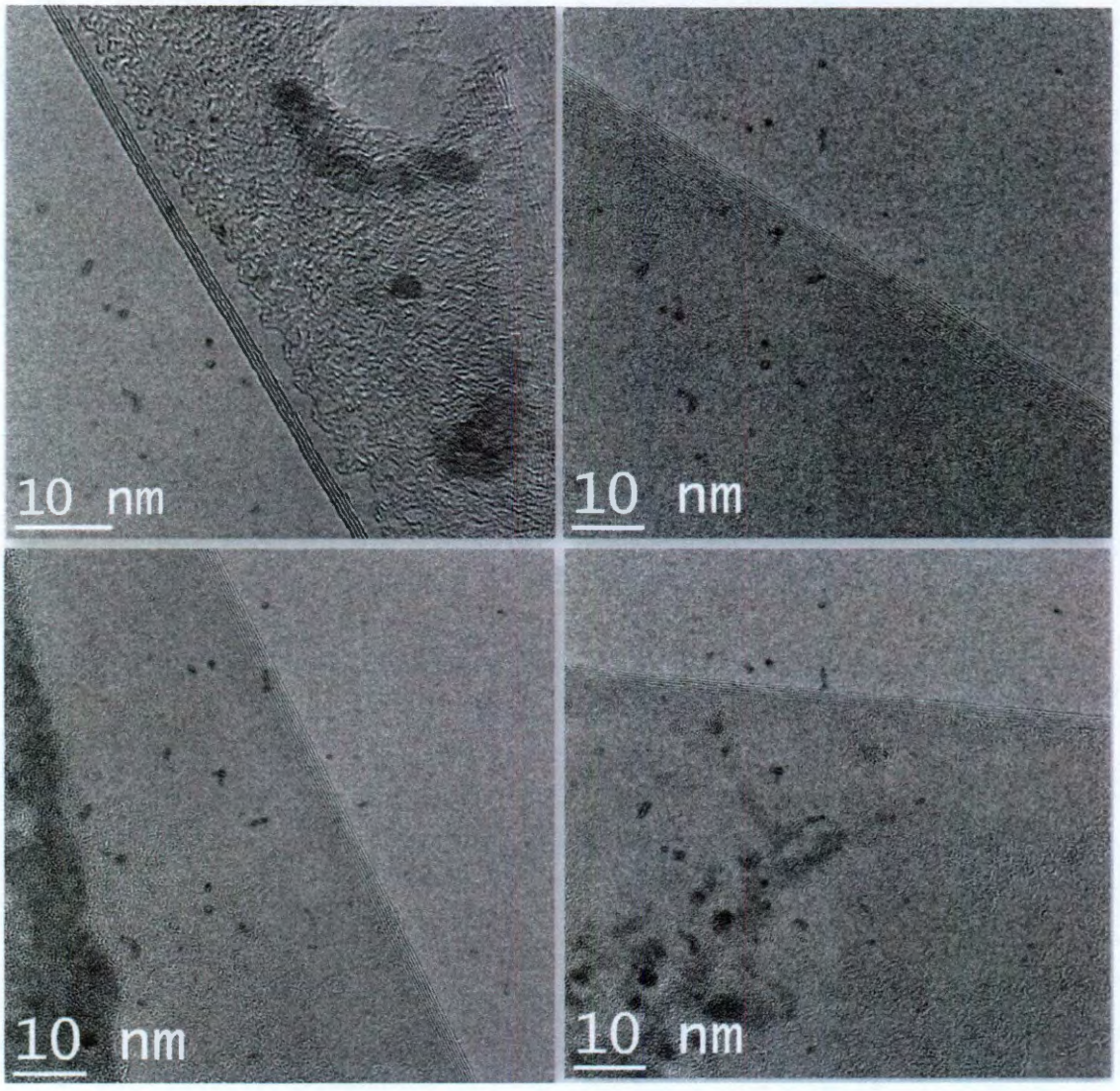

Fig. 3.10 TEM of graphene flakes exfoliated from $FeCl_3$ GIC. The number of layers at the edge is less than 10 layers.

3.6. Materials and Methods

Modified Hummers' method. The starting carbon nanomaterials (carbon black, MWCNTs or SWCNTs) were suspended in concentrated sulphuric acid (H_2SO_4)

for a period of 1–12 h and then treated with 500 wt% (relative to carbon weight) potassium permanganate ($KMnO_4$). The reaction mixture was stirred at room temperature for 1 h and then heated to 55–70 °C for an additional 1 h (for carbon black, the temperature is 90 °C). It should be noted that this procedure is explosive. All experiments should be done behind a shield. When all of the $KMnO_4$ had been consumed, the reaction mixture was quenched by pouring over ice (~1000 wt% relative to reaction mixture) containing a small amount of 30% hydrogen peroxide (H_2O_2). The solution was filtered over a polytetrafluoroethylene (PTFE) membrane (0.2 μm pore size), and the remaining solid was washed with HCl (5% in water) followed by ethanol/ether

$FeCl_3$ intercalation and exfoliation. 0.5 g graphite and 5 g anhydrous $FeCl_3$ were sealed at the two ends of a vacuum tube (10^{-2} Torr) without mixing. The tube was heated to 200 °C for 5 h and 300 °C for 1 d. After this, the intercalated graphite powders were collected and dispersed in $ClSO_3H$ (25 mL) and stirred for 2 d at room temperature. Then the reaction mixture was quenched in an ice bath by adding H_2O_2 (30% aqueous) drop by drop until no bubbles were evolved (~30 mL H_2O_2). The solution was filtered over a polytetrafluoroethylene (PTFE) membrane (0.2 μm pore size), and the remaining solid was washed with HCl (5% in water) followed by ethanol/ether.

3.7. Conclusion

Oxidation, unzipping, intercalation and exfoliation chemistry plays a critical role in the processing of carbon materials. Different forms of carbon nanomaterials were processed with such chemistries, producing various results. Unlike graphite and carbon nanotubes, carbon black is more oxidation-resistant because exfoliation is more difficult, therefore, only the near-outer surface could be oxidized. SWCNTs could be unzipped with the modified Hummers' protocol; however, the edges structure could not be preserved due to the oxidation interruptions. A less aggressive unzipping method could be less destructive to these elegant slim structures. GIC is a promising starting material to produce n-layer graphene. The technique to preserve separated graphene flakes in solution without surface functionalization is still the most challenging problem to be overcome.

Author Contributions:

Z. S. did all the wet chemistry and performed the TEM, SEM and XRD characterizations. Zengxing Zhang performed the device fabrication and electrical measurement of Part 3.3 Graphene nanoribbon unzipping.

References

1. Sun, Z.; Kohama, S.; Zhang, Z.; Lomeda, J. R.; Tour, J. M. Soluble graphene through edge-selective functionalization. *Nano Research* **2010**, *3*, 117-125.
2. http://en.wikipedia.org/wiki/Carbon_black
3. Hummers, W. S.; Offeman, R. E. Preparation of graphitic oxide. *J. Am. Chem. Soc.* **1958**, *80*, 1339-1339.
4. Staudenmaier, L. Verfahren zur darstellung der graphitsäure, *Ber. Dtsch. Chem. Ges.* **1898**, *31*, 1481-1489.
5. Liu, Z.; Robinson, J. T.; Sun, X. M.; Dai, H. J. PEGylated nanographene oxide for delivery of water-insoluble cancer drugs. *J. Am. Chem. Soc.* **2008**, *130*, 10876–10877.
6. Kosynkin, D. V., Higginbotham, A. M., Sinitskii, A., Lomeda, J. R., Dimiev, A., Price, B. K. and Tour, J. M. Longitudinal unzipping of carbon nanotubes to form graphene nanoribbons. *Nature* **2009**, *458*, 872-876.
7. Gomez-Navarro, C., Weitz, R. T., Bittner, A. M., Scolari, M., Mews, A., Burghard, M. and Kern, K. Electronic transport properties of individual chemically reduced graphene oxide sheets. *Nano Lett.* **2007**, *7*, 3499-3503.
8. Luo, Z. T., Lu, Y., Somers, L. A. and Charlie Johnson, A. T. High yield preparation of macroscopic graphene oxide membranes. *J. Am. Chem. Soc.* **2009**, *131*, 898-899.
9. Shih, C. J., *et al.* Bi- and trilayer graphene solutions. *Nat. Nanotech.* **2011**, *6*, 439-445.
10. Dresselhaus, M. S. and Dresselhaus G, Intercalation compounds of graphite. *Adv. Phys.* **2011**, *51*, 1-186.

Chapter 4

DOMAIN SIZE AND STACKING ORDER OF GRAPHENE

4.1. Introduction

CVD prepared graphene has been produced on different metal substrates, including Ni and Cu [1-3]. Compared to the micron-sized exfoliated graphene produced from wet-chemical methods[4], the size of CVD-derived graphene films have been greatly improved, ranging up to several inches[5], favoring wafer-scale optoelectronics production. One of the central challenges for the CVD synthesis method is how to assess and improve the quality of the graphene films produced. The quality means several specific aspects for graphene and is directly reflected in its physical properties.

For monolayer graphene, its quality includes the defect concentration, which can be monitored by Raman spectroscopy[6], and the domain size, which can be

mapped with dark field transmission electron microscopy (DF-TEM) or selected area electron diffraction (SAED) patterns [7]. For graphene with more than one layer, the stacking order also needs to be considered, because the stacking orders affect the symmetry and coupling between graphene layers, thereby affecting the graphene films' electronic structure under biased electrical field[8]. Fully decoupled graphene stacks behave as individual monolayer in both electrical and spectroscopic aspects[9]. Other than intrinsic qualities, adventitious contamination is always a big problem for graphene, which prevents it from its theoretical high performance. This adventitious effect will be discussed in Chapter 8.

4.2. Graphene Domains

Graphene in its purest form would be a 2D single crystal[10-12]. Such structural perfection would produce a material with extraordinary electrical and physical properties that could be harnessed to enable exceptional advances in technology. However, real-world graphene films are dominated by polycrystalline domains[1-3]. The multi-domains are knitted together with randomly oriented topological defects (grain boundaries), where the efficiency of electrical transport falls dramatically[13, 14]. This anisotropic structure also induces variable electrical properties across misaligned domains, which is one of the largest obstacles for its use in graphene-based electronic devices[15-17]. Therefore, fewer defects and larger domain size are favorable qualities to strive for in high quality graphene growth. Single crystalline graphene has been claimed to have been grown on clean-cut single-crystals Ni(111) and Ru(0001) surfaces[18, 19], however, the domain sizes were not measured. In

addition, the process could be difficult to scale-up because of the expensive single-crystalline metal substrates. Here, we have investigated the domain sizes of different graphene films. Single crystalline graphene with a tested domain size as large as 1.25 mm was grown from polycrystalline Cu substrates. The conditions for growth were optimized and a mechanism for growth of large single-crystalline graphene under these conditions is proposed.

A variety of methods to grow graphene with fewer defects and higher quality have been studied[20-22]. The defects in graphene have different dimensions. In monolayered graphene, there are point defects (zero-D defects), grain boundaries (1-D defects) and holes (2-D defects). For bilayered graphene and few-layered graphene, interlayer stacking faults (3-D defects) could exist. Among all these defects, only grain boundaries are related to the domain size. In both spectroscopic and microscopic analytical methods, the domain size of graphene is not easily determined.

Raman spectroscopy could be a powerful tool to evaluate the defect concentration in graphene, especially the ratio of sp^3-hybridized and sp^2-hybridized carbon through I_D/I_G ratio[23]. However, the dimension of the defects cannot be determined from Raman spectroscopy since all of the defect information would be combined into one Raman peak (D peak at 1350 cm^{-1}) and cannot be separated through peak deconvolution. Therefore, Raman is neither a qualitative nor a quantitative analytical technique to assess graphene's domain size, or the concentration of the grain boundaries.

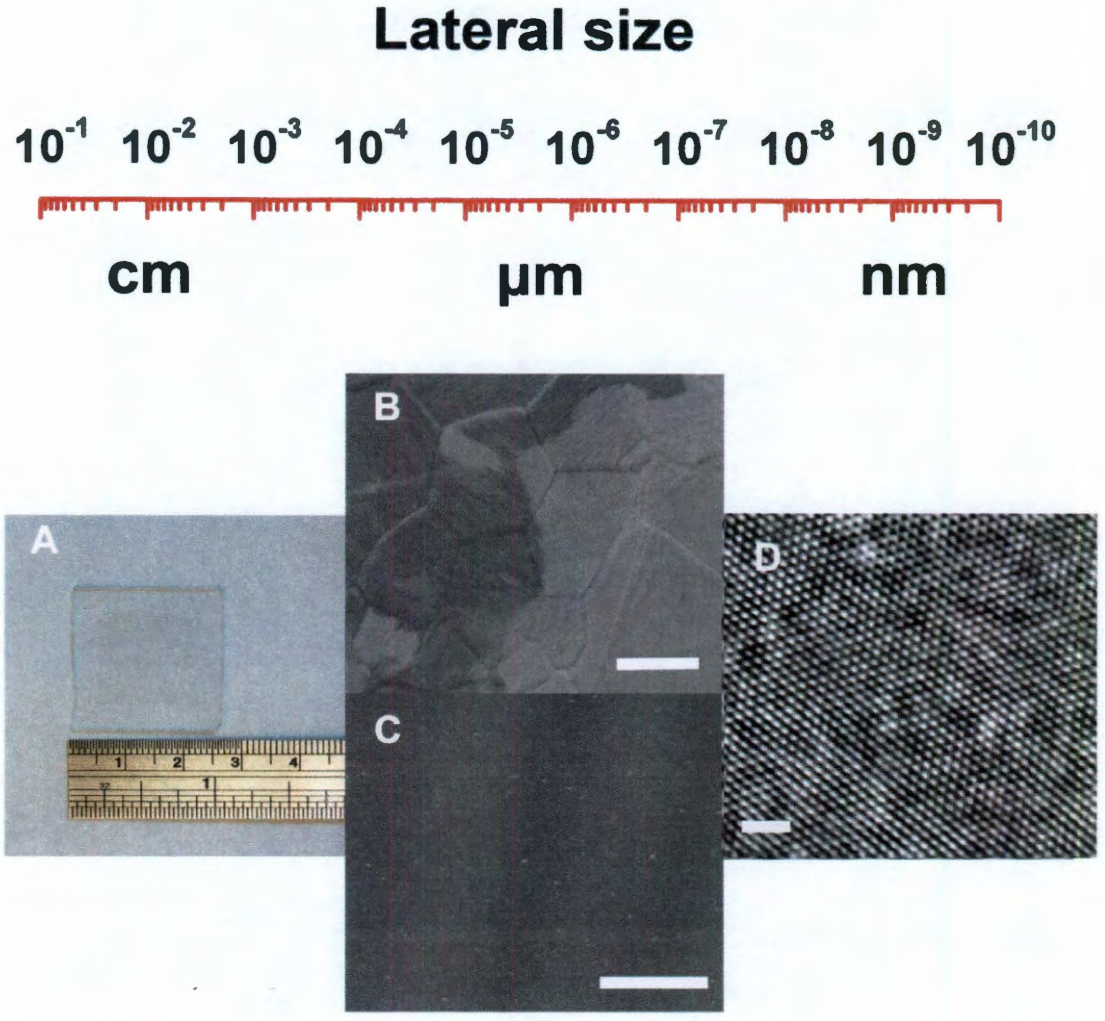

Fig. 4.1 Graphene's lateral size evolution: cm, μm to nm. Graphene images with featured lateral size are correlated below. (A) A cm-sized CVD graphene film transferred to a glass slide. (B) SEM image of graphene grown on a Ni substrate. The terrace structures are the polycrystalline Ni domains. Graphene's thickness variation is indicated by the different contrasts of the layers. The scale bar is 10 μm. (C) SEM image of graphene grown on a Cu substrate with no step morphology or contrast variation. The scale bar is 10 μm. (D) HRTEM image of CVD graphene's hexagonal lattice structure. The scale bar is 1 nm.

Graphene films with large lateral size do not necessarily have large domain size. CVD-derived graphene (CVDG) films can be centimeters in lateral size (Fig. 4.1A). This continuous, covalently bonded carbon matrix is a single molecule. However, continuity alone is insufficient for a single crystal. Amorphous and polycrystalline carbon films can also have continuous morphology. Besides the continuity, a single-crystalline material has to be coherent in symmetry with no grain boundaries. Based on Fig. 4.1A, it is difficult to assess whether the CVDG film is actually single-crystalline or polycrystalline. With a scanning electron microscope (SEM), graphene can be analyzed with μm-sized resolution. Certainly, higher magnification provides more information about the morphology of graphene and the metal substrates. Fig. 4.1B and 4.1C are SEM images of graphene grown on Ni and Cu substrates, respectively. The Ni substrate surface displayed terrace-like morphology after the CVD growth, while no obvious grain boundaries were observed for the CVD graphene on Cu of the same lateral size. Since graphene is a single-atom thick, and extremely flexible, its surface profile generally conforms to the metal substrate's morphology[24]. Therefore, based on the SEM images, it is hard to distinguish graphene's intrinsic ripples from its grain boundaries. However, the domain size of the underlying metal substrates could be estimated. Cu has a larger domain size than Ni, favoring the single-crystalline growth of graphene. But the resolution of SEM is insufficient to unveil graphene's crystalline structure: neither the symmetry nor the grain boundaries. High resolution microscopic techniques such as transmission electron microscopy (TEM) and scanning tunneling microscopy (STM) can be used to investigate the graphene crystalline structure with

enormous precision. Even point defects and grain boundaries can be individually imaged[25, 26]. Fig. 4.1D is a high resolution transmission electron microscopy (HRTEM) image taken of CVDG grown from Ni substrate, which clearly shows graphene's honeycomb crystalline structure. However, with HRTEM single frame's size of only several nm, it is very difficult to assess the crystallography of an entire CVDG film using HRTEM.

4.2.1. SAED Mapping of Graphene Domains

SAED can quickly and unambiguously determine graphene's crystallography. It has been used to determine the single crystallography for different 1D nano-material, including inorganic nanowires, nanotubes and nanoribbons[27-29] and small graphene single crystals[1]. However, it has never been applied to large 2D nano-material like millimeter-sized graphene. With the same concept behind, for a single-crystalline material, there is only one SAED pattern due to the crystal's coherent symmetry. Polycrystalline materials usually have more than one SAED pattern, with a tilted angle because of the misaligned domains. If the domain number is large enough, the overlapping patterns would appear as circles with no specific orientation, which is the characteristic topology of a polycrystalline material. However, a single SAED pattern analysis only covers an area of μm-sized graphene. In order to assess a large piece of graphene, SAED patterns were taken randomly across the entire film and the data were overlaid. If the entire graphene film shares the same SAED pattern, it is single-crystalline graphene. Otherwise, it is polycrystalline.With this SAED mapping, the investigation of graphene's domain size

becomes feasible. Large-area graphene films were grown on Ni and Cu substrates via different CVD methods (*4-6*). The graphene films were then wet-transferred onto a c-flat TEM grid (Protochips, Inc.) for further characterization. The thickness of the graphene was estimated with TEM by imaging the edges. For graphene grown from Ni, few-layer edges were observed (< 10 layers). For graphene grown from Cu, only mono- and bi-layer edges were observed and confirmed with Raman mapping with an I_{2D}/I_G ratio < 1.0 (Fig. 4.2). The thickness of different kind of graphene corresponds well with other reports (*4-6*). The typical TEM images of such films are shown in Fig. 4.3. Under low magnification, monolayer graphene film is transparent under the electron beam. Only ripples or folding could be observed. Few-layered graphene grown from Ni is strong enough to be supported directly on lacey carbon TEM grid (Ted Pella, Inc.) and is easily observed under SEM (Fig 4.4).

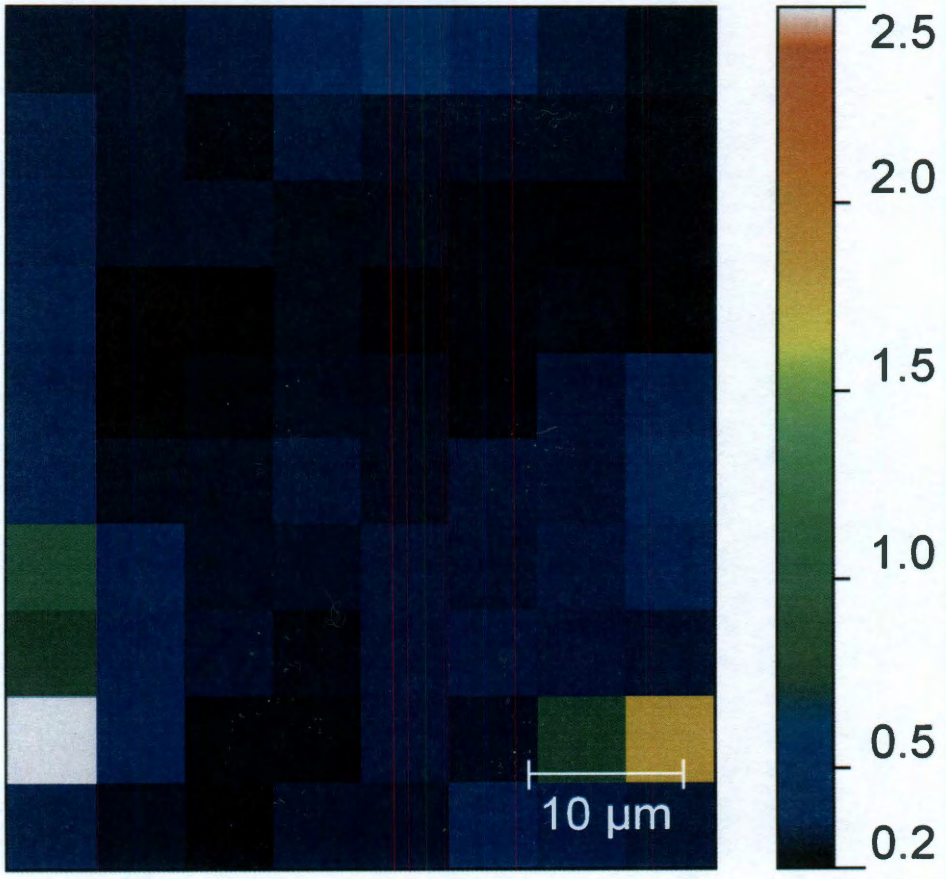

Fig. 4.2 Raman mapping of I_{2D}/I_G ratio of a typical graphene film grown on Cu. More than 95% of the film has a mono-, bi-layer coverage.

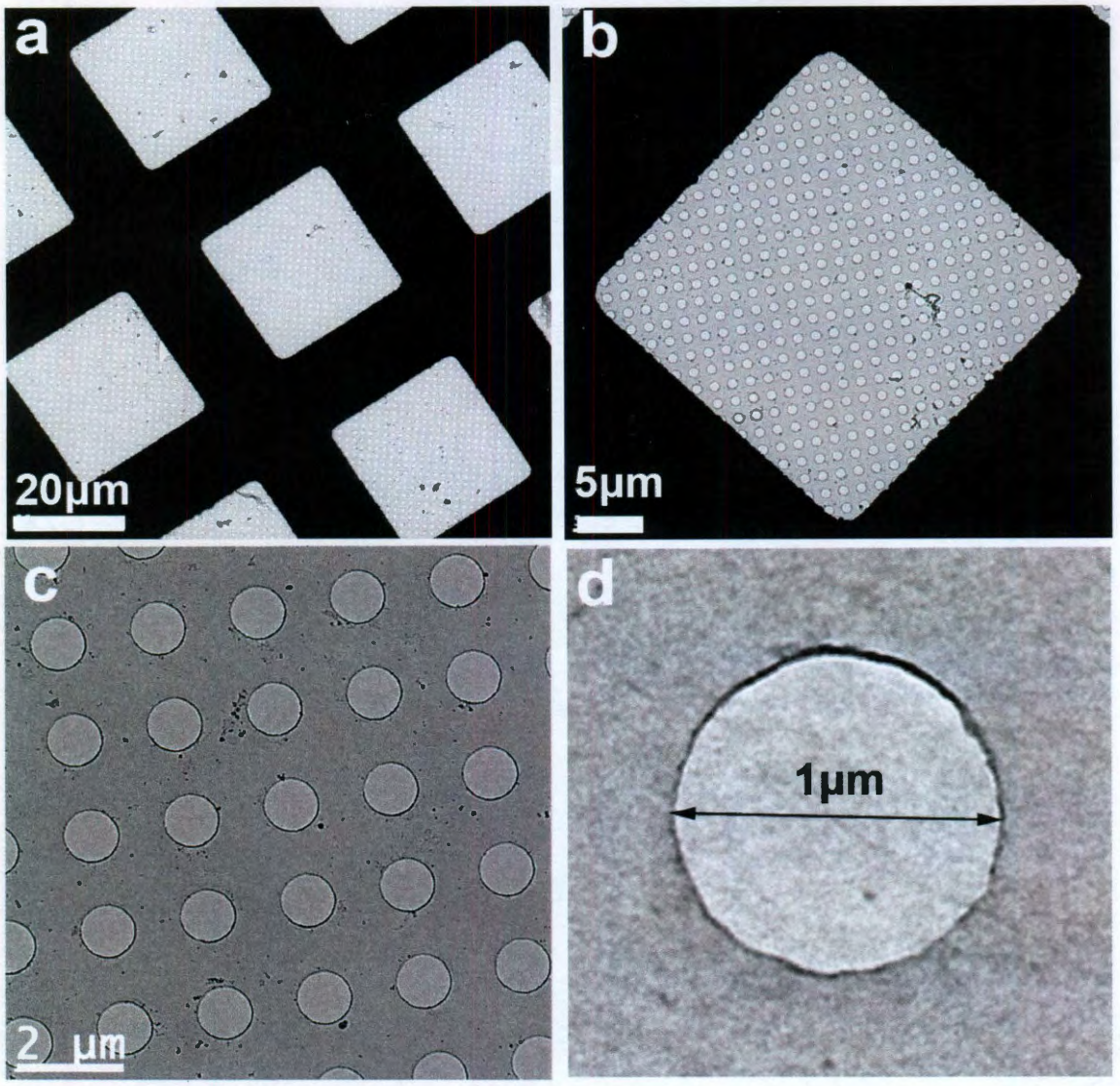

Fig. 4.3 Monolayer graphene film grown from Cu on c-flat TEM grid (Protochips, Inc.). The graphene film is invisible under low magnification in (a), (b) and (c). At higher magnification, only the ripples and contaminations on graphene could be observed in (d).

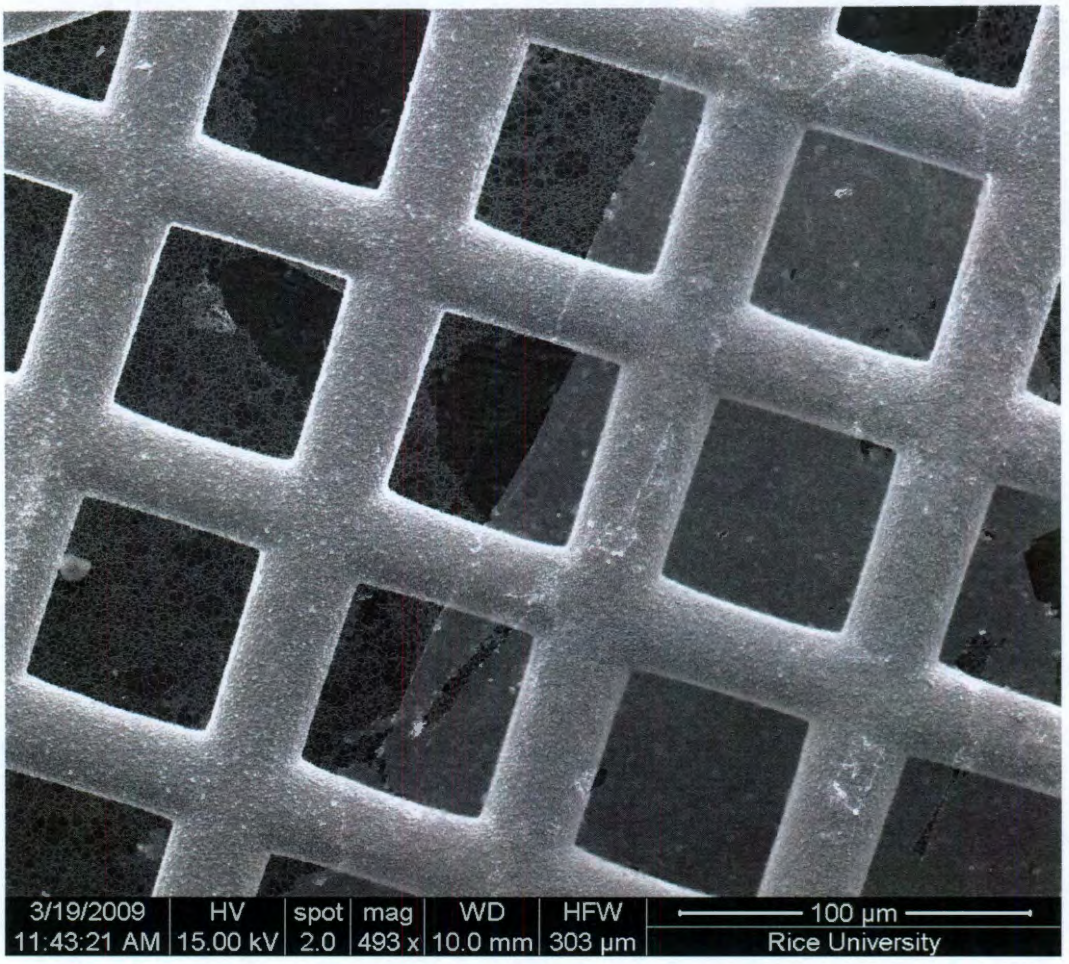

Fig. 4.4 SEM image of few-layered graphene film grown from Ni on lacey carbon TEM grid.

Fig. 4.5A is the SAED mapping of CVDG from Ni. Each SAED pattern was labeled by its position in the TEM, marked by its X, Y coordinates. Similar SAED patterns share the same color, indicated that they are from a single domain. According to this SAED map, the average domain size of the CVDG grown from a Ni substrate is less than 10 µm. All of the SAED patterns were overlaid to produce a combined pattern (Fig. 4.5B). The spread of the spectral images indicates that there is no preferred angle between adjacent domains, which is strong evidence that the

domains grew independently until they met at the grain boundaries[30, 31]. Despite the fact that, in each SAED acquisition area, this CVD graphene had a single-crystalline signature, the film as a whole was polycrystalline.

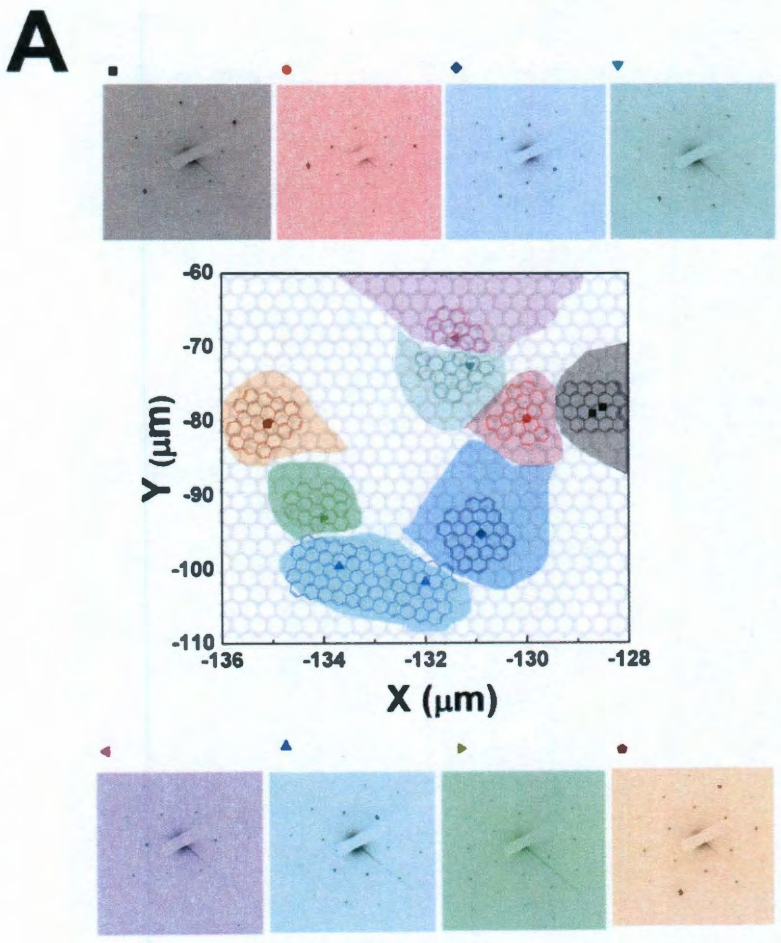

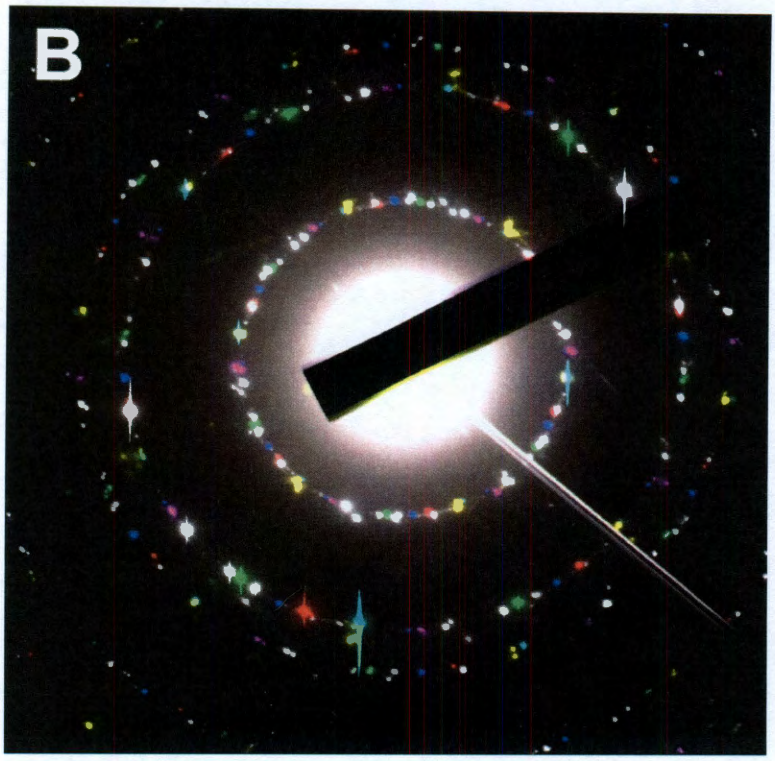

Fig. 4.5 Domain size of CVD graphene grown from Ni. (A) SAED mapping of CVD graphene from Ni. Different domains are labeled with different colors. Each domain has only one diffraction pattern. Related SAED patterns are above or below the central map. The SAED positions are marked on the central map. The graphene structure in the background is a cartoon and is not to scale. (B) Overlaying of all SAED patterns from the graphene film. There is no correlation between the colors in (A) and (B).

The CVDG grown from Cu had much more coherent SAED maps than the graphene grown from Ni. No divided domains were observed as shown in Fig. 4.6A. All of the SAED patterns have precisely the same orientation, indicating a single-crystalline lattice structure of CVDG (Fig. 4.6B). Based on the data in Fig. 4.6A, this graphene film has a single domain size as large as 1.25 mm, across the entire

graphene film suspended on the TEM grid. The slight offset in the SAED patterns is due to the intrinsic corrugation in the graphene film or accidental folding during the transfer.

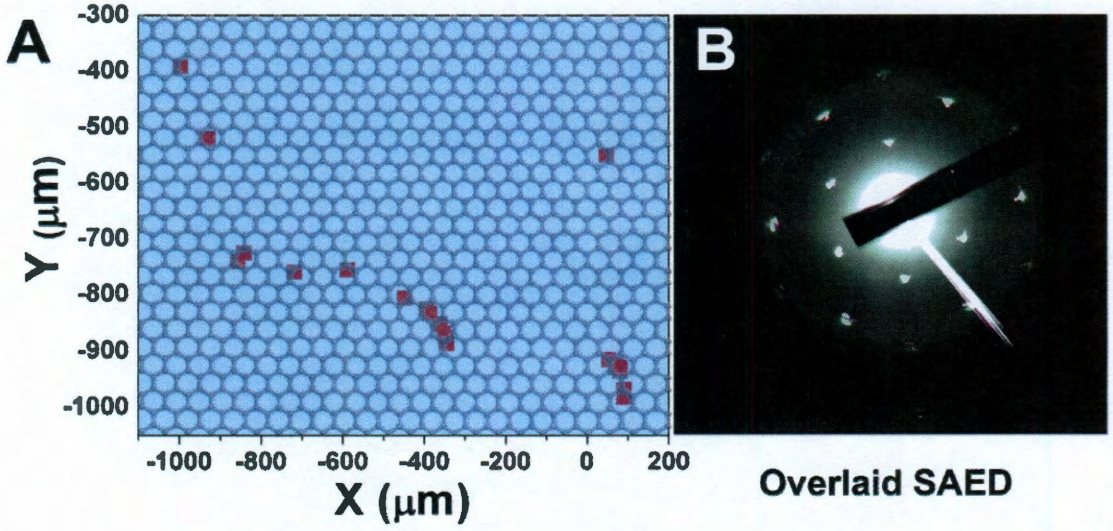

Fig. 4.6 Domain size of CVD graphene grown from Cu. (A) SAED mapping of CVD graphene from Cu. A single domain was observed with only one set of SAED patterns across the 1.25 mm-sized film. The SAED positions are marked on the map. The graphene structure in the background is a cartoon and is not to scale. (B) Overlaying of all SAED patterns from the graphene film.

Graphene made from poly(methyl methacrylate) (PG) on Cu substrates also had a large single domain size (see Fig. 4.7)[32]. Although the SAED analysis positions were randomly chosen, due to the limitations of the wet transfer technique, some areas of the graphene film were broken or wrapped together. All of the SAED analysis points avoided these areas. For statistical purposes, 24 SAED patterns were recorded separately at different positions on this graphene film, as shown in Fig. 4.8.

The lateral size of the graphene single crystal is as large as 1.25 mm and it could be overestimated only when sub-domains with exactly aligned orientation or graphene twins exist (see Fig. 4.9).

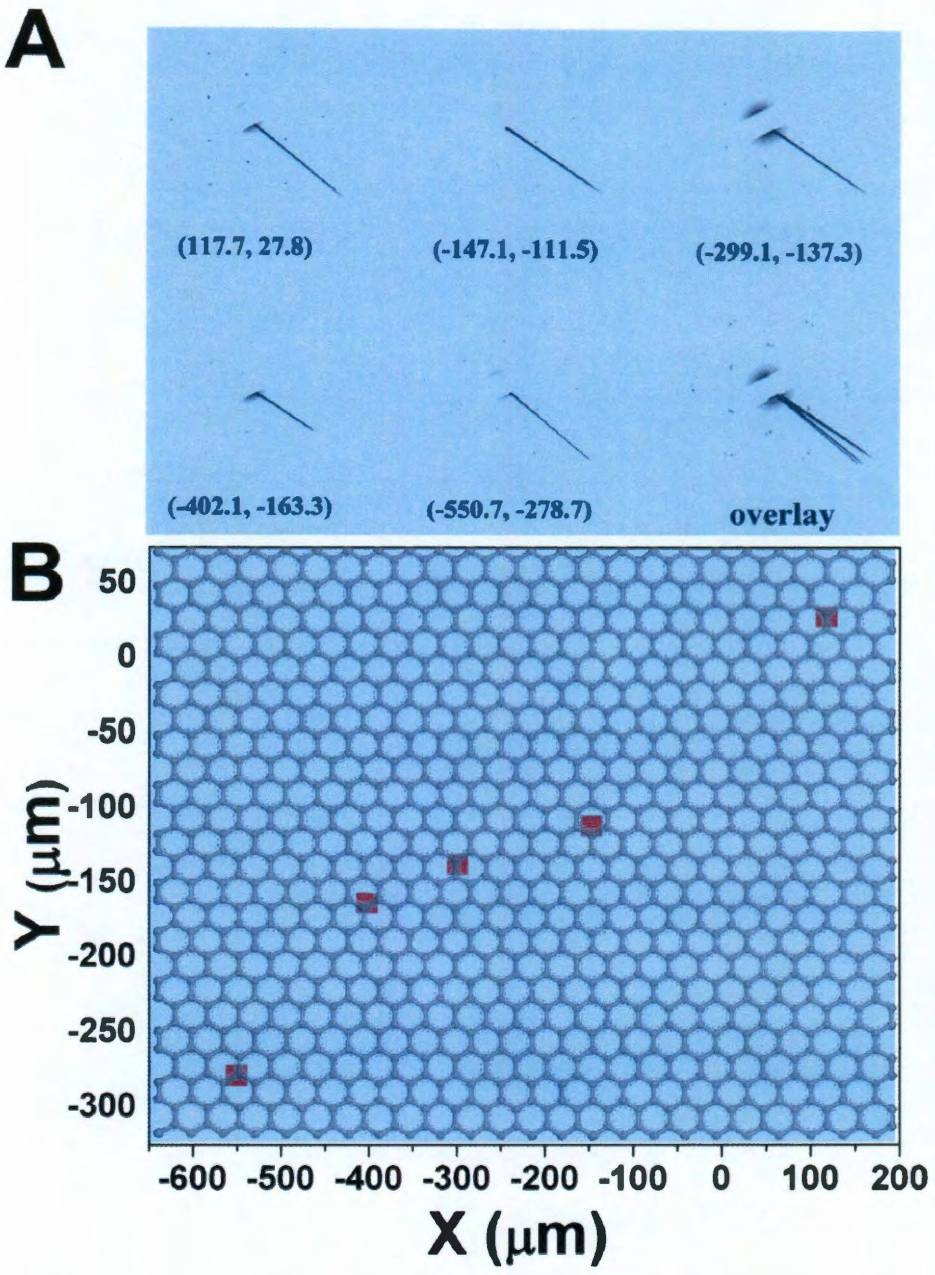

Fig. 4.7 Domain size of PG grown from Cu. (A) SAED patterns and overlayed SAED patterns from different position. (B) SAED map of PG.

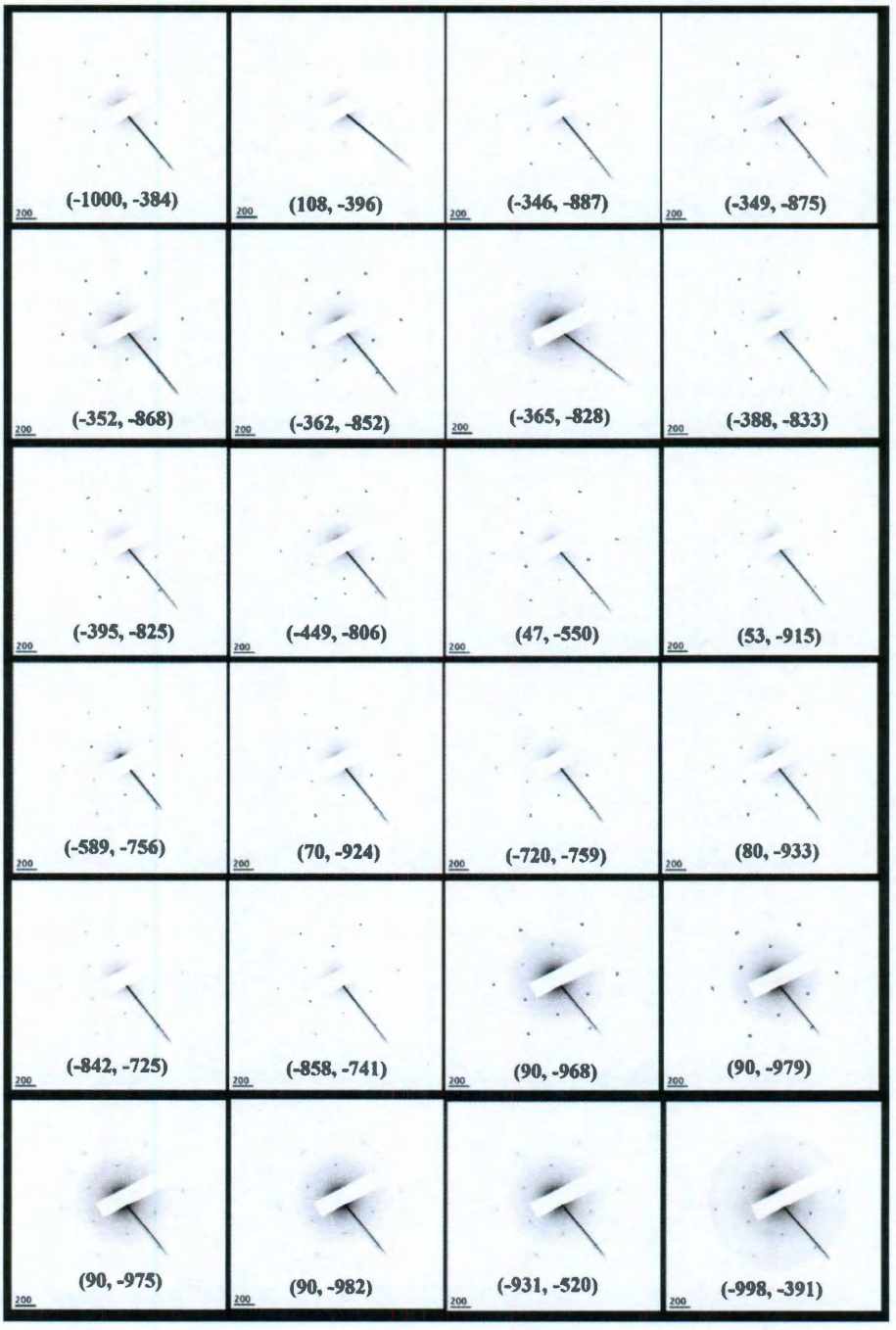

Fig. 4.8 Statistic SAED patterns (24 different positions) were acquired on monolayer graphene film, CVD grown from Cu and suspended on TEM grid.

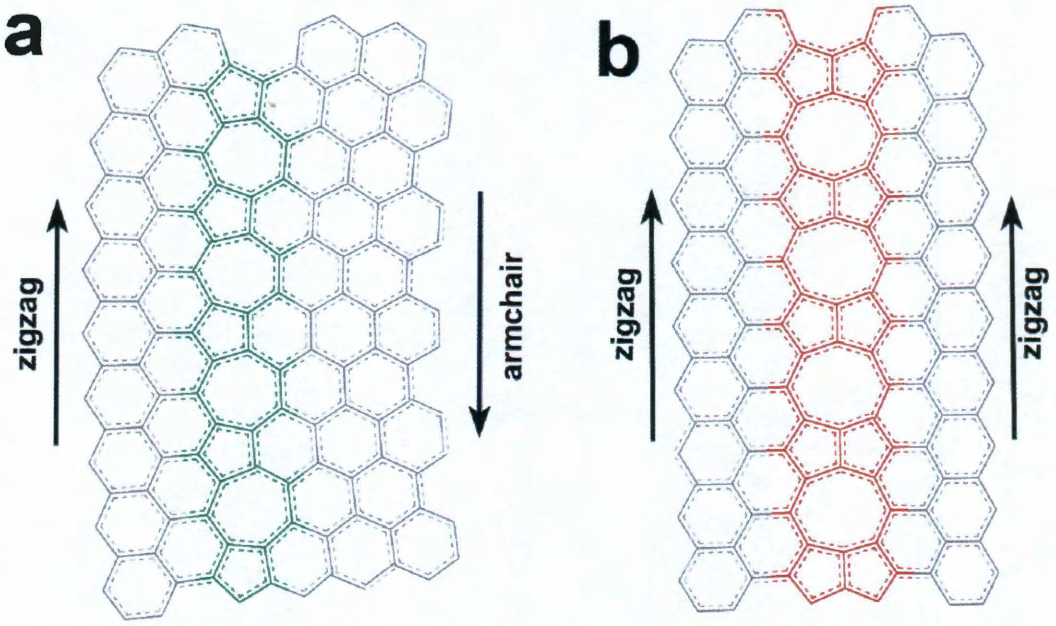

Fig. 4.9 Simulated grain boundaries with typical (a) mis-aligned domains and (b) aligned domains or graphene twins.

It is challenging to image the GBs of the CVD graphene directly using HRTEM, as they normally are covered with small molecules or residual PMMA contamination introduced during the wet transferring procedures. However, with SAED and FFT patterns, it is possible to locate the GBs within sub-10 nm areas. As shown in Fig 4.10, two distinctive FFT patterns were observed on either side of the GBs. Right atop the GBs, the FFT characteristics displayed combination patterns from both domains.

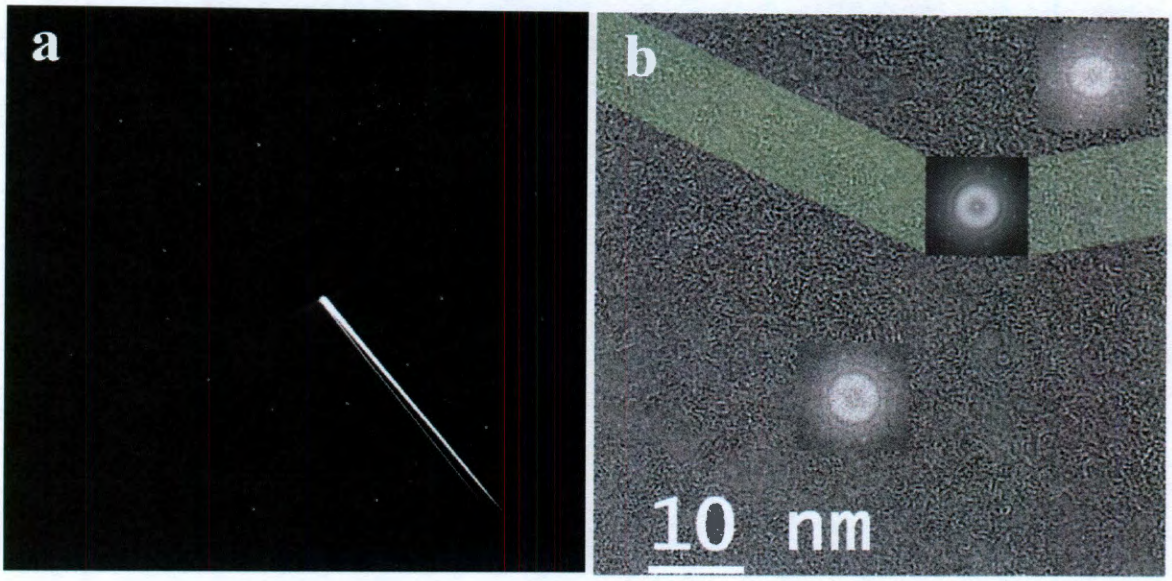

Fig. 4.10 (a) SAED pattern of two adjacent domains (on GB). (b) GB located through FFT patterns in HRTEM image. Two distinct FFT patterns are divided by the GB. The GB's location can be narrowed to within a sub-10 nm band (green), where the FFT pattern shows a combination of the FFT from both graphene gains. The atomic resolution of the GB is obscure due to the coverage of the surface with small molecules of contamination introduced during the wet transferring procedure.

4.2.2. Graphene-Directed Crystal Facet Flipping and the Mechanism of Growing Single-Crystalline Graphene from Polycrystalline Substrates

X-ray diffraction (XRD) was used to investigate crystallographic changes in the metal substrates. To our knowledge, XRD has been rarely used in early graphene studies. One reason is that there is only one reflection plane for single-layered graphene, which gives no constructive interference according to Bragg's diffraction law (Fig. 4.11). However, the XRD does contain the crystallographic information of the underlying catalyst, which is related to the formation of the graphene.

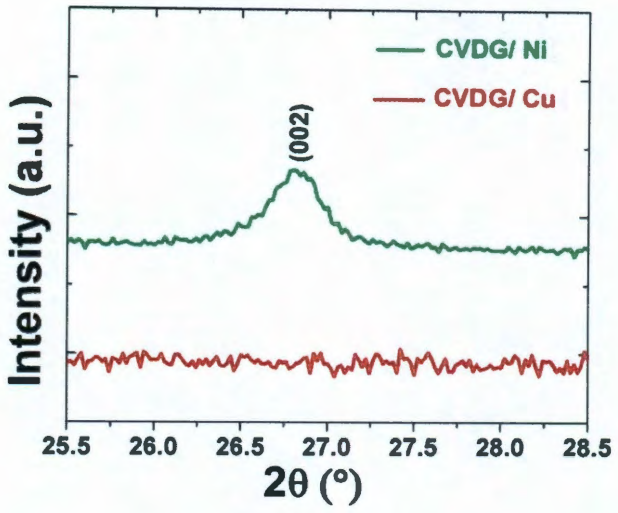

Fig. 4.11 XRD of the graphite (002) peak aquired from different CVDG samples. The spectra of the CVDG grown atop Ni (top) and Cu (bottom). On Ni, a stack comprised of a few graphene layers accounts for the broadened (002) peak at 26.8°. No (002) peak appears in single-layered graphene on Cu.

Fig. 4.12 shows the XRD spectra of the Cu substrates before and after the graphene growth. The fresh Cu foil has a (200) facet facing the incident X-ray before growth suggesting a strong (200) preferred orientation.. Meanwhile, it is polycrystalline material according to its SEM image (Fig. 4.13). The gain structure of the Cu foil has also been investigated by SEM by other groups[3, 5]. After the graphene growth, the (111) peak becomes the most prominent peak in the XRD spectrum, suggesting phase transition of the Cu crystal facet. Considering that in most cases the growth temperature (1000 ° C) is so close to Cu's melting point (1085 ° C), and any impurities (carbon sources) can lower the melting point, the Cu foil might partially melt starting from its surface[33]. The surface melting is also related to the

crystal phase transition of Cu. Because the phase transition occurs from surface to bulk, some center parts of the Cu foil might still be (200), which can be detected by XRD as a small peak. Bulk melting was not involved in the process.

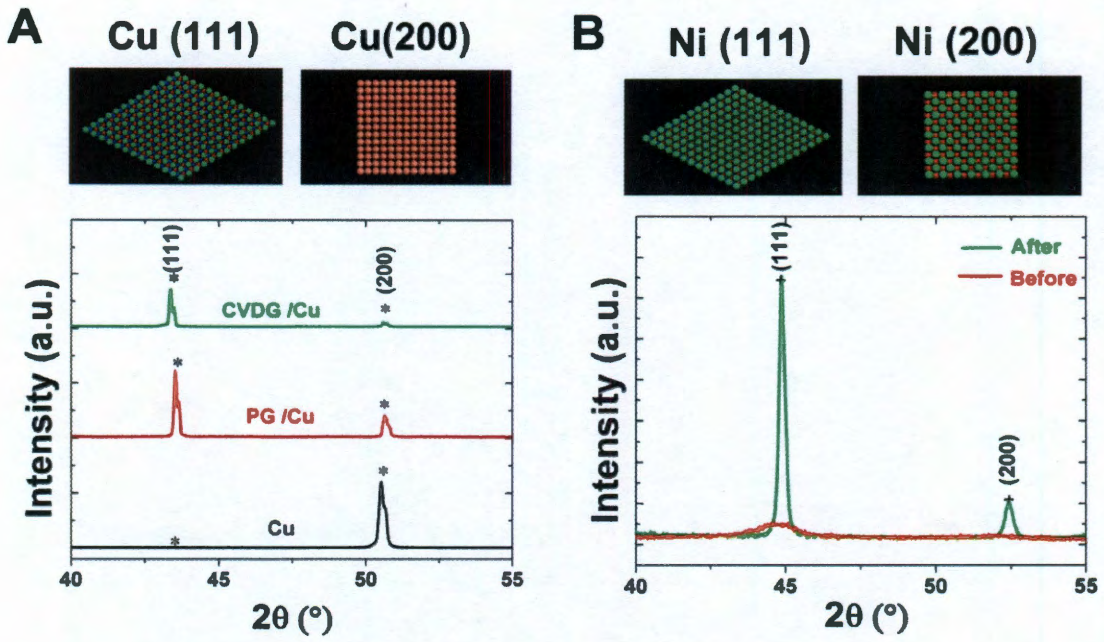

Fig. 4.12 Crystallography of the catalyst substrates before and after graphene growth. (A) XRD pattern of the Cu film before graphene growth (black), after PG growth (red) and after CVDG growth (green). After graphene growth, the (200) peak in Cu was shorter and the (111) peak becomes the primary peak. The corresponding lattice structures of the Cu(111) plane and Cu(200) plane are shown above the XRD spectrum. (B) XRD pattern of the Ni substrate (500 nm Ni deposited on 200 nm SiO_2/Si wafer) before (red) and after CVDG growth (green). Both the (111) and (200) peaks were more pronounced after the graphene growth. The corresponding lattice structures of the Ni(111) plane and Ni(200) planes are shown above the spectrum.

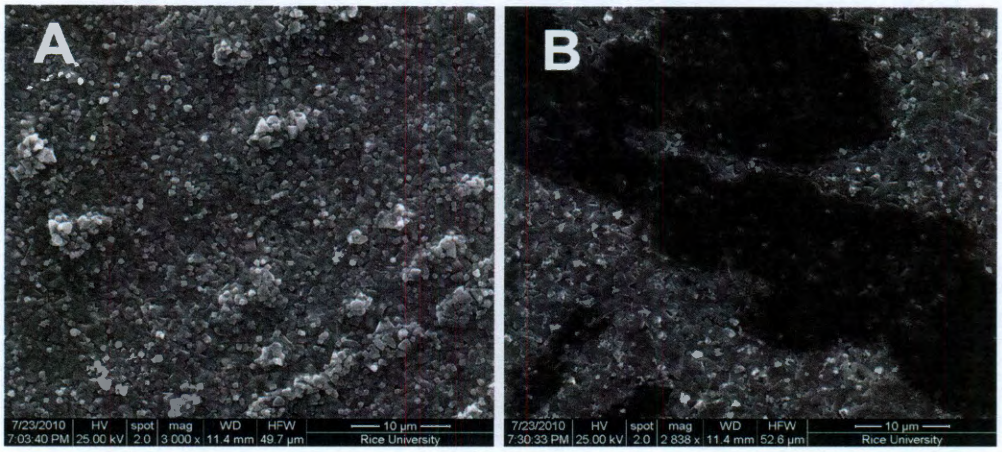

Fig. 4.13 SEM images of Cu's polycrystalline domains. (A) Before the CVD growth, preferred orientation of Cu (200) facets with a rotational disorder. (B) After the CVD growth, preferred orientaion of Cu (111) facets with a rotaional disorder. The Cu films were treated with the echant for 5~10 s before aquiring the SEM images.

According to the vapor-liquid-solid (VLS) mechanism, which explains the formation of single crystal Si nanowire[34], large crystalline graphene could grow from the Cu's liquid surface. Since liquid Cu has no grain boundaries, "floating" graphene films could form larger, single-crystalline domains during the thermodynamically driven process. As large graphene crystals keep growing, they might consume small crystals to produce graphene with no GBs after the coalescence. To merge two larger crystals, more energy and longer time is needed. When the energy barrier is too high to be overcome, polycrystalline graphene forms. Once the Cu surface is covered with graphene, the carbon atoms in the gas stop penetrating into Cu and the graphene growth is limited in 1 or few layers[3]. It is thought that the solubility of carbon in Cu is negligible[3], the soluble carbon atoms,

together with other impurities, lower the Cu's surface melting point and the phase transition temperature dramatically. In a separate experiment, annealing Cu without any carbon sources at 1000 ° C does not alter the crystal orientation (Fig. 4.14), confirming the key role of CVD carbon sources in Cu's surface melting and recrystallization.

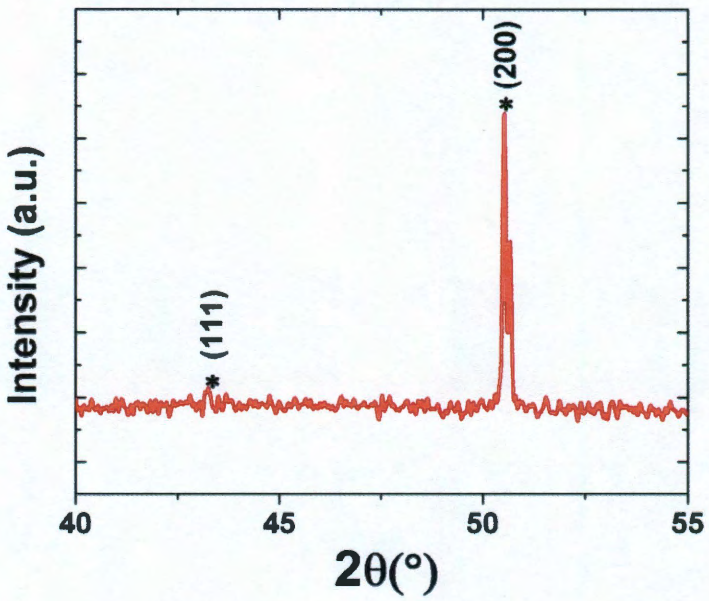

Fig. 4.14 XRD of the annealed Cu foil at 1000 °C for 30 min with a H_2 flow rate of 50 sccm under low pressure. Potential carbon sources (both gas phase and solid phase) were carefully purged from the chamber before the annealing.

To achieve the best lattice match between the graphene honeycomb structure and the Cu(111) plane, it could be more energetically favorable for the mobile Cu atoms to recrystallize along the (111) direction, with lower interfacial energy.

Temperature-dependent experiments illustrate that the carbon sources in the CVDG growth lowers Cu's phase transition temperature to 900~950 ° C (Fig. 4.15). It might vary with the amount of carbon sources or impurities in the CVD system.

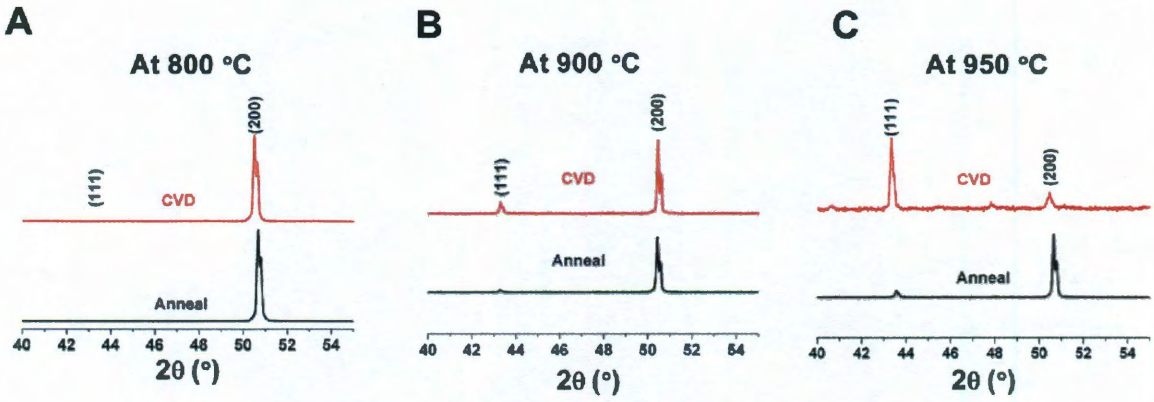

Fig. 4.15 XRD of Cu foils heated with C sources (CVD) and without C sources (anneal) for 30 min with a H_2 flow rate of 50 sccm under low pressure (1 Torr) at different temperatures: (A) 800 °C, (B) 900 °C and (C) 950 °C.

According to this proposed mechanism, the surface liquification of the Cu could produce a smooth surface with no grain boundaries, leading to the formation of single-crystalline graphene. The carbon lowers Cu's melting point, meanwhile, the graphene lattice works as crystallization seeds for Cu and facilitates its recrystallization along (111) facet. However, in the CVD process, several factors might affect the graphene's growth and its domain size. Not all graphene grown on Cu has a single-crystalline structure. Even when grown from the same Cu substrate, graphene's domain size is variable. In order to achieve a single crystalline graphene,

the growth conditions have to be optimized. According to our experimental results and proposed mechanism, higher temperature (1050 ° C) and longer (60 min) growth periods provide the energy and time to fully flip Cu's facets and ripen the graphene crystals atop the surface. A higher H_2 flow rate (> 300 sccm) also favors large single crystals formation. Other CVD factors that might affect the growth are still under investigation.

Compared to Cu, no crystal facet flipping was observed in graphene atop Ni. In Fig. 4.12B, the original Ni (500-nm thermally evaporated film on SiO_2/Si wafer) shows broad peaks, indicating the Ni film is composed of numerous micro-crystals. After the growth, both the (111) and (200) peaks are more pronounced, as the crystal size grows. Although the (111) facet of Ni matches best with the graphene's lattice structure, no favorable facet is observed on Ni after the growth by XRD. This is probably because Ni has a much higher melting point (1453 °C) than Cu, thus requiring a higher temperature to complete the recrystallization. Besides, at temperature close to Ni's melting point, it becomes more challenging to limit the graphene's thickness because carbon is much more soluble in Ni at higher temperature. Tilted domains and the step structure in Ni limit the epitaxial single-crystalline graphene formation[27]. The different graphene growth mechanism on Cu and Ni was also investigated by ^{13}C isotope labeling by Li. *et al* [31].

4.2.3. The Domain Size Affects the Electrical Transport

The domain size is also reflected in graphene's electrical transport behavior. Larger domain size corresponds to smaller intrinsic sheet resistance (4-probe

method). Following the SAED mapping described above, three CVDG samples with different domain sizes (grown from Cu under same conditions) were assessed as monolayer films atop SiO_2. The sample with the largest domain size, > 1.25 mm, has the lowest sheet resistance of 700 Ω/□ . For the sample with a domain size of ~ 100 μm, the sheet resistance was ~ 2400 Ω/□ . The graphene with the smallest domain size, 10 μm, has the largest sheet resistance of ~ 2 MΩ/□ . The domain size determines graphene's intrinsic electrical transport properties. However, extrinsic factors might also affect graphene's electrical transport. For example, substrate trapped scattering centers are known to decrease the mobility in graphene[35]. Chemical doping might manipulate graphene's conductivity[36]. For these reasons, correlation between the domain size and the sheet resistance might not be linear. By eliminating those extrinsic defects, and the intrinsic defects described here, it may be possible to push graphene's properties to their theoretical limits. The yield of mm-sized single crystal graphene is still low according to our most recent experiments, which is only about 5% in all CVD graphene grown. Substrates might play a key role for such large domain graphene formation. It is also sensitive to CVD system conditions. Further experiments are undergoing to increase the yield of the high-quality graphene.

4.3. Stacked Graphene Synthesis with Precise Thickness Control

A few-layer graphene, with Bernal stacked order, is of particular interests to the graphene community because of its unique tunable electronic band structures[8, 9]. A way to continuously tune the thickness of graphene from 1 to 10 layers would be

ideal to supply chemists and physicists with the complete graphene catalog. Also, exploring the stacking mechanism between graphene layers will help researchers to obtain better understanding of Cu-surface growth mechanism.

In exploring the parameters of CVD growth, different metal catalysts were tried in order to obtain monolayer graphene[1-3]. Since the report of Cu-based CVD graphene synthesis [3]; graphene research groups have been focusing on optimizing the use of this material. Unfortunately, CVD systems vary from one to the other. Parameters variables that can control graphene growth include the vacuum pressure in the system, flow rate, growth pressure (partial pressure for both growth gas and carry gas), growth temperature, cooling rate and so on[37-40]. These parameters were analyzed in separate papers, but have not been analyzed systematically nor were the varying parameter effects studied in concert. Here we summarize the growth conditions from different growth systems with various graphene samples. After analysis, what appears to be the controlling parameter for graphene thickness was determined and a comprehensive growth map is summarized with the various growth partial pressures (both carbon sources and H_2 gas) being expressed in detail. With this optimization, a series of Bernal stacked graphene films with precise thickness control has been synthesized.

4.3.1. Reported Graphene Growth Conditions

Table 4.1 summarizes the reported CVD growth conditions for monolayer, bilayer and multilayer graphene. Some of them are using flow rate (sccm) of H_2 and CH_4 and the total growth pressure to mark the growth conditions, which were

converted into partial pressure in Table 4.1. From these preliminary growth data, the following hypothesis could be developed:

(1) Bi- and multilayer graphene form under higher partial pressure of CH_4 and lower or zero H_2 partial pressure.

(2) When the temperature is above 1000 °C, it has little affect on the thickness of the graphene.

(3) Monolayer graphene forms under lower CH_4 partial pressure, whereas the total growth pressure can be low pressure CVD (LPCVD) or atmospheric pressure CVD (APCVD).

Table 4.1 Graphene growth summary from other literature.

Samples	Growth pressure (Torr)	Growth Temp (°C)	H_2 pressure (Torr)	CH_4 pressure (Torr)	Notes
1[37]	760	1050	24.5	0.006	Monolayer Single crystal
2[38]	760	1000	76	0.068	Monolayer no D peak
3[38]	760	1000	76	3	Multilayer no D peak
4[38]	760	1000	707.25	62.75	Multilayer With D

					peak
5[39]	0.2	1035	0.04	0.16	Monolayer no D peak
6[40]	0.45	1000	0	0.45	Bilayer With D peak

4.3.2. Precise Control of Graphene Thickness in a CVD System

These listed data in Table 4.1 are reported from different research groups, which have considerably large deviation. In order to confirm our hypothesis and to generate a comprehensive map to control the thickness control of graphene growth, a series of CVD experiments with continuous tuning of the partial pressure of growth gases were performed.

As shown in Table 4.2, in our own CVD system, an optimized growth condition for monolayer graphene was chosen as the first data point of the series, Sample 1. The flow rates of H_2 and CH_4 were 300 sccm and 9 sccm, respectively. These two flow rate were kept the same throughout the rest of the samples in this series. A needle valve was used to precisely manipulate the pumping rate, which controls the total pressure of the CVD system, thereby controlling the growth partial pressure. The pressure ratio between H_2 and CH_4 is fixed was ~28, while the total

pressure was tuned from 5.8 to 740 Torr, ranging from a low pressure growth condition to an almost atmospheric pressure growth condition.

Table 4.2 Growth conditions in CVD system.

Sample	Growth pressure (Torr)	Growth Temp (°C)	H_2 pressure (Torr)	CH_4 pressure (Torr)	Notes
1	5.8	1000	5.6	0.2	Monolayer
2	11.6	1000	11.2	0.4	Monolayer
3	23.2	1000	22.4	0.8	Monolayer
4	46.4	1000	44.8	1.6	Monolayer
5	93.3	1000	89.5	3.6~3.8	Bilayer
6	139.2	1000	134.4	4.8	2-3 layer
7	185.6	1000	179.2	6.4	2-3 layer
8	277.6	1000	268.8	9.6	4-layer
9	370	1000	358.4	12.8	>5-layer
10	555	1000	537.6	19.2	>10 layer
11	740	1000	716.8	25.6	> 10 layer

The graphene films were grown and transferred onto different substrates using the method described previously[32], the thickness of the graphene films was subsequently investigated with UV, Raman and HRTEM. UV was used to assess large area (cm-scale) thin films absorption for graphene at 550 nm. However, the detailed uniformity of the thin film cannot be revealed due to its limited spatial resolution. Raman is a powerful tool to determine both the quality and the thickness of graphene film over a micron-sized area according to its laser spot size. Using Raman mapping, ~100 × 100 μm sized graphene can be confirmed with both the thickness and the uniformity in micron-scale. HRTEM brought the characterization down to nanometer level, where it is a straightforward method to counting the thickness of graphene directly at its edges.

Optical images of this series of samples on glass slides are shown in Fig. 4.16. The graphene films become darker as the sample's growth pressure increases, suggesting that thicker films were grown with higher growth partial pressure of CH_4. This is also confirmed by their UV absorption data acquired at 550 nm.

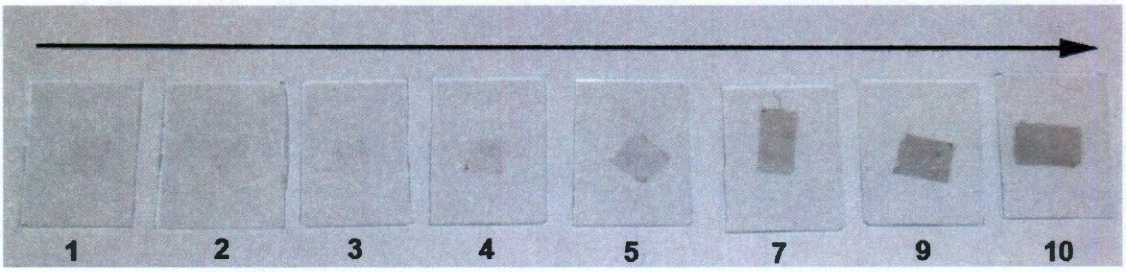

Fig. 4.16 Optical photograph of graphene films transferred onto glass substrates. The arrow direction starts from monolayer graphene to multilayer

graphene with its CH_4 partial pressure increasing from 0.2 to 12.8 Torr. Samples numbers correlate with the number in Table 4.2.

When the partial pressure of CH_4 was below 1.6 Torr, only monolayer graphene films would grow, with a UV absorption of ~2.0%. This was confirmed by the Raman spectra in Fig. 4.17. At 1.6 Torr, bi-layer graphene starts to form. Sample 4 is a hybrid of mono- and bilayer graphene film according to its UV absorption of ~3% and its optical image. When the partial pressure of CH_4 is between 3.2 and 3.8 Torr, the graphene films display a uniform bilayer characteristic over randomly chosen spots. Thicker graphene films (3 to 10 layer) are also synthesized (samples 6 to 11) as the Raman spectra have a continuous evolution in Fig. 4.17A. The G peak at ~1585 cm^{-1} becomes more pronounced and the 2D peak ~ 2700 cm^{-1} broadens and blueshifts, suggesting a thicker graphene films' Raman signature. The exact 2D peak positions are recorded in Fig. 4.17B. The blueshift starts from 2690 cm-1 (monolayer) and rises to 2717 cm^{-1} (>10-layer), which is consistent with the results from mechanical exfoliated graphene[23].

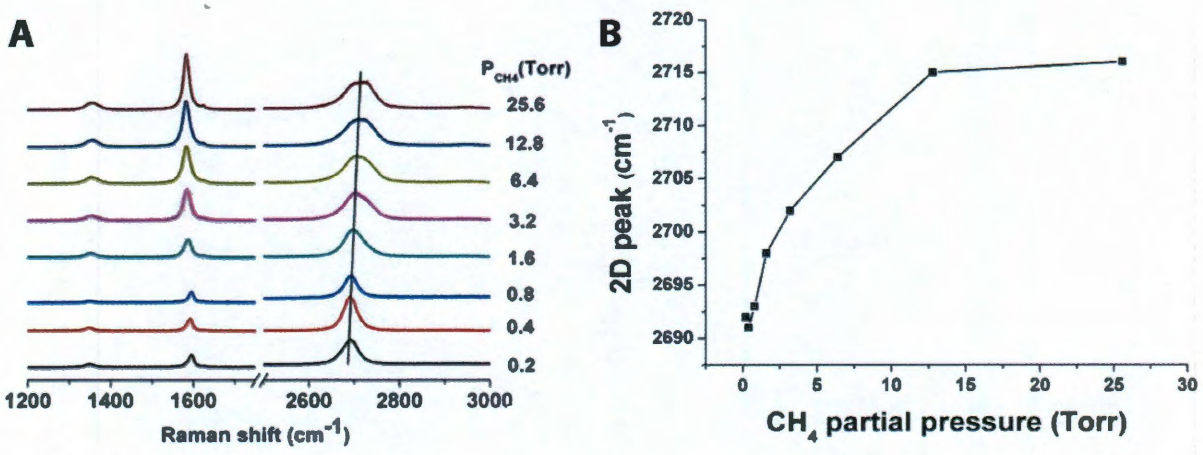

Fig. 4.17 Raman characterization of graphene films. (A) Raman evolution of graphene grown with increased CH_4 pressure. (B) 2D peak position of Raman spectra in (A).

The Raman mappings in Fig. 4.18 were acquired from samples 1, 5 and 8, respectively. Fig. 4.18A shows that more than 90% of the graphene film is monolayer with a G/2D intensity ratio below 0.5. In sample 5, no monolayer Raman spectrum is observed on any pixel of the Fig.. More than 85% of the film has a G/2D ratio of 0.85±0.1, suggesting a bilayer graphene. For sample 8, only 5 of 196 spectra in the map have a bilayer signature. More than 80% of the film has a G/2D ratio of 1.4±0.1. According to its UV absorption at 550 nm of ~8.5%, this graphene is a tetralayer graphene film.

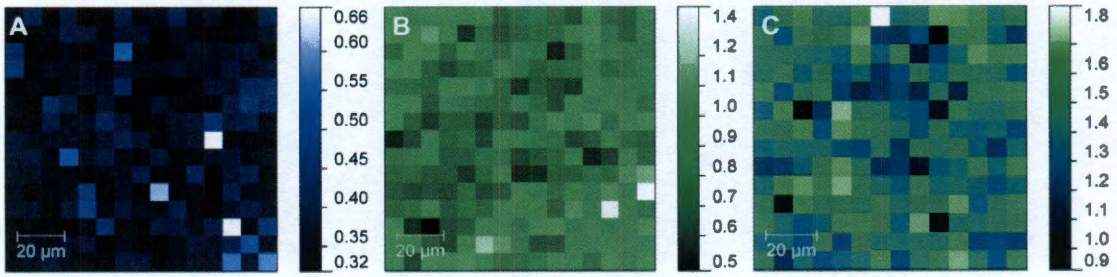

Fig. 4.18 Raman mapping of (A) Sample 1(monolayer), (B) Sample 5 (bilayer) and (C) Sample 8 (tetralayer).

SAED patterns and HRTEM spectra are complementary techniques to further analyze graphene's thickness, and its stacking order. Fig. 4.19 shows the representative diffraction pattern from Sample 1, with the (1-210) and (1-100)

intensity ratio of ~1 , which is characteristic of a monolayer graphene. The edge in HRTEM also confirms this.

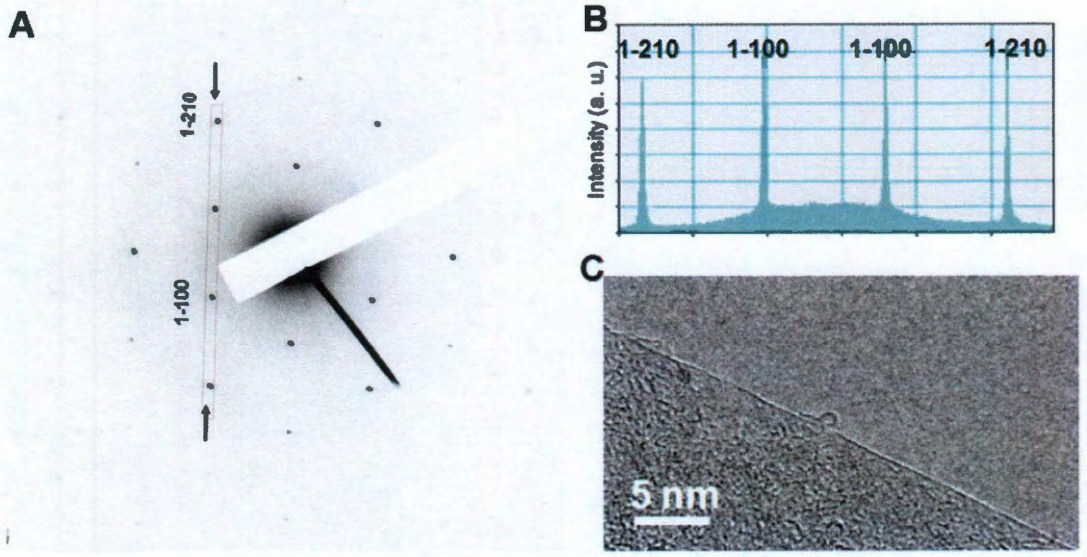

Fig. 4.19 SAED (A and B) and TEM (C) characterization of mono-layer graphene.

Bilayer graphene was prepared from Sample 5 and imaged with SAED and HRTEM in Fig. 4.20. The diffraction intensity of (1-210) is about 3 × of that of (1-100), which is a typical bilayer graphene. The randomly chosen edge in Fig. 4.19C confirms this bilayer graphene.

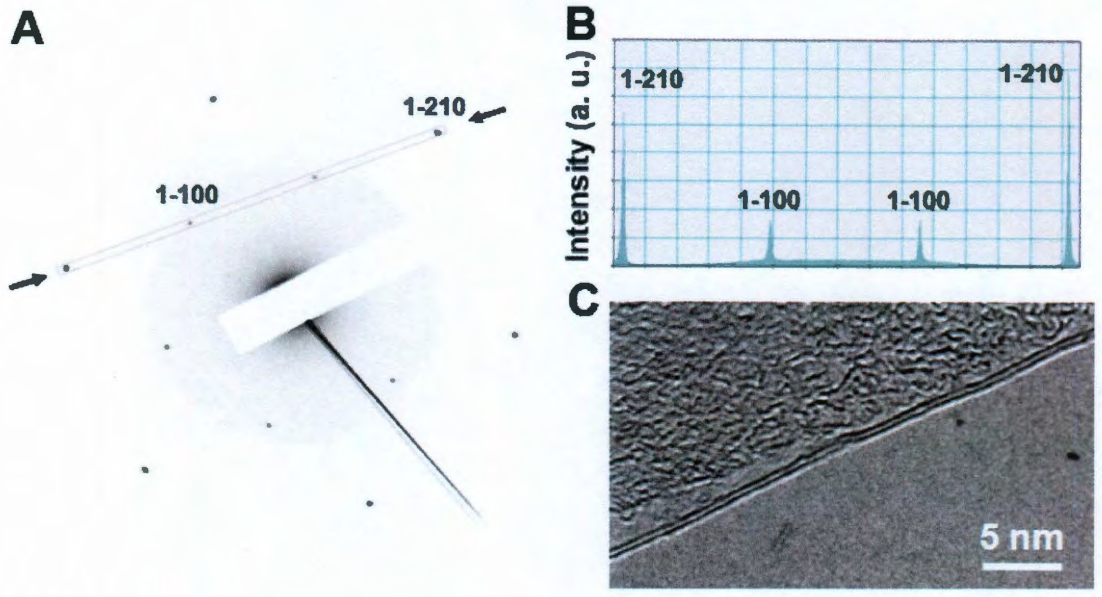

Fig. 4.20 SAED (A and B) and TEM (C) characterization of bilayer graphene.

Tetralayer graphene (Sample 8) was transferred and investigated in the same way as the other two samples. In its typical diffraction pattern, the (1-210) diffraction spot is about 4 × of the intensity of the (1-100). This intensity contrast between (1-210) and (1-100) is larger than bilayer graphene, suggesting a thicker graphene film. Most of the edges are tetralayer (Fig. 4.21). More interestingly, the diffraction patterns in Fig. 4.20 and 4.21, show only one set of patterns, suggesting the graphene films are Bernal stacked. These various thickness Bernal-stacked graphene films are expected to have the strongest electrical coupling between layers. Because of the coupling, their electronic band structures are different from each other, which is quite useful in optoelectronic applications.

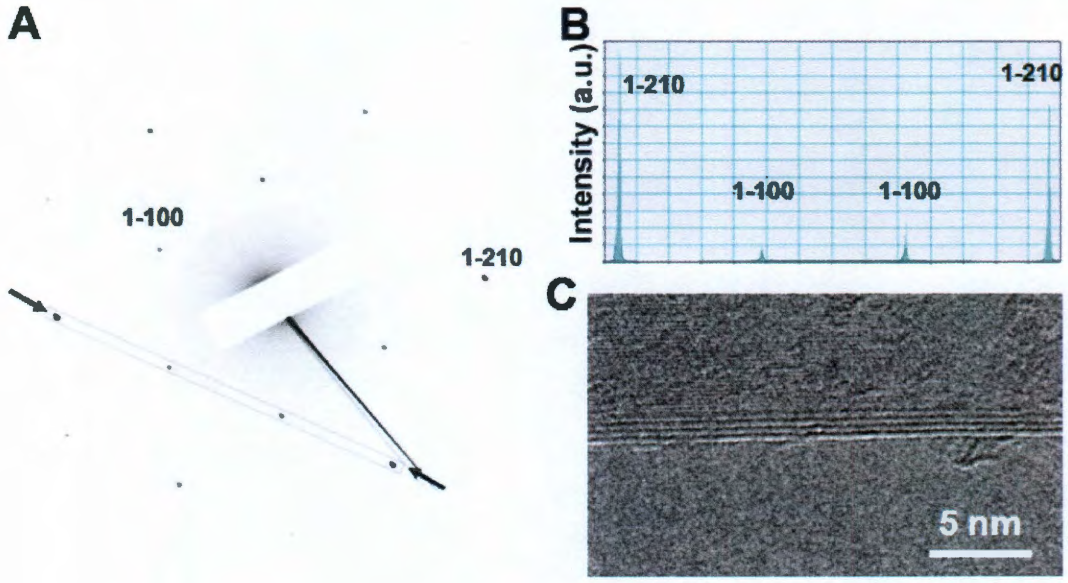

Fig. 4.21 SAED (A and B) and TEM (C) characterization of 4-layer graphene.

In the HRTEM image of sample 10 (Fig. 4.22), the thickness of graphene could be over 10 layers, which is the limit of the graphene definition.

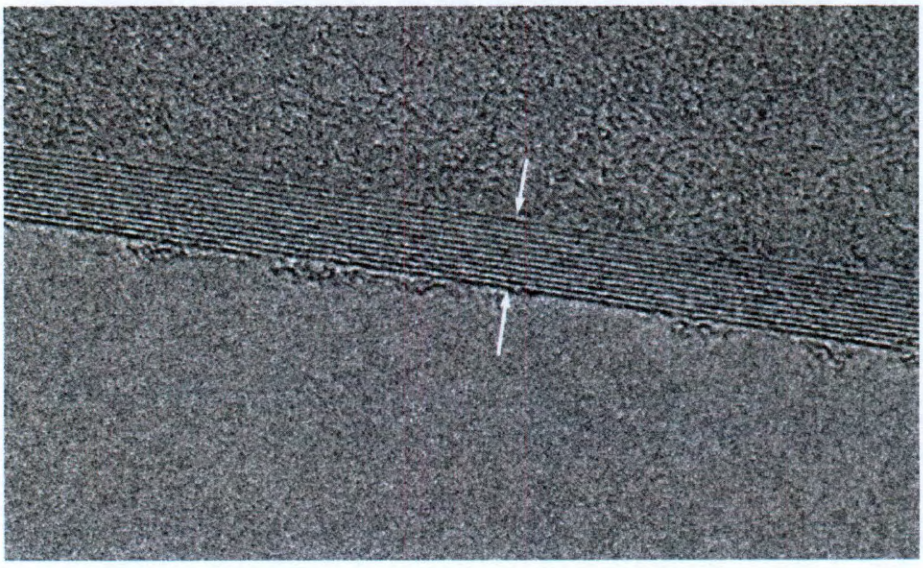

Fig. 4.22 Graphite films with graphene stacking over 10 layers (sample 10).

In conclusion, Bernal stacked graphene films with a thickness from 2 to 10 layers could be precisely synthesized through tuning the partial pressure of the growth gases, especially the pressure of CH_4 within traditional CVD systems. This is fundamentally different from non-Bernal stacked graphene, which behaves like individual monolayer.[41]

Author Contributions:

Z. S. did all the graphene growth and performed the characterizations. Abdul-Rahman Raji helped with the growth and characterizations of Part 4.3 Bernal stacked graphene synthesis with precise thickness control.

References

1. Reina, A. *et al.* Large area, few-layer graphene films on arbitrary substrates by chemical vapor deposition. *Nano Lett.* **2009**, *9*, 30-35.
2. Kim, K. S. *et al.* Large-scale pattern growth of graphene film for stretchable transparent electrodes. *Nature* **2009**, *457*, 706-710.
3. Li, X. *et al.* Large-area synthesis of high-quality and uniform graphene films on copper foils. *Science* **2009**, *324*, 1312-1312.
4. Gomez-Navarro, C., Weitz, R. T., Bittner, A. M., Scolari, M., Mews, A., Burghard, M. and Kern, K. Electronic transport properties of individual chemically reduced graphene oxide sheets. *Nano Lett.* **2007**, *7*, 3499-3503
5. Bae, S. et al. Roll-to-roll production of 30-inch graphene films for transparent electrodes, *Nat. Nanotechnol.* **2010**, *5*, 574-578.
6. Cancado, L. G. et al. Quantifying defects in graphene via raman spectroscopy at different excitation energies, *Nano Lett.* **2011**, *11*, 3190-3196.
7. Huang, P. Y. *et al.* Grains and grain boundaries in single-layer graphene atomic patchwork quilts, Nature **2011**, *469*, 389-392.
8. Zhang, Y. *et al.* Direct observation of a widely tunable bandgap in bilayer graphene, *Nature* **2009**, *459*, 820-823.
9. Taisuke Ohta, *et al.* Controlling the electronic structure of bilayer graphene. *Science* **2006**, *313*, 951-954.
10. Geim, A. K. Graphene: status and prospects. *Science* **2009**, *324*, 1530-1534.
11. Novoselov, K. S. *et al.* Two-dimensional atomic crystals. *Proc. Natl. Acad. Sci. U.S.A.* **2005**, *102*, 10451-10453.

12. Novoselov, K. S. *et al.* Electric field effect in atomically thin carbon films. *Science* **2004**, *306*, 666-669.

13. Liu, Y. & Yakobson, B. I., Cones, pringles, and grain boundary landscapes in graphene topology. *Nano Lett.* **2010**, *10*, 2178-2183.

14. Oleg, O. V. & Louie, S. G. Topological defects in graphene: dislocations and grain boundaries. *Phys. Rev. B* **2010**, *81*, 195420.

15. Schwierz, F. Graphene transistors. *Nature. Nanotech.* **2010**, *5*, 487-496.

16. Araújo, J. S., Chacham, H. & Nunes, R. W. Gap opening in topological-defect lattices in graphene. *Phys. Rev. B* **2010**, *81*, 193405.

17. Malola, S., Häkkinen, H. & Koskinen, P. Structural, chemical, and dynamical trends in graphene grain boundaries. *Phys. Rev. B* **2010**, *81*, 165447.

18. Gamo Y., Nagashima, A., Wakabayashi, M., Terai, M. & Oshima, C. Atomic structure of monolayer graphite formed on Ni(111). *Surf. Sci.* **1997**, *374*, 61-64.

19. Pan, Y. *et al.* Highly ordered, millimeter-scale, continuous, single-crystralline graphene monolayer formed on Ru(0001). *Adv. Mater.* **2009**, *21*, 2777-2780.

20. Li, X. *et al.* Transfer of large-area graphene films for high performance transparent conductive electrodes. *Nano Lett.* **2009**, *9*, 4359-4363.

21. Levendorf, M. P., Ruiz-Vargas, C. S., Garg, S. & Park, J. Tansfer-free batch fabrication of single layer graphene transistors. *Nano Lett.* **2009**, *9*, 4479-4483.

22. Reina, A. *et al.* Growth of large-area single- and bi-layer graphene by controlled carbon precipitation on polycrystalline Ni surfaces. *Nano Res* **2009**, *2*, 509-516.

23. Ferrari, A. C. *et al.* Raman spectrum of graphene and graphene layers. *Phys. Rev. Lett.* **2006**, *97*, 187401.

24. Lui, C. H., Liu, L., Mak, K. F., Flynn, G. W. & Heinz, T. F. Ultraflat graphene. *Nature* **2009**, *462*, 339-341.

25. Girit, C. Ö. *et al.* Graphene at the edge: stabiltiy and dynamics. *Science* **2009**, *323*, 1705-1708.

26. Lahiri, J., Lin, Y., Bozkurt, P., Oleynik, I. I. & Batzill, M. An extended defect in graphene as a metallic wire. *Nature. Nanotech.* **2010**, *5*, 326-329.

27. Tian, B., Xie, P., Kempa, T. J., Bell, D. C. & Lieber, C. M. Single-crystalline kinked semiconductor nanowire superstructures. *Nature Nanotech.* **2009**, *4*, 824-829.

28. Goldberger, J. *et al.* Single-crystal gallium nitride nanotubes. *Nature* **2003**, *422*, 599-602.

29. Hu, J., Bando, Y., Liu, Q. & Golberg, D. Laser-ablation growth and optical properties of wide and long single-crystal SnO_2 ribbons. *Adv. Funct. Mater.* **2003**, *13*, 493-496.

30. Presland, A. E. B. & Walker. Jr., P. L. Growth of single-crystal graphite by pyrolysis of acetylene over metals. *Carbon* **1969**, *7*, 1-4.

31. Li, X., Cai, W., Colombo, L. & Ruoff, R. S. Evolution of graphene growth on Ni and Cu by carbon isotope labeling. *Nano Lett.* **2009**, *9*, 4268-4272.

32. Sun, Z.; Yan, Z.; Yao, J.; Beitler, E.; Zhu, Y.; Tour, J. M. Growth of Graphene from Solid Carbon Sources. *Nature* **2010**, *468,* 549-552.

33. Brune, H. Thermal dynamics at surfaces. *Ann. Phy. (Berlin)* **2009**, *18*, 675-698.

34. Wagner, R. S. & Ellis, W. C. Vapor-liquid-solid mechanism of single crystal growth. *Appl. Phys. Lett.* **1964**, *4*, 89-90.

35. Chen, J. H., Jang, C., Xiao, S., Ishigami, M. & Furher, M. S. Intrinsic and extrinsic

performance of graphene devices on SiO_2. *Nature. Nanotech.* **2008**, *3*, 206-209.

36. Schedin, F. *et al.* Detection of individual gas molecules absorbed on graphene. *Nature. Mater.* **2007**, *6*, 652-655.
37. Yu, Q. K. *et al.* Control and characterization of individual grains and grain boundaries in graphene grown by chemical vapour deposition, *Nat. Mater.* **2011**, *10*, 443-449.
38. Bhaviripudi, S.; Jia, X.; Dresselhaus, M. S.; Kong, J. Role of kinetic factors in chemical vapor deposition synthesis of uniform large area graphene using copper catalyst. *Nano Lett.* **2010**, *10*, 4128-4133.
39. Li, X. *et al.* Graphene films with large domain size by a two-step chemical vapor deposition process. *Nano Lett.* **2010**, *10*, 4328-4334.
40. Lee, S.; Lee, K.; Zhong, Z. Wafer scale homogeneous bilayer graphene films by chemical vapor deposition. *Nano Lett.* **2010**, *10*, 4702-4707.
41. Hass, J.; Varchon, F.; Millan-Otoya, J. E.; Sprinkle, M.; Sharma, N.; de Heer, W. A.; Berger, C.; First, P. N.; Magaud, L.; Conrad, E.H. Why Multilayer graphene on 4h-sic behaves like a single sheet of graphene. *Phys. Rev. Lett.* **2008**, *100*, 125504.

Chapter 5

GRAPHENE FROM SOLID CARBON SOURCES

5.1. Introduction

After being first obtained as a transferable one-atomic-thick material in 2004, graphene and its growth quickly caught the attention of physicists, chemists and material scientists[1-4]. Much of the research has focused on obtaining large sheets of monolayered or bilayered graphene. This has been recently achieved by chemical vapor deposition (CVD) of CH_4 or C_2H_2 gases on Cu or Ni substrates[5-7]. However, CVD is limited to the use of gaseous raw materials, making it difficult to apply the technology to a wider variety of feedstock. In this chapter, we demonstrate that large area, high-quality graphene with controllable thickness can be grown from different solid carbon sources such as polymer films or small molecules, at temperatures as low as 800 °C. Both pristine graphene and doped graphene were

grown with this one-step process using the same experimental set-up. Furthermore, graphene was grown from impure sources such as food, wastes and insects. This self-purifying process turns the carbon elements in negative or low value feedstock into high quality graphene. Finally, a transfer-free technique is also explored with this solid carbon source growth.

With its extraordinary electronic and mechanical properties, graphene is showing promise in a plethora of applications[7-13]. In Chapter 1-4, different approaches to obtain graphene have been discussed. From the original mechanical peeling method of highly oriented pyrolytic graphite (HOPG) [1], the liquid exfoliation and reduction of graphene oxide methods[14, 15], to Si sublimation from SiC, growth from amorphous carbon and CVD methods, the size, thickness and quality of the produced graphene is approaching industrially useful specifications[5-7, 16, 17]. However, intrinsic graphene is a zero band gap material which shows a weak ambipolar behavior. These graphene based transistors show small ON/OFF ratios, therefore they are too metallic for many designed electronics applications[18]. In order to modify the Fermi level of graphene and manipulate its electronic and optical properties, doping the graphene matrix with heteroatoms is a straightforward way to make an n-type, p-type or hybrid doped graphene[19-22].

5.2. PMMA Derived Graphene and Graphene from Other Solid Carbon Sources

In the section, the growth of monolayered pristine graphene from solid carbon sources atop metal catalysts is demonstrated as shown in Fig. 5.1a. The first solid carbon source used was a spin-coated poly(methyl methacrylate) (PMMA) thin film (~100 nm) and the metal catalyst substrate was a Cu film. At a range as low as 800 °C or as high as 1000 °C (tested limit) for 10 min, with a reductive gas flow (H_2/Ar) and under low pressure conditions, a single uniform layer of graphene was formed on the substrate. The graphene material thus produced was successfully transferred to different substrates for further characterization.

The Raman spectrum of this monolayered PMMA-derived graphene (PG) is shown in Fig. 5.1b and the spectrum is characteristic of >10 locations recorded over 1 cm^2 of the sample. The two most pronounced peaks in this spectrum are the G peak at 1580 cm^{-1} and the 2D peak at 2690 cm^{-1}. The I_{2D}/ I_G intensity ratio is about 4 and the full width at half maximum (FWHM) of the 2D peak is about 30 cm^{-1}, indicating that the graphene is monolayered. The D peak (~ 1350 cm^{-1}) is in the noise level for PG, indicating the presence of few sp^3 carbon atoms or defects[23].

The electrical properties of the PG were evaluated with back-gated graphene-based field-effect transistor (FET) devices atop a 200 nm thick SiO_2 dielectric. Typical data for the FET devices is shown in Fig. 1c. For this particular device, the estimated carrier (hole) mobility is ~410 $cm^2V^{-1}s^{-1}$ at room temperature and the ON/OFF ratio is ~2, which is expected in graphene-based FET devices of this size[20].

Although the graphene was pristine without any doping atoms, it still shows a weak p-type behavior with the Dirac point (DP) moved to positive gate voltage, probably arising from the physisorption of small molecules such as H_2O[8]. Placing these graphene FETs under high vacuum (10^{-5} Torr) for several days moves the DP to zero (Fig. 5.2), confirming that the weak p-type behavior was due to physisorption of volatile molecules[8].

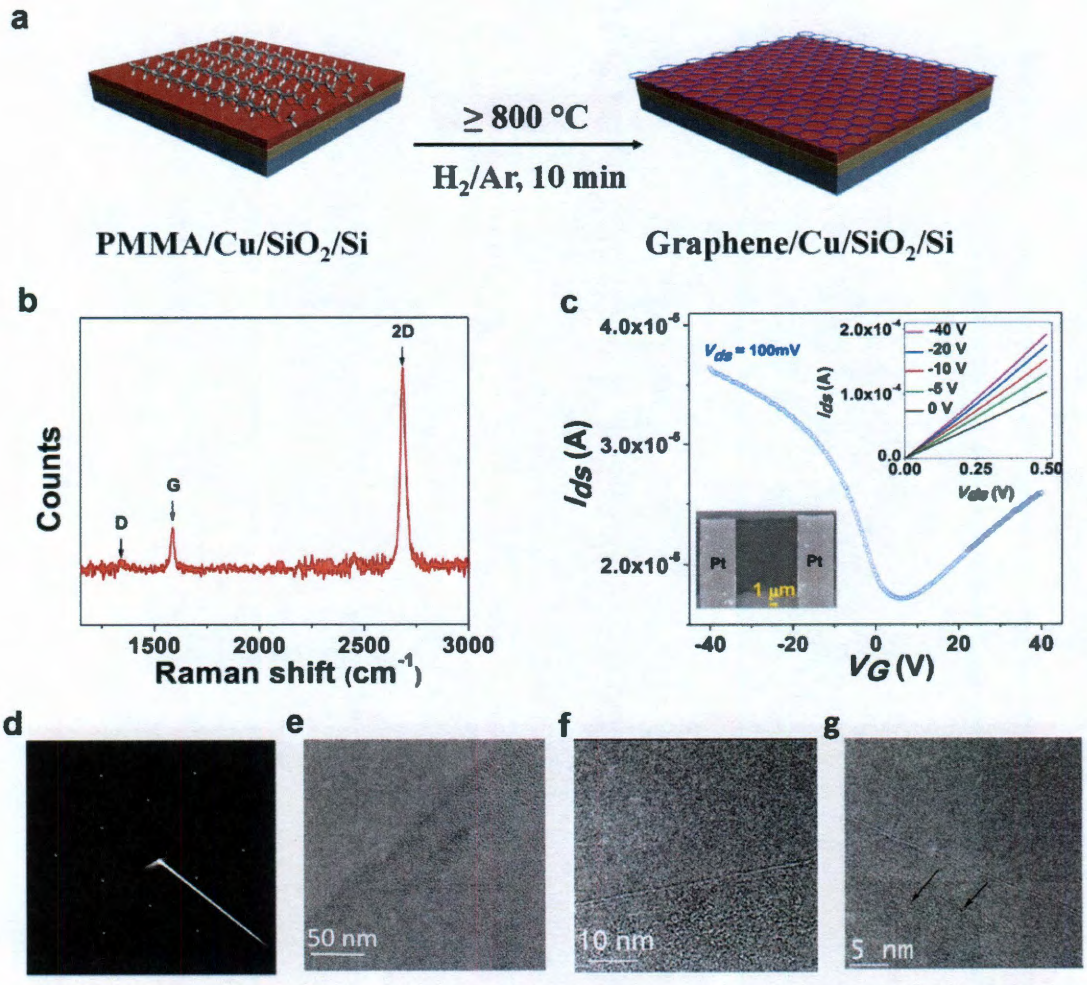

Fig. 5.1 Synthetic protocol, spectroscopic analysis and electrical properties of PG. (a) Monolayered PG is derived from the solid PMMA films on Cu

substrates at 800 °C or higher, up to 1000 °C. (b) Raman spectrum (514 nm excitation) of a monolayered PG obtained at 1000 °C. (c) Room temperature I_{ds}-V_G curve on a PG-based back-gate FET device. The upper inset shows the I_{ds}-V_{ds} characteristics as a function of V_G. V_G changes from 0 V (bottom) to -40 V (top). The lower inset in (c) is the SEM (JEOL-6500 microscope) image of this device where the PG is perpendicular to the Pt leads. (d) SAED pattern of PG. (e, f and g) HRTEM images of PG films. Black arrows in (g) indicate the Cu atoms.

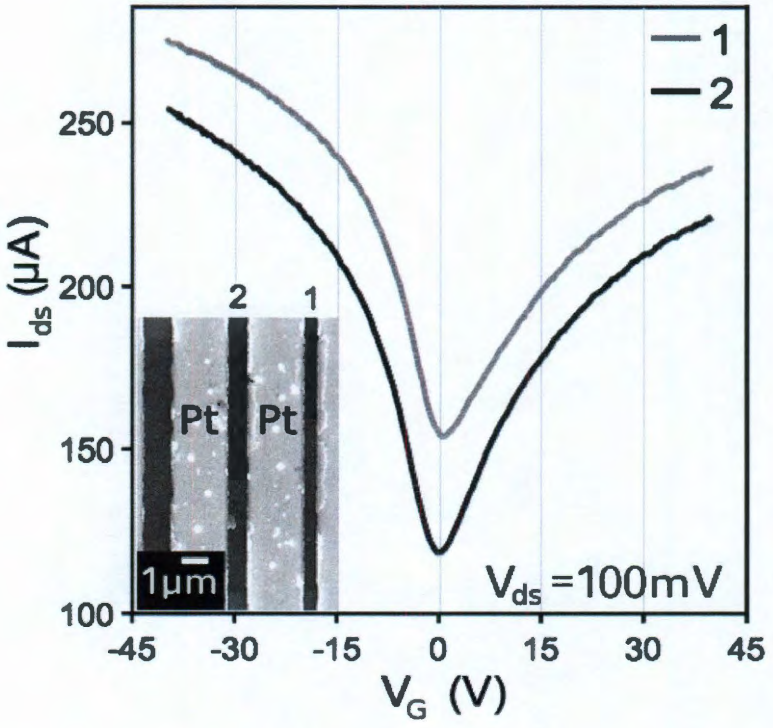

Fig. 5.2 Additional FETs after prolonged evacuation. Two representative pristine graphene FETs atop 200 nm SiO_2 with highly doped p^{++} Si back gate measured after storage at 10^{-6} Torr for 7 days. Under vacuum, the Dirac point recovers from positive gate voltages and stabilizes at zero as surface adsorbents are removed. Mobilities of ~400 $cm^2 V^{-1}s^{-1}$ at room temperature were achieved.

Transmission electron microscopy (TEM) images of the pristine PG and its diffraction pattern are shown in Fig. 5.1d-g. The selected area electron diffraction (SAED) pattern in Fig. 5.1d displays the typical hexagonal crystalline structure of graphene. The layer count on the edges of the images indicates the thickness of the PG. The PG edges in Fig. 5.1e-g were randomly imaged under TEM and most were monolayered or bilayered PG, which corroborates with the Raman data. Although most of the PG surface was continuous and crystalline according to its diffraction pattern, there there is adsorbed PMMA resulting from the transfer step. Metal atoms or ions were also found to be trapped on the PG surface (see black arrows in Fig. 5.1g) and became charge impurities, which should increase the charge density but decrease the mobility of the PG[24]. Similar phenomena have been observed with CVD-generated graphene[5-7]. AFM was used to characterize the surface profile of PG on a SiO_2/Si substrate. In Fig. 5.3, the thickness of the PG is about 0.7 nm, which confirms the monolayer nature of this material. However, limited by the wet-transfer technique, graphene's intrinsic corrugation is still obvious in the AFM image.

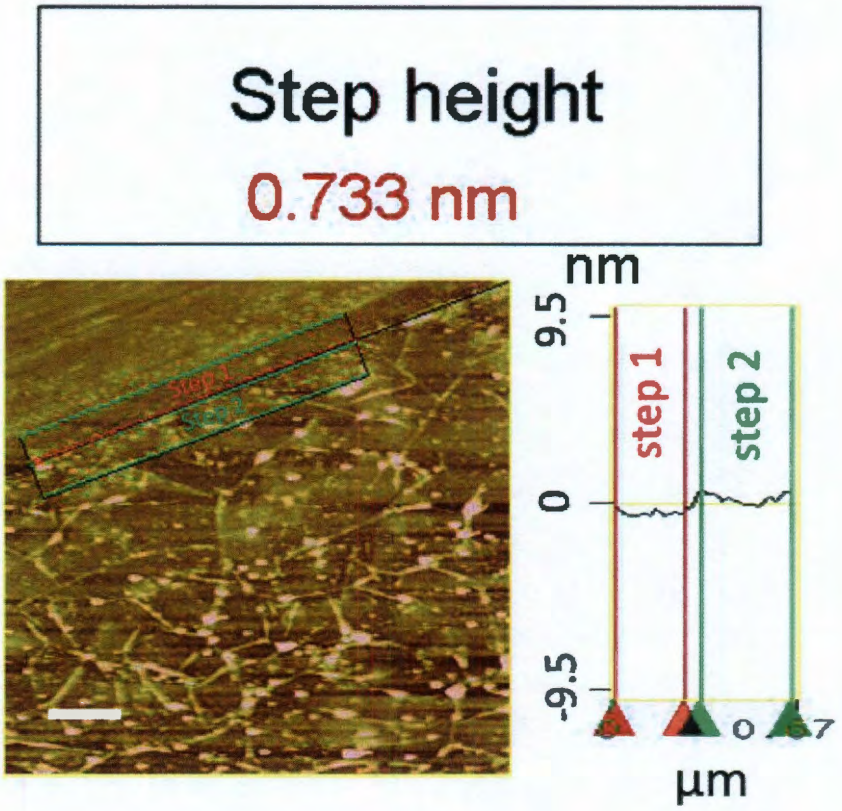

Fig. 5.3 | AFM Characterization of PG. AFM image (left) and the height profile (right) of a monolayer PG on a SiO_2/Si substrate. Step 1 (red) is the SiO_2/Si substrate; step 2 (green) is the graphene edge. Step height is ~ 0.7 nm, suggesting the thickness of PG. Scale bar in AFM is 1 μm.

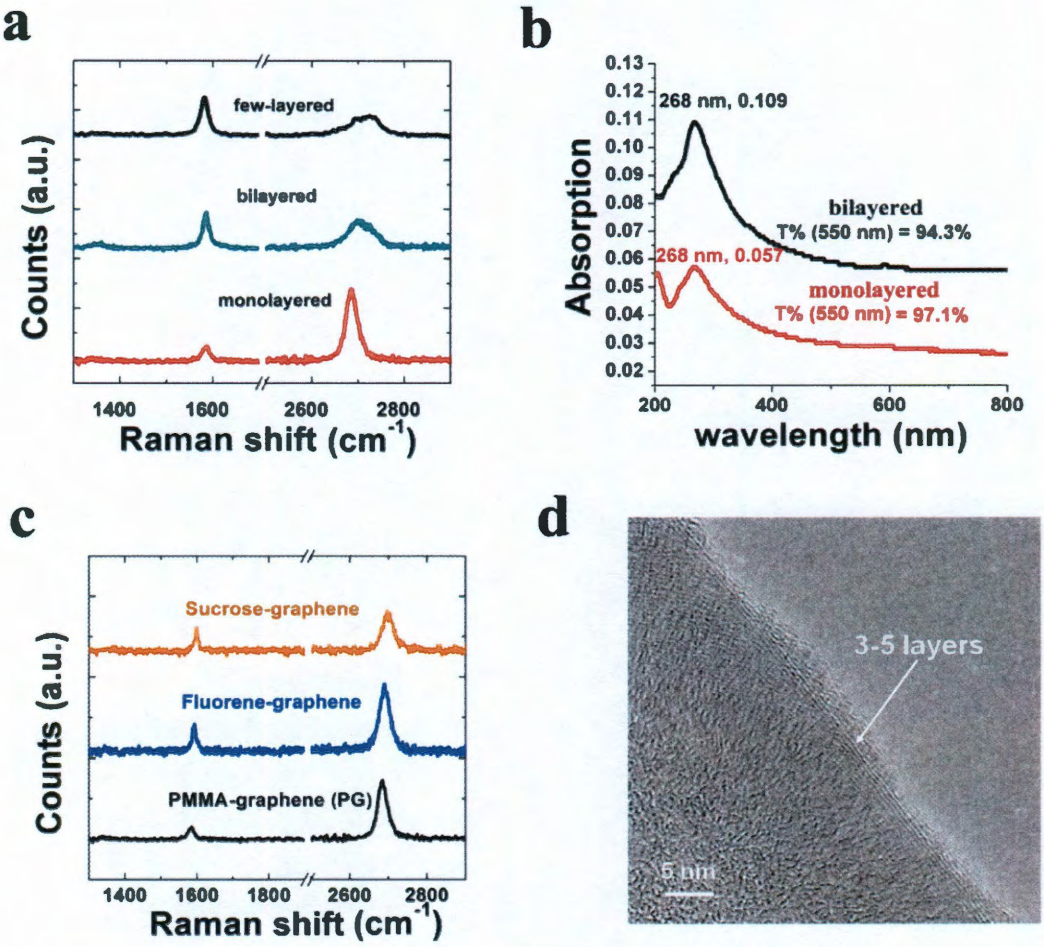

Fig. 5.4 Controllable growth for pristine graphene films. (a) Difference in Raman spectra from PG samples with controllable thicknesses derived from different flow rates of H_2. (b) The ultraviolet-visible (UV) absorption spectra of monolayered graphene and bilayered graphene. The UV transmittance (T%) of the corresponding PG is measured at 550 nm. (c) Raman spectra of graphene derived from sucrose, fluorene and PMMA. (d) HRTEM picture of PG grown on a Ni film. The PG was 3—5 layers at the edges.

Graphene's electronic properties are strongly associated with its thickness[25]. Therefore, it would be useful to be able to control the thickness when producing the graphene by tuning the growth parameters. We have found that PG's thickness can be controlled from monolayer, to bilayer to a few layers by changing the Ar and H_2 gas flow rate. Typical thicknesses were evaluated by Raman spectroscopy (Fig. 5.4a) and UV transmittance (Fig. 5.4b) of the graphene. At 1000 °C, a bilayered PG was obtained when the Ar flow rate was 500 sccm and the H_2 flow rate was 10 sccm. When the Ar flow rate was 500 sccm and the H_2 flow rate was 3-5 sccm, few-layered PG formed. When the H_2 flow rate increased to 50 sccm or higher, only monolayered graphene was formed on the Cu substrate. Monolayered graphene showed a transmittance of 97.1% (Fig. 5.4b). It had a sheet resistance (R_s) of 1200 Ω/sq by the 4-probe method, which makes it a transparent electrode material of interest. The bilayered graphene's transmittance is 94.3%, which shows linear enhancement in the UV absorption. The few-layered PG sheet in Fig. 5.4a has a transmittance of 83% at 550 nm, which can be estimated as a 6-layered PG. Both the shape and the positions of the 2D peak are significantly different from monolayered graphene to bilayered graphene and few-layered graphene (Fig. 5.5). For monolayered graphene, the 2D peak can be fitted with single sharp Lorentz peak. The observed 2D splitting in bilayered and few-layered graphene can be assigned to the electronic band splitting caused by the interaction of the PG planes[23]. The Raman mapping of the G to 2D peak ratio illustrates the uniformity of the graphene films over 70-75 μm^2 areas investigated (Fig. 5.6). For monolayered graphene, more than 95% of the film has this signature with $I_G/I_{2D} < 0.4$. The bilayered graphene has more than 85%

coverage, with an $I_G/I_{2D} \sim 0.8$. H_2 acts as both the reducing reagent and the carrier gas to remove C atoms that are extruded from the decomposing PMMA during growth. A slower H_2 flow leaves more C sources for the growth of multilayered graphene. Due to the low concentration and solubility of the carbon source in Cu, traditional CVD-grown graphene on Cu usually terminates as a monolayer. In this experiment, highly concentrated and uniformly dispersed carbon sources favor multilayered graphene when the H_2 flow is low. The higher order layers might form through graphitization directly atop the first layer, which blocks the contact of the carbon sources with the metal catalyst. Some metal catalysts, such as Ni, are known to reverse graphene growth by converting graphene to hydrocarbon products, therefore cutting graphene along specific directions[26]. This reverse reaction does not appear to occur on the PG which is atop the Cu.

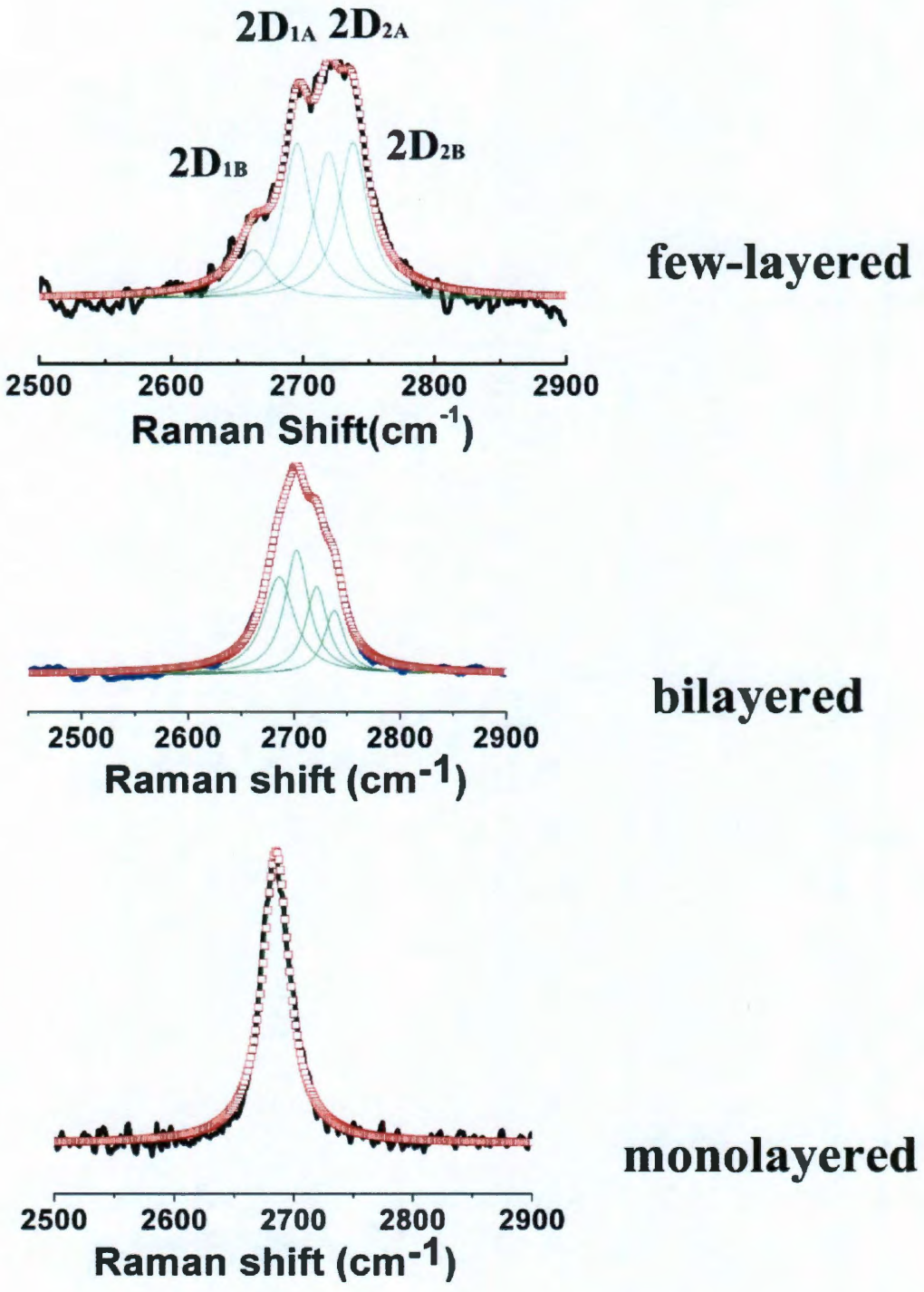

Fig. 5.5 Fitted Raman Spectra. Raman 2D peak fittings of different layered PGs; monolayered PG's 2D band was fitted with a single Lorentz peak. Bilayered and

few-layered graphene 2D bands were split into 4 components: $2D_{1B}$, $2D_{1A}$, $2D_{2A}$, $2D_{2B}$ (green peaks, from left to right) [2]. Solid lines are the original data. Square points are the fitting curves.

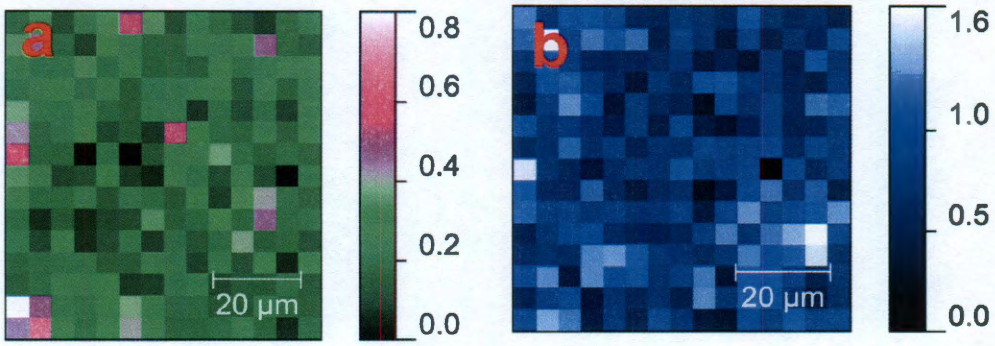

Fig. 5.6 Raman spectral mapping. Two-dimensional Raman (514 nm) mapping of (a) monolayered graphene film (70 × 75 μm^2) and (b) bilayered graphene film (75 × 75 μm^2). The color gradient bar to the right of each map represents the G/2D peak ratio. The green and black areas in (a) are monolayer graphene with an I_G/I_{2D} <0.4, suggesting at least 95% monolayer coverage[3]. The blue area in (b) represents bilayered graphene with an I_G/I_{2D} ~0.8. More than 85% in (b) is bilayered PG. The lateral scale bars are 20 μm.

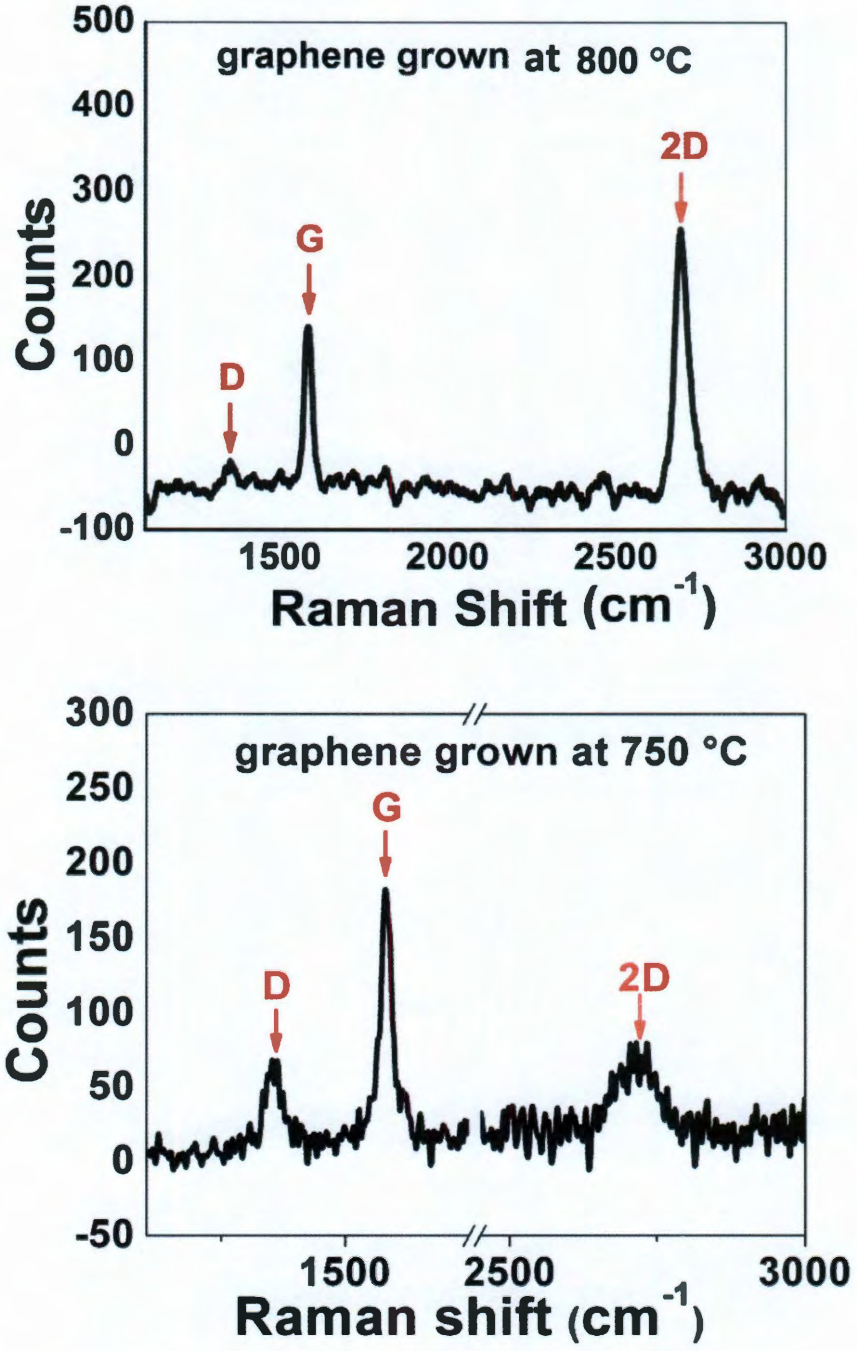

Fig. 5.7 Raman spectra of PG at lower growth temperatures. Raman spectra of PG grown at 800 °C (top) and 750 °C (bottom). PG (800 °C) has a D/G

ratio less than 0.1. For PG grown at 750 °C, the D/G ratio is greater than 0.35. Therefore, 800 °C is the low temperature limit for high quality PG growth.

High quality monolayered PG was obtained at 800 °C by this method, lower than the original report for CVD growth temperature on Cu[6] (Fig. 5.7). For the semiconductor industry, the lower processing temperature used is favorable because temperatures as high as 1000 °C would be problematic in the fabrication of the multi-layered stacks of heterogenous materials. Therefore, in addition to changing the Ar/H_2 flow rate, the graphene growth process was conducted using different temperatures. The quality of the graphene films was monitored by the D/G peak ratio from Raman spectroscopic analysis. The D/G ratio for graphene sheets obtained at 800 °C is less than 0.1. At 750 °C, the D/G peak ratio was ~0.35; hence 800 °C is the lower limit for high quality graphene from PMMA. We used other solid carbon sources including fluorene ($C_{13}H_{10}$) and sucrose ($C_{12}H_{22}O_{11}$) to grow monolayered graphene on Cu catalyst under the same growth conditions as was used for the PG. Because these precursors are powders not films, 10 mg of each as a finely grinded powder was placed directly on a 1 cm^2 Cu foil. After subjecting the powder-coated Cu films to the same reaction conditions as used for PG, Raman spectra indicated that all of the solid carbon sources have been transformed into monolayered graphene with no D peak observed (Fig. 5.4c). Although these solid carbon precursors contain potential topological defect generators (the five-member ring in fluorene) or high concentration of heteroatoms (oxygen), they produce high quality pristine graphene. It is possible that at elevated temperatures under vacuum, C has a higher affinity for the metal catalyst surface than the heteroatoms; atom

rearrangement occurs and most of the topological defects are self-healed as the graphene is formed.

Other substrates such as Ni, Si<100> with native oxide and 200-nm thick SiO_2 thermally grown were also tested to determine if they would grow graphene when coated with PMMA. Fig. 5.4d is the HRTEM image of PG grown on a Ni catalyst, which clearly illustrates the few-layered structure around the edges of PG. The Raman spectra in Fig. 5.8 confirm that Ni is an efficient catalytic substrate to convert PMMA into highly crystalline graphene materials with no D peak around 1350 cm^{-1}. Under the same growth conditions, neither graphene nor amorphous carbon were obtained on Si or SiO_2 substrates according to the Raman spectroscopic analysis of the surface after the reaction. This demonstrates the potential to grow patterned graphene from a thin film of shaped Ni or Cu deposited directly on SiO_2/Si wafers without post lithographic treatment since PG will not grow on the Si or SiO_2 surfaces.

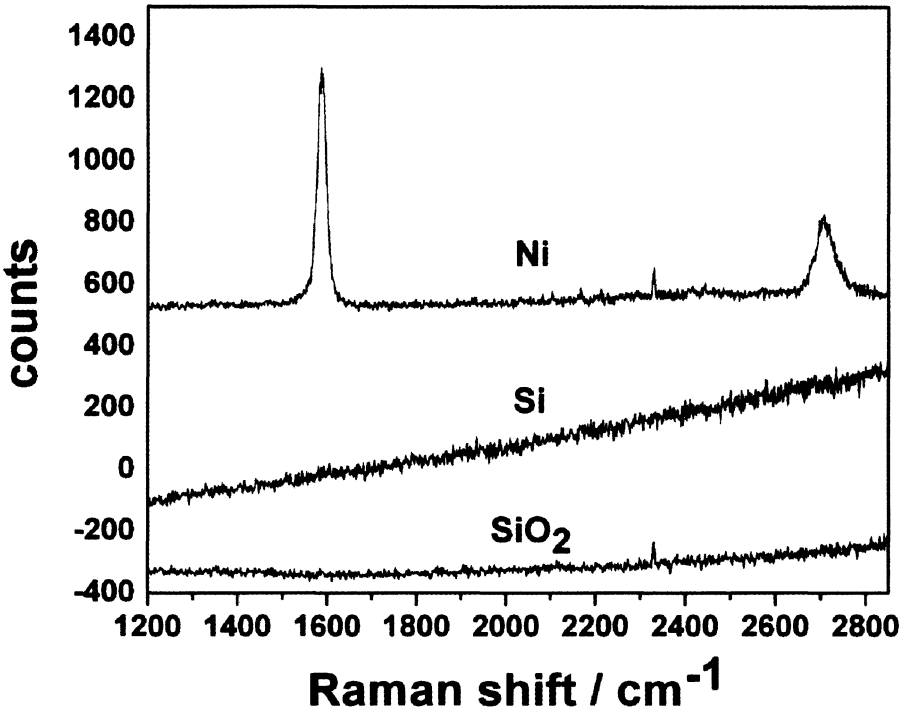

Fig. 5.8 PG growth or attempted growth on other surfaces. Raman spectra of PMMA films that were heated on Ni, Si with native oxide or thermally grown SiO_2.

5.3. Doped Graphene Growth from Solid Carbon Sources

Pristine graphene can show weak p-type or n-type behavior due to physisorption of small molecules such as H_2O or NH_3[8]. However, this chemical doping effect induced by physisorption is labile because it can be easily desorbed under heat or vacuum. Therefore, intrinsically nitrogen-doped (N-doped) graphene is more challenging to make compared to pristine graphene. Intrinsically N-doped graphene has been obtained by two methods: introducing a doping gas (NH_3) into

the CVD systems during the graphene growth[20] or treatment of synthesized graphene or graphene oxide with NH_3 by annealing or plasma[19, 27, 28]. Here, by using the solid carbon sources and solid doping reagents, doped graphene can be grown in one step without any changes to the CVD system.

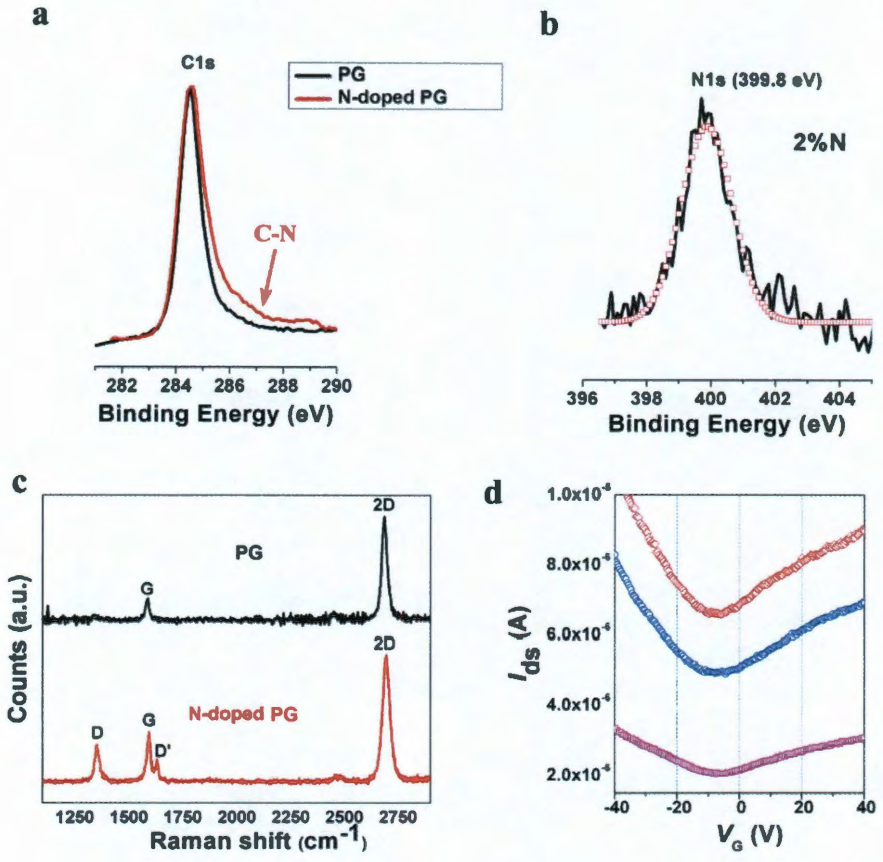

Fig. 5.9 Spectroscopic analysis and electrical properties of PG and N-doped PG. (a) XPS analysis from the C1s peak of PG (black) and N-doped PG (red); the shoulder can be assigned to the C-N bond. (b) XPS analysis of the N1s peak (black line) and its peak fitting (square points) of N-doped PG. The atomic

concentration of N for this sample is about 2% (C is 98%). No N1s peak was observed for PG. (c) Raman spectra for PG and N-doped PG. (d) Room temperature, I_{ds}-V_G curves with n-type behavior obtained from three different N-doped graphene-based back-gate FET devices.

A doping reagent melamine ($C_3N_6H_6$) was mixed with PMMA and spin-coated onto the Cu surface. In order to keep the nitrogen-atom concentration in the systems, we use conditions similar to the PG growth except that the growth was done under atmospheric pressure. The prepared polymer films were successfully converted into N-doped graphene, with an N content of 2—3.5%. The XPS data (Fig. 5.9a) shows the difference of the C1s peaks between PG and N-doped PG. The shoulder around 287 eV can be assigned to the C-N bonding. The N1s peak of N-doped PG indicates that only one type of N is present, at 399.8 eV, corresponding to graphitic N in graphene. Although high-temperature (1,000 °C) growth favors quaternary N in the N-doped graphene film[28], our assignment of 399.8 eV (N 1*s*) for monolayer N-doped graphene is different from the Li *et al.*[28] assignment, because their assignment of 401 eV (N 1*s*) is for thick N-doped graphene films. In our experiments, when we used poly(ethylene imine) as a growth source, multilayer N-doped graphene was attained and similarly gave 401.2 eV (N 1*s*) as the assignment. Therefore, either there is a difference between the thick film assignments of Li *et al.*[28] and our assignment of monolayer N-doped graphene on SiO_2 substrates, or the N signals in our material are more pyridinic and/or pyrrolic in content. This new N1s peak also has a 1~2 eV shift from that in melamine, which has N 1*s* in the ring at 397.8 eV and N 1*s* external to the ring at 398.7 eV. The new N1s peak suggests that

the N1s signal does not come from the melamine but that the N atoms are uniformly bound into the graphene structure. The D peak of this material is always present in the Raman spectra because the heteroatoms break the graphene symmetry and thereby introduce defects that are detected by Raman analysis (Fig. 5.9c). The D' peak is also found in doped graphene materials obtained by the other doping methods[21, 27]. The 2D peak position and I_{2D}/I_G intensity ratio reveals that this N-doped PG is monolayered graphene. Compared to PG, the I_{2D}/I_G decreased from 4 to 2, implying a successful doping according to the electrostatically gated Raman results[29].

Doping effects were also demonstrated by N-doped PG-based FETs. The n-type behavior shown in Fig. 5.9d, with the DP shifted to negative gate voltage, is consistently observed for devices on the same piece of N-doped PG. After keeping the N-doped PG-based FET devices under vacuum (10^{-6} Torr) for 24 h, their DP did not move to zero, indicative of the covalent bonding between carbon and nitrogen rather than just physisorption; the dopant N atoms donate free electrons to graphene. Meanwhile, the N-doped graphene's mobility calculated from the N-doped FETs was about 1 order of magnitude lower than in PG[20]. Due to the broken symmetry of the N-doped graphene's lattice structure, the N atoms act as scattering centers that suppress its mobility[25]. Patterned hydrogenation on graphene already shows its band gap opening[30]. Similarly, if the doping atoms are periodically dispersed in graphene's matrix, they can not only tune the Fermi level of graphene, but tailor its band gap. However, in the present N-doped graphene, the ON/OFF ratio does not increase, which suggests that the N atoms are randomly incorporated

into the graphene matrix. In order to manipulate both the Fermi level and the band gap of graphene, patterned doping has to be achieved[30].

In the first part of this chapter, we have demonstrated a one-step method for the controllable growth of both pristine graphene and doped graphene using solid carbon sources. This stands as a complementary method to CVD growth while permitting growth at lower temperature.

5.4. Graphene Growth from Food, Insects and Waste

The carbon source for graphene growth can be a gas, such as methane or acetylene, or solid carbon sources, such as poly(methyl methacrylate) (PMMA) or sucrose[31]. All of these carbon sources are purified chemicals.

In this section, we will demonstrate that much less expensive carbon sources, such as food, insects and waste, can also be used without purification to grow high-quality monolayer graphene directly on the backside of Cu foils under the H_2/Ar flow. For food, a Girl Scout cookie and chocolate were investigated. For waste with low or negative monetary value, we used bulk polystyrene plastic, a common solid waste, blades of grass and dog feces. For insects, another often negative value carbon source, a cockroach leg was used. Growing high-quality graphene from these carbon sources opens a new way to convert the waste carbon into a high-value-added product, as graphene is one of the most expensive materials in the world[32]. We propose a possible purification and growth mechanism. The graphene forms as the solid carbon sources decompose and diffuse to the backside of the Cu foil,

leaving the other elemental residues on the original side. Using this procedure, only high quality pristine graphene with few defects and ~97% transparency was grown on the backside of the Cu foil, as confirmed by Raman and UV-Vis spectroscopy. No heteroatoms were detected in the monolayer graphene according by X-ray photoelectron spectroscopy (XPS), suggesting its pristine nature. Analysis by selected area diffraction pattern (SAED) in transmission electron microscopy (TEM) confirms the hexagonal lattice structure of the graphene.

In a typical growth experiment, as shown in Fig. 5.10A, 10 mg of the dry carbon source was placed atop a Cu foil, and the foil was introduced into a 1050 °C tube furnace. The sample was annealed for 15 min under low pressure with H_2 and Ar at a flow rate of 100 cm^3 STP min^{-1} and 500 cm^3 STP min^{-1}, respectively. For the grass and dog feces, the samples were heated in a 65 °C vacuum (102 Torr) oven for 10 h to remove excess moisture. The experimental setup and procedures are similar to the method used to grow PMMA-derived graphene[31]. The main difference in this work is that the high quality monolayer graphene only forms on the backside of Cu foil, while the PMMA-derived graphene grows on both sides of the Cu foil. In Fig. 5.10B, photographic images of different growth stages are shown and black residue is present after the growth in Fig. 5.10Bc. Based on the experimental evidence during the growth, most of the carbon segments from the decomposition of the solids are carried away as gases by the H_2 /Ar flow.

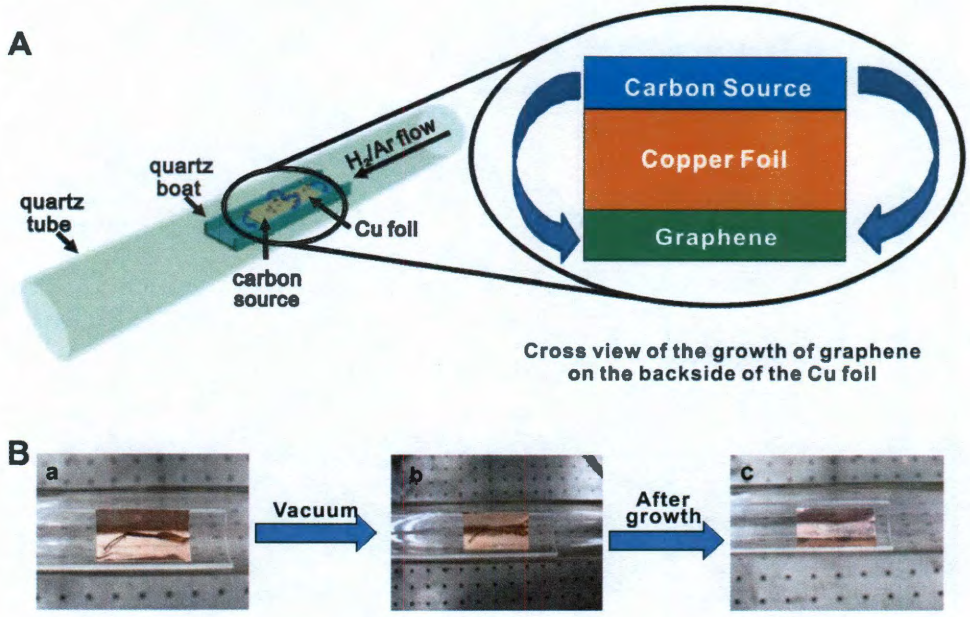

Fig. 5.10 (A) Diagram of the experimental apparatus for the growth of graphene from food, insects or waste in a tube furnace. On the left, the Cu foil with the carbon source contained in a quartz boat is placed at the hot zone of a tube furnace. The growth is performed at 1050 °C under low pressure with a H_2/Ar gas flow. On the right is a cross view that represents the formation of pristine graphene on the backside of the Cu substrate. (B) Growth of graphene from a cockroach leg. (a) One roach leg on top of the Cu foil. (b) The roach leg under vacuum. (c) The residue from the roach leg after annealing at 1050 °C for 15 min. The pristine graphene grew on the bottom side of the Cu film (not shown).

Since the carbon sources contain non-carbon elements, non-volatile residue may remain on the Cu foil after annealing. Fig. 5.11 shows SEM images of both sides of the Cu foil after a growth experiment. On the original frontside, many residual particles were found, as shown in Fig. 5.11A, while almost no particles were observed on the backside of the Cu foil where the graphene is formed (Fig. 5.11B).

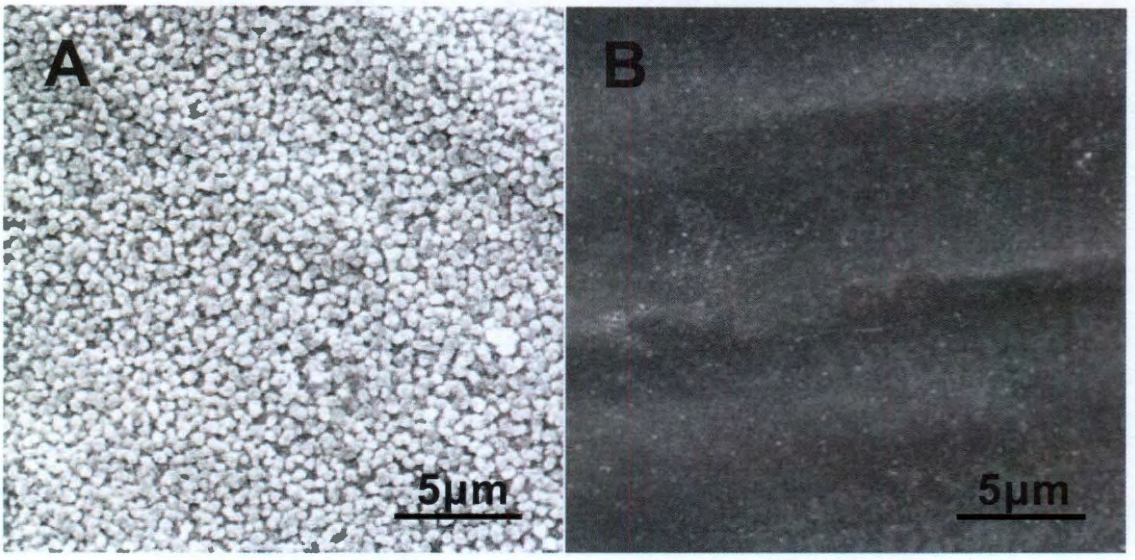

Fig. 5.11 SEM images of the Cu foil after growth of graphene from a Girl Scout cookie. (A) The original frontside of the Cu foil; there was a large quantity of particle residue after the pyrolysis of the cookie. (B) The backside of the Cu foil.

However, since the quartz boat has a semicircular shape, the slightly bent Cu foil is supported by the quartz boat and a portion of the carbon source diffused to the backside of the Cu foil, forming a monolayer graphene film. It is not known whether the diffusion is through the Cu foil or *via* the edges. As a comparison experiment, if the solid carbon sources were placed 5 cm ahead of the Cu substrate (but still in the quartz boat) and both were introduced into the hot furnace at the same time, only amorphous carbon formed on both sides of the Cu foil; the representive Raman spectrum of the film displays a large D peak as shown in Fig. 5.12.

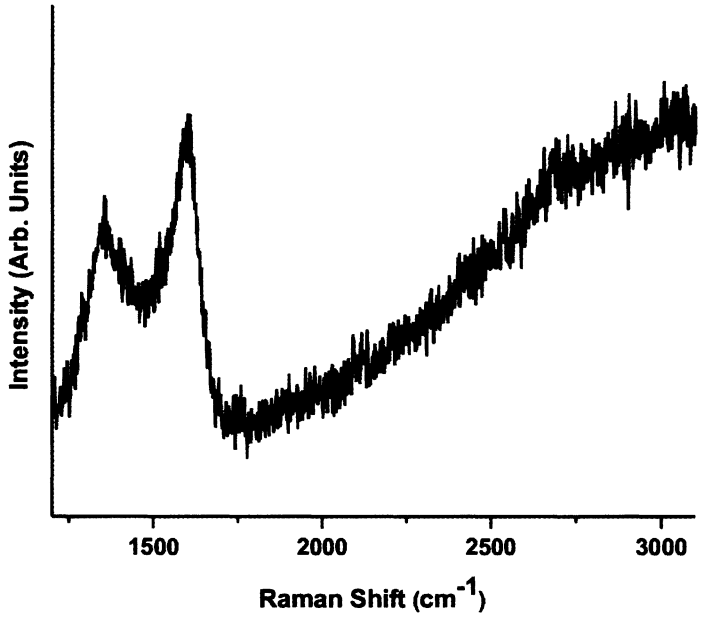

Fig. 5.12 Representative Raman spectrum of amorphous carbon grown on the backside of Cu foil when the Girl Scout cookie fragments were placed 5 cm ahead of the Cu foil in the tube furnace.

After the monolayer graphene samples on the backside of the Cu foil were transferred onto a 100 nm SiO_2/Si wafer using standard protocols[31], the product was analyzed using Raman spectroscopy at 514 nm laser excitation. As shown in Fig. 5.13, all of the graphene samples grown have small or no D peaks in their Raman spectra, an indication of few graphene defects[23]. The large 2D/G ratio suggests that it is high quality monolayer graphene. The exact G and 2D peak positions and their full-width at half-maximum (FWHM) for each spectrum were measured and are summarized in Table 5.1; the results are similar to the reported data[33]. The G and 2D peaks are located at 1585.5-1591.4 cm^{-1} and 2682.6-2693.9 cm^{-1}, respectively.

The FWHM of the G peak and 2D peak are 14.1-16.3 cm^{-1} and 32.0-35.1 cm^{-1}, respectively.

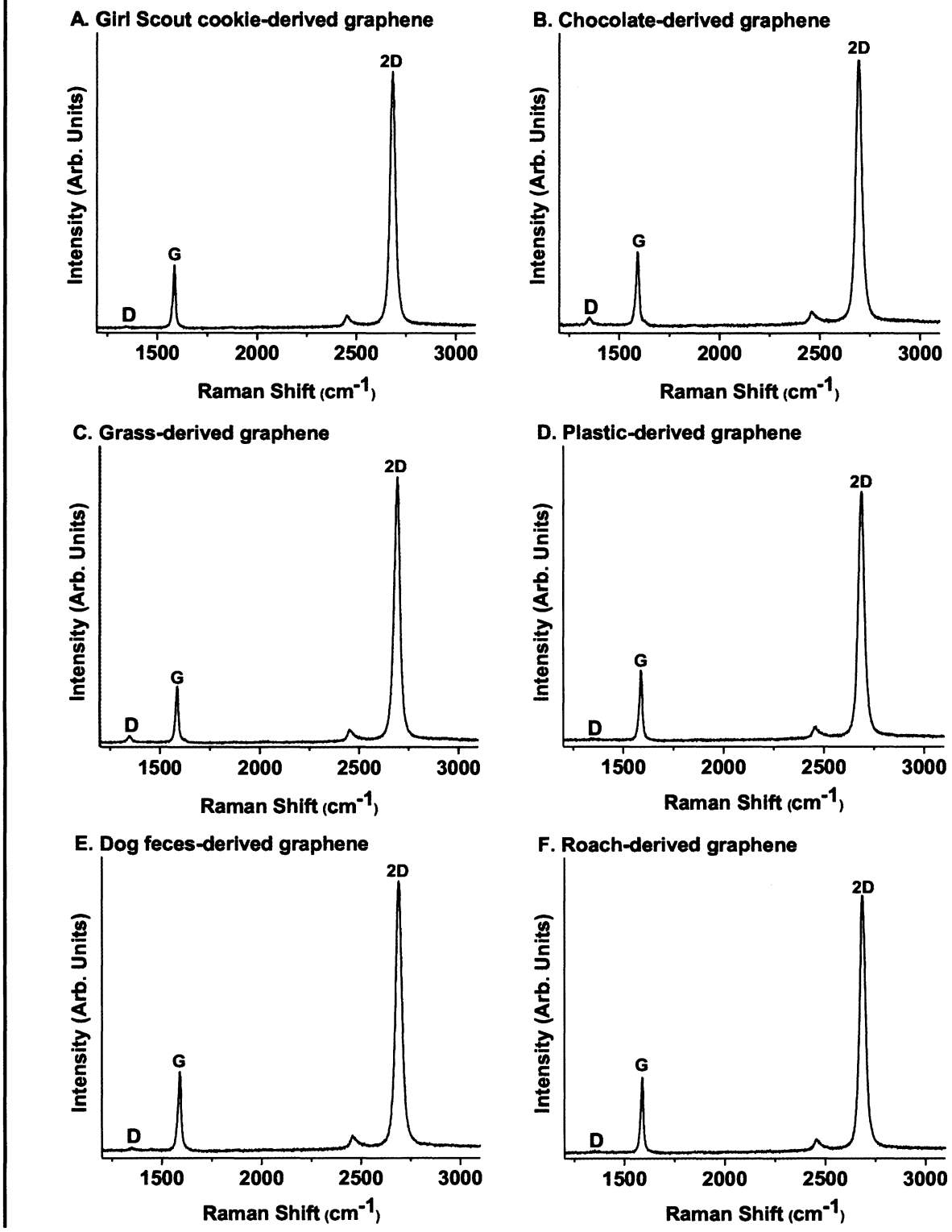

Fig. 5.13 Raman spectra of monolayer graphene from six different carbon sources. The Raman spectra graphene were derived from (A) Girl Scout cookie; (B) chocolate; (C) grass; (D) plastic (polystyrene Petri dish); (E) dog feces and (F) a cockroach leg. There was only a trace D peak in some of the spectra, and the 2D to G peak intensity ratios were ~ 4, indicating monolayer graphene.

Table 5.1 The wavelength number of the G and 2D peak, and their FWHM for graphene samples derived from six different carbon sources.

Carbon Source	G peak (cm^{-1})	G peak FWHM (cm^{-1})	2D peak (cm^{-1})	2D peak FWHM (cm^{-1})
Cookie	1585.5	14.1	2682.6	32.0
Chocolate	1591.4	15.9	2693.9	32.6
Grass	1585.7	16.0	2692.1	33.1
Plastic	1587.7	15.8	2685.7	34.8
Dog feces	1589.6	16.3	2689.7	35.1
Roach	1588.4	14.6	2687.4	33.5

In order to investigate the uniformity of the graphene film, a Raman mapping over a 100×100 μm^2 area (graphene derived from dog feces) was acquired. Over 95% of the scanned area had a signature of $I_{2D}/I_G > 1.8$ and $I_D/I_G < 0.1$, which further demonstrated the high quality of the monolayer graphene, as shown in Fig. 5.14.

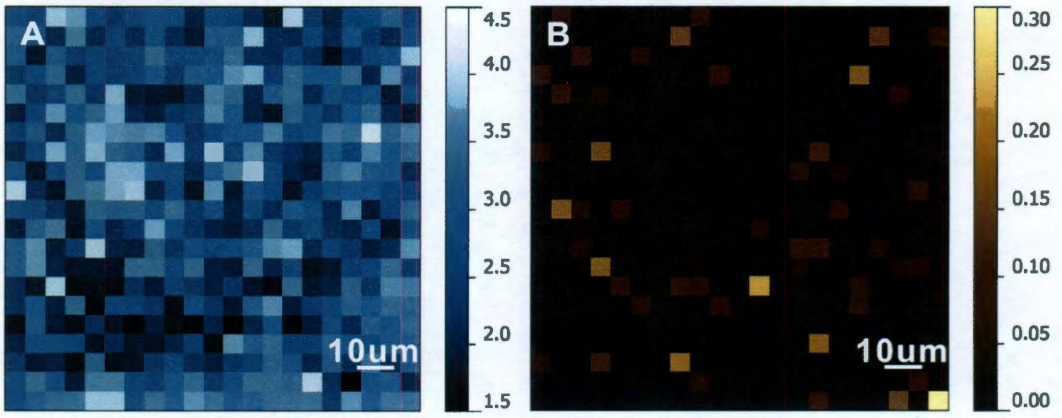

Fig. 5.14 Raman spectra mapping of graphene from dog feces. The scanning was performed at every 5 μm over an area of 100 μm × 100 μm. (A) Raman spectral mapping of 2D/G ratio, over 95% of the scanning area has the signature of I_{2D}/I_G > 1.8. (B) Raman spectral mapping of D/G ratio; note that over 95% of the scanning area has the signature of I_D/I_G < 0.1. This is confirmation of high-quality monolayer graphene.

XPS analysis of the graphene films was performed to confirm the elemental composition and the chemical environment of the C atoms. In Fig. 5.15, only a sharp peak at 284.5 eV with an asymmetric tailing towards high bonding energy is observed for C1s peak, suggesting a sp^2 graphitic peak[34-36]. The FWHM was ~ 1.1 eV for each C1s peak. Although the raw carbon sources contain other elements such as oxygen, nitrogen, iron, sulfur, or phosphorus, the obtained graphene consisted of carbon, with none of these other elements found in the XPS survey spectra,

confirming the graphene's pristine composition.

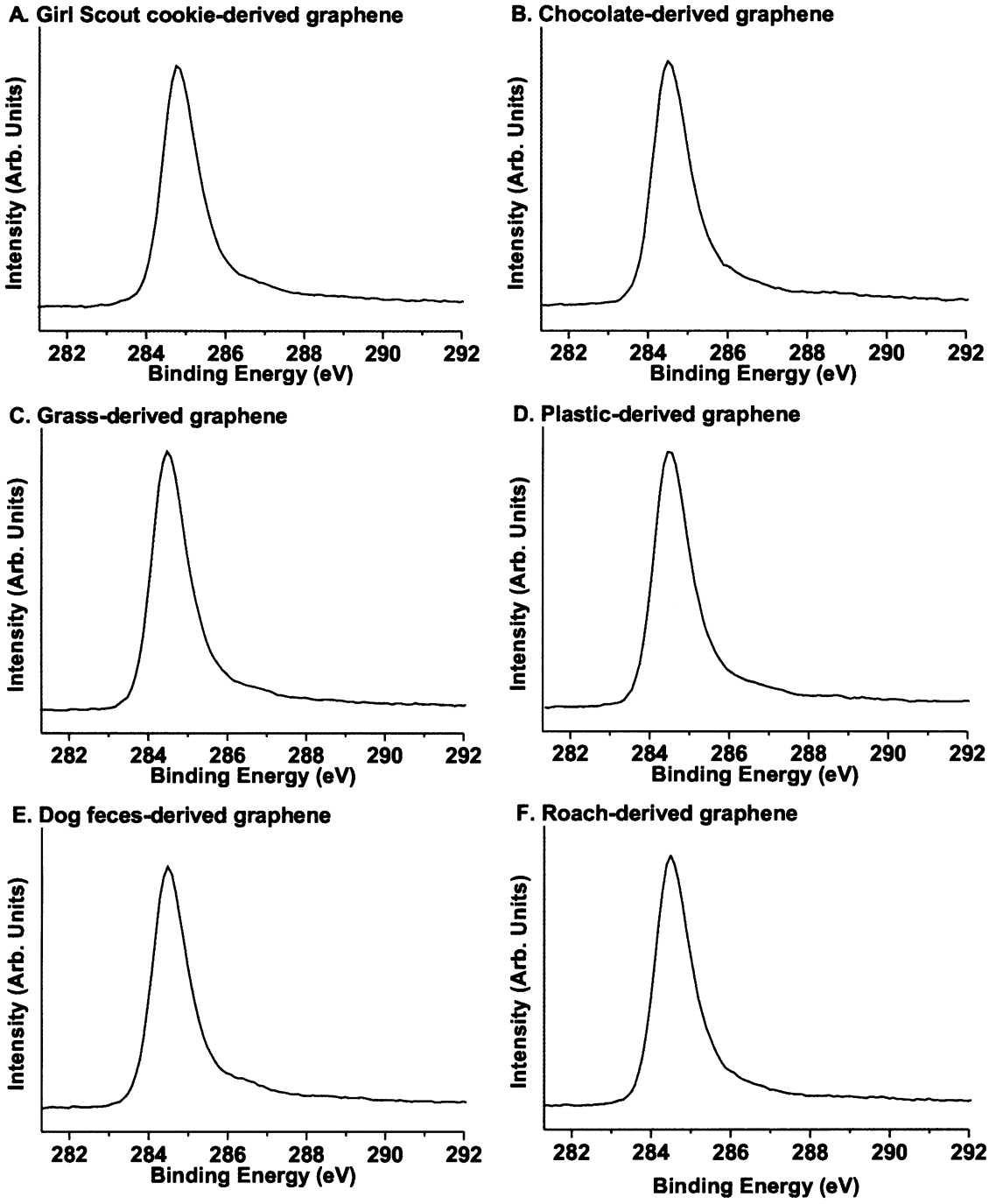

Fig.5.15 XPS spectra of graphene from six carbon sources. The C1s XPS spectra of the randomly selected detection spots on graphene derived from the various sources.

In the growth system, the H_2 gas might act as both a reducing reagent and a carrier gas. Since carbon is the most abundant element in these materials and graphene is the most thermodynamically stable form of carbon[37], only pristine graphene forms on the Cu. According to the C-C bond length (0.142 nm) in the hexagonal lattice of graphene[38], the surface area of one side of a monolayer of graphene is about 1315 m^2/g[39]. Theoretically, it only takes 228 ng of carbon to cover one side of a 2 cm × 3 cm Cu foil with monolayer graphene. In our growth system, the size of the graphene is ultimately limited by the size of the tube furnace, which limits the size of the Cu substrate that can be used. With a larger furnace, larger-sized graphene could be produced with 10 mg of the carbon source. Therefore, the limiting reagent in this work is the Cu foil, though scrolled Cu foil could provide enhanced surface areas.

All the graphene films were transferred to a quartz slides before UV-Vis analysis. In the spectra, each graphene film exhibits a peak at 268 nm, a typical $\pi \rightarrow \pi^*$ transition for the aromatic C-C bond in graphene[40,41], and the typical (2.4% ± 0.1%) absorption at 550 nm corresponding to the monolayer nature of graphene,[31,42] as shown in Fig. 5.16. In the photographic images, the graphene films on quartz slides are unifom and transparent. Also, the sheet resistance (R_s) of the graphene was in the range of 1.5 - 3.0 kΩ/square by the four-probe method.

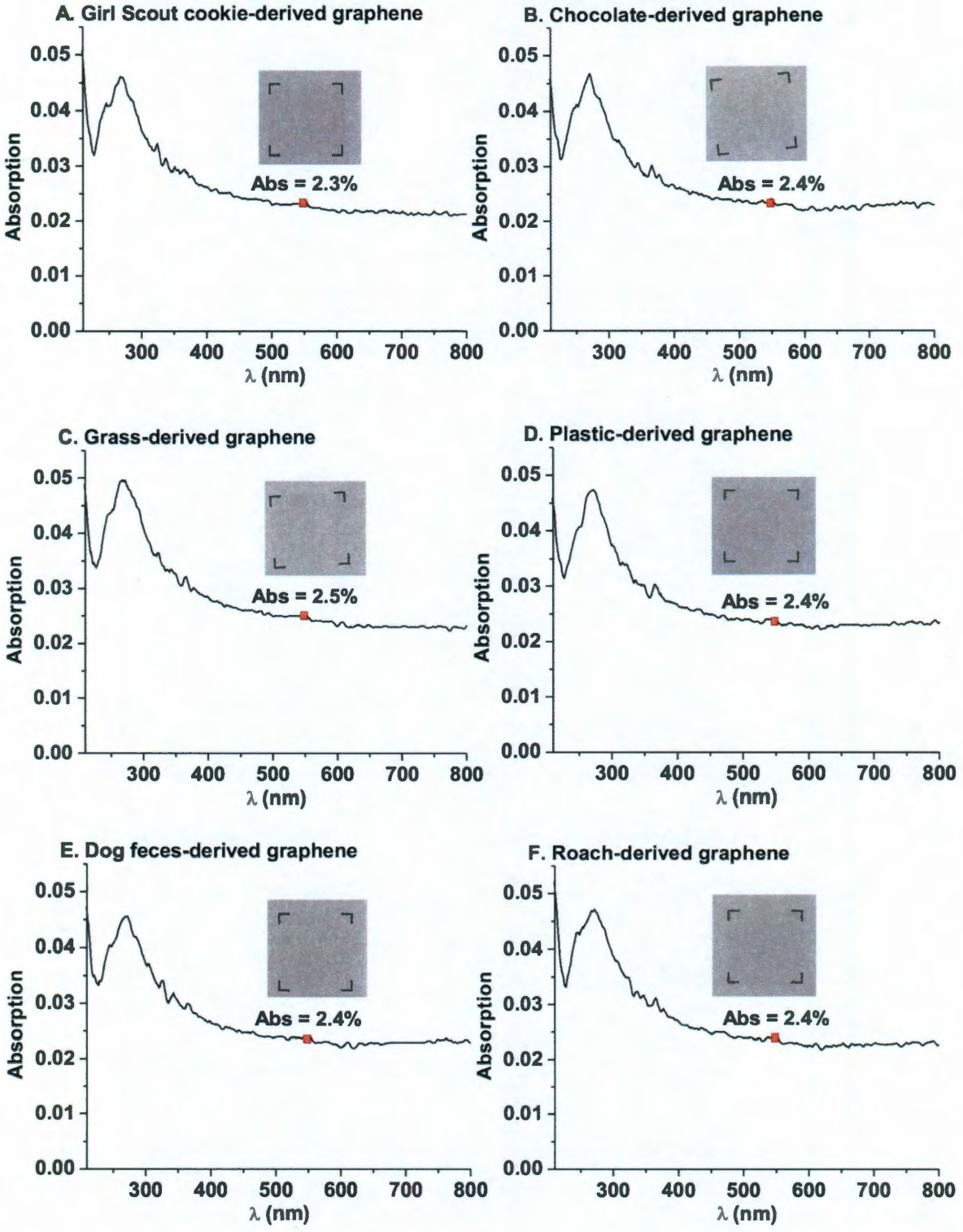
A. Girl Scout cookie-derived graphene
Abs = 2.3%
B. Chocolate-derived graphene
Abs = 2.4%
C. Grass-derived graphene
Abs = 2.5%
D. Plastic-derived graphene
Abs = 2.4%
E. Dog feces-derived graphene
Abs = 2.4%
F. Roach-derived graphene
Abs = 2.4%
Absorption
λ (nm)
0.00
0.01
0.02
0.03
0.04
0.05
300
400
500
600
700
800

0.1%). On the right top of each spectrum is the photographic image of the monolayer graphene film of ~1 cm × 1 cm in size on a 1-mm-thick quartz slide, labeled with a dashed square.

TEM images and the selected area electron diffraction (SAED) pattern were taken to determine the crystal structure of a representative graphene sample derived from the cookie. The graphene was transferred to a c-flat TEM grid (Protochips), where most of the area of the graphene was determined to be crystalline by its hexagonal diffraction pattern (Fig. 5.17A) and was continuous as shown in Fig. 5.17B. A randomly chosen monolayer edge of the graphene was imaged in Fig. 5C. The thickness of the graphene corresponds to monolayer graphene, corroborating the UV-Vis spectra and Raman data. The dark spots in the image in Fig. 5.17C might arise from the PMMA residues introduced during the etching and transferring step[31].

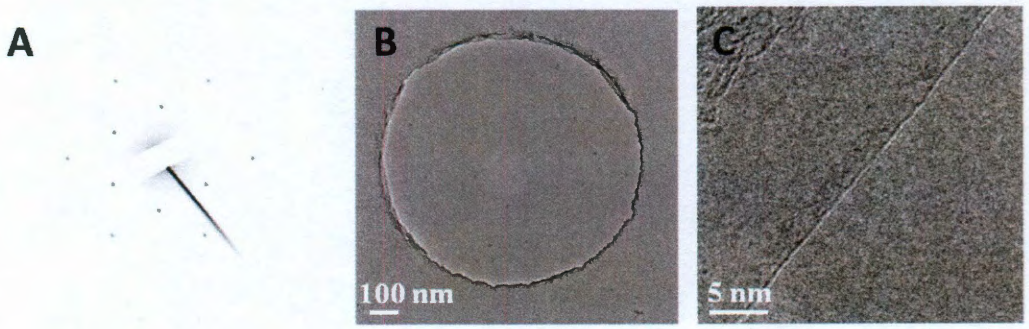

Fig. 5.17 Diffraction pattern and TEM images of the cookie-derived graphene. (A) SAED pattern, (B) suspended graphene film on a 1 μm diameter hole and (C) the edge of monolayer graphene.

In this part, We have demonstrated a general method to grow high-quality graphene from various raw carbon materials at 1050°C under vacuum and H_2/Ar

flow. The carbon sources were foods (cookie and chocolate), waste (grass, plastic, dog feces) and insect-derived. With this technique, many kinds of solid materials that contain carbon can potentially be used without purification as the feedstocks to produce high-quality graphene without pre-purification. Furthermore, through this method, low-valued foods and negative-valued solid wastes are successfully transformed into high-valued graphene which brings new solutions for recycling of carbon from impure sources.

5.5. Transfer-Free Method to Grow Graphene from Solid Carbon Sources

Another promising aspect using solid carbon sources to grow graphene is that the solid carbon feedstock can be embedded between metal catalysts and insulating substrates, therefore, a transfer-free method could be developed. In this section, we will discuss a general transfer-free method to directly grow large areas of uniform bilayer graphene on insulating substrates (SiO_2, h-BN, Si_3N_4 and Al_2O_3) from solid carbon sources such as films of poly(2-phenylpropyl)methysiloxane (PPMS), poly(methyl methacrylate) (PMMA), polystyrene (PS), and poly(acrylonitrile-*co*-butadiene-*co*-styrene) (ABS), the latter leading to N-doped bilayer graphene due to its inherent nitrogen content. Or, the carbon feeds can be prepared from a self-assembled monolayer (SAM) of butyltriethoxysilane atop a SiO_2 layer. The carbon feedstocks were deposited on the insulating substrates and then caped with a layer of nickel. At 1000 °C, under low pressure and a reducing

atmosphere, the carbon source was transformed into a bilayer graphene film on the insulating substrates. The Ni layer was removed by dissolution affording the bilayer graphene directly on the insulator with no traces of polymer left from a transfer step.

In the present work, the scheme of direct growth of bilayer graphene on insulating substrates is shown in Fig.5.18a. Here, SiO_2 (500 nm)/Si^{++} and PPMS were used as the insulating substrate and the carbon source, respectively. The SiO_2/Si^{++} wafer was cleaned with oxygen-plasma and piranha solution (4:1 sulfuric acid:hydrogen peroxide). Then, a PPMS film (~ 4 nm thick) was deposited on the SiO_2 by spin-coating 200 μL of PPMS solution in toluene (0.1 wt %) at 8000 rpm for 2 min. A 500-nm Ni film was deposited on top of the PPMS film using a thermal evaporator (Edwards Auto 306); the Ni was used as the metal catalyst for graphene formation. At a temperature of 1,000 °C for 7 to 20 min, with a reductive gas flow (H_2 /Ar) and under low pressure conditions (~ 7 Torr), a 1-cm^2 homogeneous bilayer of graphene was synthesized between the insulating substrate and the Ni film. Marble's reagent was used to dissolve the Ni layer. The end result was that bilayer graphene was directly synthesized on the insulating surface, eliminating the transfer process. Instead of using a polymer film, a SAM of butyltriethoxysilane was made on the SiO_2. Using the same Ni deposition and growth conditions, a bilayer of graphene was formed.

Raman spectroscopy was used to identify the number of layers and to evaluate the quality and uniformity of graphene derived from PPMS on a SiO_2/Si^{++}

substrate. Fig. 5.18b shows the Raman spectrum of the PPMS-derived graphene, which is characteristic of 10 locations recorded over 0.5 cm^2 of the sample. The two most pronounced peaks in the spectrum are the G peak at ~1,580 cm^{-1} and the 2D peak at ~2,700 cm^{-1}. The full-width-at-half maximum (FWHM) of 2D peak and the I_G/I_{2D} peak intensity ratio for bilayer graphene are significantly different from monolayer graphene and few-layer graphene (Fig. 5.19)[23, 43,44]. Fig. 5.18b shows that the FWHM of the 2D peak is about 50 cm^{-1} and the intensities of the G peak and 2D peak are comparable. Furthermore, the 2D peak in Fig. 5.18b displays an asymmetric lineshape and can be well-fitted by four components: $2D_{1B}$, $2D_{1A}$, $2D_{2A}$, $2D_{2B}$ (Fig. 5.18c, yellow peaks, from left to right), individually with FWHM of 30 to 35 cm^{-1}. This data indicates that the PPMS-derived graphene is indeed bilayered[43,44].

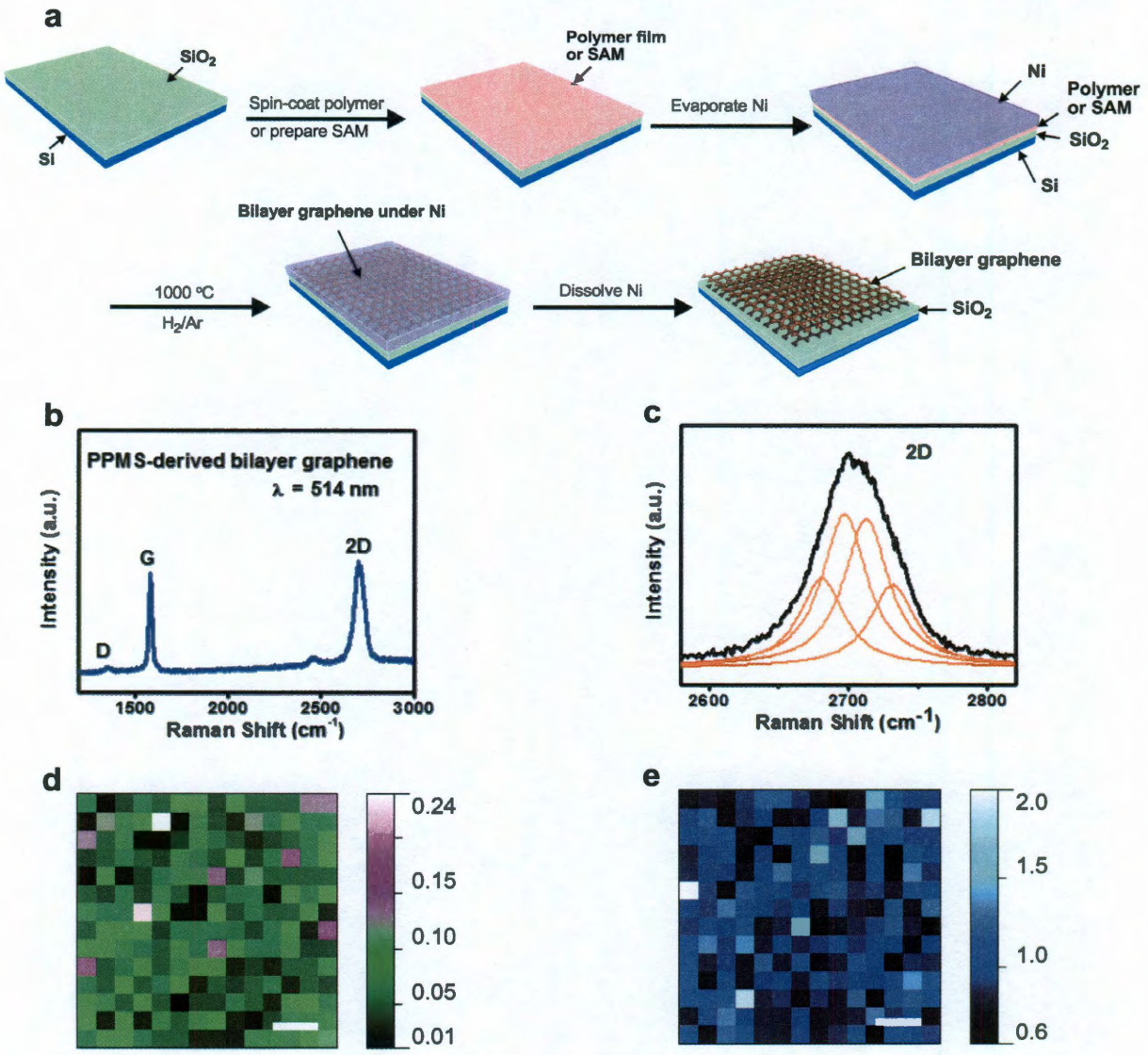

Fig. 5.18 Synthetic protocol and spectroscopic analysis of bilayer graphene. a, Bilayer graphene is derived from polymers or SAMs on SiO_2/Si substrates by annealing the sample in an H_2/Ar atmosphere at 1,000 °C for 15 min. b, Raman spectrum (514 nm excitation) of bilayer graphene derived from PPMS. See text for details. c, Bilayered 2D peaks were split into four components: $2D_{1B}$, $2D_{1A}$, $2D_{2A}$, $2D_{2B}$ (yellow peaks, from left to right) [43,44]. d-e, Two-dimensional Raman (514 nm) mapping of the bilayer graphene film (112 × 112 μm²). The color gradient bar to the

right of each map represents the D/G peak ratio (d) or G/2D peak ratio (e) showing ~90% bilayer coverage. The scale bars in d and e are 20 μm.

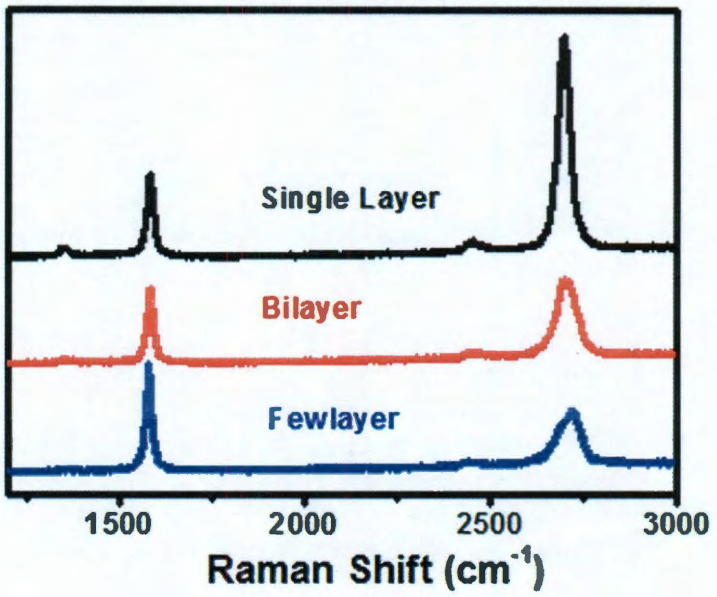

Fig. 5.19 | Raman spectra of graphene derived from PPMS. Black curve is the Raman spectra of single-layer region with less 3% coverage shown in Fig.5.18e. Red curve is the Raman spectra of bilayer region with around 90% coverage shown in Fig.5.18e. Blue curve is the Raman spectra of few-layer region with around 7% shown in Fig.5.18e.

The D peak (1,350 cm^{-1}) corresponds to defects in the graphene film. Fig.5.18b shows that the D peak is very low ($I_D/I_G < 0.1$), indicating few defects in the PPMS-derived graphene. The quality of PPMS-derived graphene over the large area was demonstrated by Raman mappings of the D to G peak ratio (Fig. 5.18d). Areas of 112 ×112 μm^2 were investigated. In the green and black regions (Fig. 5.18d), the D/G peak ratio is below 0.1, suggesting that high-quality graphene

covers ~ 95% of the surface[31]. The quality of PPMS-derived graphene was further confirmed by the low sheet resistance of the graphene film, which is ~ 2,000 Ω sq^{-1} by the four-probe method[31]. The uniformity and the coverage of PPMS-derived bilayer graphene were illustrated by the Raman mappings of the G to 2D peak ratio (Fig 5.18e). Again, an area of 112 × 112 μm^2 was investigated and the bilayer region was identified by areas I_G/I_{2D} valued of ~ 1[43,44]. The blue region in Fig. 5.18e is bilayer graphene, suggesting bilayer coverage of ~ 90%.

Although, the PPMS-derived graphene does not need to be transferred to another substrate in order to be used in most applications, the graphene film was peeled from the SiO_2/Si^{++} substrates using buffered oxide etch (BOE) for transmission electron microscopy (TEM) measurements. TEM images of the pristine PPMS-derived graphene and its diffraction pattern are shown in Fig. 5.20 The suspended graphene films on the TEM grids are continuous over a large area as seen under low-resolution TEM (Fig. 5.20a and 5.20b). The selected area electron diffraction (SAED) pattern in Fig. 5.20c displays the typical hexagonal crystalline structure of graphene. A 5° rotation is found between the two layers, suggesting non-AA or AB-stacked bilayer graphene films. The diffraction analysis shows that most of the area of the bilayer film is non-Bernal (non-AB) stacked graphene (Fig. 5.20c). The layer count on the edges indicates the thickness of this PMMA-derived graphene. The edge in Fig. 5.20d is randomly imaged under TEM and most is bilayer graphene, which corroborates the Raman data and further confirms the bilayer nature of this material.

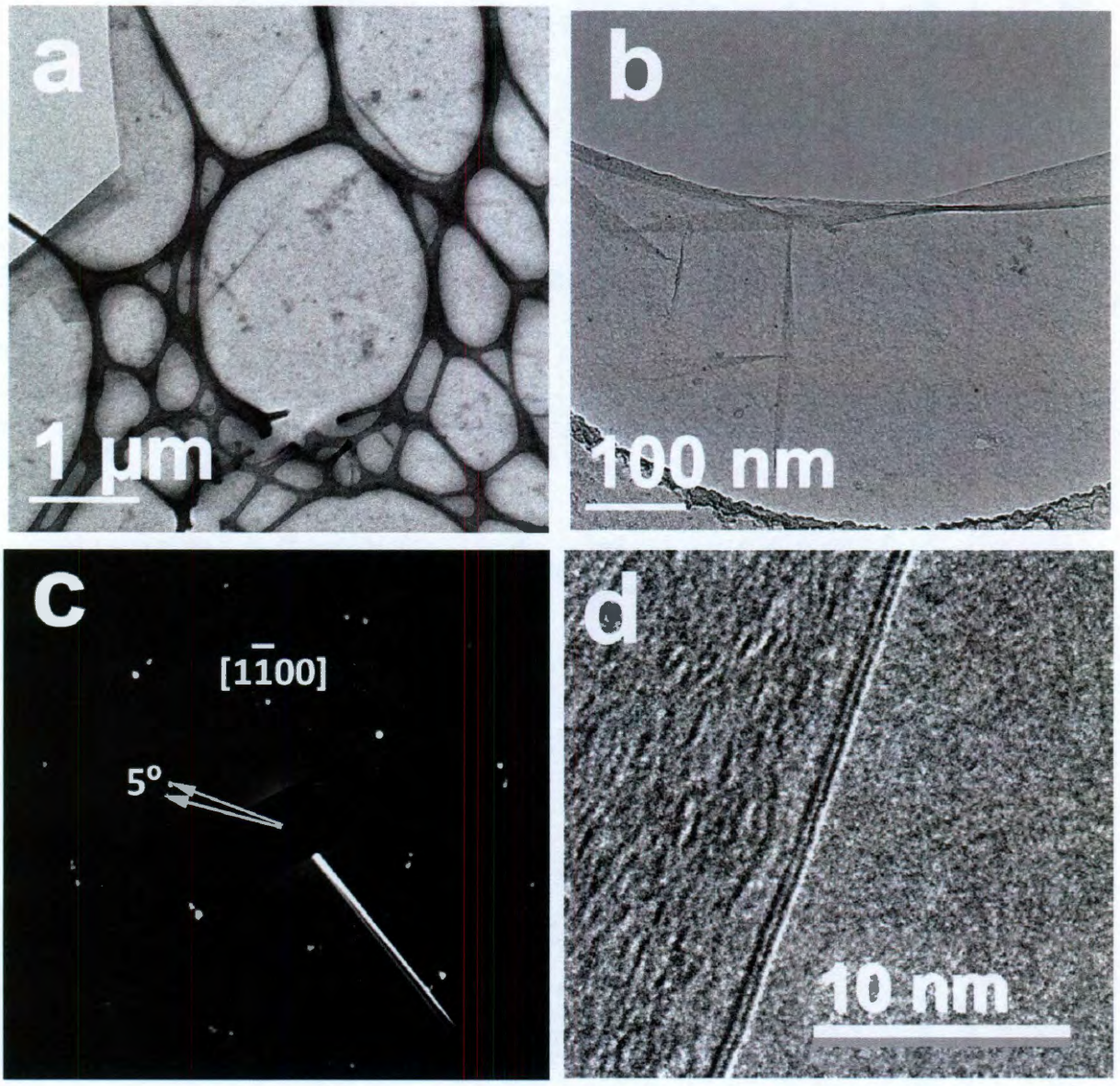

Fig. 5.20 TEM analysis of PPMS-derived bilayer graphene. a-b, Low-resolution TEM images showing bilayer graphene films suspended on a TEM grid. c, Hexagonal SAED pattern of the bilayer graphene with a rotation in stacking of 5° between the two layers. d, HRTEM picture of PPMS-derived graphene edges. The PPMS-derived graphene was 2 layers thick at random exposed edges.

Only a small portion (3-5%) appears to be Bernal (AB) stacked (Fig. 5.21).[45, 46] This is quite promising if we could increase the yield of Bernal bilayer graphene in our future work.

Fig. 5.21 Hexagonal SAED pattern of bernal stacked graphene.

The electrical properties of the obtained graphene were evaluated with back-gated graphene-based field-effect transistor (FET) devices on a 500-nm-thick SiO_2 dielectric. The drain-source current was modulated by applying a back gate voltage. Standard electron-beam lithography and lift-off processes were used to define the source and drain electrodes (30-nm-thick Au) in the graphene devices. Graphene stripes (10 μm wide) were further defined by oxygen-plasma etching. Fig. 5.22a and b show the schematic and the SEM image of the as-made device.

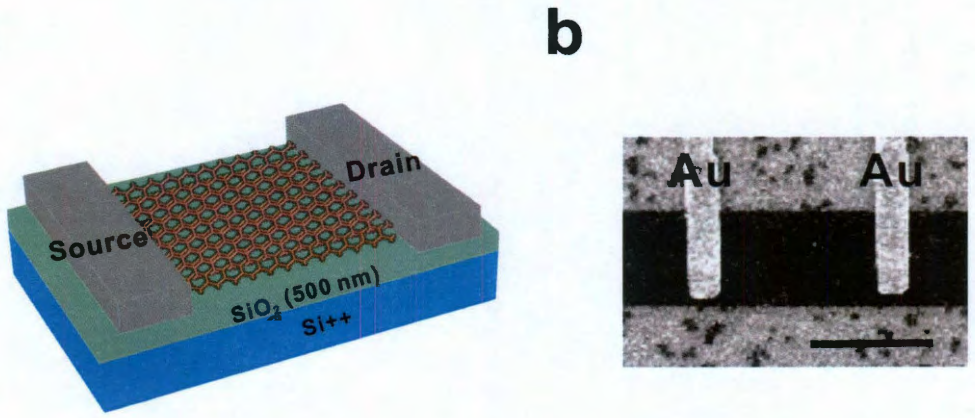

Fig. 5.22 The Scheme and SEM Image for PPMS-derived bilayer graphene-based device. Fig. 5.22a shows a schematic of the graphene device. Fig. 5.22b is the SEM images of the as-made device and the scale bar is 10 μm.

Typical data for the FET devices are shown in Fig. 5.23a. The PPMS-derived graphene FET shows an ambipolar behavior, which is similar to that of CVD-grown graphene.[6] For this particular device, the carrier (hole) mobility estimated from the slope of the conductivity variation with respect to the gate voltage is ~220 $cm^2 V^{-1} s^{-1}$ at the room temperature. In the experiments, more than five devices were made, with the mobilities of approximately 220, 180, 150, 130 and 120 $cm^2 V^{-1} s^{-1}$ at room temperature.

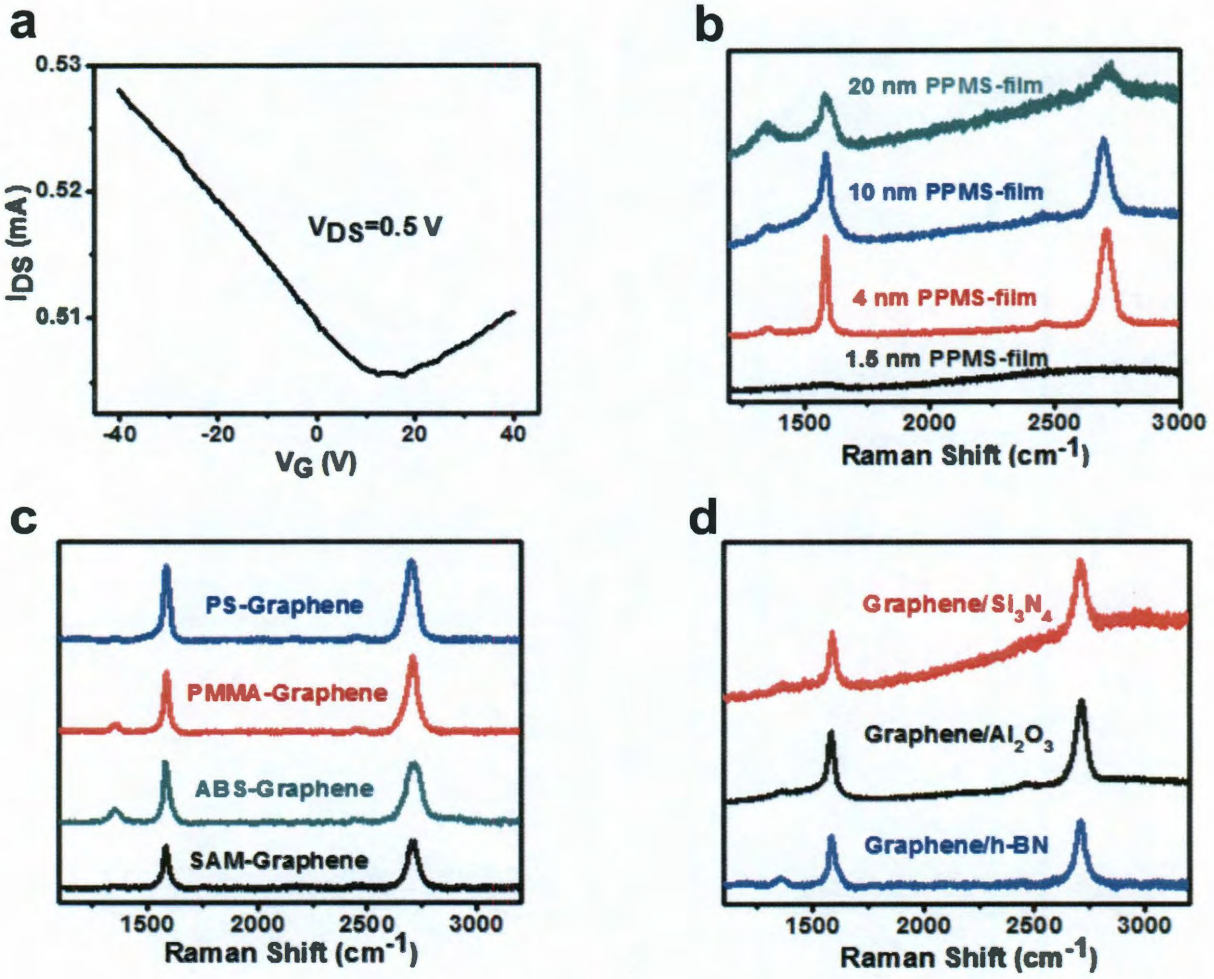

Fig. 5.23 Electrical properties of PPMS-derived graphene and spectroscopic analysis of graphene from different carbon sources and different substrates. a, Room temperature I_{DS}-V_G curve from a PPMS-derived bilayer graphene-based back-gated FET device. I_{DS}, drain-source current; V_G, gate voltage; V_{DS}, drain-source voltage. b, Difference in Raman spectra from PMMS-derived bilayer graphene samples prepared from different thicknesses of the starting PPMS film. c, Raman spectra of graphene derived from PS, PMMA, ABS and the SAM made from butyltriethoxysilane. d. Raman spectra of graphene derived from PPMS on h-BN, Si_3N_4 and Al_2O_3

(sapphire). The baseline has been subtracted from the Raman spectrum of graphene synthesized on h-BN.

The top Ni surface was analyzed after the reaction and it indeed had its own graphene layer, and it often appeared by Raman analysis to be a bilayer, though the signal is more difficult to analyze when on metal. Hence, some carbon below the Ni had diffused through the 500-nm-thick Ni film and formed a top graphene bilayer (Fig. 5.24).

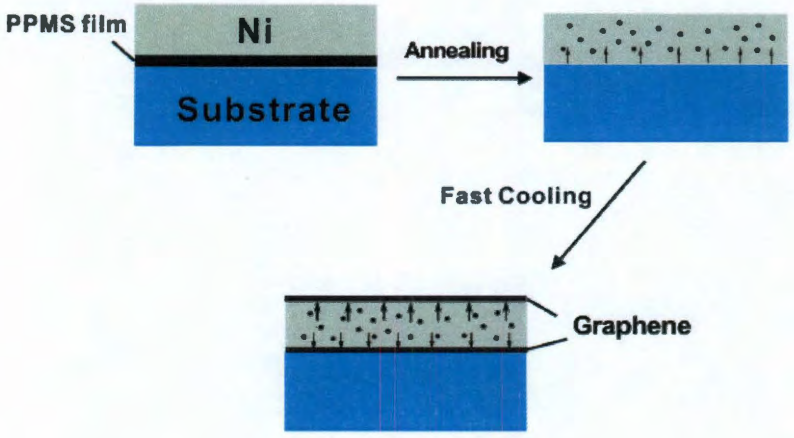

Fig. 5.24 The scheme for the proposed growth mechanism of PPMS-derived bilayer graphene. As shown in the Fig., PPMS film decomposed and dissolved into the Ni film during the annealing process (1000 °C). When the sample was removed from the hot-zone of the furnace and cooled to room temperature, the part of that carbon that dissolved in the bulk metal precipitated from the both sides of the Ni to form graphene on both the top and the bottom of the Ni layer.

In one case, we treated the top bilayer graphene film with UV-ozone (directed at the top-surface of the Ni), thereby destroying the top-bilayer graphene as verified by Raman analysis (Fig. 5.25). After Ni dissolution, the bottom graphene

bilayer was pristine. Hence, this excludes the possibility that the graphene on top of the Ni drops to the bottom surface after the Ni dissolution.

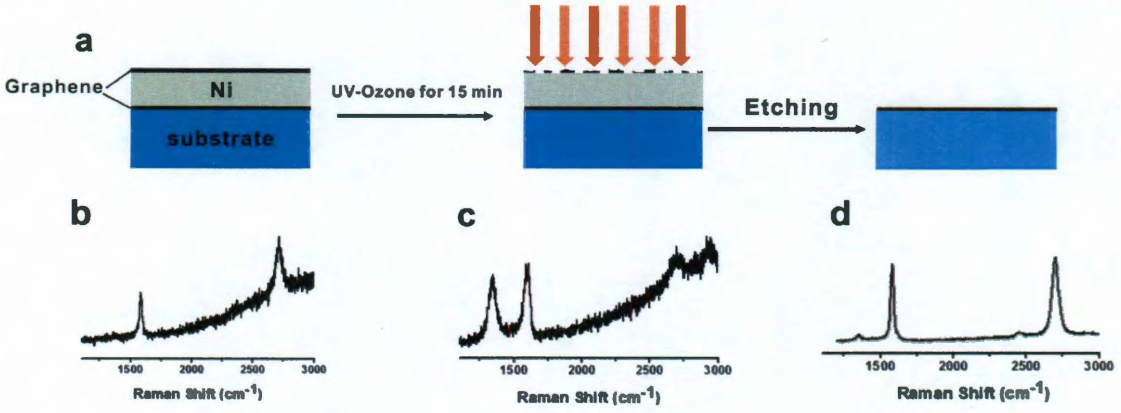

Fig. 5.25 Raman spectra analysis of PPMS-derived bilayer graphene on SiO_2/Si^{++}. After annealing Ni/PPMS/SiO_2/Si^{++} at 1000 °C with H_2/Ar for 15 min, the top surface of Ni was characterized by Raman spectra (Fig. 5.25b). Fig. 5.25b suggests that graphene was also grown on the top surface of Ni. After placing the sample in UV-Ozone for 15 min, the graphene on the top surface of Ni was badly damaged by UV-Ozone (Fig. 5.25c). Then the Ni was removed by etchant, and high-quality bilayer graphene was still obtained on SiO_2 /Si^{++} (Fig. 5.25d). Thus, the following conclusions can be made from the above experiments: (1) graphene was grown on the both sides of the Ni-film due to the diffusion of C at the high temperature; (2) the graphene that formed on the SiO_2/Si^{++} was from the bottom side of the Ni-film. All of the three Raman spectra are characteristic of 10 locations recorded over 0.5 cm^2 of the samples.

We propose a limited carbon source precipitation process for the growth mechanism of the polymer and SAM-derived bilayer graphene. In the CVD method, the thickness of graphene is difficult to control when using Ni as the substrate due to

the continuous supply of carbon and the high solubility of carbon in Ni[5, 7]. In our present method, the amount of feed carbon is limited and fixed between the insulating substrate and the Ni film at the start of the experiment. The amount of carbon in the 4-nm-thick PPMS film corresponds to ≤ 20% of the saturated carbon concentration in a 500-nm-thick Ni-film at 1000 °C[47]. As illustrated in Fig. 5.25, the 4-nm-thick PPMS film decomposed and dissolved into the Ni film during the annealing process. When the sample was removed from the hot-zone of the furnace and rapidly cooled, graphene films precipitated from the Ni. The sub-saturated carbon concentration in the Ni film facilitates the growth of bilayer graphene rather than few-layer graphene[48].

According to the above proposed mechanism, the amount of carbon in PPMS films will affect the graphene growth. Indeed, we controlled the thicknesses of PPMS films by adjusting the concentrations of PPMS-film-forming solutions; the thicknesses of PPMS films were determined by ellipsometry. A 200 μL sample with a concentration of 0.025, 0.1, 0.5 and 1 wt% of PPMS in toluene yielded thicknesses of approximately 1.5, 4, 10 and 20-nm-PPMS films, respectively, at spin-coat rates of 8,000 rpm. Fig. 5.23b shows that 4-nm-thick PPMS film was the optimal thickness for the growth of high-quality bilayer graphene (the red curve in Fig. 5.23b). When the thickness of PPMS film was 1.5 nm, the amount of carbon in the related PPMS-film is apparently not enough for the formation of graphene (Fig. 5.23b). Too much carbon caused the growth of multilayer graphene with increased defects. Interestingly, the amount of carbon in ~ 4-nm-thick film of PPMS is very similar to the amount of carbon in four layers of graphene where there is a bilayer below the

Ni and an approximate bilayer above the Ni (Fig 5.25). When this amount of carbon is exceeded, multilayers and amorphous carbons are formed. When the amount of carbon is insufficient, discontinuous graphene films are formed (Fig. 5.23b).

The optimized reaction temperature was 1000 °C. A lower temperature (950 °C) leads to a larger D-peak in the Raman spectrum (Fig. 5.26a), meaning more defects in the obtained graphene. The highest temperature studied was 1080 °C, at which bilayer graphene with a low D peak was still obtained (Fig. 5.26b).

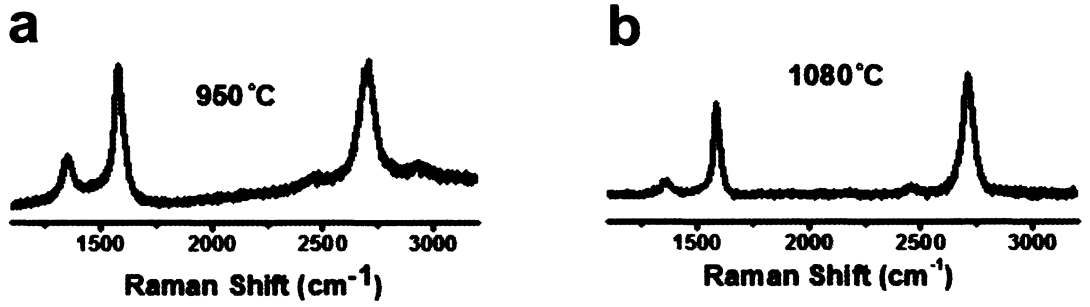

Fig. 5.26 Raman spectra analysis of PPMS-derived bilayer graphene. (a) Bilayer graphene grown on SiO_2/Si^{++} at 950 °C. (b) Bilayer graphene grown on SiO_2/Si^{++} at 1080 °C.

For the SAM, we used butyltriethoxysilane as the precursor to make a carbon layer on SiO_2. Fig. 5.23c shows that the SAM was successfully transformed into bilayer graphene. The sheet resistance was similar to that of PPMS-derived graphene at ~ 2,000 Ω sq^{-1}. Copper was also used as the catalyst for the direct growth of graphene on insulating substrates. Fig. 5.27 shows that copper transformed a 4-nm-thick PPMS film into amorphous carbon while the SAM was transformed into multilayer graphene with a large D peak. The growth of graphene

on Cu is due to surface catalysis rather than precipitation of carbon from the bulk metal as occurs in Ni[6].

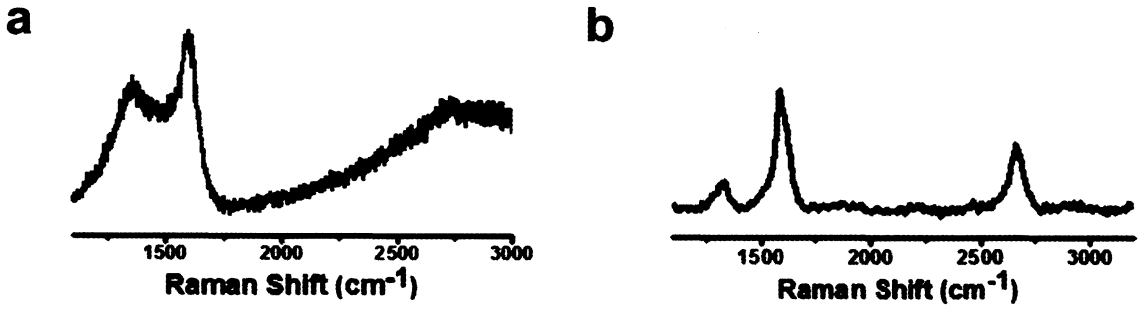

Fig. 5.27 Raman spectra analysis of graphene using copper as catalysts. a, When a 4-nm PPMS film was deposited between SiO_2/Si and a copper film (500 nm), and other conditions were the same as those for using Ni as the catalyst, amphorous carbon was produced rather than graphene. b, When the SAM derived from butyltriethoxysilane was used as the carbon source, multilayer graphene was obtained.

Other polymers, PS, PMMA and ABS, were used as carbon feed sources for the direct growth of graphene on insulating substrates. We selected SiO_2/Si^{++} (500 nm SiO_2) as the substrate and the reaction conditions were the same as those used for the PPMS-derived graphene. The Raman spectra in Fig. 5.23c indicated that all these carbon sources were transformed into bilayer graphene when their thicknesses were fixed at ~ 4 nm. For PMMA and ABS, the Raman spectrum of the obtained graphene showed slightly larger D peaks (Fig. 5.23c). In ABS, where N-doped bilayer graphene is obtained, a larger D peak is expected due to the broken lattice symmetry[31]. The sheet resistance for PMMA-derived graphene was ~ 3,000 Ω sq^{-1}

and the sheet resistance for ABS-derived graphene was ~ 5,000 Ω sq^{-1}, larger than that of PPMS-derived graphene. The X-ray photoemission spectroscopy (XPS) characterization of ABS-derived graphene demonstrates that ABS films were converted into N-doped graphene, with an N content of 2 % (Fig. 5.28). For PS-derived graphene, the low-D peak demonstrates the high quality of the obtained graphene film. Its sheet resistance is ~ 2,000 Ω sq^{-1}, similar to that of the PPMS-derived graphene. This can be further understood in that PS only contains carbon and hydrogen.

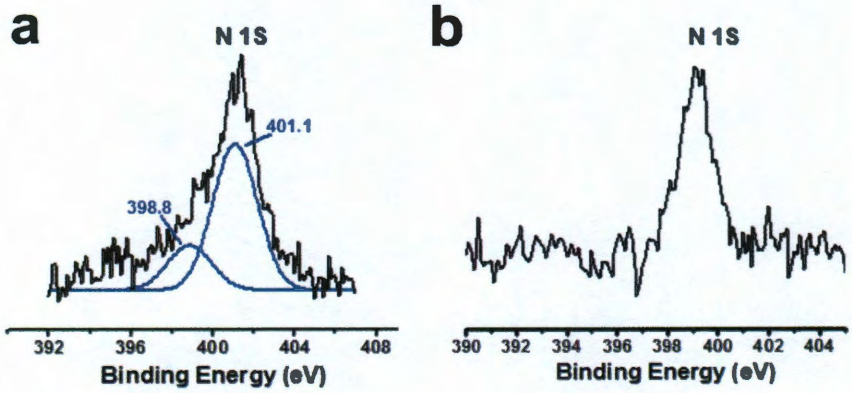

Fig. 5.28 XPS analysis of ABS-derived graphene. Fig. 5.28a shows the N 1s peaks in ABS-derived graphene, demonstrating two types of N and corresponding to pyridinic N (398.8 eV) and quaternary N (401.1 eV) in graphene[7]. The N 1s peaks in Fig. 5.28a have obvious shifts from that of R-CN (399.1 eV, Fig. 5.28b) in ABS (~ 3% N content), suggesting the N 1s signals do come from graphene instead of ABS.

Using similar conditions, bilayer graphene was also synthesized on several other insulating substrates, thereby underscoring the universality of this direct bilayer graphene growth. The conditions were kept the same as those used for

graphene growth on SiO_2 substrates except for replacing the insulating substrates with hexagonal boron nitride (h-BN), Si_3N_4 or Al_2O_3 (sapphire). Large area h-BN was synthesized by CVD of ammonia borane on copper[49] and then transferred onto the SiO_2/Si. After annealing Ni/PPMS/h-BN/SiO_2/Si at 1000 °C for 15 min and dissolving Ni, Raman spectra of the film had G peak and 2D peak signals with comparable intensities, demonstrating the successful synthesis of bilayer graphene on h-BN (Fig. 5.23d). While pure h-BN is non-conductive[49], the sheet resistance of the obtained graphene/h-BN hybrid film was ~ 2,000 Ω sq^{-1}, measured by the four-probe method. Graphene films were also synthesized on Si_3N_4 or Al_2O_3 as shown in Fig 5.23d. The sheet resistances of the graphene films on these substrates were both ~2,000 Ω sq^{-1}.

In this section, following the same protocol of solid carbon source growth, we have developed a general route for the direct synthesis of large-size and homogeneous bilayer graphene on various insulating substrates. This method is a new controllable transfer-free route based on the solid carbon sources growth technique, which opens the pathway for scalable bilayer graphene growth with direct compatibility to device construction.

Author Contributions:

Z.S. designed the experiments, discovered the procedures for graphene growth from solid carbon sources, and performed the spectroscopic characterizations and analysis. Zheng Yan optimized the growth conditions,

developed the transfer-free technique and contributed to the spectroscopic characterizations. Gedeng Ruan optimized the growth conditions from wastes and insects. Zhiwei Peng optimized the growth conditions of transfer-free technique. Jun Yao performed the electrical measurements and analysis. Elvira Beitler contributed to the electrical measurements and analysis. Yu Zhu carried out the sheet resistances and transmittance measurements.

References

1. Novoselov, K. S. *et al.* Electric field effect in atomically thin carbon films. *Science* **2004**, *306*, 666.
2. Geim, A. K. & Novoselov, K. S. The rise of graphene. *Nature Mater.* **2007**, *6*, 183–191.
3. Novoselov, K. S. *et al.* Two-dimensional gas of massless Dirac fermions in graphene. *Nature* **2005**, *438*, 197–200.
4. Ruoff, R. S. Graphene: Calling all chemists. *Nature Nanotech.* **2008**, *3*, 10-11.
5. Reina, A. *et al.* Large area, few-layer graphene films on arbitrary substrates by chemical vapor deposition. *Nano Lett.* **2009**, *9*, 30-35.
6. Li, X. *et al.* Large-area synthesis of high-quality and uniform graphene films on copper foils. *Science* **2009**, *324*, 1312-1314.
7. Kim, K. S. *et al.*, Large-scale pattern growth of graphene films for stretchable transparent electrodes. *Nature* **2009**, *457*, 706.
8. Lin, Y. *et al.*, Operation of graphene transistors at gigahertz frequencies. *Nano Lett.* **2009**, 9, 422-426.
9. Lin, Y. *et al.*, 100-GHz transistors from wafer-scale epitaxial graphene. *Science* **2010**, *327*, 662.
10. Schedin, F. *et al.*, Detection of individual gas molecules adsorbed on graphene. *Nature Mater.* **2007**, *6*, 652-655.
11. Stankovich, S. *et al.*, Graphene-based composite materials. *Nature* **2006**, *442*, 282-286.
12. Stoller, M. D. *et al.*, Graphene-based ultracapacitors. *Nano Lett.* **2008**, *8*, 3498-

3502.

13. Schlapbach, L. & Andreas Züttel. Hydrogen-storage materials for mobile applications. *Nature* 2001, *414*, 353-358.

14. Hernandez, Y. *et al.*, High-yield production of graphene by liquid-phase exfoliation of graphite. *Nature Nanotech.* **2008**, *3*, 563-568.

15. Stankovich, S. *et al.* Synthesis of graphene-based nanosheets via chemical reduction of exfoliated graphene oxide. *Carbon* **2007**, *45*, 1558-1565.

16. Berger, C. *et al. Elec*tronic confinement and coherence in patterned epitaxial graphene. *Science* **2006**, *312*, 1191-1196.

17. Zheng, M. *et. al.* Metal-catalyzed crystallization of amorphous carbon to graph*ene. Appl. Phys. Lett.* **2010**, *96, 063110*.

18. Li, X. *et al. C*hemically derived, ultrasmooth graphene nanoribbons semiconductors. *Science* **2008**, *319*, 1229-1232.

19. Wang, X. *et al.* N-doping of graphene through electrothermal reactions with ammonia. *Science* **2009**, *324*, 768-771.

20. Wei, D. *et al.* Synthesis of N-doped graphene by chemical vapor deposition and its electrical properties. *Nano Lett.* **2009**, *9*, 1752-1758.

21. Ci, L. *et al.* Atomic layer of hybridized boron nitride and graphene domains. *Nature Mater.* **2010**, *9*, 430-435.

22. Rao, C. N. R. *et al.* Some novel attributes of graphene. *J. Phys. Chem. Lett.* **2010**, *1*, 572-580.

23. Ferrari, A. C. *et al.* Raman spectrum of graphene and graphene layers. *Phys. Rev. Lett.* **2006**, *97*, 187401-187404.

24. Chen, J. H. *et al.* Charge-impurity scattering in graphene. *Nature Physics* **2008**, *4*, 377-381.

25. Zhang, Y. *et al.* Direct observation of widely tunable bandgap in bilayer graphene. *Nature* **2009**, *459*, 820-823.

26. Ci, L. *et al.* Controlled nanocutting of graphene. *Nano Research* **2008**, *1*, 116-122.

27. Lin, Y. *et al.* Controllable graphene N-doping with ammonia plasma. *Appl. Phys. Lett.* **2010**, *96*, 133110.

28. Li, X. *et al.* Simultaneous nitrogen doping and reduction of graphene oxide. *J. Am. Chem. Soc.* **2009**, *131*, 15939-15944.

29. Das, A. *et al.* Monitoring dopants by Raman scattering in an electrochemically top-gated graphene transistor. *Nature Nanotech.* **2008**, *3*, 210-215.

30. Balog, R. *et al.* Bandgap opening in graphene induced by patterned hydrogen adsorption. *Nature Mater.* **2010**, *9*, 315-319.

31. Sun, Z.; Yan, Z.; Yao, J.; Beitler, E.; Zhu, Y.; Tour, J. M. Growth of Graphene From Solid Carbon Sources. *Nature* **2010**, *468*, 549-552.

32. Geim, A. K.; Kim, P. Carbon Wonderland. *Sci Am.* **2008**, *298*, 90-97.

33. Wang, Y. Y.; Ni, Z. H.; Yu, T.; Shen, Z. X.; Wang, H. M.; Wu, Y. H.; Chen, W.; Wee, A. T. S. Raman Studies of Monolayer Graphene: The Substrate Effect. *J. Phys. Chem. C* **2008**, *112*, 10637-10640.

34. Yumitori, S. Correlation of C1s Chemical State Intensities with the O1s Intensity in the XPS Analysis of Anodically Oxidized Glass-like Carbon Samples. *J. Mater. Sci.* **2000**, *35*, 139-146.

35. Evans, S.; Thomas, J. M. The Chemical Nature of Ion-Bombarded Carbon: A Photoelectron Spectroscopic Study of 'Cleaned' Surfaces of Diamond and Graphite. *Proc. R. Soc. Lond. A.* **1977**, *353*, 103-120.

36. Kozlowski, C.; Sherwood, P. M. A. X-ray photoelectron spectroscopic studies of carbon-fibre surfaces. Part 4.-The Effect of Electrochemical Treatment in Nitric Acid. *J. Chem. Soc., Faraday Trans. 1*, **1984**, *80*, 2099-2107.

37. Gilje S.; Han S.; Wang M.; Wang K. L.; Kaner R. B. A Chemical Route to Graphene for Device Applications. *Nano Lett.* **2007**, *7*, 3394-3398.

38. Heyrovska, R. Atomic Structures of Graphene, Benzene and Methane with Bond Lengths as Sums of the Single, Double and Resonance Bond Radii of Carbon. http://arxiv.org/abs/0804.4086.

39. Stoller, M. D.; Park, S. J.; Zhu, Y. W.; An, J. H.; Ruoff, R. S. Graphene-Based Ultracapacitors. *Nano Lett.* **2008**, *8*, 3498-3502.

40. Li, D.; Müller, M. B.; Gilje, S.; Kaner, R. B.; Wallace, G. G. Processable Aqueous Dispersions of Graphene Nanosheets. *Nat. Nanotechnol.* **2008**, *3*, 101-105.

41. Feng, M.; Zhan, H.; Chen, Y. Nonlinear Optical and Optical Limiting Properties of Graphene Families. *Appl. Phys. Lett.* **2010**, *96*, 033107.

42. Nair, R. R.; Blake, P.; Grigorenko, A. N.; Novoselov, K. S.; Booth, T. J.; Stauber, T.; Peres, N. M.; Geim, A. K. Fine Structure Constant Defines Visual Transparency of Graphene. *Science* **2008**, *320*, 1308-1308.

43. Lee, S.; Lee, K.; Zhong, Z.; Wafer Scale Homogeneous Bilayer Graphene Films by Chemical Vapor Deposition. *Nano Lett.* **2010**, *10*, 4702-4707.

44. Luo, Z.; Yu, T.; Shang, J.; Wang, Y.; Lim, S.; Liu, L.; Gurzadyan, G. G.; Shen, Z.; Lin, J.

Large-scale Synthesis of Bi-layer Graphene in Strongly Coupled Stacking Order. *Adv. Funct. Mater.* **2011**, *21*, 911-917.

45. Meyer, J. C.; Geim, A. K.; Katsnelson, M. I.; Novoselov, K. S.; Booth, T. J.; Roth, S. The Structure of Suspended Graphene Sheets. *Nature* **2007**, *446,* 60-63.

46. Hass, J.; Varchon, F.; Millan-Otoya, J. E.; Sprinkle, M.; Sharma, N.; de Heer, W. A.; Berger, C.; First, P. N.; Magaud, L.; Conrad, E.H. Why Multilayer Graphene on 4H-SiC Behaves like A Single Sheet of Graphene. *Phys. Rev. Lett.* **2008**, *100*, 125504.

47. Singleton M.F.; Nash P., C-Ni (Carbon-Nickel), Binary Alloy Phase Diagrams, 2nd Ed., Ed.T.B. Massalski, Vol. 1, 1990, p 866-867.

48. Garaj, S.; Hubbard, W.; Golovchenko, J. A. Graphene Synthesis by Ion Implantation. *Appl. Phys. Lett.* **2010**, *97*, 183103.

49. Ci, L.; Song, L.; Jin, C.; Jariwala, D.; Wu, D.; Li, Y.; Srivastava, A; Wang, Z. F.; Storr, K.; Balicas, L.; *et al.* Atomic Layers of Hybridized Boron Nitride and Graphene Domains. *Nature Mater.* **2010**, *9,* 430-435.

Chapter 6

HYBRID SUPERLATTICES IN GRAPHENE

6.1. Introduction

The controllable and reversible modification of properties in graphene by chemical functionalization can modulate the graphene's optical and electronic properties[1-3]. In this chapter, we experimentally demonstrate the ability to controllably pattern graphane/graphene superlattices within a single sheet of graphene. By exchanging the sp^3 C-H bonds in graphane with sp^3 C-C bonds through functionalization, sophisticated multifunctional superlattices can be fabricated on both the macroscopic and microscopic scales. These patterns are visualized using fluorescence quenching microscopy techniques[4] and confirmed using Raman spectroscopy. By tuning the extent of hydrogenation, the density of the sp^3 C functional groups on graphene's basal plane can be controlled from 0.4% to 3.5%

with this two-step method. Using such a technique, which allows for both spacial and density control of the functional groups, a route to multifunctional electrical circuits[5] and chemical-sensors[6] might be realized across a single graphene sheet, facilitating the development of graphene-based devices.

Graphene has emerged as a remarkable material for diverse electronics applications due to the large-scale synthetic routes to produce it in monolayer form, its extraordinary carrier mobility and conductivity, and its versatility for band structure engineering[1,7-16]. Controllably tailoring graphene's electronic structure with selective synthetic methods could better shape this 2D semimetal material for use in different applications. It is known that physisorption of graphene with chemical species can temporarily alter its electrical properties; however adsorbents are too volatile for long-term usage[17]. With stronger binding energy and electronic coupling, covalent functionalization can permanently change the electronic structure of graphene. Hydrogenation is one straight-forward route to render graphene, which has a bandgap of zero, into a wide-gap semiconductor, and recent studies have indicated that this method is controllable and reversible[1,2]. However, hydrogenation produces a single type of functional group, a sp^3 C-H bond, which may prevent the material from being useful in more complicated applications. To convert the proton into more diverse chemical substituents, an additional chemical step, functionalization using a diazonium salt reaction, is demonstrated here. Reaction of diazonium salts with mechanically cleaved graphene was found to be selective to the edges and defects rather than the pristine basal plane[18,19]. However, for electronic applications of graphene, there is a need for more uniformity in

grafting functionality to the surface. Here, using the hydrogenated graphene as the activated precursor, C-H bonds are effectively exchanged with C-C bonds through diazonium salt functionalization, which controllably endows this material with a new spectrum of chemical and electrical properties.

Furthermore, superlattices formed with built-in multifunctional regions in desired templates could yield characteristics necessary for the development of applications in, for example, chemical sensors, thermoelectrics and metamaterials[3,6,20]. In many cases, to produce materials relevant for these applications requires controlled attachment of complex molecules into patterns[21]. Alternatively, the ability to take a single template, such as graphene, and use existing processes such as lithographic patterning to create such structures on a molecular level, facilitates a route toward the rapid development of such desired architectures. The ability to produce large-scale graphene transferable to varied host surfaces also makes graphene an excellent template for the development of well-established top-down patterning approaches for device fabrication. Recent theoretical studies have emphasized the viability of this route for making quantum dots from patterned interfaces of hydrogenated and pristine graphene[22], and we extend this idea to large-scale patterning of multifunctional domains on graphene.

6.2. Graphane/Graphene Superlattice and FQM

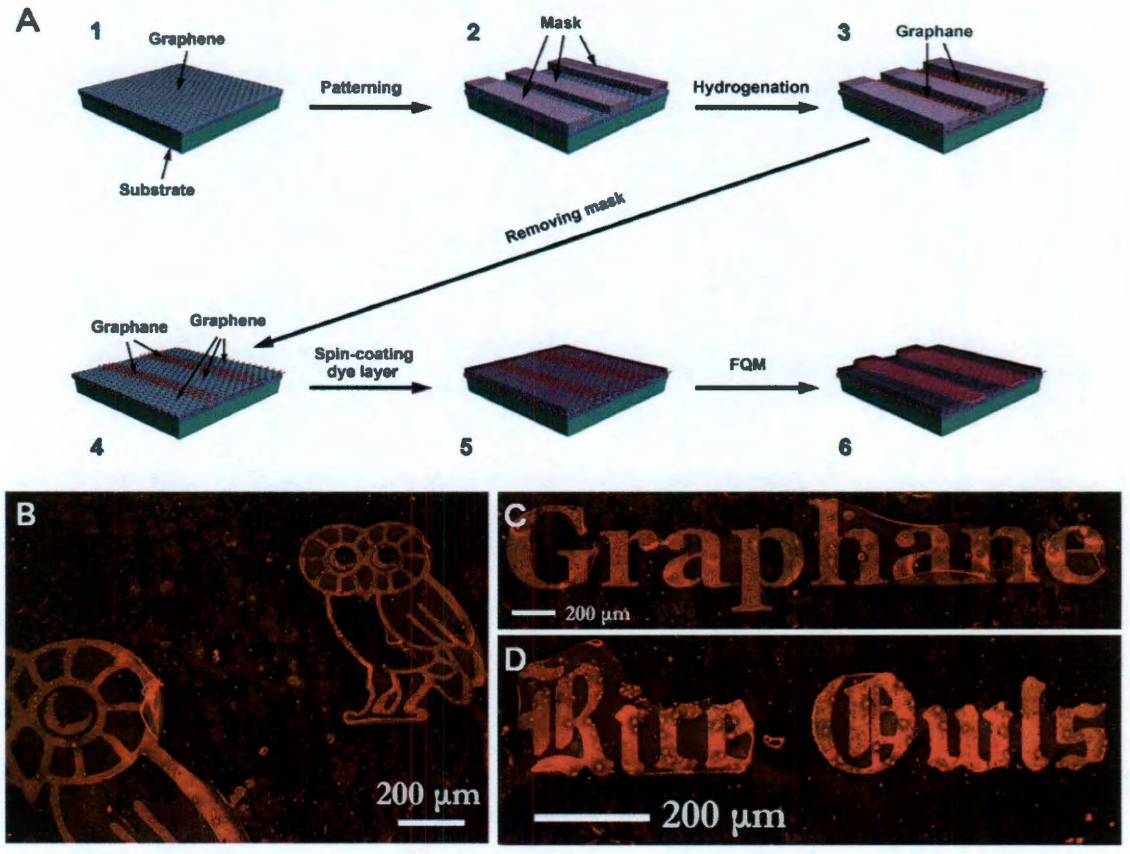

Fig. 6.1 Graphane/graphene superlattices fabrication and imaging. (A) Schematic illustration to fabricating the graphane/graphene superlattices and subsequent FQM imaging. (B to D) FQM imaging of the graphene with different graphane/graphene patterns.

The typical process to pattern hydrogenated graphene domains and the subsequent imaging using fluorescence quenching microscopy (FQM) is illustrated in Fig. 6.1A. First, large-area graphene, grown from Cu substrates by CVD or solid carbon methods, were transferred to an insulating substrate such as quartz or SiO_2/Si, using the PMMA protection procedure as described[11,12]. Following this,

conventional photolithography was employed with a photoresist mask to define patterns atop the graphene films. Next, the exposed area of graphene was hydrogenated using atomic hydrogen generated by a tungsten hot filament at low H_2 pressure (10 to 20 Torr). The sample takes 2 h to be hydrogenated thoroughly at ~ 10 °C. This procedure was found to be effective for controlled hydrogenation, minimizing graphene etching that originates at defects or edges[23]. Finally, the photoresist mask was removed to yield a conductive graphene sheet patterned with domains of insulating graphane-containing regions. Although the fabrication of the graphane/graphene superlattices, as we demonstrate here, was largely reliant on conventional techniques, the challenge is determining a straight-forward and rapid method for imaging the product of the process, namely the substructure of the graphene/graphene hybrid material. Therefore, the FQM technique[4,24], discovered by Treossi, E. *et al.*, was used to image the existing hybrid patterns. According to the excited-state energy transfer mechanism, graphene may serve as an acceptor to quench the fluorescence of a thin spin-coated dye layer (0.02 % rhodamine B mixed with 5% PMMA in acetone)[4]. Because graphene and its functionalized form are different in their conjugation, the differential quenching ability of the hybrid graphane/graphene pattern can be readily observed using FQM[4]. Using the technique illustrated in Fig. 6.1A, graphane/graphene patterns have been made with photolithography, hydrogenation, and then imaged with FQM as shown in Fig. 6.1B to D.

It should be noted that in all cases conventional photolithography was used, which is only capable of accuracy down to length scales of ~ 1 μm in our laboratory

(Fig. 6.2). However, well-defined structures that can be achieved using more advanced lithographic techniques can extend this technique to finer patterning[25]. In the photos, all of the dark areas are pristine graphene, which more efficiently quenches the fluorescence of the thin top dye layer. The bright areas are graphane; its fluorescence quenching ability is much weaker than in graphene due to the loss of conjugation in the former. This verifies that the formation of insulating domains on a conductive graphene sheet can be readily achieved (Fig. 6.2D).

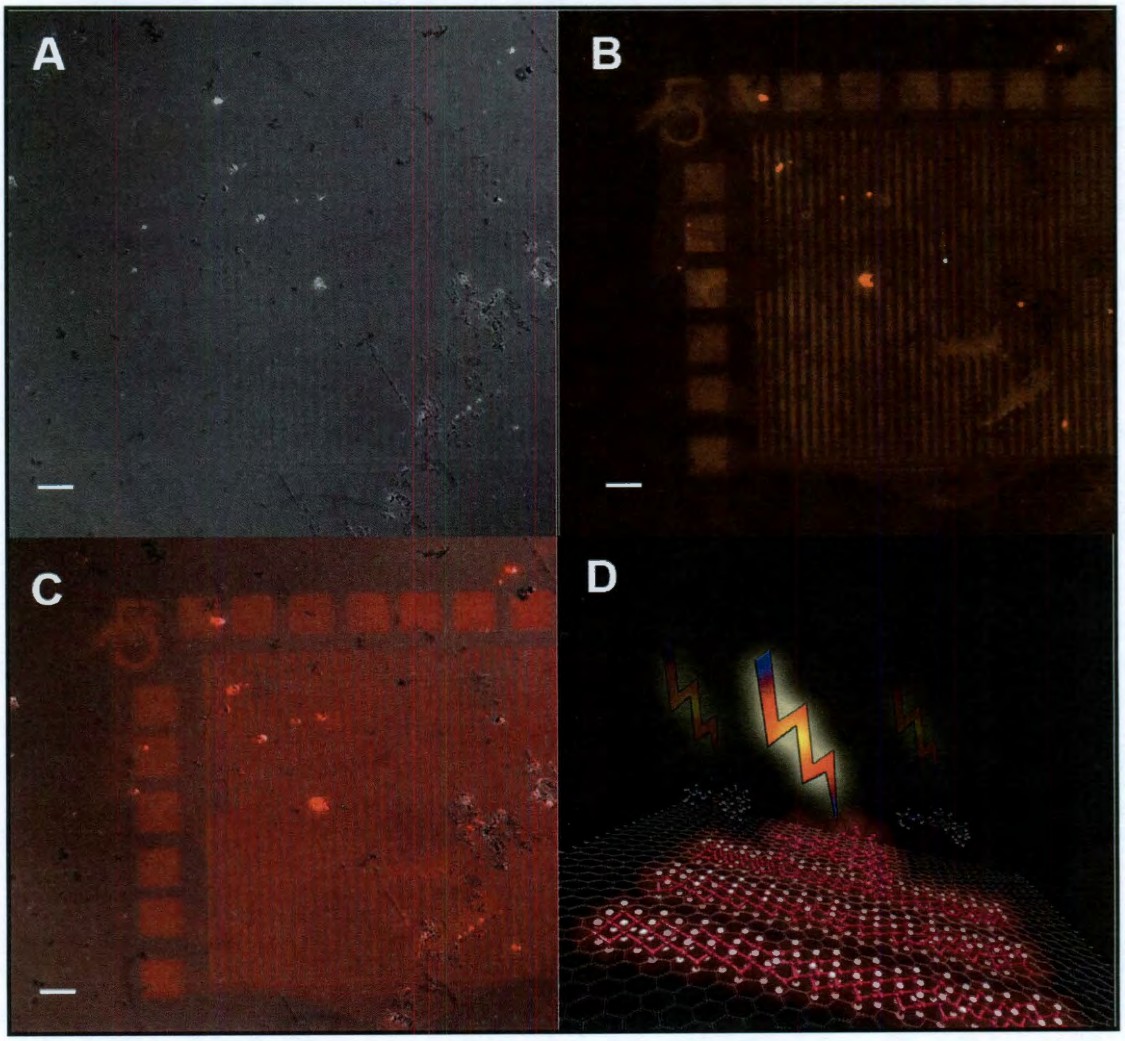

Fig. 6.2 FQM imaging of the graphane/graphene heterostructure. (A) Optical microscopy image of graphane/graphene pattern. (B) FQM image of the

graphane/graphene pattern at the same area as (A). (C) Overlap image of optical microscopy image (A) and FQM image (B). Scale bars are 50 μm. (D) Schematic mechanism of FQM. The dye molecules (Rhodamine B) situated on graphene surface quenches its fluorescence, whereas the ones on graphane emit the fluorescence light.

Typical atomic models of graphane and graphane/graphene superlattices are shown in Fig. 6.3A and 6.3B. Although, in our cases, full hydrogenation is not achieved due to the substrate hindering effect; the hydrogenated section has more sp^3 carbon characteristics than does the pristine section, as seen by the pronounced D peak in the Raman spectrum. The Raman spectra displayed in Fig. 6.3C correspond well with those reported for single-layer graphene before and after hydrogenation[2]. With extended hydrogenation time, more sp^3 C characteristics or higher D peaks were observed. In Raman spectra of pristine monolayer graphene, the D peak (1350 cm^{-1}) is much lower than the G peak (1580 cm^{-1}), and the 2D peak (2685 cm^{-1}) is about 4 times more intense than the G peak. After 180 min of hydrogenation, the D peak is almost as high as the G peak. An additional D' peak (1620 cm^{-1}) is detected on the shoulder of the G peak and the 2D peak is suppressed due to the chemical functionalization.

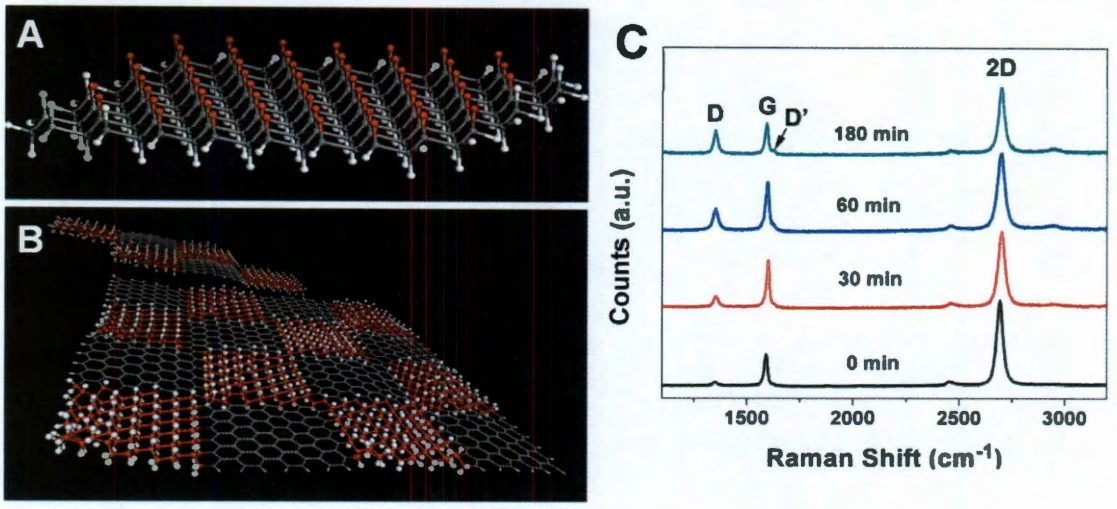

Fig. 6.3 Molecular models of graphane and graphane/graphene superlattices and corresponding Raman spectra of experimental products. (A) Fully hydrogenated graphene structure. (B) Graphane/graphene superlattices structures. (C) Raman spectra of graphene and graphane with extended hydrogenation time. The D peak increases as the hydrogenation time increases from 0 min (bottom) to 180 min (top).

The D peak intensity was also recorded as a 2-dimensional map to confirm the formation of a graphene/graphane patterns in Fig. 6.4. However, compared to FQM that only takes a few seconds to image a large area of the sample, Raman mapping is relatively time-consuming (7 h for 50 × 50 μm^2 area in Fig. 6.4) with a resolution limited by the laser spot size of the Raman instrument.

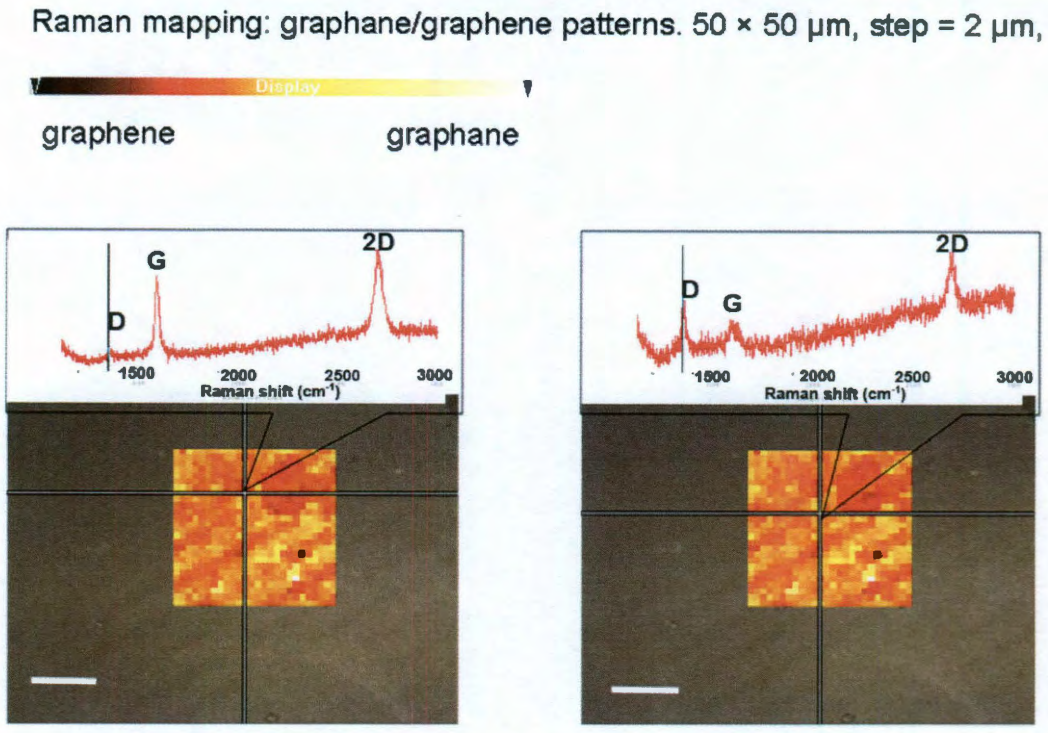

Fig. 6.4 Raman mapping (50 × 50 µm) of the hydrogenated graphane/graphene superstructures overlaid with its bright field image. Scale bar is 20 µm. Graphene area is marked using dark color while graphane using light color. Representative graphene (left) and graphane (right) spectra at specific spots are displayed above the microscopic image.

Four-probe electrical measurements before and after the hydrogenation demonstrate a gradual transformation from semimetallic graphene to near-insulating graphane-like material. After annealing at 520 °C for 30 min under high vacuum (10^{-6} – 10^{-7} Torr), the graphane is partially converted back to graphene based on the partial recovery of its conductivity (Fig. 6.5). This provides additional evidence that insulating graphane domains formed from a conductive graphene template[2].

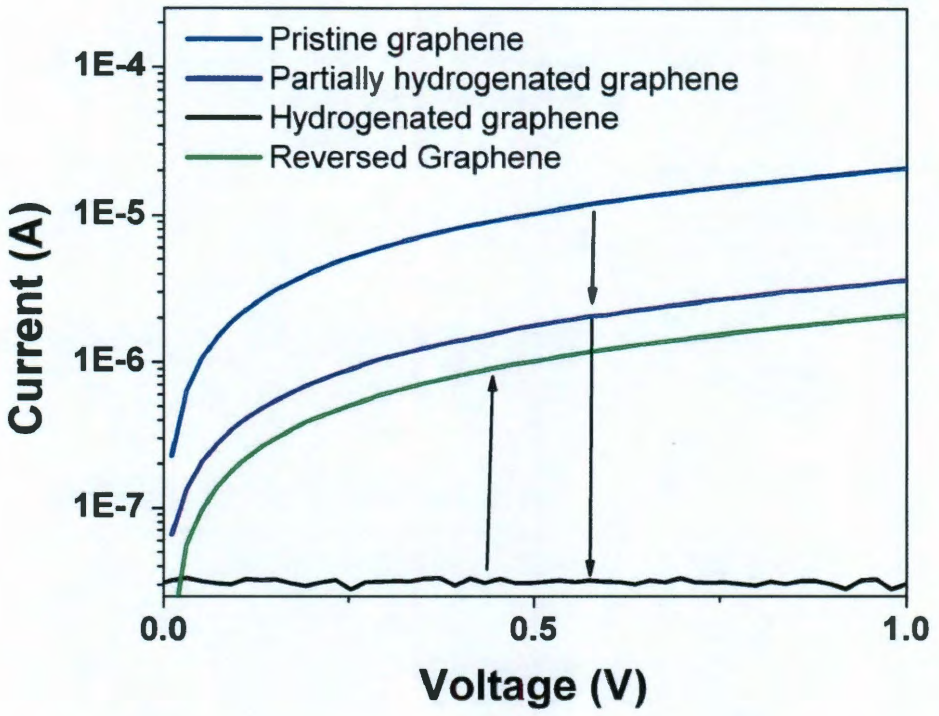

Fig.6.5 Four-probe electrical measurements of graphene (blue), partially hydrogenated graphene (violet), hydrogenated graphene (black) and reversed graphene (green) made by heating the hydrogenated graphene to 520 °C for 30 min under high vacuum (10^{-6} – 10^{-7} Torr). The bumps in the black curve are instrumental noise due to instrument limitation and the log plot enhancement.

6.3. Hybrid Superlattice Through Diazonium Reaction

With this graphane/graphene superlattice in hand, the material can be additionally functionalized using diazonium salts. The diazonium salt reaction with the graphane/graphene intermediate is most likely to go through a free radical

mechanism, as had been proposed for the diazonium functionalization of a hydrogen passivated Si surface[26]. As shown in Fig. 6.6, in this case we propose a spontaneous electron transfer from the surface of the graphane/graphene substrate to the diazonium salt, generating an aryl radical upon loss of N_2 and a graphane/graphene radical cation. A proton is eliminated from the graphane/graphene to form HBF_4 and a graphane/graphene radical. Within a common solvent shell, the free aryl radicals attack the surface near the sp^3 C-H bond sites to form the new covalent sp^3 C-C bonds.

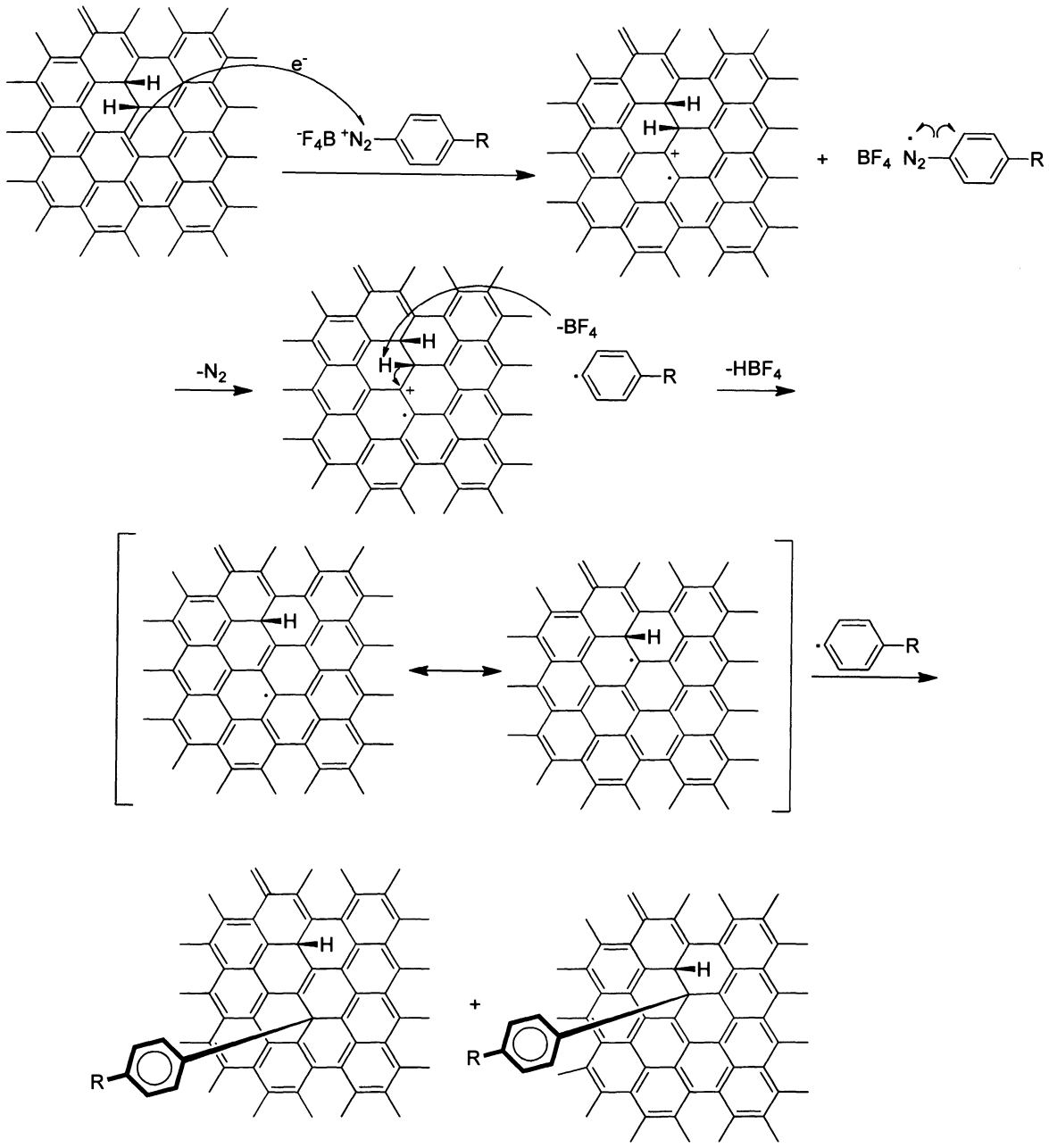

Fig. 6.6 A proposed mechanism of spontaneous diazonium activation by a hydrogenated graphene surface. Only two regioisomers are shown in the final product, though others are possible.

Thermodynamically, pristine graphene is inert to many organic reactions except at structurally reactive spots with relatively high chemical potential, which make these latter sites more reactive. For example, the edges, strain sites (ripples) and the Stone-Wale defects are more reactive than the crystalline basal planes of graphene based on experimental and theoretical studies[19,28,29]. Nevertheless, hydrogenation functionalizes the basal plane of graphene in a controllable, uniform and reversible manner. Here we show that hydrogenation also activates the basal plane toward diazonium functionalization. Similar to aryl radicals in the diazonium reaction, the atomic H works as a free radical (H•). This H-radical generated by the hot tungsten filament overcomes the high energy barrier to break the sp^2 bond in graphene and it thereby forms a new sp^3 bond. Fig. 6.7 displays the reaction energy scheme for both the direct diazonium reaction (addition reaction, sp^2 bond to sp^3 bond) and the diazonium reaction after hydrogenation (substitution reaction, sp^3 bond to sp^3 bond).

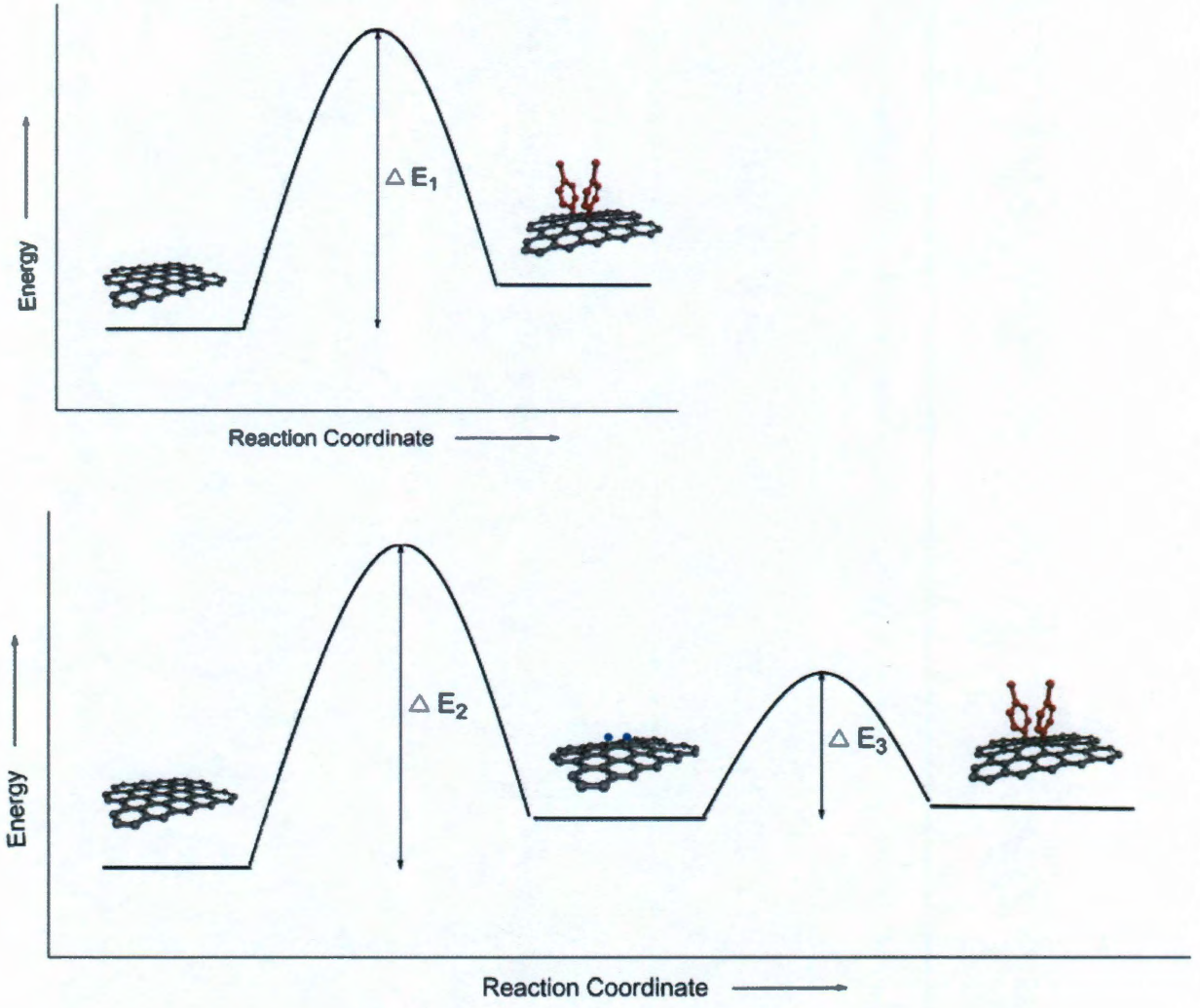

Fig. 6.7 Proposed reaction energy diagram of diazonium salt reaction with graphene (top) and diazonium salt reaction with hydrogenated graphene (bottom).

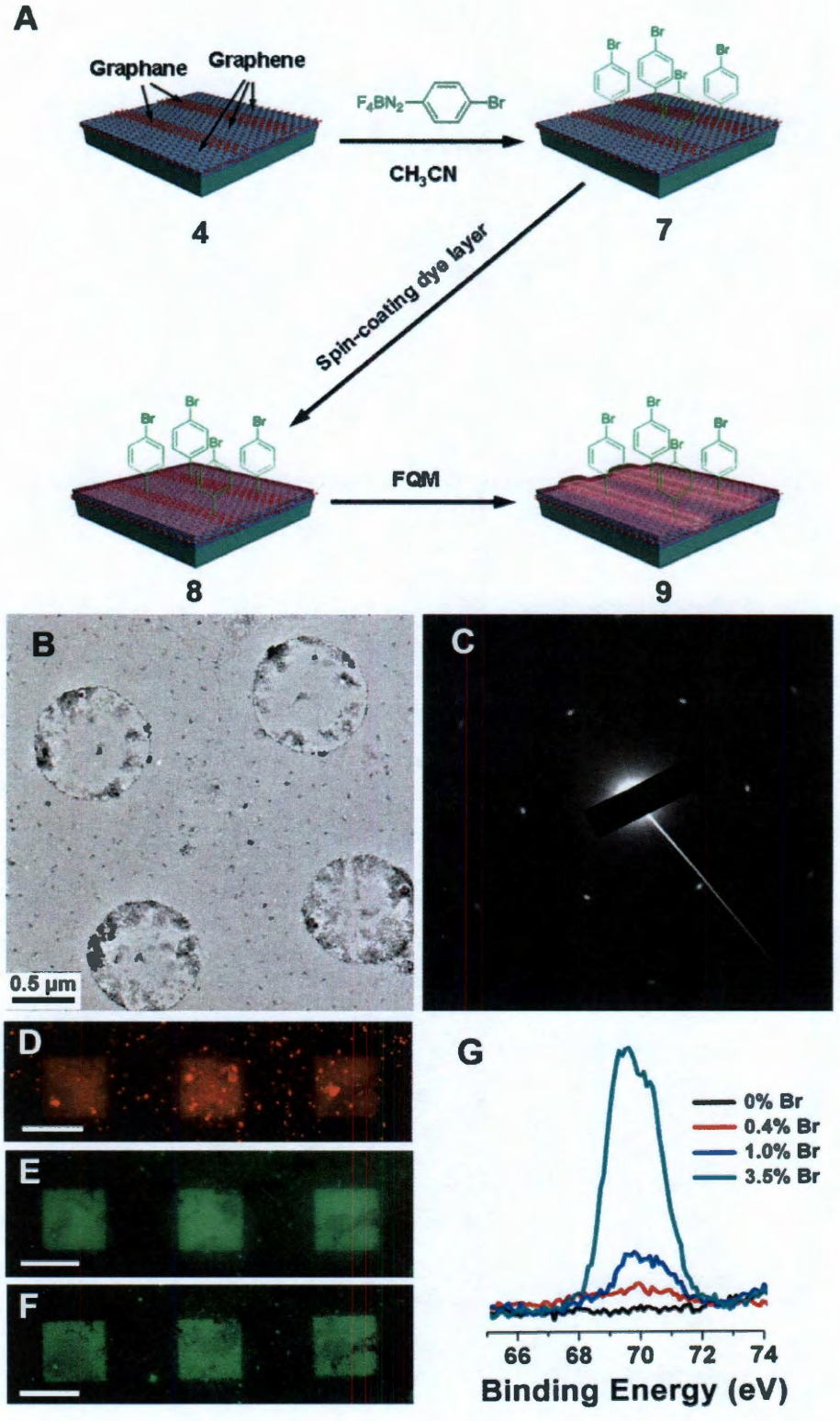
A
Graphane
Graphene
F_4BN_2
Br
CH_3CN
4
7
Spin-coating dye layer
FQM
8
9
B
0.5 μm
C
D
E
F
G
0% Br
0.4% Br
1.0% Br
3.5% Br
66
68
70
72
74
Binding Energy (eV)

Fig. 6.8 Controllable exchange of sp^3 C-H bonds with sp^3 C-C bonds using 4-bromophenyldiazonium tetrafluoroborate and its spectroscopic analysis. (A) Schematic illustration of the fabrication of sp^3 C-C exchanged superlattices and subsequent FQM imaging. (B) TEM image of diazonium functionalized graphene film covering a TEM grid with four suspended areas shown. (C) SAED pattern of diazonium functionalized graphene. (D to F) FQM images of diazonium functionalized graphene superlattices. The dye molecules used in FQM are rhodamine B in (D), FITC in (E) and fluoroscein sodium in (F). The scale bars are 50 μm. (G) XPS of samples containing different percentages of 4-bromophenylene functionality by tuning the hydrogenation process. The bromine content could be controlled from 0 to 3.5%.

The diazonium functionalized graphene film was lifted off from a SiO_2/Si wafer and transferred onto a c-flat TEM grid (Protochips) with the PMMA protection method[12]. The etchant used here is buffered oxide etchant (J. T. Baker, Buffered Oxide Etch 6:1). In Fig. 6.8B and C, the TEM image and selected area electron diffraction (SAED) pattern prove that the graphene sample is maintained after the chemical process of hydrogenation and diazonium reaction. FQM was used to image the same diazonium functionalized graphene superlattices with different dye molecules, such as rhodamine B, fluorescein isothiocyanate (FITC), and fluoroscein sodium in Fig. 6.8D to F, respectively. The diazonium functionality introduced was determined by analysis of the bromine content of the functionalized product using X-ray photoelectron spectroscopy (XPS); the Br content was due to the 4-bromophenyldiazonium tetrafluoroborate used in the functionalization. As shown in

Fig. 6.8G, under the same reaction conditions, pristine graphene has only 0.4% bromine content after functionalization with the diazonium salt, while graphane has bromine content > 1%. The more graphane that is present in the sample, the more bromophenyl-functionalization that is introduced. The sample with the most graphane had a bromine content of 3.5%, which is approximately one new sp^3 C-C bond in every 21.5 C atoms in the graphane domains.

With this two-step functionalization method, graphene's basal surface can be controllably grafted with Br content from 0.4% to 3.5%, with a lithographically defined spacial resolution. Furthermore, to visualize the patterns, we used FQM, which, when combined with Raman spectroscopy, provides the necessary analytical tools to characterize the heterostructures. The two-step controlled covalent functionalization process described here permits modulation of the electronic properties of graphene's basal planes and could hold promise for optoelectronic and sensor devices based upon this exciting new material.

6.4. Experimental Summary

6.4.1. Graphane/Graphene Superlattices Fabrication

Graphene films were grown on 25-μm thick Cu foils (99.8%, Alfa Aesar, item No. 13382) and transferred onto various substrates, such as glass, quartz, and 100 nm SiO_2/Si, according to the methods reported[1, 2]. Graphene patterns were fabricated using a photoresist (Microposit S1813) mask in a standard photolithography process or a PMMA mask in an e-beam lithography process.

Hydrogenation was performed in a vacuum system equipped with a hot tungsten filament (diameter = 0.25 mm, 99.95%, Alfa Aesar) which splits the H_2 gas into H atoms. Before the hydrogenation, the graphene samples (or graphene patterns) were heated in vacuum (10^{-6} Torr) at 400 °C (200 °C with polymer defined patterns) for 15 min to remove physisorbed polymers and other contaminants which might block the hydrogenation of the graphene surface. 50 sccm H_2 was then introduced into the system and the pressure was controlled at ~ 10 Torr using a valve connected to the vacuum pump. The filament current was slowly increased to ~ 13 A and the total power was maintained at ~ 60~65 W. The graphene samples were placed ~ 2 cm from hot filament for various times (15 min, 30 min, 1 h, 2 h or 3 h) to produce different levels of hydrogenation. The FQM patterns samples were made from the superlattices that had been hydrogenated for 2 h. After the hydrogenation, the polymer masks were removed by rinsing with 10 mL acetone 3×.

6.4.2. FQM Imaging the Graphane/Graphene Superlattices

A thin layer of dye (0.02 wt% Rhodamine B, FITC or fluoroscein sodium, mixed with 5 wt% PMMA acetone solution) was deposited onto the superlattice sample surfaces by spin-coating at 5000 rmp for 1 min (Headway Research, Inc.). The samples were imaged under a fluorescence microscope (Zeiss Axioplan 2 imaging Optical Microscope). It was equipped with a Mercury Arc lamp (HBO 100 W) and in combination with a set of filters, coordinates the excitation and emission wavelengths corresponding to a particular fluorophore. In this work, Texas of Red (Ex: 555, 595/ Em: 615 nm) and Cy3 (Ex: 514, 554 / Em: 566, 615 nm) channels

were used for rhodamine B, and FITC (Ex: 493/ Em: 517 nm) channel was used for FITC and fluoroscein sodium. Images were recorded and processed at room temperature using a Photometrics Cool Snap HQ camera and MetaMorph software. The objectives used were 10X, 20X, and 40X in air; 63X and 100X in oil. The diazonium functionalized graphane/graphene superlattices have the same contrast as the unfunctionalized precursors, namely the graphane-graphene superlattices.

6.4.3. Diazonium Functionalization of Hydrogenated Graphene

In the diazonium functionalization experiments, the substrates (graphene hydrogenated for varied times of 0, 15, 30, 60, 120 to 180 min) were placed in a N_2-purged, freshly prepared 1 mg/1 mL diazonium salt solution (4-bromobenzenediazonium tetrafluoroborate in CH_3CN) in the dark at room temperature for 20 h. The reactions could also be performed under UV light (254 nm) in 2 h. After the diazonium reaction, the samples were rinsed in CH_3CN 3× to thoroughly remove any physisorbed diazonium salt residue and they were then dried using a flow of N_2 before further characterization.

Author Contributions:

Z.S. designed the experiments, discovered the procedures for making graphene-based superlattices, performed the spectroscopic characterizations and analysis. Cary L. Pint performed the hydrogenation reactions and electrical measurement. Chenguang Zhang optimized the hydrogenation conditions. Daniela C. Marcano performed the FQM characterization. Gedeng Ruan prepared the graphene

samples for hydrogenation. Jun Yao fabricated the lithographic patterns. Zheng Yan and Yu Zhu contributed to the patterning for graphene samples.

References

1. Balog, R.*et al.* Bandgap opening in graphene induced by patterned hydrogen adsorption. *Nature Mater.* **2010**, *9*, 315-319.
2. Elias, D. C.*et al.* Control of graphene's properties by reversible hydrogenation: Evidence for graphane. *Science* **2009**, *323*, 610-613.
3. Vakil, A.; Enghata, N. Transformational optics using graphene. *Science* **2011**, *332*, 1291-1294.
4. Kim, J.; Cote, L. J.; Kim, F.; Huang, J. Visualizing graphene based sheets by fluorescence quenching microscopy. *J. Am. Chem. Soc.* **2010**, *132*, 260-267.
5. Lin, Y. *et al.* Wafer-scale graphene integrated circuit. *Sicence* **2011**, *332*, 1294-1297.
6. Fowler, J. D.*et al.* Practical chemical sensors from chemically derived graphene. *ACS Nano* **2009**, *3*, 301-306.
7. Novoselov, K. S.*et al.* Electric field effect in atomically thin carbon films. *Science* **2004**, *306*, 666-669.
8. Kim, K. S.*et al.* Large-scale pattern growth of graphene films for stretchable transparent electrodes. *Nature* **2009**, *457*, 706-710.
9. Bae, S.*et al.* Roll-to-toll production of 30-inch graphene films for transparent electrodes. *Nature Nanotechnol.* **2010**, *5*, 574-578.
10. Reina, A.*et al.* Large area, few-layer graphene films on arbitrary substrates by chemical vapor deposition. *Nano Lett.* **2009**, *9*, 30-35.
11. Li, X.*et al.* Large-area synthesis of high quality and uniform graphene films on copper foils. *Science* **2009**, *324*, 1312-1314.

12. Sun, Z.*et al.* Growth of graphene from solid carbon sources. *Nature* **2010**, *468*, 549-552.

13. Kosynkin, D. V.*et al.* Longitudinal unzipping of carbon nanotubes to form graphene nanoribbons. *Nature* **2009**, *458*, 872-876.

14. Jiao, L.; Zhang, L.; Wang, X.; Diankov, G.; Dai, H. Narrow graphene nanoribbons from carbon nanotubes. *Nature* **2009**, *458*, 877-880.

15. Bai, J.; Zhong, X.; Jiang, S.; Huang, Y.; Duan, X. Graphene nanomesh. *Nature Nanotechnol* **2010**, *5*, 190-194.

16. Zhang, Y.*et al.* Direct observation of a widely tunable bandgap in bilayer graphene. *Nature* **2009**, *459*, 820-823.

17. Schedin, F.*et al.* Detection of individual gas molecules adsorbed on graphene. *Nature Mater.* **2007**, *6*, 652-655.

18. Sun, Z.; Kohama, S.; Zhang, Z.; Lomeda, J. R.; Tour, J. M. Soluble graphene through edge-selective functionalization. *Nano Research* **2010**, *3*, 117-125.

19. Lim, H.; Lee, J. S.; Shin, H. J.; Shin, H. S.; Choi, H. C. Spatially resolved spontaneous reactivity of diazonium salt on edge and basal plane of graphene without surfactant and its doping effect. *Langmuir* **2010**, *26*, 12278-12284.

20. Dragoman, D.; Dragoman, M. Giant thermoelectric effect in graphene. *Appl. Phys. Lett.* **2007**, *91*, 203116.

21. Zhang, J.; Wang, Z. L.; Liu, J.; Chen, S.; Liu, G. Y. *Self-assembled Nanostructures* Kluwer Academia/Plenum, NewYork, NY **2003**.

22. Singh, A. K.; Penev, E. S.; Yakobson, B. I. Vacancy cluster in graphane as quantum dots. *ACS Nano* **2010**, ***4***, 3510-3514.

23. Yang, R.*et al.* An anisotropic etching effect in the graphene basal plane. *Adv. Mater.* **2010**, *22*, 4014-4019.

24. Treossi, E*et al.* High-contrast visualization of graphene oxide on dye-sensitized glass, quartz, and silicon by fluorescence quenching. *J. Am. Chem. Soc.* **2009**, *131*, 15576-15577.

25. Gates, B. D.*et al.* New approaches to nanofabrication: Molding, printing, and other techniques. *Chem. Rev.* **2005**, *105*, 1171-1196.

26. Stewart, M. P.*et al.* Direct covalent grafting of conjugated molecules onto Si, GaAs, and Pd surfaces from aryldiazonium salts. *J. Am. Chem. Soc.* **2004**, *126*, 370-378.

27. Boukhvalov, D. W.; Katsnelson, M. I. Enhancement of chemical activity in corrugated graphene. *J. Phys. Chem. C.* **2009**, *113*, 14176-14178.

28. Boukhvalov, D. W.; Katsnelson, M. I. Chemical functionalization of graphene with defects. *Nano Lett.* **2008**, *8*, 4373-4379.

Chapter 7

MANIPULATION OF GRAPHENE'S ELECTRONIC PROPERTIES THROUGH PLACEMENT ON SELF-ASSEMBLED MONOLAYERS

7.1. Introduction

In previous chapters, doped graphene was synthesized through direct substitution of C atoms with heteroatoms such as N, which endows graphene with n-type behavior. In this chapter, non-substitutional doping of graphene is investigated through assembly chemistry. Normally, physical absorbed dopants are volatile, therefore could not consistently manipulate the electronic structure of graphene. In order to overcome this, self-assembled monolayers (SAMs) of aminopropyl-, ammoniumpropyl-, butyl-, and 1*H*,1*H*,2*H*,2*H*-perfluorooctyltriethoxysilanes were covalently deposited in-between graphene and

the SiO_2 substrate. A controlled doping of graphene was realized with a threshold voltage ranging from -18 V to 30 V. In addition, the SAMs are covalently bonded to the SiO_2 surface rather than the graphene surface, thereby producing minimal effects on the mobility of the graphene. Finally, it is more stable than conventional non-covalent dopants.

Since its first isolation in 2004, graphene, has attracted enormous attention for its excellent electronic properties[1-4]. In particular, its extremely high mobility and potential for use in top-down fabrication of electronic devices has made it a promising candidate for high frequency transistors[5-6]. Pristine graphene exhibits a standard ambipolar behavior with a zero neutrality point in field-effect transistors (FETs) on standard SiO_2 substrates, and the ambipolar properties limit its electronics applications. In this regard, many efforts have been made to modify the electronic structure of graphene to make n- and p-type FETs[7-17]. Present doping methods either suppress graphene's mobility or are not stable long-term[9-17]. Thereafter, for both pristine graphene and doped graphene, different methods to produce high quality, monolayer graphene films have been disclosed[17-19]. Similar to the use of silicon in the semiconductor industry, doping and controlling the electrical structure of graphene has become important if it is to be used in place of or in addition to silicon. Direct substitution with boron and nitrogen in the graphene lattice can lead to p- and n-type doping, respectively[14-17]. However heteroatom substitutions break the symmetrical structure of the graphene lattice and lead to a 10—100-fold decrease in graphene's carrier motilities[14-17]. Other methods include physically or chemically doping graphene with small molecules[10-13]. Physically

adsorbed molecules are not stable and are easily desorbed under vacuum or heat, while chemically functionalization suppresses the mobility of graphene due to the newly formed sp^3 C-C bonds.

The transport behaviors of graphene transistors can be significantly affected by the substrates used in making the devices. It is known that graphene FET devices on SiO_2 substrates have lower carrier mobility than suspended devices or devices on boron nitride substrates[20-21]. In both cases, the research was focused on graphene's mobility. The use of self-assembled monolayers (SAMs) is a technique well-known for modification of surfaces including SiO_2[22-31]. The use of SAMs has made a significant impact on the electrical properties of organic thin film transistors (TFTs) and single-walled carbon nanotube (SWCNT) field effect transistors.[22-26] However, limited research has been done to provide controllable doping, both n-type and p-type, in graphene FET devices by functionalizing the SiO_2 substrates with SAMs[28].

In this chapter, the electrical transport behavior of graphene transistors was investigated after the modification of the SiO_2 substrates with alkyltriethoxysilane-based SAMs. The threshhold voltage shift (V_{th}), which directly corresponds to the neutrality point in graphene FET devices, can be systematically controlled. Both n-type and p-type FET behaviors have been demonstrated through this technique. Additionally, the SAM-induced doping has a limited impact on graphene's mobility and the SAMs remain stable even in vacuum.

7.2. Pristine Graphene

Before we investigate the doping effect of graphene, its pristine form has to be confirmed. If the graphene is already doped, either substitutionally or un-substitutionally, its electronic behavior will be too complex to be predicted. In our study, the graphene film was grown using a solid carbon source[17]. That it was monolayer graphene was confirmed by both Raman spectroscopy and high resolution transmission electron microscopy (HRTEM) (Fig. 7.1a, b). The sharp 2D peak in the Raman spectrum at 2690 cm^{-1} has a full width half maximum (FWHM) of ~ 30 cm^{-1} and the I_{2D}/I_G ratio is about 3, hence indicative of a typical monolayer graphene. The hexagonal fast Fourier transform (FFT) pattern for the HRTEM image suggests the graphene film is highly crystalline with few defects, a finding which correlates with the presence of the small D peak (1350 cm^{-1}) in the Raman spectrum. A highly doped Si substrate (ρ = 0.005 Ohm-cm) capped with a 100 nm thick SiO_2 layer was used for the back gated graphene FETs and a SEM of the as-made device is shown in Fig. 7.1c. The source and drain electrodes (30 nm thick Pt) were defined by conventional electron-beam lithography and lift-off processes on the graphene devices. Graphene stripes (5 μm wide) were further defined by oxygen-plasma etching. Fig.7.1d shows the I_{ds}/V_g curve of the control sample, which exhibits a weak p-type behavior due to the unintentional doping induced by water, oxygen or other species adsorbed from the atmosphere.

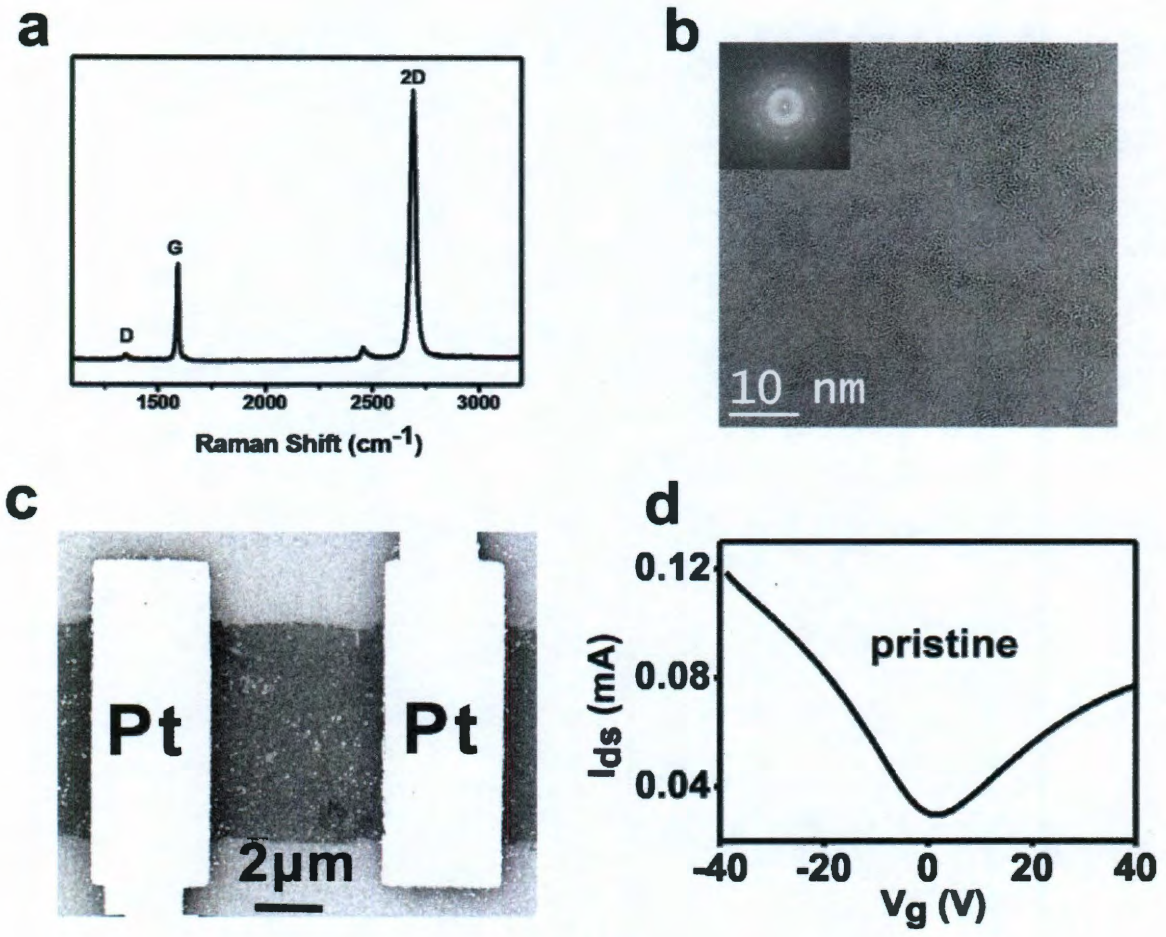

Fig. 7.1 Characterisitics of pristine graphene. (a) Raman spectrum (laser 514 nm) of a monolayer graphene film transferred on a SiO_2/Si substrate. (b) HRTEM images of a suspended graphene film onto a TEM grid. Inset is the hexagonal FFT pattern of the image, which indicates the single-crystalline structure of the graphene. (c) SEM image of a graphene-based FET device (4 μm × 5 μm (L × W)) atop a 100 nm SiO_2/Si wafer with 30 nm Pt as the source and drain electrodes. (d) The FET *I-V* curve of pristine graphene on untreated SiO_2/Si substrate (I_{ds} = 100 mV).

7.3. SAMs on SiO2 Substrate

Three alkyltriethoxysilane compounds were used to prepare SAMs on the SiO_2 and four different SAM films were ultimately prepared. The alkyltriethoxylsilanes used to prepare the SAMs were: 1*H*,1*H*,2*H*,2*H*-perfluorooctyltriethoxysilane, (F-SAMs); butyltriethoxysilane, (CH_3-SAMs); 3-aminopropyltriethoxysilane (H_2N-SAMs); and the protonated form produced from the H_2N-SAMs, H_3N^+-SAMs. The detailed processes to prepare and characterize the SAMs films on SiO_2 are listed below.

SiO_2 substrate cleaning. Prior to the transferring of graphene, the SiO_2 surface underwent a hydrophilic treatment by oxygen-plasma etching for 10 min followed by immersion in piranha solution (3:1 sulfuric acid to hydrogen peroxide) for 30 min. SiO_2 surfaces were thoroughly cleaned with DI water and were dried by nitrogen flow.

H_2N-SAMs. The process was as follows: (1) the cleaned silicon wafers were placed in sealed vials, which were backfilled with nitrogen through a septum; (2) the 3-aminopropyltriethoxysilane (1 mL) was added to the sealed vials followed by the addition of anhydrous toluene (2 mL) to form a 33% solution of 3-aminopropyltriethoxysilane in toluene by volume; (3) the silicon wafers were kept in the vials for 1 h at 75 °C; (3) the silicon wafers functionalized with the H_2N-SAMs were washed with toluene, followed by methanol and DI water; (4) the functionalized silicon wafers were immersed in DI water for 24 h at room temperature to complete the hydrolysis of residual ethoxy groups; (5) the

functionalized silicon wafers were placed in aqueous NaOH (~0.01 mM) at pH 9 for 30 s to remove any adsorbed CO_2; (6) the functionalized wafers were further cleaned by rinsing with DI water; and (7) the functionalized wafers were dried with nitrogen.

H_3N^+-SAMs. The protonated SAMs were prepared by submersion of the H_2N-SAMs in 1 M H_2SO_4 solution for 24 h followed by rinsing with DI water.

F-SAMs and CH_3-SAMs. The process for functionalizing the silicon wafers with F- or CH_3-SAMs was similar, as follows: (1) the cleaned wafers were placed in a 65 cm^3 vessel with a glass container filled with ca. 0.2 cm^3 of *1H,1H,2H,2H*-perfluorooctyltriethoxysilane or butyltriethoxysilane; (2) the vessel was sealed with a cap and heated in an oven at 120 °C for 2 h; (3) after cooling to room temperature, the functionalized wafers were removed from the deposition chamber and were washed with toluene, followed by methanol and DI water; and (4) the functionalized wafers were dried with nitrogen.

In Fig. 7.2, both XPS and water contact angle measurements support the conclusion that the SAMs were successfully prepared on SiO_2. Fig. 7.2a and 7.2b demonstrates the F1s and C1s high-resolution spectra of the F- and CH_3-SAMs, respectively, which agree well with the reported values[27]. Fig. 7.2c displays the N1s high-resolution spectra for the H_2N-SAMs. The N1s peak in Fig. 7.2c can be fitted with two components centered at 399.1 (90%) and 401.5 eV (10%), which can be assigned to the free amine (H_2N-) and the ammonia cation (H_3N-$^+$), respectively.[31] The H_3N^+-SAMs were obtained through protonation of the H_2N-SAMs with 1.0 M

sulfuric acid for 24 h. The H_3N^+-SAMs XPS spectrum (Fig. 7.2d) displays a large contribution of the ammonia cation (90%) and only a small portion of the free amine (10%).

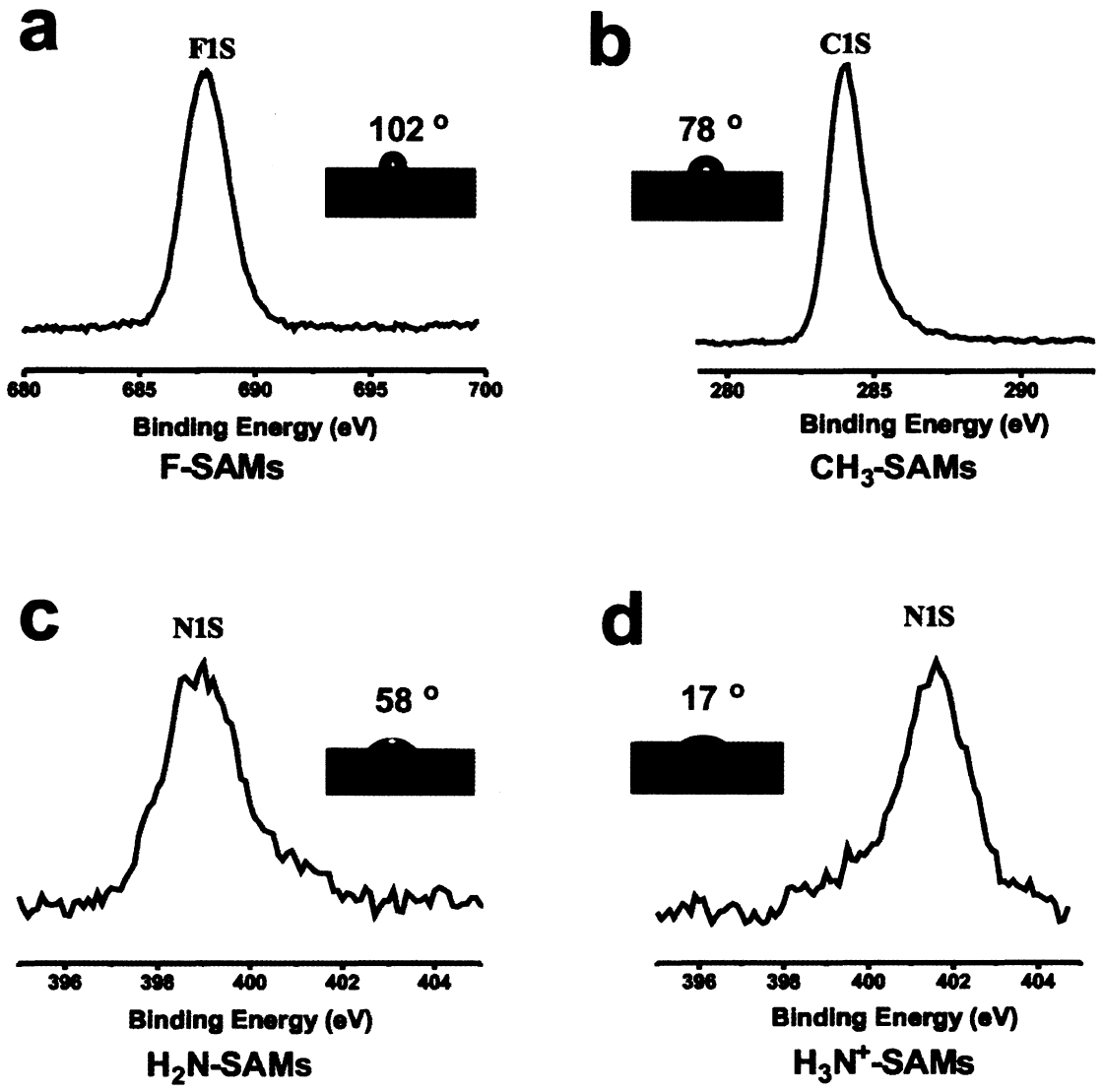

Fig. 7.2 Characteristics of SAM films. (a) XPS analysis from the F1s peak (688 eV) and the water contact angle of F-SAMs film (102°). (b) XPS analysis of the C1s peak (284.5 eV) and the water contact angle of CH_3-SAMs film (78°). (c) XPS analysis

from the N1s peak (398.8 eV) and the water contact angle of H_2N-SAMs film (58°). (d) XPS analysis of the N1s peak (401.8 eV) and the water contact angle of H_3N^+-SAMs film (17°). No F1s, C1s or N1s peaks were observed for the untreated substrate.

The thicknesses of the SAM films were determined by ellipsometry and the values are listed in Table 7.1. All four SAM films showed an average thickness ~ 1 nm, implying a monolayer level coverage[22-23,27].

Table 7.1. Summary of Characterization Data on SAMs in the Study

	End group	**CF_3**	**CH_3**	**H_2N**	**H_3N^+**
SAMs thickness (Å)	Present results	11.1	6.2	10	11
	Calculated results	10.6[27]	5.3[23]	5.5[22]	n/a
Water contact angle (°)	Present Results	102	78	58	17
	Reported results	105[27]	75[23]	60[29]	n/a

7.4. Doping from Modified Substrates

After forming the SAMs, graphene films were transferred to the SAMs/SiO_2/Si substrates and made into FET devices. Fig. 7.3 shows a schematic

structure of the completed devices, where the SAM layers are in-between the graphene and SiO_2 and directly bonded to the SiO_2 substrates.

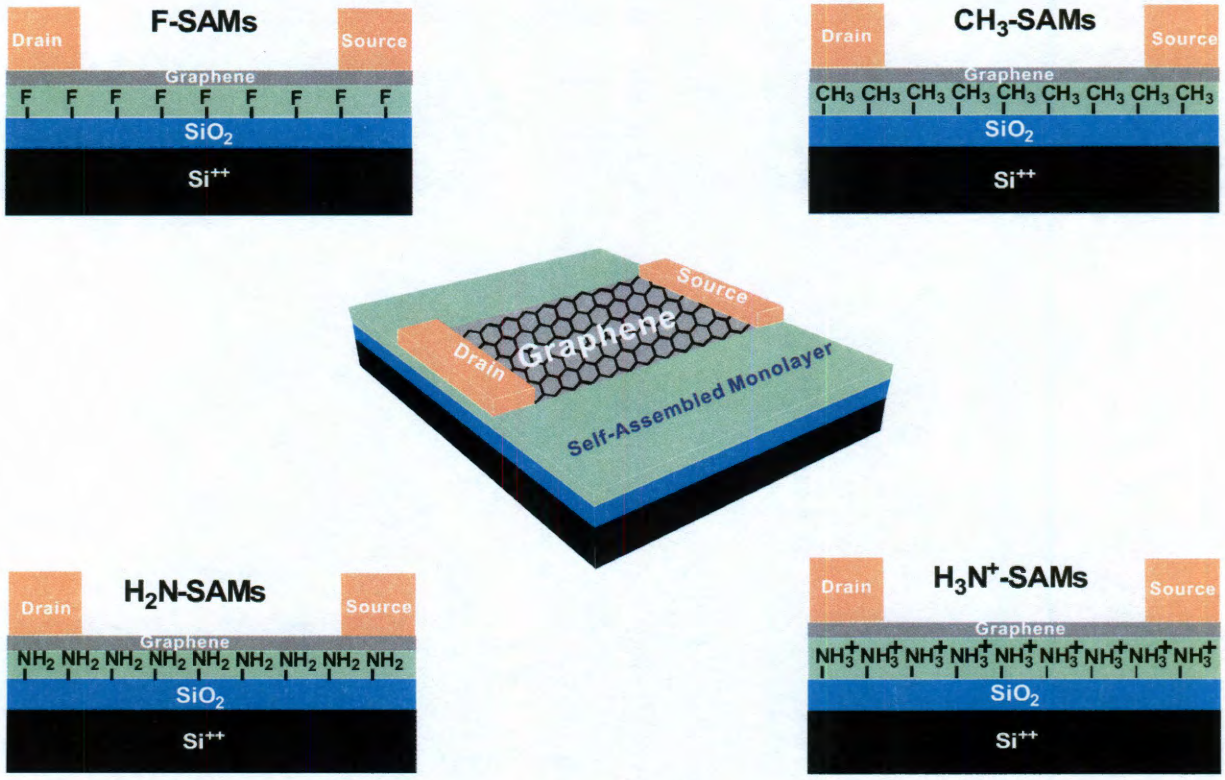

Fig. 7.3. Schematic diagram of the graphene FET devices fabricated in this study.

To determine the doping effects of the SAMs, the transport properties of the graphene FETs on different SAMs were measured in vacuum (Fig. 7.4). For the graphene FET device made atop F-SAMs, the most positive V_{th} shift was observed (~ +30 V, Fig. 4a), while only ~ -8 V V_{th} shift (Fig. 7.4b) was observed for the device made on CH_3-SAMs, indicating butyl groups lead to a weak n-doping effect in the graphene FET devices. For the device fabricated on H_2N-SAMs, the V_{th} is downshifted to ~ -18 V (Fig. 7.4c), suggesting that aminopropyl SAMs have a relative strong n-doping in the graphene FET device. Compared to H_2N-SAMs, the

opposite doping effect is shown in Fig. 7.4d on H_3N^+-SAMs supported devices, with a V_{th} upshifted to ~ +20 V. With the four different SAMs, a wide range of V_{th} values have been obtained, from -18 V (H_2N-SAMs, n-doping) to +30 V (F-SAMs, p-doping). For each SAM films, more than five devices were fabricated and similar results were observed for each set (standard deviation < 3).

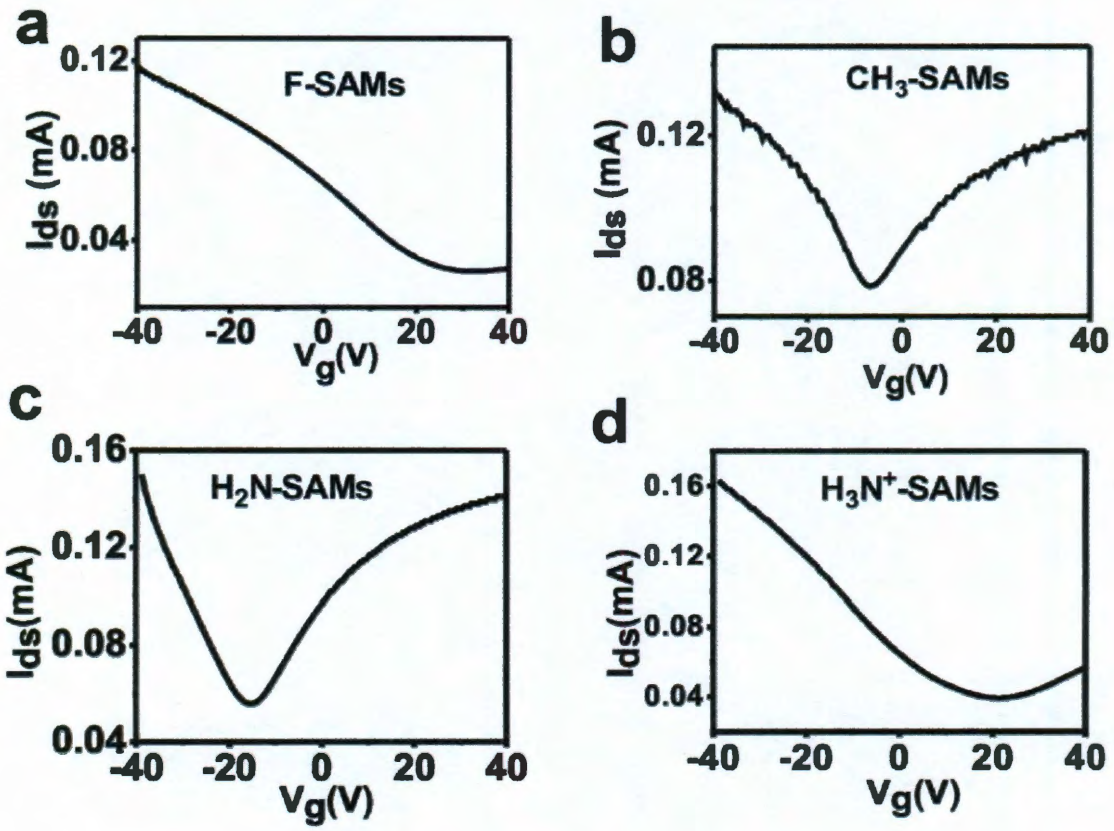

Fig. 7.4. I_{ds}/V_g characteristics of graphene based FET devices on different SAMs. Room temperature I_{ds}-V_g curves of the FET devices fabricated on (a) F-SAMs, (b) CH_3-SAMs, (c) H_2N-SAMs and (d) H_3N^+-SAMs at V_{ds} = 100 mV.

The observed systematic doping can be explained by built-in electric dipoles and the charge transfer between SAMs and the graphene channels. The dipole

alignment of the SAM molecules is thought to produce a built-in electric field and modify the carrier density of organic field-effect transistors[22, 24]. The theoretical model works well in explaining CH_3- and F-SAMs induced doping in graphene transistors. The dipoles of molecules similar to F-SAMs and CH_3-SAMs have been calculated by Kobayashi *et al.* using density function theory (DFT) [22]. The dipole moments along the molecular axes were computed as -2.202 and 0.831 Debye for F-SAM and CH_3-SAM, respectively. The built-in electric field inside the SAMs can be estimated by $E = N(\mu/d\varepsilon\varepsilon_0)$ [22,32], where N is the molecular density, d is the length of the SAM molecule, ε is the effective dielectric constant inside the SAM molecules and ε_0 is the permittivity of free space. For the SAMs in this study, N is about $1 - 2 \times 10^{14}$ cm^{-2}, $d_{F\text{-}SAMs}$ is 1.1 nm, $d_{CH3\text{-}SAMs}$ is 0.6 nm and ε is between 2 and 3[22]. According to the above formula, the calculated electric fields inside the SAMS are $E_{F\text{-}SAMs} = -(2.5$ to 7.4) MV/cm and $E_{CH3\text{-}SAMs} = 0.94$ to 2.8 MV/cm. To produce the same electric field by applying a voltage across the 100-nm-thick SiO_2 gate insulator, a gate voltage of 25 - 74 V for F-SAMs and $-(9.4$ to 28) V for CH_3-SAMs is necessary, which agrees well with the shifts in electrical transport characteristics observed in our devices (Table 7.2).

Table 7.2. Threshold Voltage V_{th} and Field-Effect Mobility μ Determined in the Study

End group	H_2N	CH_3	Untreated	H_3N^+	CF_3
V_{th} (V)	-18	-8	4	20	30
μ ($cm^2V^{-1}s^{-1}$)	661	460	449	363	450

However, since the amine group bears a lone pair of electrons and the ammonium group is positive charged, H_2N-SAMs and H_3N^+-SAMs induced doping in graphene transistors cannot be understood simply by using the built-in electric field model. Dai *et. al.* have discussed the possible charge transfer mechanism between carbon nanotubes and aminopropyltriethoxysilane molecules[35]. A charge transfer mechanism was also proposed to explain small molecule-induced doping[33]. The amine group in H_2N-SAMs can donate its lone pair to graphene's channel, increasing electron carrier density and inducing n-doping. In H_3N^+-SAMs, the lone pairs are occupied by H^+. The ammonium cations in H_3N^+-SAMs are positively charged, which is anticipated to withdraw electrons from graphene channel, decreasing electron carrier density and inducing hole doping.

In order to define the impact of the SAMs on graphene's mobility, field-effect mobilities were extracted from the I_{ds}/V_g curves using the following formula: $\mu = [(\Delta I_{ds}/V_{ds})(L/W)]/C_{ox}\Delta V_g$[34]. The calculated data are summarized in Table 7.2. Of particular interest, the carrier mobilities of transistors on SAMs are of the same order of magnitude as transistors fabricated on untreated SiO_2 substrates. SAM doping arises from electric dipoles and charge transfer which do not introduce more scattering centers into the graphene lattice than into the bare SiO_2 substrates, therefore having limited effects on the mobilities. In addition, unlike small molecule doping that is caused by physisorption on the graphene plane[10-13], SAMs are covalently attached to the SiO_2 surface and cannot be cleaved even in vacuum. Two SAM doping cases, H_2N-SAMs and F-SAMs were tested under vacuum. After keeping the samples under vacuum (10^{-6} Torr) for 7 d, only a small positive threshold

voltage shift was observed in comparison with that obtained after keeping the samples under vacuum (10^{-6} Torr) for 3 d, which was attributed to the desorption of species adsorbed from the prolonged evauation[17].

7.5. Conclusion

In conclusion, producing stable doping and high mobility is a problem for graphene-based electronics. For such an electrically sensitive material, modulating electrical characteristics of the substrate controls the electrical characteristics of the device. By adapting the SAM techniques, systematic modulation of graphene's electronic properties becomes available without affecting its mobility. A wide doping range has been achieved with hundreds of SAMs hitherto unexplored. This technique provides a simple solution for the development of more controllable graphene devices.

Author Contributions:

Zheng Yan discovered the method, performed the wet chemistry and most of the characterization. Z.S. helped to design the experiments, performed the spectroscopic characterizations and analysis.

References

1. Novoselov, K. S.; Geim, A. K.; Morozov, S. V.; Jiang, D.; Zhang, Y.; Dubonos, S. V.; Grigorieva, I. V.; Firsov. A. A. Electric Field Effect in Atomically Thin Carbon Films. *Science* **2004**, *306*, 666-669.
2. Geim, A. K.; Novoselov, K. S. The Rise of Graphene. *Nature Mater.* **2007**, *3*, 183-191.
3. Novoselov, K. S.; Geim, A. K.; Morozov, S. V.; Jiang, D.; Katsnelson, M. I.; Grigorieva, I. V.; Dubonos, S. V.; Firsov. A. A. Two-dimensional Gas of Massless Dirac Fermions in Graphene. *Nature* **2005**, *438*, 197-200.
4. Ruoff, R. S. Graphene: Calling All Chemists. *Nature Nanotech.* **2008**, *3*, 10-11.
5. Lin, Y. M.; Dimitrakopoulos, C.; Jenkins, K. A.; Farmer, D.B.; Chiu, H. Y.; Grill, A.; Avouris, Ph. 100-GHz Transistors From Wafer-Scale Epitaxial Graphene. *Science* **2010**, *327*, 662.
6. Liang, X.; Jung, Y.; Wu, S.; Ismach, A.; Olynick, D.; Cabrini, S.; Bokor, J. Formation of Bandgap and Subbands in Graphene Nanomeshes with Sub-10nm Ribbon Width Fabricated via Nanoimprint Lithography. *Nano Lett.* **2010**, *10*, 2454-2460.
7. Wang, X.; Li, X.; Zhang, L.; Yoon, Y.; Weber, W.; Wang, H.; Guo, J.; Dai, H. N-doping of Graphene Through Electrothermal Reactions with Ammonia. *Science* **2009**, *324*, 768-771.
8. Li, X.; Wang, H.; Robinson, J.; Sanchez, H.; Diankov, G, Dai, H. Simultaneous Nitrogen Doping and Reduction of Graphene Oxide. *J. Am. Chem. Soc.* **2009**, *131*, 15939-15944.
9. Farmer, D. B.; Golizadeh-Mojarad, R.; Perebeinos, V.; Lin, Y.; Tulevski, G.; Tsang, J.;

Avouris, P. Chemical Doping and Electron-Hole Conduction Asymmetry in Graphene Devices. *Nano Lett.* **2009**, *9*, 388-392.

10. Das, B.; Voggu, R.; Rout, C.; Rao, C. N. R. Changes in the Electronic Structure and Properties of Graphene Induced by Molecular Charge-Transfer. *Chem. Commun.* **2008**, 5155-5157.
11. Gierz. I.; Riedl, C.; Starke, U.; Ast, C.; Kern, K. Atomic Hole Doping of Graphene. *Nano Lett.* **2008**, *8*, 4603-4607.
12. Chen, J. H.; Jang, C.; Adam, S.; Fuhrer, M. S.; Williams, E. D.; Ishigami, M. Charged-Impurity Scattering in Graphene. *Nature Physics.* **2008**, *4*, 377-381.
13. Dong, X.; Fu, D.; Fang, W.; Shi, Y.; Chen, P.; Li, L. Doping Single-Layer Graphene with Aromatic Molecules. *Small.* **2009**, *5*, 1422-1426.
14. Guo, B.; Liu, Q; Chen, E.; Zhu, H.; Fang, L.; Gong, J. Controllable N-Doping of Graphene. *Nano Lett.* **2010**, *10*, 4975- 4980.
15. Wei, D.; Liu, Y.; Wang, Y.; Zhang, H.; Huang, L.; Yu, G. Synthesis of N-Doped Graphene by Chemical Vapor Deposition and Its Electrical properties. *Nano Lett.* **2009**, *9,* 1752-1758.
16. Panchakarla. L. S.; Subrahmanyam, K. S.; Saha, S. K.; Govindaraj, A.; Krishnamurthy, H. R.; Waghmare, U. V.; Rao, C. N. R. Synthesis, Structure, and Properties of Boron- and Nitrogen- Doped Graphene. *Adv. Mater.* **2009**, *21*, 4726-4730.
17. Sun, Z.; Yan, Z.; Beitler, E.; Zhu, Y.; Tour, J. Growth of Graphene From Solid Carbon Sources. *Nature 2010, 468, 549-552.*
18. Li, X.; Cai, W.; An, J.; Kim, S.; Nah, J.; Yang, D.; Piner, R.; Velamakanni, A.; Jung, I.;

Tutuc, E.; Banerjee, S.; Colombo, L.; Ruoff, R. Large-Area Synthesis of High-Quality and Uniform Graphene Films on Copper Foils. *Science* **2009**, *324*, 1312-1314.

19. Kim, K. S.; Zhao, Y.; Jang, H.; Lee, S.; Kim, J.; Kim, K.; Ahn, J.; Kim, P.; Choi, J.; Hong, B. Large-Scale Pattern Growth of Graphene Films for Stretchable Transparent Electrodes. *Nature* **2009**, *45*, 706-710.
20. Dean, C. R.; Young, A. F.; Meric, I.; Lee, C.; Wang, L.; Sorgenfrei, S.; Watanabe, K.; Taniguchi, T.; Kim, P.; Shepard, K. L.; Hone, J. Boron Nitride Substrates for High-Quality Graphene Electronics. *Nature Nanotech.* **2010**, *5*, 722-726.
21. Du, X.; Skachko, I.; Barker, A.; Andrei, B. Approaching Ballistic Transport in Suspended Graphene. *Nature Nanotech.* **2008**, *3*, 491-495.
22. Kobayashi, S.; Nishikawa, T.; Takenobu, T.; Mori, S.; Shimoda, T.; Mitani, T.; Shimotani, H.; Yoshimoto, N.; Ogawa, S.; Iwasa, Y. Control of Carrier Density by Self-Assembled Monolayers in Organic Field-Effect Transistors. *Nature Mater.* **2004**, *3*, 317-322.
23. Ito, Y.; Virkar, A.; Mannsfeld, S.; Oh, J.; Toney, M.; Locklin, J.; Bao Z. Crystalline Ultrasmooth Self-Assembled Monolayers of Alkylsilanes for Organic-Field-Effect Transistors. *J. Am. Chem. Soc.* **2009**, *131*, 9396-9404.
24. Pernstich. K. P.; Haas, S.; Oberhoff, D.; Goldmann, C.; Gundlach, D. J.; Batlogg, B.; Schitter, G. Threshold Voltage Shift in Organic Field Effect Transistors by Dipole Monolayers on the Gate Insulator. *J. Appl. Phys.* 2004, *96*, 6431-6438.
25. Possanner, S. K.; Karin, Z.; Peter, P.; Egbert, Z.; Ferdinand, S. Threshold Voltage Shifts in Organic Thin-Film Transistors Due to Self-Assembled Monolayers at the

Dielectric Surface. *Adv. Funct. Mater.* 2009, *19*, 958-967.

26. Vosgueritchian. M.; Lemieux, M.; Dodge, D.; Bao, Z. Effect of Surface Chemistry on Electronic Properties of Carbon Nanotube Network thin Film Transistors. *ACS Nano* 2010, *4*, 6137-6145.
27. Hozumi, A.; Ushiyama, K.; Sugimura, H.; Takai, O. Fluoroalkylsilane Monolayers Formed by Chemical Vapor Surface Modification on Hydroxylated Oxide Surfaces. *Langmuir* **1999**, *15*, 7600–7604.
28. Wang, R.; Wang, S.; Zhang, D.; Li, Z.; Fang, Y.; Qiu, X. Control of Carrier Type and Density in Exfoliated Graphene by Interface. *ACS Nano* DOI: 10.1021/nn102236x.
29. Hozumi, A.; Yokogawa, Y.; Kameyama, T.; Sugimura, H.; Hayashi, K.; Shirayama, K.; Takai, O. Amino-Terminated Self-Assembled Monolayer on a SiO_2 Surface Formed by Chemical Vapor Deposition. *J. Vac. Sci. Technol. A* **2001**, *19*, 1812–1816.
30. Howarter, J. A.; Youngblood, J. Optimization of Silica Silanization by 3-Aminopropyltriethoxysilane. *Langmuir* **2006**, *22*, 11142-11147.
31. Lee, S.; Lin, W.; Kuo, C.; Karakachian, M.; Lin, Y.; Yu, B.; Shyue, J. Photooxidation of Amine-Terminated Self-Assembled Monolayers on Gold. *J. Phys. Chem. C* **2010**, *114*, 10512-10519.
32. Gonen, A.; Cahen, D.; Cohen, R.; Shanzer, A.; Vilan, A. Molecular Engineering of Semiconductor Surfaces and Devices. *Acc. Chem. Res.* **2002**, *35*, 121-128.
33. Rao, C. N. R.; Sood, A. k.; Subrahmanyam, K. S.; Govindaraj, A. Graphene: the New Two-Dimensional Nanomaterial. *Angew. Chem. Int. Ed.* **2009**, *48*, 7752-7777.
34. Wu, Y. Q.; Ye, P. D.; Capano, M. A.; Xuan, Y.; Sui, Y.; Qi, M.; Copper, J. A. Top-Gated

Graphene Field-Effect-Transistors Formed by Decomposition of SiC. *Appl. Phys. Lett.* **2008**, *92*, 092102.

35. Shim, M.; Javey, A.; Kam, N; Dai, H. et al. Polymer Functionalization for Air-Stable N-Type Carbon Nanotube Field-Effect Transistors. *J. Am. Chem. Soc.* **2001**, *123*, 11512-11513.

Chapter 8

GRAPHENE BIOCOMPATIBILITY

8.1. Introduction

Graphene oxides (GOs) are layered, oxygenated graphene sheets with epoxide, carboxyl and hydroxyl groups on their basal planes and edges. Although traditionally seen as a precursor to large-scale graphene synthesis[1], GO has recently received more attention for its other possible uses[2,3]. GOs are being promoted as useful compounds for incorporation into polymers, ceramics and metals[4-9], as novel forms of thin film electronic materials[10-13], as potential chemotherapeutic delivery vehicles[14,15], as antibiotics[16], for hydrogen storage compositions[17] and for enhanced oil recovery[18,19]; the latter being where larger volumes would enter the environment. Given the wide-ranging applications for this material, it is likely to enter into large-scale production[18,19]. Inevitably, this will lead to the introduction of GO into environmental systems and interfere with the existing ecosystem. Thus, it is

important to understand whether there is a natural and rapid route for its conversion to graphite, the layered stacks of graphene that can form after the reduction of GO. Graphite is a naturally occurring mineral that is already used abundantly and poses no threat to the environment. Towards this end, we have conducted laboratory studies to assess the interactions between GO and model environmental microbes from the genus *Shewanella*.

Shewanella comprise a group of heterotrophic, facultative anaerobes. They have been found in a wide variety of environments including lake and marine sediments, estuaries, hydrothermal vents, various fish species, oil brines, ocean water, and spoiled foods[20]. These microbes have the ability to use a large array of organic and inorganic compounds as terminal electron acceptors in their respiratory pathway. In addition to oxygen, other electron acceptors available to *Shewanella* include arsenate, chromium oxides, uranium oxides, dimethylsulfoxide, trimethylsulfoxide, iron oxides, manganese oxides, nitrates and silver oxide[21, 22]. With respect to toxic metals such as chromium and uranium, *Shewanella* are able to remove them from solution by reducing them to their insoluble form[21]. These bacteria are known as exoelectrogens[16] because some of these compounds, such as iron oxide, are solids, requiring the bacteria to engage in extracellular electron transfer (EET) [20,21,23].

8.2. Reduction of Graphene Oxide via Bacterial Respiration

The ability of these organisms to use solids as terminal electron acceptors, their capacity to immobilize toxic metals and their environmental ubiquity makes them good candidates to study how microbes might interact with graphitic nanomaterials. Here we present that graphene oxide (GO) can act as a terminal electron acceptor for heterotrophic, metal-reducing, environmental bacteria. The conductance and physical characteristics of bacterially converted graphene (BCG) are comparable to other forms of chemically converted graphene (CCG). Electron transfer to GO is mediated by cytochromes MtrA, MtrB and MtrC/OmcA, while mutants lacking CymA, another cytochrome associated with extracellular electron transfer, retain the ability to reduce GO. Our results demonstrate that biodegradation of GO can occur under ambient conditions and at rapid timescales. The capacity of microbes to degrade GO, restoring it to the naturally occurring ubiquitous graphite mineral form, presents a positive prospect for its bioremediation. This capability also provides an opportunity for further investigation into the application of environmental bacteria in the area of green nanochemistries.

Table 8.1. Bacterial Strains Used in This Study

Strain	Origin
[1]*Shewanella oneidensis* MR-1	Lake Oneida, New York

[1]*Shewanella putrefaciens* CN32	Uranium Mine, New Mexico
[1]*Shewanella amazonensis* SB2B	Amazon River Delta
[1]*Shewanella putrefaciens* W3-18-1	Pacific Ocean Marine Sediments
[2]*Shewanella baltica* 10735^T	Oil-brine, Japan

[1]Bacterial strains provided by the *Shewanella* Federation (www.shewanella.org); [2]Strain provided by Dr. Masataka Satomi, National Research Institute of Fisheries Science (http://nrifs.fra.affrc.go.jp/).

Five strains from this genus were used, representing a variety of ecological habitats (Table 8.1). Reduction was evident at 24 h due to the precipitation of graphene from solution (Fig. 8.1); however, the incubations were allowed to continue for approximately 72 h.

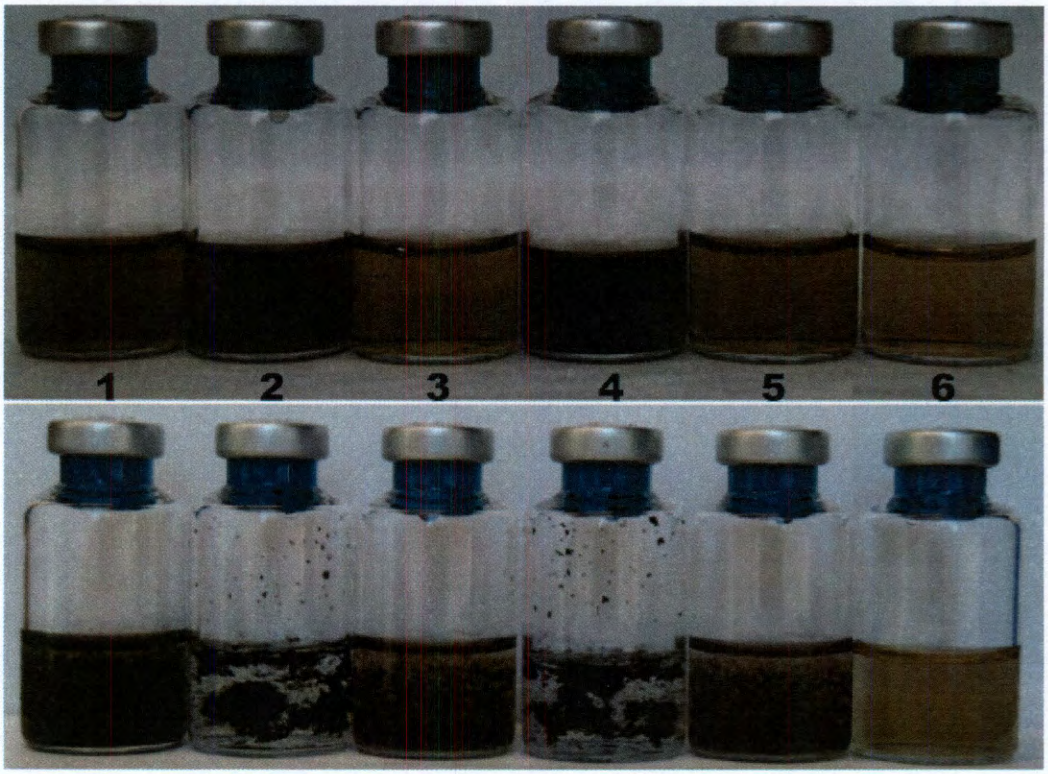

Fig. 8.1. Microbial reduction of GO occurs under ambient conditions. Digital photographs of anaerobic serum bottles containing different strains of *Shewanella* and GO (10 mL solution). 1 = MR-1; 2 = CN32; 3 = SB2B; 4 = W3-18-1; 5 = 10735^{t}; 6 = blank control. The top panel shows the condition of GO after 24 h, while the bottom panel shows conditions after 72 h. The changes in color and solubility of the material in bottles 1 through 5 indicate extensive reduction of GO by bacteria as the initially soluble GO solution forms graphene precipitates upon reduction. Each bottle was photographed individually with a Nikon D40 SLR camera (set to manual focus) under natural lighting, and subsequently combined into one Fig..

X-ray photoelectron spectroscopy (XPS) was used to characterize the GOs before and after incubation with bacteria. The C 1s XPS spectra for GO had peaks at

287 and 288 eV for the C-OH and C=O bonds, respectively. The C-C bond at 284.5 eV was much less prominent. Analysis of these peak intensities indicated that the biologically mediated reduction of GO was extensive (Fig. 8.2).

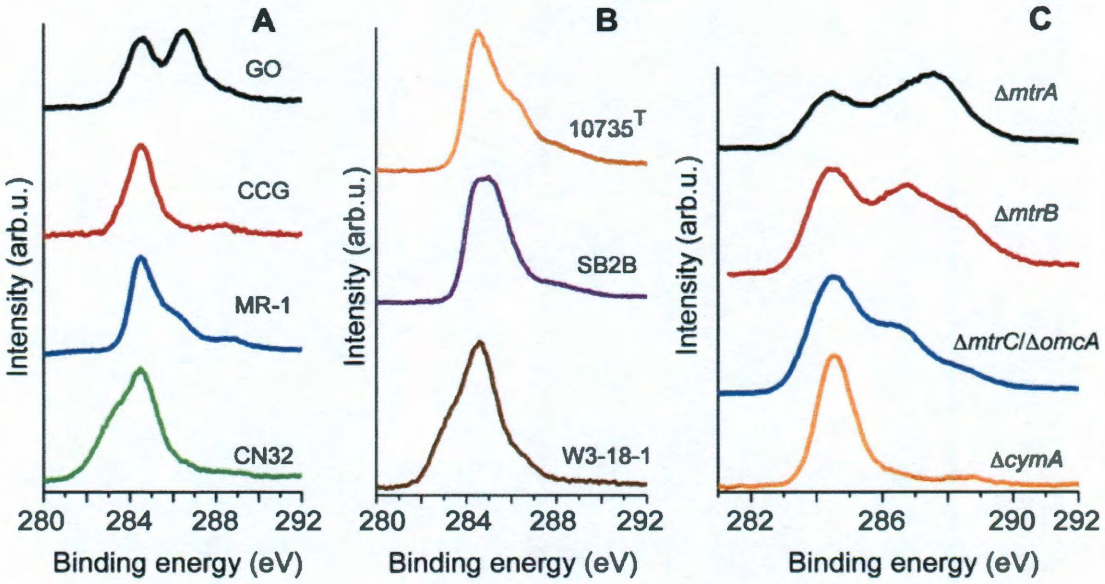

Fig. 8.2. Reduction of GO by bacteria is extensive as observed by XPS. Panels A and B display XPS spectra for BCG produced by various strains of *Shewanella*. GO and CCG are shown in panel A for reference. Panel C displays results from reduction experiments using mutant strains of *S. oneidensis* MR-1. The results in panels A and B demonstrate that in all cases of GO respiration, loss of oxygen is pronounced. The percentage of C-C bonds increases from approximately 28% in GO to 90-95% in the bacterial products. Panel C shows results for deletion mutants of c-cytochromes associated with metal reduction in *S. oneidensis* MR-1. Spectra indicate that MtrA is essential for GO reduction, while CymA is not.

As reported previously[24], after chemical reduction the C-OH and C=O peaks decrease in intensity, and the strongest signal comes from the C-C bond. After incubation with bacteria, this was also the case; as much as 95% of the carbon in the biologically converted graphene (BCG) was in the reduced state and there was no indication of any epoxy or carboxyl groups in the reacted samples (Fig. 8.2, Table 8.2). Not all of the strains tested reduced GO to the same extent (Table 8.2). This variability may be due to the rate at which the GO was reduced, or to the possibility that the test conditions were not optimal for some strains. Work using other solid-phase terminal electron acceptors has shown that *Shewanella* exhibit different rates or respiration[25], and the rates and extent of reduction can vary as a function of medium composition[26]. Among a number of strains, the peak at 287 eV was reduced to a shoulder in the C-C peak, indicating that although reduction did occur, some hydroxyl groups still remained in these samples.

Table 8.2. Fraction of Reduced Carbon in BCG

	%C-C
GO	28
CCG[a]	83
S. oneidensis MR-1	56
S. putrefaciens CN32	91
S. amazonensis SB2B	75

S. sp. W3-18-1	>95
S. baltica 10735^T	54
S. oneidensis MtrA	31
S. oneidensis MtrB	40
S. oneidensis MtrC/OmcA	55
S. oneidensis CymA	81

[a]chemically converted graphene

Observation with transmission electron microscopy (TEM) indicated that the BCG samples had single-layer thickness (Fig. 8.3). The reduced graphene oxide preserves the hexagonal lattice structure from its mother material.

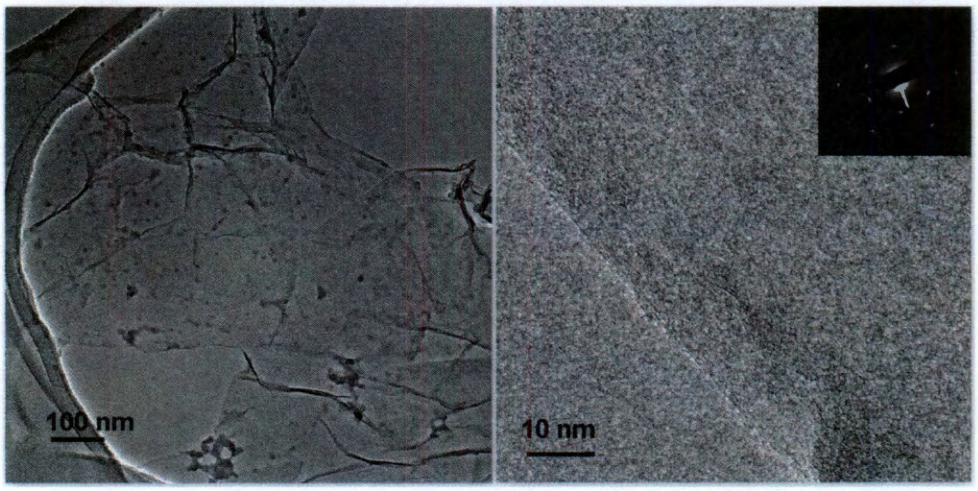

Fig. 8.3. TEM image of bacterially converted graphene. A) Single-layered BCG flakes; B) single-layered BCG edge. The inset in 'B' is the selected area diffraction pattern (SAED) of BCG, showing the material's hexagonal crystalline structure.

S. oneidensis MR-1 was incubated with GO thin films in order to test the capacity of bacteria to reduce GO films deposited on a substrate. The conductance of BCG was observed to increase by 10^3-10^4 over the starting GO material (Fig. 8.4). This is comparable to the conductance of chemically converted graphene (CCG) obtained from chemical reduction of GO[1,27]. Although work done with *S. putrefaciens* CN32 showed no significant difference in conductance when compared with MR-1, the variation in conductance of BCG as a function of bacterial strain is currently under investigation.

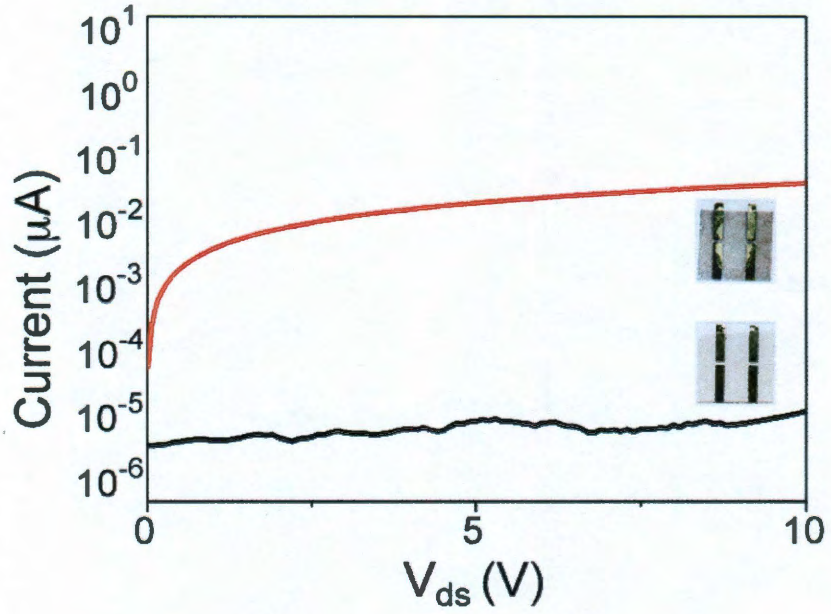

Fig. 8.4. Conductance plots taken of GO films before and after incubation with bacteria demonstrate a decrease in film resistance of up to 10^4. Black = before;

red = after. Reduction is apparent via the darkening in film color (inset where the film is underneath the four electrodes and the before is on the bottom and the after is on the top). The inset was photographed as described in Fig. 8.1.

EET by *S. oneidensis* MR-1 has been attributed to a group of periplasmic (MtrA) outer-membrane (MtrB and MtrC) and inner-membrane (CymA) multihaem *c*-type cytochromes that are common to all *Shewanella* capable of metal reduction[23]. In order to determine their role in reduction of GO, strains of MR-1 deficient in each of these proteins were incubated with GO as the terminal electron acceptor. While *cymA* mutants retained the ability to reduce GO, reduction of GO was greatly inhibited by the loss of the *mtrA* gene, but not as inhibited in *mtrB* and *mtrC/ omcA* mutants (Fig. 8.2C, Table 8.2).

While the CymA protein has been shown to be involved in anaerobic respiration[28], the present work indicates that it is not required for GO reduction. Taken together, these results suggest that in the case of GO reduction, electrons flow from the inner-membrane quinone pool to the periplasmic MtrA protein via a route not involving CymA, and that while MtrB and MtrC/OmcA are involved in GO reduction, other outer-membrane proteins may play a role as well (Fig. 8.2C, Fig. 8.5). Additionally, the extent of GO reduction is variable among the tested strains (Figs. 8.1 and 8.2). The *Shewanella* genome encodes 42 putative c-type cytochromes located throughout the inner-membrane, periplasm and outer-membrane[29]. Further work is needed to understand the EET network used by various *Shewanella* in GO reduction.

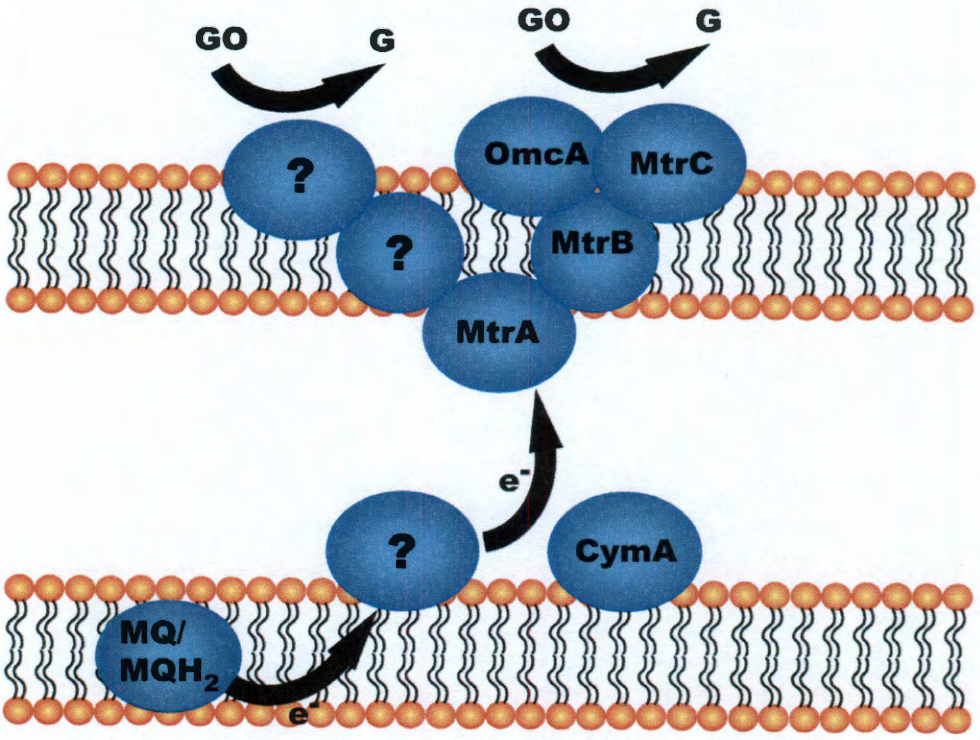

Fig. 8.5. MtrA mediates electron transfer from the inner membrane to the outer membrane in the case of GO reduction. MtrA, MtrB, MtrC and CymA are known to be involved in the reduction of solid materials such as iron oxide and manganese oxide. Work presented here indicates that in the case of GO reduction, *Shewanella* does not use CymA to mediate electron flow from the quinone pool to the periplasmic cytochrome, MtrA. Additionally, other outermembrane cytochromes may be involed in GO reduction.

This study determined the capability of microbes to process functionalized graphene compounds. These results raise not only the possibility of using environmental bacteria to process graphitic nanomaterials for the purpose of bioremediation, but also the potential of using bacteria such as *Shewanella* in green

chemistry approaches to materials synthesis. The development of green chemistries has taken on greater prominence[30], and recent work highlights the attempt to produce graphene using fewer contaminants[27,31]. Exoelectrogens provide the opportunity to investigate how redox-active enzymes might be employed in these efforts. Finally, the results here show promise for some graphitic nanotechnologies to be environmentally benign.

8.3. Materials and Methods

Bacterial cultures. Bacteria were inoculated from frozen stocks into Luria-Bertani (LB) broth and grown overnight at room temperature, shaking at approximately 125 rpm. The overnight cultures were washed in saline solution to remove all traces of LB. Bacteria were inoculated into serum bottles containing 10 mL of *Shewanella* Federation defined medium, with lactate, and 2 mg of GO. Prior to inoculation, the serum bottles (containing medium and GO) were gassed with ultra-pure N_2 to remove traces of oxygen. Final cell concentrations were approximately 10^8 cells/mL. The samples were done in triplicate and incubated in the dark, at room temperature. Mutant strains were prepared in the same fashion as the wild type strains. Negative controls contained all the elements described above, but without bacteria.

Graphene oxide preparation and characterization of bacterially converted graphene. GO was prepared from graphite powder using the method of Hummers and Offeman.[32] The samples, including controls, were collected and

washed using the following sequence: 18 M water (Millipore Milli-Q Gradient), followed by a 3–5 min wash in 80% ethanol, followed by 18 M water, followed by a 3–5 min. wash in 1 N HCl, followed by 18 M water. The samples were then air-dried and analyzed with XPS. Analysis was carried out on a PHI Quantera SXM Scanning X-ray Microprobe with a base pressure of 5×10^{-9} Torr. The X-ray source was an Al cathode ray, set at 100 W and a pass energy of 140.00 eV (survey scan) and 26.00 eV (high-resolution scan) takeoff angle was 45°, and beam size was 100 μm. Quantification of carbon functional groups was based on Yang *et al.*[33], and is summarized as follows: the C1s peak was fitted into 4 peaks. The sp2 C-C peak was assigned at 284.5 eV. Chemical shifts of +1.5, +2.5 and +4.0 eV were assigned to C–OH, C=O, and O=C-OH functional groups, respectively. Additionally, epoxide groups (C-O-C) were assumed to have a C1s binding energy similar to C-OH[34].

GO thin films and conductivity measurements. To test the conductivity of BCG, 3 mL of GO_{aq} (0.5 mg/mL H_2O) was sprayed onto a glass slide. Immediately after application to each slide, the material was dried and annealed on a hot plate at 100 °C. Au was then sputtered into the edges of the slide, atop the GO, to a thickness of 10 nm. The conductance of the GO was determined. The slides were then incubated anaerobically with strain MR-1 for approximately 72 h. After incubation, the slides were collected, washed gently with 18 M water to remove as much biomass as possible and dried thoroughly. The conductance of the BCG was then determined. Conductance was measured with a 2-point probe at room temperature

using an Agilent 4155C semiconductor parameter analyzer under vacuum (10^{-6} Torr).

8.4. Graphene Bioprocessing and Biodegradation

The former sections discussed the bioprocessing of the GO, which suggests that the GO is non-toxic to the *Shewanella* bacteria and can be reduced to graphene through an extracellular electron transfer (EEF) route. In order to investigate the biocompatibility of graphene, CVD monolayer graphene transferred onto glass slides were chosen as substrates for bacteria and fungi incubation. *Shewanella* bacteria and Phanerochaete chrysosporium fungi were incubated on the graphene surface for 2 weeks. Fluorescence quenching microscopy (FQM) mapping was used to evaluate the graphene films after the 2 weeks of bioprocessing. The incubation details were the same as those described in part 8.3. As shown in Fig. 8.6, a graphene film can quench the fluorescence of the dye molecules, while bacteria, fungi and glass slides without graphene coverage will emit fluorescence. For fungi processed graphene in Fig. 8.6a and b, part of the graphene are gone, either because of biodegradation or bio-exfoliation. Considering fungi cells are moving on the graphene surface, the missing graphene could be consumed or metabolized by the fungi. For bacteria processed graphene in Fig. 8.6c and d, a large number of bacteria are found on the graphene surface, suggesting the CVD graphene is non-toxic to this bacteria strain. However, no missing graphene film was detected in the FQM image.

Biodegradation could happen when the bacteria are immobilized on graphene surfaces, where the degraded graphene films are hidden underneath the bacteria.

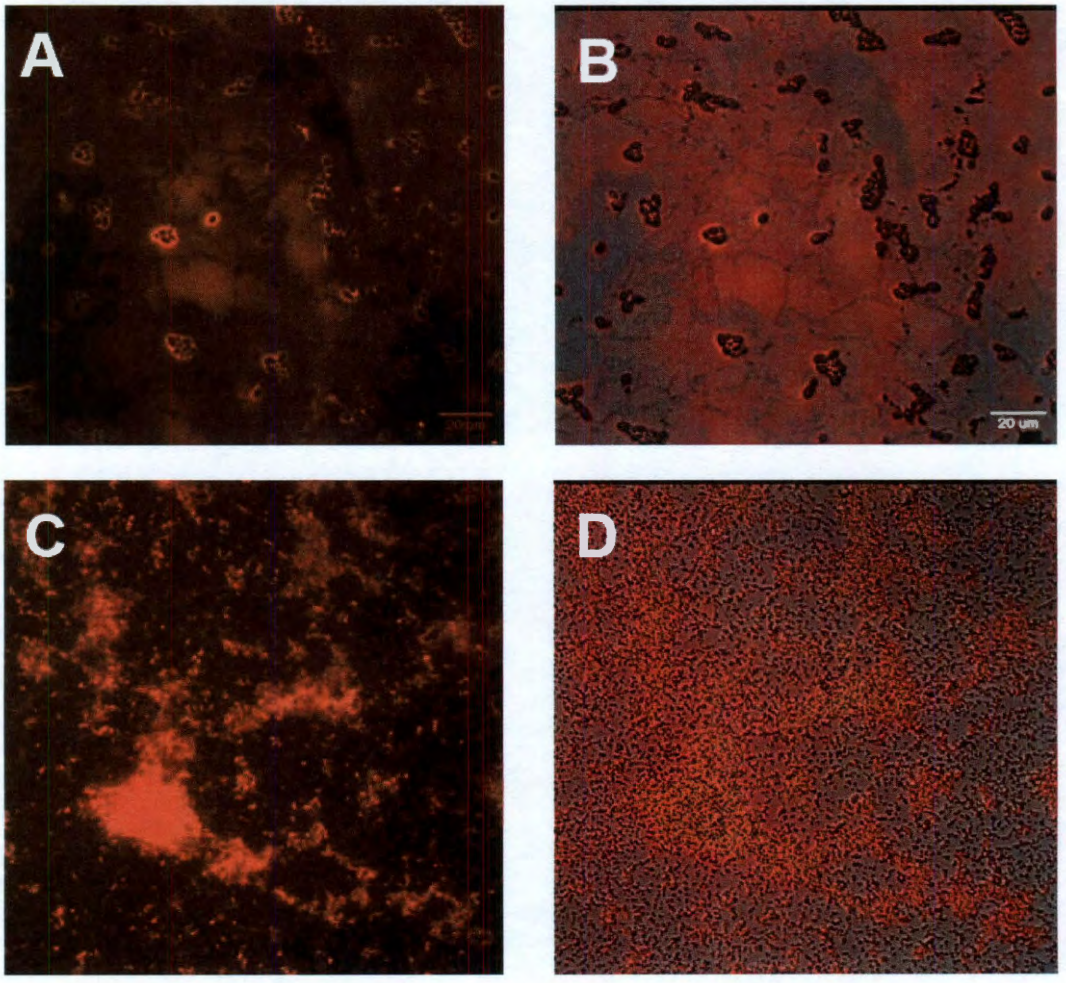

Fig. 8.6 FQM and optical image of fungi processed graphene films (A) and (B), bacteria processed graphene film (C) and (D). (B) and (D) are optical images overlaid with FQM images.

8.5. Perspective of Biodegradation of Carbon Nanomaterials

Graphite is a natural mineral. It has already been widely used by human and it appears to be benign. Its nano-relatives, such as graphene, graphene oxide and CNTs might be thought to inherent part of these characteristics. However, biochemically, these new materials have not been thoroughly investigated and evaluated since they just joined the families of carbon allotropes a short time ago. Our studies show that graphene and GO are non-toxic to both *Shewanella* bacteria and Phanerochaete chrysosporium fungi. In addition, the fungi show some capability to process the graphene films and consume them either by metabolization or physical damage. In order to explore the exact mechanism, carbon isotope labeling experiment is needed in the future.

Author Contributions:

Z.S. performed the material graphene oxide and graphene preparation, spectroscopic characterizations and analysis. Everett C. Salas performed bacteria and fungi incubation experiments. Daniela C. Marcano performed the FQM characterization.

References

1. Gilje, S.; Han, S.; Wang, M.; Wang, K. L.; Kaner, R. B. A chemical route to graphene for device applications. *Nano Lett.* **2007**, *7*, 3394-3398.

2. Geim, A. K. Graphene: status and prospects. *Science* **2009**, *324*, 1530-1534.

3. Rao, C. N. R.; Sood, A. K.; Subrahmanyam, K. S.; Govindaraj, A. graphene: the new two-dimensional nanomaterial. *Angew. Chem.Int. Ed.* **2009**, *48*, 7752-7777.

4. Dikin, D. A.; Stankovich, S.; Zimney, E. J.; Piner, R. D.; Dommett, G. H. B.; Evmenenko, G.; Nguyen, S. T.; Ruoff, R. S. Preparation and characterization of graphene oxide paper. *Nature* **2007**, *448*, 457-460.

5. Higginbotham, A. L.; Lomeda, J. R.; Morgan, A. B.; Tour, J. M. Graphite oxide flame-retardant polymer nanocomposites. *ACS Appl. Mat. Int.* **2009**, *1*, 2256-2261.

6. Qi, X. Y.; Pu, K. Y.; Zhou, X. Z.; Li, H.; Liu, B.; Boey, F.; Huang, W.; Zhang, H. Conjugated-polyelectrolyte-functionalized reduced graphene oxide with excellent solubility and stability in polar solvents. *Small* **2010**, *6*, 663-669.

7. Kong, B. S.; Geng, J. X.; Jung, H. T. Layer-by-layer assembly of graphene and gold nanoparticles by vacuum filtration and spontaneous reduction of gold ions. *Chem. Commun.* **2009**, 2174-2176.

8. Sanchez-Jimenez, P. E.; Raj, R. Lithium insertion in polymer-derived silicon oxycarbide ceramics. *J. Am. Cer. Soc.* **2010**, *93*, 1127-1135.

9. Nouchi, R.; Tanigaki, K. Charge-density depinning at metal contacts of graphene field-effect transistors. *Appl. Phys. Lett.* **2010**, *96*, 253503-1-253503-3.

10. Watcharotone, S.; Dikin, D. A.; Stankovich, S.; Piner, R.; Jung, I.; Dommett, G. H. B.; Evmenenko, G.; Wu, S. E.; Chen, S. F.; Liu, C. P.; *et al.* Graphene-silica composite thin films as transparent conductors. *Nano Lett.* **2007**, *7*, 1888-1892.

11. De Arco, L. G.; Zhang, Y.; Schlenker, C. W.; Ryu, K.; Thompson, M. E.; Zhou, C. W. Continuous, highly flexible, and transparent graphene films by chemical vapor deposition for organic photovoltaics. *ACS Nano* **2010**, *4*, 2865-2873.

12. He, Q.; Sudibya, H. G.; Yin, Z.; Wu, S.; Li, H.; Boey, F.; Huang, W.; Chen, P.; Zhang, H. Centimeter-long and large-scale micropatterns of reduced graphene oxide films: fabrication and sensing applications. *ACS Nano* **2010**, *4*, 3201-3208.

13. Yu, A. P.; Roes, I.; Davies, A.; Chen, Z. W. Ultrathin, Transparent and flexible graphene films for supercapacitor application. *Appl. Phys. Lett.* **2010**, *96*, 253105-1-253105-3.

14. Liu, Z.; Robinson, J. T.; Sun, X. M.; Dai, H. J. PEGylated nanographene oxide for delivery of water-insoluble cancer drugs. *J. Amer. Chem. Soc.* **2008**, *130*, 10876-10877.

15. Sun, X. M.; Liu, Z.; Welsher, K.; Robinson, J. T.; Goodwin, A.; Zaric, S.; Dai, H. J., Nano-graphene oxide for cellular imaging and drug delivery. *Nano Res.* **2008**, *1*, 203-212.

16. Akhavan, O.; Ghaderi, E., Photocatalytic reduction of graphene oxide nanosheets on tio_2 thin film for photoinactivation of bacteria in solar light irradiation. *J. Phys. Chem. C* **2009**, *113*, 20214-20220.

17. Wang, L.; Lee, K.; Sun, Y. Y.; Lucking, M.; Chen, Z. F.; Zhao, J. J.; Zhang, S. B. B. Graphene oxide as an ideal substrate for hydrogen storage. *ACS Nano* **2009**, *3*, 2995-3000.

18. Graphene additive for drilling fluids. http://bit.ly/2bRU9C (accessed 21 March 2010).

19. Porretto, J. New technology aimed at increasing oil production. http://abcnews.go.com/Business/wireStory?id=8204044 (accessed 21 March 2010).

20. Hau, H. H.; Gralnick, J. A. Ecology and biotechnology of the genus shewanella. *Annu. Rev. Microbiol.* **2007**, *61*, 237-258.

21. Nealson, K. H.; Scott, J. Ecophysiology of the genus *shewanella*. in *the prokaryotes*, Dworkin, M.; Falkow, S.; Rosenberg, E.; Schleifer, K.-H.; Stackebrandt, E., Eds. Springer: New York, 2006; Vol. 6, pp 1133-1151.

22. Weisener, C. G.; Babechuk, M. G.; Fryer, B. J.; Maunder, C. Microbial Dissolution of Silver Jarosite: Examining its trace metal behaviour in reduced environments. *Geomicrobiol. J.* **2008**, *25*, 415-424.

23. Fredrickson, J. K.; Romine, M. F.; Beliaev, A. S.; Auchtung, J. M.; Driscoll, M. E.; Gardner, T. S.; Nealson, K. H.; Osterman, A. L.; Pinchuk, G.; Reed, J. L.; *et al.* Towards environmental systems biology of shewanella. *Nature Rev. Microbiol.* **2008**, *6*, 592-603.

24. Kosynkin, D. V.; Higginbotham, A. L.; Sinitskii, A.; Lomeda, J. R.; Dimiev, A.; Price, B. K.; Tour, J. M. Longitudinal unzipping of carbon nanotubes to form graphene nanoribbons. *Nature* **2009**, *458* (7240), 872-875.

25. Salas, E. C.; Berelson, W. M.; Hammond, D. E.; Kampf, A. R.; Nealson, K. H. The impact of bacterial strain on the products of dissimilatory iron reduction. *Geochim. Et Cosmochim. Acta* **2010**, *74*, 574-583.

26. Fredrickson, J. K.; Kota, S.; Kukkadapu, R. K.; Liu, C. X.; Zachara, J. M. Influence of electron donor/acceptor concentrations on hydrous ferric oxide (hfo) Bioreduction. *Biodegradation* **2003**, *14*, 91-103.

27. Gao, J.; Liu, F.; Ma, N.; Wang, Z.; Zhang, X. Environment-friendly method to produce graphene that employs vitamin c and amino acid. *Chem. Mater.* **2010**, *22*, 2213-2218.

28. Myers, C. R.; Myers, J. M. Cloning and sequence of cyma a gene encoding a tetraheme cytochrome c required for reduction of iron(iii), fumarate, and nitrate by shewanella putrefaciens MR-1. *J. Bacteriol.* **1997**, *179*, 1143-1152.

29. Meyer, T. E.; Tsapin, A. I.; Vandenberghe, I.; De Smet, L.; Frishman, D.; Nealson, K. H.; Cusanovich, M. A.; Van Beeumen, J. J. Identification of 42 possible cytochrome c genes in the shewanella oneidensis genome and characterization of six soluble cytochromes. *Omics* **2004**, *8*, 57-77.

30. Horvath, I. T.; Anastas, P. T. Innovations and green chemistry. *Chem. Rev.* **2007**, *107*, 2169-2173.

31. Guo, H. L.; Wang, X. F.; Qian, Q. Y.; Wang, F. B.; Xia, X. H. A green approach to the synthesis of graphene nanosheets. *ACS Nano* **2009**, *3*, 2653-2659.

32. Hummers, W. S.; Offeman, R. E. Preparation of graphitic oxide. *J. Am. Chem. Soc.* **1958**, *80*, 1339-1339.

33. Yang, D.; Velamakanni, A.; Bozoklu, G.; Park, S. J.; Stoller, M. D.; Piner, R. D.; Stankovich, S.; Jung, I.; Field, D. A.; Ventrice, C. A.; *et al.* Chemical analysis of graphene oxide films after heat and chemical treatments by x-ray photoelectron and micro-raman spectroscopy. *Carbon* **2009**, *47*, 145-152.

34. Kozlowski, C.; Sherwood, P. M. A. X-ray photoelectron spectroscopic studies of carbon-fiber surfaces. part 4. the effect of electrochemical treatment of nitric acid. *J. Chem. Soc. Farady Trans. I* **1984**, *80*, 2099-2107.